

Faculty of Science and Engineering
Department of Imaging and Applied Physics

Mapping and Monitoring The Environmental Impacts Of Mining Using
Hyperspectral Data

Cindy Chin Hui Ong

This thesis is presented as part of the requirements
for the award of Doctor of Philosophy of
Curtin University of Technology

2014

Certification

To the best of my knowledge and belief this thesis contains no material previously published by any other person except where due acknowledgment has been made. This thesis contains no material which has been accepted for the award of any other degree or diploma in any university.

Cindy C.H. Ong

February 2014

ACKNOWLEDGEMENTS

This study would not have been possible without the support of many, many organisations and people.

BHPBIO, PIRSA, Anglo American, MERIWA and the CSIRO Earth Observation Community provided the financial support for the research and development. I would especially like to thank Mark Piggott from BHPBIO for not only providing financial support but also sharing the vision of the operational use of hyperspectral sensing technology for mine environmental monitoring, for your wisdom, insights and crazy ideas but mostly your friendship.

Many colleagues at the DEC and DoIR provided much useful knowledge on regulation, environmental assessment and monitoring requirements for the mining industry. I would like to especially thank Bill Biggs for always having the time to advice and share, for your believe in the work I do, your enthusiasm, excitement and sharing the vision of operational use of the technology.

Colleagues at the Spectral Laboratories in the USGS in Denver provided assistance for the application of Tetracorder. I am most grateful to Gregg Swayze and Roger Clark for their help, good humour and warm jacket.

Having good mentors is one of the most important ingredients for a successful career. Two very important people who I believe are my strongest advocates and who totally believed I could complete this PhD are my Uncle M and Tony Milnes. Thank you for always having time to advise me, a listening ear and looking out for me all these years.

I believe I have been blessed with many colleagues and managers who have provided much support throughout my career as a remote sensing scientist. Thank you to colleagues from the Department of Environment especially Nick D'Adamo and Chris Simpson; Alex Wyllie and Red Shaw at DOLA; Michael Caccetta, Tom

Cudahy, Peter Hick, Erick Ramanaidou, Andrew Rodger, Lew Whitbourn, Brent McInnes and Chris Yeats at CSIRO.

I had the privilege of being part of the big family of Merv Lynch's physics students. I am most grateful to Merv for providing me the opportunity to undertake my PhD with him, being so patient and helpful especially in the last stages of my PhD with reviewing the thesis and other administrative assistance.

Thanks to Angelo Vartesi for helping me with the graphics. Thanks especially to Cheryl Harris for formatting and editorial assistance and for being the best PA.

Lastly, I am most grateful to my family who supports me unconditionally (even when I had to complete a thesis throughout the Christmas holidays!) and are always so proud of the work that I do.

Abstract

The use of multi-temporal remotely-sensed hyperspectral data for monitoring environmental conditions associated with mining activities is in its infancy and few publications provide the necessary workflow and guidelines to generate quantitative information. The goal of this thesis is to provide the environmental professional practicing in mine regulation and mining industry with quantitative tools to make informed decisions.

Two case studies for the application of hyperspectral remote sensing for environmental monitoring have been carefully selected, namely, Port Hedland and Brukunga. Port Hedland, located at 1640 km north of Perth, the capital of Western Australia, is a major iron ore bulk handling facility where dust contamination had been identified as a significant environmental issue. The focus on this test site was the monitoring of the iron-derived dust on the mangrove habitat. The second test site is the Brukunga abandoned pyrite mine, located 40 km east-south-east of Adelaide, the capital of South Australia. Brukunga has been classified as a major source of acid drainage in Australia and the study focus on monitoring the resulting pH related neoformed minerals.

Laboratory studies involve the collection of spectral data and ancillary independent measurements to assess the spectral behaviour of the materials critical for the monitoring. The laboratory data were used to build the algorithms for transforming hyperspectral data into environmental parameters. At Port Hedland, Partial Least Squares (PLS) analysis demonstrated that the dust deposition on leaves was linearly correlated to ferric oxides. The spectral algorithm relating the main ferric oxides absorption was valid for the two major mangrove species at Port Hedland. At Brukunga, PLS analysis indicated a significant linear relationship between spectral behaviour and pH-related neoformed minerals.

Airborne hyperspectral images were acquired over both test sites over an extended period of time. At Port Hedland, data were acquired over a 10 year time period and

there were four acquisitions at Brukunga. As a preamble to the airborne quantification, the influence of atmosphere, airborne hyperspectral sensors instrument spectral biases in particular mis-calibration and, flight planning were assessed. The CSIRO-AtComp atmospheric correction package associated with ground calibration provided the most accurate results. Wavelength recalibrations emphasised the importance of accurate instrument calibration as wavelength mis-calibrations of only 1-2 nanometres respectively for each of the instrument's detector can translated to a downstream impact of increasing the uncertainties in iron oxide dust levels by 34%. The examination of the impact of the changes with the instrument calibration indicates that the uncertainty in the iron oxide dust levels that may be introduced when the bandpasses and bandwidths vary is significant. The optimum region where bi-directional difference factor effect is wavelength-independent and multiplicative occurs between 760 and 1000 nm coincidental with the main ferric oxides absorption. The dust maps generated from this wavelength region from two adjacent flight lines shows a one-to-one relationship between the flight lines on the overlap area.

Validation of the environmental maps generated from the remotely-sensed hyperspectral data was performed by comparing an independent set of ground truth data to the airborne maps. The results of the validation indicated that (1) spectral data can be used to reliably produce ferric oxide dust maps with a small uncertainty; (2) acid drainage (AD) mineral maps produced using the Tetracorder software are 70.1% accurate; and, (3) validation of the pH maps generated from the airborne imagery indicate that pH can be reliably predicted using airborne hyperspectral data.

The environmental information product maps demonstrate the ability of remotely-sensed hyperspectral data to provide quantitative and spatially-comprehensive measurement of the critical environmental parameters. For example, the ferric oxide dust maps provided for the first time a regional view of the distribution of dust across Port Hedland handling facility. At Brukunga, the maps of the pH-related neoformed minerals provide environmental practitioners with a spatially-

comprehensive outlook of the entire mine that underpins the progress of rehabilitation efforts or pinpoint areas to concentrate efforts.

Table of content

Chapter 1	1
Introduction	1
1.1 <i>Thesis objectives</i>	3
1.2 <i>Hyperspectral sensing</i>	5
1.3 <i>Publications on the use of hyperspectral sensors for environmental assessment and monitoring of mines</i>	7
1.4 <i>Mining related environmental concerns in Australia</i>	8
1.4.1 Acid drainage, acid mine drainage, acid rock drainage and impacts on the Australian mining industry	9
1.4.2 Dust and its impact on the Australian mining industry	11
Chapter 2	15
Location of test sites, environment and landscape settings and data collection	15
2.1 <i>Port Hedland, Western Australia</i>	15
2.1.1 Climate	16
2.1.2 Source of dust	17
2.1.3 Landforms	17
2.1.4 Vegetation	18
2.1.4.1 Mangroves and their relevance	18
2.2 <i>Brukunga, South Australia</i>	20
2.2.1 Climate	21

2.2.2	Geology	22
2.2.3	Mining practices	23
Chapter 3	25
Instrumentation and spectral analysis and processing techniques	25
3.1	<i>HyMap</i>	25
3.2	<i>GER-IRIS Mk IV</i>	26
3.3	<i>ASD FieldSpec® Pro FR</i>	28
3.4	<i>PIMA</i>	29
3.5	<i>Analysis and processing tools</i>	30
3.5.1	Partial least square analysis.....	30
3.5.2	Parameterisation of spectral features	32
3.5.3	Pixel Mean Normalisation.....	33
3.5.4	Continuum removal.....	34
3.5.5	Atmospheric correction	34
Chapter 4	36
Laboratory studies	36
4.1	<i>Introduction</i>	36
4.2	<i>The Port Hedland dust case study</i>	36
4.2.1	Experimental procedures and issues addressed.....	37
4.2.2	Site and sample selection and preparation	45

4.2.3	Configuration of spectral measurements.....	47
4.2.4	Measurement of dust levels.....	47
4.2.5	Dust sample preparation and calculation of dust levels.....	48
4.2.6	Results.....	49
4.2.6.1	Impacts of the time difference between sample collection and measurement	49
4.2.6.2	Effectiveness of dust removal procedure	51
4.2.6.3	Relationship between spectra and dust measurements using PLS analysis	52
4.2.6.4	Relationship between spectra, via spectral parameterisation of the 900 nm ferric iron oxide crystal field absorption feature, and dust measurement	54
4.2.6.5	Relationship between dust levels on the adaxial and abaxial surfaces	57
4.2.6.6	Validation of dust algorithm	57
4.2.7	Conclusion and discussion	59
4.3	<i>The acid case study in Brukunga</i>	62
4.3.1	Methodology	62
4.3.1.1	Field sampling method.....	63
4.3.1.2	Spectral laboratory measurements	66
4.3.2	Chemical analysis.....	68
4.3.3	Results	69

4.3.3.1	Relationship between sample spectra and chemistry	69
4.3.4	Conclusion and discussion	72
4.4	<i>Summary</i>	72
Chapter 5	76
Quantifying the difference between atmospheric correction packages, impacts of flight planning and sensor biases		76
5.1	<i>Introduction</i>	76
5.2	<i>Method</i>	83
5.3	<i>Datasets used for analysis</i>	86
5.3.1	Airborne data.....	87
5.4	<i>Field spectral data acquired concurrent with airborne acquisition</i>	88
5.4.1	Port Hedland	88
5.5	<i>Results</i>	95
5.6	<i>Summary</i>	121
Chapter 6	124
Maps of environmental information products.....		124
6.1	<i>Introduction</i>	124
6.2	<i>Method</i>	124
6.3	<i>Airborne datasets analysed</i>	126
6.4	<i>Results</i>	127

6.4.1	Dust maps of Port Hedland, W.A.	127
6.4.2	Mineral maps of Brukunga, S.A.	136
6.4.3	pH maps of Brukunga, S.A.	142
6.5	<i>Summary</i>	145
Chapter 7		148
Validation of environmental information products.....		148
7.1	<i>Introduction</i>	148
7.2	<i>Method</i>	148
7.2.1	Validation for dust maps	149
7.2.2	Validation of Tetracorder mineral maps	151
7.2.2.1	X-ray diffraction (XRD)	151
7.2.2.2	Spectral interpretation	152
7.2.3	Validation of pH maps	154
7.2.4	Site location.....	154
7.3	<i>Results</i>	154
7.3.1	Dust map	154
7.3.2	Mineral maps.....	155
7.4	<i>Validation of pH maps</i>	158
7.5	<i>Summary</i>	159
Chapter 8		161

Detection of temporal variation	161
8.1 <i>Introduction</i>	161
8.2 <i>Method</i>	161
8.3 <i>Results</i>	163
8.4 <i>Summary</i>	179
Chapter 9	181
Conclusion and the implications of study for mine environmental monitoring.....	181
Appendices	188
A.1 A recipe for the environmental practitioner	188
A.2 Methods and uncertainties in chemical analysis of Brukunga samples	193
A.3 Airborne data acquired over Brukunga	194
A.4 Published outputs by the author on the current research.....	197
References	203

Table of Figures

Figure 1: Spectra of water, vegetation and soil in the visible to shortwave infrared range.....	6
Figure 2: Location map of Port Hedland in Western Australia and Brukunga in South Australia.	16
Figure 3: Mean (over a 56 year period) maximum and minimum daily temperatures, monthly rainfall and mean daily evaporation for Port Hedland. Data source: http://www.bom.gov.au/climate/averages/tables/cw_004032.shtml	17

Figure 4: Climatic chart for Mt. Barker (closest weather station to Brukunga). Data source: http://www.bom.gov.au/climate/averages/tables/cw_023733.shtml	22
Figure 5: Brukunga Mine Site layout (map reproduced from (Taylor and Cox, 2003).	24
Figure 6: HyMap sensor.....	26
Figure 7: Photo of the experimental set up showing the IRIS, location of lamp, Spectralon and samples.	27
Figure 8: ASD FieldSpec® Pro FR.....	28
Figure 9: PIMA-II spectrometer	29
Figure 10: Spectra of naturally clean (grey) and dusted (black) (a) topside and (b) underside of mangrove leaves measured with an GER-IRIS MkIV field spectrometer. The arrows show the location of the ferric iron oxide crystal field absorption feature at 860 nm. The 860 nm absorption indicates that the ferric iron oxide dust is hematite-rich and/or less than 20 µm in particle size (Cudahy and Ramanaidou, 1997).	40
Figure 11: A typical ferric iron oxide spectrum is plotted with crosses together with the third order polynomial curve fit of the spectrum plotted with a solid line. Note that the spectrum is a continuum removed spectrum. The minima of the curve is also marked. The depth of the 900 nm ferric iron oxide CFA feature illustrated on the graph.....	41
Figure 12: Photo showing a typical mangrove habitat at Port Hedland. Note the orientation of the leaves which show both the abaxial and adaxial surfaces. The photo also shows two depositional gauges which were used to measure the dust impact on the mangroves.	46
Figure 13: Photos showing a close-up view of mangroves used in this study. The left photo shows a tree affected by dust and the right shows a tree that was in an area that	

was not dusty. Note that the orientation of the leaves which show both the abaxial and adaxial surfaces.46

Figure 14: Spectra of a clean *Avecennia marina* leaf collected at Six Mile Creek that was subjected to heat stress over a period of two days. The red crosses show the average spectrum of leaf at the start of the experiment. The red dashed lines show range of the data. The blue crosses show the average spectrum of the leaf after one hour of exposure to heat stress. The blue dashed lines show the range of the data at that stage of the experiment. The magenta crosses show the average spectrum of the leaf at the end of the experiment after the leaf has been exposed to heat stress and left to dry for two days. The magenta dashed lines show the range of the data at the end of experiment.....50

Figure 15: Spectra of highly dusted leaves collected at Funicane Island and Burgess Point. The plot show the spectra of the same leaves after they have been cleaned compared with naturally clean collected in areas that were not affected by dust and cleaned leaves from at Six Mile Creek. These data were collected over three field trips on 5 August 2000, 12 November 2000 and 12-16 December 2001. The mean spectrum from each site on each date is plotted.51

Figure 16: Dust levels measured in laboratory plotted against dust levels predicted from spectral measurements for the calibration dataset.52

Figure 17: Final regression coefficient results from partial least squares analysis of dust quantity (black dots) and spectra plotted together with a typical dusted leaf spectrum (grey dots). The arrows illustrate significant final regression coefficient. 54

Figure 18: Relationship between mass per unit area and the depth of the CFA feature near 900 nm.55

Figure 19: Scatterplot of depth of the CFA feature near 900 nm for ferric iron oxide and the mass per unit area of dust on the leaves.56

Figure 20: Scatterplot of the levels of dust (based on the depth of the 900 nm ferric iron oxide CFA feature) on the abaxial and adaxial surface of <i>Avecinnia marina</i> leaves. Data collected in April, July, August and November 1999.	57
<i>Figure 21: Scatterplot of Actual vs predicted dust amounts for <i>Avecinnia marina</i> leaves.</i>	<i>58</i>
Figure 22: Scatterplot of actual versus predicted dust amounts for <i>Rhizophora stylosa</i> leaves.	59
Figure 23: Location of samples collected during the 1999 field campaign at Brukunga.	64
Figure 24: Location of samples collected during the 2001 field campaign at Brukunga.	65
Figure 25: The ASD FieldSpec® Pro FR configured for laboratory measurements of samples collected at Brukunga.	67
Figure 26: Plastic containers used for holding samples for spectral measurement.	68
Figure 27: Scatter plot of chemically determined pH measurements against spectral-predicted pH measurements for the calibration dataset. The predicted values were obtained by applying the PLS results to the spectral calibration dataset (laboratory ASD measurements).	70
Figure 28: Final regression coefficient (FRC) results from partial least squares (PLS) analysis of pH (yellow) and spectra plotted together with spectra collected in the field in Brukunga (red and orange) and some typical AD related secondary minerals from the USGS library (Clark et al., 2007) (dark blue, dark green, blue and cyan). The vertical lines illustrate significant coefficients from the PLS analysis.	71
Figure 29: Spectra of sand bank calibration target located at C.T.2 on Figure 32. The average of spectra acquired in 2002 is plotted in red and the green spectrum is the average of spectra acquired in 2006.	89

Figure 30: Differences between 2006 and 2002 for the sand bank calibration target (C.T.2).....	90
Figure 31: Average spectrum of the sand bank calibration target, C.T.2. The minimum and maximum of all the spectra measured are shown. The measurements were made in 2002 concurrent with airborne hyperspectral data acquisitions.	91
Figure 32: Map of Port Hedland. The locations of the calibration and validation target sites are identified on the map and labelled. C.T. denotes calibration and validation target. The brown areas show the confines of the port handling facility, the areas in green are areas of the township and blue indicate water or the sea.	93
Figure 33: Calibration/validation target C.T.1: Carpark at the boat ramp on Richardson St. in Port Hedland.....	94
Figure 34: Calibration/validation C.T.2: Coastal sand strip next to the Yacht Club on Sutherland St. in Port Hedland.....	94
Figure 35: Calibration/validation C.T.3: Large cleared surface on Wedge St., Port Hedland.	94
Figure 36: Calibration/validation C.T.4: Carpark on Wedge St., Port Hedland.	94
Figure 37: calibration/validation C.T.5: Internal road on the side of the conveyor and stockpile at Burgess Point in the BHPB port operations.....	94
Figure 38: Comparison between CSIRO-MODTRAN-SODA, FLAASH and HyCORR when applied to airborne hyperspectral data acquired in 2006. The blue, pink and green lines (axis on left hand side) show the ratio between the atmospherically corrected data and the ground truth data. The atmospheric transmittances are plotted (in black and axis on right hand side) to illustrate the relationship between the offsets remaining after atmospheric correction and the atmospheric constituents.	96

Figure 39: Comparisons for 1) with and without application of wavelength recalibration and 2) between CSIRO-MODTRAN-SODA and FLAASH. The airborne data shown were acquired in 2006.....98

Figure 40: Multi-temporal comparison of the ratio between ground truth and airborne reflectances for the sand bank site. The broken line indicates that the airborne data were acquired using the HyMap1 sensor while the solid line indicates data acquired using the HyMap2 sensor..... 102

Figure 41: Airborne hyperspectral data acquired on 13th November 1998. Adjoining flight line 2 (lower) and 3(upper) are shown here together with an illustration of the approximate position with respect to the imagery and a description of the sun azimuth (Az) and elevation (El) at the time of acquisition. The flight direction was approximately E-W. 103

Figure 42: Mean spectra of polygons of vegetated cover extracted from the overlap areas of adjacent flight lines acquired from airborne hyperspectral data on 13th November 1998. Note that the spectra shown are reflectance×100. ph2 on the legend indicate that the polygon was extracted from flight line 2 (lower image on Figure 41) and ph3 indicate that the polygon was extracted from flight line 3 (upper image on Figure 41). Following that, the legend indicates the cover type. For example, ph2:veg1 indicate cover type veg1 on flight line 2. 6 different vegetated cover types are shown namely veg1, veg2, veg3, veg4, veg5 and veg6..... 105

Figure 43: Mean spectra of polygons of non-vegetated cover extracted from the overlap areas of adjacent flight lines acquired by an airborne hyperspectral sensor on 13th November 1998. Note that the spectra shown are reflectance×100. ph2 on the legend indicate that the polygon was extracted from flight line 2 (lower image on Figure 41) and ph3 indicate that the polygon was extracted from flight line 3 (upper image on Figure 41). Following that, the legend indicates the cover type. For example, ph2:sand1 indicate cover type sand1 on flight line 2. 6 different non-vegetated cover types are shown namely sand1, sand2, sand3, stockpile, stockpile2, minesoil and rail. 106

Figure 44: Mean PMN spectra of polygons of vegetated cover extracted from the overlap areas of adjacent flight lines collected on 13th November 1998. ph2 on the legend indicate that the polygon was extracted from flight line 2 (lower image on Figure 41) and ph3 indicate that the polygon was extracted from flight line 3 (upper image on Figure 41). Following that, the legend indicates the cover type. For example, ph2:veg1 indicate cover type veg1 on flight line 2. 6 different vegetated cover types are shown namely veg1, veg2, veg3, veg4, veg5 and veg6..... 107

Figure 45: Mean PMN spectra of concurrent polygons of non-vegetated material extracted from the overlap areas of adjacent flight lines collected on 13th November 1998. ph2 on the legend indicate that the polygon was extracted from flight line 2 (lower image on Figure 41) and ph3 indicate that the polygon was extracted from flight line 3 (upper image on Figure 41). Following that, the legend indicates the cover type. For example, ph2:sand1 indicate cover type sand1 on flight line 2. 6 different non-vegetated cover types are shown namely sand1, sand2, sand3, stockpile, stockpile2, minesoil and rail. 108

Figure 46: Airborne hyperspectral data acquired on 24th April 1999. Adjoining flight line 2 (lower) and 3(upper) are shown here together with an illustration of the approximate position with respect to the imagery and a description of the sun azimuth (Az) and elevation (El) at the time of acquisition. 109

Figure 47: Mean reflectance spectra for polygons of vegetated cover extracted from the overlap areas of adjacent flight lines collected on 24th April 1999. Note that the spectra shown are reflectance×100. ph2 on the legend indicate that the polygon was extracted from flight line 2 (lower image on Figure 46) and ph3 indicate that the polygon was extracted from flight line 3 (upper image on Figure 46). Following that, the legend indicates the cover type. For example, ph2:veg1 indicate cover type veg1 on flight line 2. 6 different vegetated cover types are shown namely veg1, veg2, veg3, veg4, veg5 and veg6..... 111

Figure 48: Mean reflectance spectra for polygons of non-vegetated cover types extracted from the overlap areas of adjacent flight lines collected on 24th April 1999.

Note that the spectra shown are reflectance $\times 100$. ph2 on the legend indicate that the polygon was extracted from flight line 2 (lower image on Figure 46) and ph3 indicate that the polygon was extracted from flight line 3 (upper image on Figure 46). Following that, the legend indicates the cover type. For example, ph2:sand1 indicate cover type sand1 on flight line 2. 6 different non-vegetated cover types are shown namely sand1, sand2, sand3, stockpile, stockpile2, minesoil and rail..... 112

Figure 49: Mean PMN spectra for polygons of vegetated cover types extracted from the overlap areas of adjacent flight lines collected on 24th April 1999. ph2 on the legend indicate that the polygon was extracted from flight line 2 (lower image on Figure 46) and ph3 indicate that the polygon was extracted from flight line 3 (upper image on Figure 46). Following that, the legend indicates the cover type. For example, ph2:veg1 indicate cover type veg1 on flight line 2. 6 different vegetated cover types are shown namely veg1, veg2, veg3, veg4, veg5 and veg6..... 113

Figure 50: Mean PMN spectra for polygons of non-vegetated cover types extracted from the overlap areas of adjacent flight lines collected on 24th November 1999. ph2 on the legend indicate that the polygon was extracted from flight line 2 (lower image on Figure 46) and ph3 indicate that the polygon was extracted from flight line 3 (upper image on Figure 46). Following that, the legend indicates the cover type. For example, ph2:sand1 indicate cover type sand1 on flight line 2. 6 different non-vegetated cover types are shown namely sand1, sand2, sand3, stockpile, stockpile2, minesoil and rail..... 114

Figure 51: The ratio between the reflectances of corresponding polygon means of vegetated materials extracted from airborne hyperspectral data acquired in 1999 plotted with the final regression coefficient (FRC) results from partial least squares analysis of laboratory reflectance and dust levels. Note that two y-axis are shown. The one on the left of the chart shows the ratio and the one on the right is the FRC. 116

Figure 52: The ratio between corresponding polygons means of non-vegetated cover types extracted from airborne hyperspectral data acquired in 1999 plotted with the

final regression coefficient (FRC) results from partial least squares analysis of field data. Note that two y-axis are shown. The one on the left of the chart shows the ratio and the one on the right is the FRC. 117

Figure 53: Scatterplot of depth of 900 nm ferric iron oxide CFA feature extracted from adjacent flight lines of airborne hyperspectral data acquired in 1998 which exhibited minimum BRDF effects. 118

Figure 54: Scatterplot of depth of 900 nm ferric iron oxide CFA feature extracted from adjacent flight lines of airborne hyperspectral data acquired in 1999 which exhibited major BRDF effects. 118

Figure 55: Comparisons of airborne spectra acquired in 2006 after applying AtComp atmospheric correction (dashed lines), after removal of atmospheric residual effects (dotted lines) and ground truth (solid lines). 119

Figure 56: Comparison of PMN spectra acquired in 2002 on the ground (green), after applying a standard atmospheric correction (blue) and after removal of atmospheric offsets (magenta). 120

Figure 57: Comparison of PMN spectra extracted from a car park used as a uniform calibration target acquired on the ground (red) and atmospherically corrected and atmospheric offset removed airborne spectra from the 1998 (blue) and 1999 (green) airborne datasets. 121

Figure 58: Processing chain to be considered when using remotely-sensed data for quantitative multi-temporal monitoring. 123

Figure 59: Map of ferric iron oxide dust levels on mangroves and other vegetation surrounding Port Hedland harbour generated from the application of dust algorithms to airborne hyperspectral data acquired on 13th November 1998. The colour coding is such that cool colours (starting with dark blue) denote low dust levels and hot colours (ending with red) are high dust levels. The dust measurements are in units of

g/m^2 . The location of Burgess Point is indicated with B.P. and Funicane Island is at F.I. 130

Figure 60: Map of ferric iron oxide dust levels on mangroves and other vegetation surrounding Port Hedland harbour generated from the application of dust algorithms to airborne hyperspectral data acquired on 24th April 1999. The colour coding is such that cool colours (starting with dark blue) denote low dust levels and hot colours (ending with red) are high dust levels. The dust measurements are in units of g/m^2 131

Figure 61: Map of ferric iron oxide dust levels on mangroves and other vegetation surrounding Port Hedland harbour generated from the application of dust algorithms to airborne hyperspectral data acquired on 20th October 2002. The colour coding is such that cool colours (starting with dark blue) denote low dust levels and hot colours (ending with red) are high dust levels. The dust measurements are in units of g/m^2 132

Figure 62: Map of ferric iron oxide dust levels on mangroves and other vegetation surrounding Port Hedland harbour generated from the application of dust algorithms to airborne hyperspectral data acquired on 4th December 2004. The colour coding is such that cool colours (starting with dark blue) denote low dust levels and hot colours (ending with red) are high dust levels. The dust measurements are in units of g/m^2 133

Figure 63: Map of ferric iron oxide dust levels on mangroves and other vegetation surrounding Port Hedland harbour generated from the application of dust algorithms to airborne hyperspectral data acquired on 21st November 2005. The colour coding is such that cool colours (starting with dark blue) denote low dust levels and hot colours (ending with red) are high dust levels. The dust measurements are in units of g/m^2 134

Figure 64: Map of ferric iron oxide dust levels on mangroves and other vegetation surrounding Port Hedland harbour generated from the application of dust algorithms to airborne hyperspectral data acquired on 24th August 2006. The colour coding is

such that cool colours (starting with dark blue) denote low dust levels and hot colours (ending with red) are high dust levels. The dust measurements are in units of g/m^2	135
Figure 65: Multi-temporal series map of secondary AD minerals produced using data collected over Brukunga Pyrite Mine over a four year period mapped by Tetracorder using the SWIR region of the spectrum.	138
Figure 66: Multi-temporal series map of secondary minerals produced using data collected over Brukunga Pyrite Mine over a four year period mapped by Tetracorder using the VNIR region of the spectrum.	139
Figure 67: Rainfall chart for the period 1997 to 2001 collected at Mt. Barker meteorological station, closest to the Brukunga Mine. The rainfall data measurements are in millimetres. The star symbols depict the time of year of acquisition of the HyMap datasets.	141
Figure 68: pH maps generated from application of a predictive algorithm (produced from laboratory chemical and spectral measurements) to multi-temporal airborne hyperspectral data collected over the Brukunga Mine using the HyMap sensor. (A) indicates location of top waste rock dump, (B) the location of the acid treatment pond, (C) the middle waste rock dump, (D) the south-western mine benches and (E) the north-western mine floors.	144
Figure 69: Scatterplot of field measured dust values plotted against airborne extracted dust measurements.....	155
Figure 70: pH measured using chemical analysis plotted against pH values predicted on the airborne hyperspectral data.	159
Figure 71: 1 metre resolution ortho photo (red) overlaid with geographically-located HyMap image (cyan). Yellow, blue and green boxes show enlarged regions in the figure below.	164

Figure 72: Selected areas at the ends and middle of the flight line enlarged for clarity. Areas of white, black and grey are where the HyMap imagery agrees with the orthophotograph. Areas in red show the correct location and areas in light blue/cyan show displacement between the orthophotograph and the geographically-located HyMap imagery..... 164

Figure 73: Three adjacent flight lines shown in red, green and blue. The overlap areas appear as yellow and cyan. The yellow boxes show enlarged regions in the figure below. 165

Figure 74: Selected areas at the ends and middle of the flight line enlarged for clarity. Areas in yellow show agreement between the flight lines whereas areas of red or green show displacements between flight lines..... 165

Figure 75: Change map of dust levels on mangroves and other vegetation surrounding Port Hedland harbour derived from airborne hyperspectral data. The difference between dust levels generated from airborne hyperspectral data acquired on 13th April 1999 and 13th November 1998 is shown. The colour coding is such that cool colours (starting with purple) denote decreased levels in 1999 when compared with 1998 and hot colours (ending with red) are increased levels. The dust measurements are in units of g/m.² 170

Figure 76: Change map of dust levels on mangroves and other vegetation surrounding Port Hedland harbour derived from airborne hyperspectral data. The difference between dust levels generated from airborne hyperspectral data acquired on 4th December 2004 and 20th October 2002 is shown. The colour coding is such that cool colours (starting with dark blue) denote decreased levels in 2004 when compared with 2002 and hot colours (ending with red) are increased levels. The dust measurements are in units of g/m.² 171

Figure 77: Change map of dust levels on mangroves and other vegetation surrounding Port Hedland harbour derived from airborne hyperspectral data. The difference between dust levels generated from airborne hyperspectral data acquired on 21st November 2005 and 4th December 2004 is shown. The colour coding is such

that cool colours (starting with dark blue) denote decreased levels in 2005 when compared with 2004 and hot colours (ending with red) are increased levels. The dust measurements are in units of g/m^2 172

Figure 78: Change map of dust levels on mangroves and other vegetation surrounding Port Hedland harbour derived from airborne hyperspectral data. The difference between dust levels generated from airborne hyperspectral data acquired on 24th August 2006 and 21st November 2005 is shown. The colour coding is such that cool colours (starting with dark blue) denote decreased levels in 2006 when compared with 2005 and hot colours (ending with red) are increased levels. The dust measurements are in units of g/m^2 173

Figure 79: Change map of dust levels on mangroves and other vegetation surrounding Burgess Point derived from airborne hyperspectral data. The difference between dust levels generated from airborne hyperspectral data acquired on 4th December 2004 and 20th October 2002 is shown. The colour coding is such that cool colours (starting with dark blue) denote decreased levels in 2004 when compared with 2002 and hot colours (ending with red) are increased levels. The dust measurements are in units of g/m^2 174

Figure 80: Change map of dust levels on mangroves and other vegetation surrounding Burgess Point derived from airborne hyperspectral data. The difference between dust levels generated from airborne hyperspectral data acquired on 21st November 2005 and 4th December 2004 is shown. The colour coding is such that cool colours (starting with dark blue) denote decreased levels in 2005 when compared with 2004 and hot colours (ending with red) are increased levels. The dust measurements are in units of g/m^2 175

Figure 81: Change map of dust levels on mangroves and other vegetation surrounding Burgess Point derived from airborne hyperspectral data. The difference between dust levels generated from airborne hyperspectral data acquired on 24th August 2006 and 21st November 2005 is shown. The colour coding is such that cool colours (starting with dark blue) denote decreased levels in 2006 when compared

with 2005 and hot colours (ending with red) are increased levels. The dust measurements are in units of g/m^2 176

Figure 82: Change map of dust levels on mangroves and other vegetation surrounding Funicane Island derived from airborne hyperspectral data showing the difference in dust levels between 4.12.2004 and 20.10.2002. The colour coding is such that cool colours (starting with dark blue) denote decreased levels in 2004 when compared with 2002 and hot colours (ending with red) are increased levels. The dust measurements are in units of g/m^2 177

Figure 83: Change map of dust levels on mangroves and other vegetation surrounding Funicane Island derived from airborne hyperspectral data showing the difference in dust levels between 21.11.2005 and 4.12.2004. The colour coding is such that cool colours (starting with dark blue) denote decreased levels in 2005 when compared with 2004 and hot colours (ending with red) are increased levels. The dust measurements are in units of g/m^2 177

Figure 84: Change map of dust levels on mangroves and other vegetation surrounding Funicane Island derived from airborne hyperspectral data showing the difference in dust levels between 24.8.2006 and 21.11.2005 is shown. The colour coding is such that cool colours (starting with dark blue) denote decreased levels in 2006 when compared with 2005 and hot colours (ending with red) are increased levels. The dust measurements are in units of g/m^2 177

Figure 85: The columns show the rainfall data. The line graph plots the monthly throughput. The broken horizontal lines show the total throughput and the solid horizontal lines depicts the total throughput from the first major rain event to the time of the data acquisition. The graphs are colour coded so that red represents 2002, green 2004, blue 2005 and black 2006. Note that the black broken line denoting the 2006 total for year is slightly overlapped with the blue broken lines denoting 2005 total for year. 178

Figure 86: A recipe for the integration of hyperspectral data for environmental monitoring. 192

Figure 87: Location of calibration targets (reproduced from http://www.street-directory.com.au/sd_new/mapsearch.cgi).....	195
Figure 88: Bitumen	196
Figure 89: Bitumen close-up.....	196
Figure 90: Concrete pavers	196
Figure 91: Concrete pavers close-up.....	196
Figure 92: Concrete.....	196
Figure 93: Concrete close-up	196

Tables

Table 1: GPS locations of field sampling sites acquired in October 2002. The map projection is AGD66, zone 50.....	43
Table 2: GPS locations of field sampling sites acquired in 1999. The map projection is AGD66, zone 50.....	45
Table 3: GPS locations of calibration and validation targets. The map projection is AGD66, zone 50.....	92
Table 4: Additional uncertainties or measurement error expected to be caused by the atmosphere when using airborne hyperspectral data for measuring ferric iron oxide dust levels. Note that these uncertainties were only calculated for the atmospheric conditions during the 2006 acquisition in Port Hedland. These figures will obviously vary with different atmospheric conditions.	98
Table 5: Uncertainties in ferric iron oxide dust levels that may be introduced when the bandpasses and bandwidths vary from the ones used to develop the dust algorithm.	103

Table 6: Description and locations of depositional gauge sites (denote with *) and additional sampling sites collected in 1998.	150
Table 7: GPS locations of field sampling sites acquired in October 2002. Datum is AGD 66, zone 50.....	151
Table 8: Minerals related to AD and their three major peaks locations. Note that there are overlaps in peaks for some minerals. For example, goethite, hematite, pyrite, gypsum and bassanite have overlapping peaks at around 2.70-2.80 and goethite, epsomite and halotrichite have overlapping peaks at around 4.20-4.30. ..	152
Table 9: (a) Mineral identification from spectral data acquired from the air compare to samples collected on the ground. (b) Minerals mapped by Tetracorder applied to the airborne data compared with minerals identified from XRD. (c) XRD compared with spectral interpretation results obtained from samples collected in 1999. The dominant minerals that could be identified using XRD and spectra are listed. The colour code for each cell is shown to the right of each table. Note that the quantification of each mineral was not performed, only presence or absence.....	158
Table 10: Pixel displacements from 2006 dataset to historical HyMap dataset.	166
Table 11: Results of the evaluation of ENVI's automatic co-registration software. PH= Port Hedland	166
Table 12: Methods and uncertainties of chemical analysis performed on the Brukung samples taken from Amdel Labs.	193
Table 13: Minerals contained in samples collected in 2001. Mineralogical information derived from spectral data collected from the samples.....	197

LIST OF ACRONYMS AND ABBREVIATIONS

ACORN	Atmopheric CORrection Now Program
AD	acid drainage
AGD	Australian Grid Datum
AIOH	aluminium hydroxide
AMD	Acid Mine Drainage
AML	Abandoned Mined Lands
AMS	Airborne Multispectral Sensor
ANSTO	Australian Nuclear Science and Technology Organisation
ASD	Analytical Spectral Devices (often used here in reference to the FieldSpec Pro Full Range Spectrometer)
ATCOR	Atmospheric Correction Program
ATREM	ATmosphere REMOval Program
ARD	Acid Rock Drainage (also known as AMD - acid mine drainage and AD – acid drainage)
AVIRIS	Airborne Visible Infrared Imaging Spectrometer
BHPB	BHP Billiton
BHPBIO	BHP Billiton Iron Ore
BRDF	Bidirectional reflectance distribution function

CFA	Ferric iron oxide crystal field absorption
CO ₂	Carbon dioxide
CSIRO	Commonwealth Scientific and Industrial Research Organisation
DEC	Department of Environment and Conservation
DEM	Digital Elevation Model
DGPS	differential global positioning system
DOIR	Department of Industry and Resources
DTM	Digital Terrain Model
ENVI	Environment for Visualising Images (software package by ITT Visual Information Solutions formerly Research Systems Inc-RSI)
EL	Empirical Line
EPA	Environmental Protection Authority
EU	European Union
FCC	False Colour Composite
FOV	field of view
FLAASH	Fast Line-of-Sight Atmospheric Analysis of Spectral Hypercubes
FRC	final regression coefficient
FMG	Fortescue Mining Group
GER	Geophysical Environmental Research Limited
GIFOV	ground instantaneous field of view
GIS	Geographical information system

GPS	global positioning system
ha	hectares
HyMap	Hyperspectral Mapper
IAR	Internal Average Reflectance
IFOV	instantaneous field of view
IMU	inertial monitoring unit
InSb	indium antimony
InGaAs	indium gallium antimony
IRIS	Infrared Intelligent Spectrometer
ISPL	Integrated Spectronics Pty Ltd
LAVPD	Leaf to Air Vapour Pressure Difference
g/m^2	gram per square metre
MEND	Mine Environment Neutral Drainage
MINEO	Monitoring and assessing the environmental Impact of mining in Europe using advanced Earth Observation Techniques
MNF	Minimum Noise Fraction
MODTRAN	MODerate resolution atmospheric TRANsmission
Mt	million tonnes
NASA	National Aeronautics and Space Administration
NDVI	Normalise Difference Vegetation Index
NeDL	Noise Equivalent Radiance

NIST	National Institute of Standards and Technology
NIR	Near infrared
n	number of samples
<i>p</i>	significance
pH	a measure of the acidity or basicity of an aqueous solution
PIMA	Portable Infrared Mineral Analyser
PIRSA	Primary Resources and Industry South Australia
PLS	Partial Least Squares
PMN	Pixel mean normalisation
r^2	coefficient of determination
RMSEP	Root Mean Square Error of Prediction
RMSEC	Root Mean Square of Calibration
RSI	Research Systems Inc
SA	South Australia
SE	Standard Error
Si	Silicon
SODA	Second order derivative algorithm
SNR	Signal to noise ratio
sr	steradian
SWIR	Shortwave infrared

TE	thermoelectric
USEPA	United States Environmental Protection Authority
USGS	United States Geological Survey
UTC	Coordinated Universal Time
UTM	Universal Trans Mercator
UV	Ultraviolet
VIS	Visible
VNIR	Visible to near infrared
W	watt
WA	Western Australia
WGS	World Geodetic System
WRD	Waste rock dump
μmol	micromole
XRD	X-ray diffraction

Chapter 1

INTRODUCTION

The mining industry is one of the backbone of the Australian economy has contributed more than \$A 500 billion to the national wealth over the past 20 years (Lloyd et al., 2002). Australia is currently experiencing a mining boom with unprecedented increase of mineral and energy exports. The increase of mining activity has strongly impacted on the environment. Although environmental issues were not a major consideration 150 years ago, nowadays the community and regulatory bodies expect and demand that the mining industry applies the highest standards of environmental management to all projects.

Hyperspectral sensing technology is a relatively new form of passive remote sensing usually collecting contiguous spectra in the visible (VIS) to shortwave infrared (SWIR) or 450 – 2500 nm range. These new sensors provide calibrated spectra and hence, can potentially be used to provide quantitative and spatially-comprehensive environmental data on a routine basis.

The impediments to their use for mining-related environmental assessment and monitoring lie firstly in the scarcity of published information on the spectral behaviour of environmental properties and associated models to transform spectral data to environmental measurements. Secondly, there is a paucity of case histories demonstrating the ability to produce accurate and repeatable measurements from remotely-sensed hyperspectral data on a multi-temporal basis especially for monitoring environmental conditions associated with mining activities.

This study seeks to address the above concerns for the operational use of remotely-sensed hyperspectral data for mining-related environmental assessment and monitoring. Two case studies were undertaken examining the application of hyperspectral data for the monitoring of the mining industry's two main environmental concerns, namely, dust and acid drainage. The study involved two

aspects: laboratory and field studies to provide the fundamental understanding of the relationships between spectral data and the environmental properties of concern and to develop predictive algorithms to transform spectral data to environmental measurements; and, the processing requirements for the remotely-sensed data. This dissertation examines the issues that needed to be addressed to enable accurate environmental measurements to be generated and, determined the expected accuracy that may be achieved when using remotely-sensed hyperspectral data to generate environmental measurements. Further, there are relatively few publications providing the necessary workflows and guidelines on the use of hyperspectral data to generate quantitative information. These are provided at the Appendix A.1.

Published outputs by the author on the current research may be found listed at the Appendix A.4.

1.1 Thesis objectives

The mining industry in Australia are constrained by regulatory requirements to demonstrate that the environments surrounding mines and mining infrastructures are not adversely impacted by exploration and mining. The gathering of quantitative environmental measurements/data is a key components required to support environmental management and policies where the data are used for various purposes including determining baseline environmental conditions before the commencement of mining, routine monitoring and evaluation of status of the environment after closure of the mine and/or infrastructures. Currently, most of this information is obtained primarily based on field point sampling, collecting traverses across “representative” sites. This can introduce a host of uncertainties. The collection of such information is a labour intensive exercise and if different observers are employed and, especially over an extended period of time, the data quality may be subjective. The remoteness and inaccessibility of some landforms, such as mangroves habitats make these measurements not only difficult to make but may not always be representative. Furthermore, access sometimes can also be restricted because of cultural or environmental issues. Consequently, concern has been expressed by both the industry and regulators regarding the inadequacy of current methods of acquiring environmental measurements for assessment and monitoring. For example, (Biggs, 2004) stated four main challenges for regulators with current measurement tools. These are: the ability to obtain accurate and representative information which are consistent over time; the ability to compare information both spatially and temporally and to a known quality standard; and, the ability to deal with issues of contamination and pollution. This sentiment is echoed by industry environmental practitioners.

Therefore, there is a gap in the Australian and international mining community for cost-effective techniques that can routinely provide objective and accurate environmental measurements in a non-invasive and spatially-comprehensive manner. The hypothesis of this research is that hyperspectral remote sensing technology can

fulfil this gap especially with the advent of future satellite-borne hyperspectral sensors such as Environmental Mapping and Analysis Programme (Stuffer et al., 2009) (EnMap) and Hyper-spectral Imager SUite (HISUI) (Iwasaki et al., 2011) scheduled to be launched in the next six years.

This thesis seeks to address some of the impediments to the use of hyperspectral remote sensing technology for monitoring minesite environments. The main impediments identified relate to the scarcity of published information on the spectral behaviour of environmental properties and associated models to transform spectral data to environmental measurements. Also of concern was the paucity of case histories demonstrating the ability to produce accurate and repeatable measurements from remotely-sensed hyperspectral data on a multi-temporal basis especially for monitoring environmental conditions associated with mining activities. Further, there are relatively few publications providing the necessary workflows and guidelines on the use of hyperspectral data to generate quantitative information. Often publications on the technology are written for the hyperspectral specialist/spectroscopist. Therefore, this thesis is written with the intention of supporting with the environmental professional practicing in the mine regulation and mining industry in mind. The hope that, in some small way, it will assist in providing the necessary information and guidelines that the environmental practitioner may require to adopt hyperspectral remote sensing technology as an essential tool in the armoury of toolkits he/she requires for his/her work. It is hoped that in time and especially when hyperspectral remote sensing becomes more accessible to the community, this document will form the framework for the development of a manual or guidelines for regulators as well as environmental practitioners on the use of this technology in the mining industry.

The first part of the study is comprised of extensive field and laboratory research and development undertaken to investigate relationships between spectral data and the environmental properties of concern and to develop predictive algorithms to transform spectral data into these environmental measurements.

The second part of the study is concerned with atmospheric interferences and sensor biases/noise which will impact on the accuracy of the measurements when transferring the laboratory developed algorithm to data acquired using airborne sensors.

Thirdly, the predictive algorithms generated from the field and laboratory studies were applied to airborne data. Multi-temporal monitoring was demonstrated for seven datasets acquired for dust site and four for AD site monitoring. Validation of these products was undertaken to verify the predicted measurements and confirm the capabilities of the technology for monitoring purposes.

1.2 Hyperspectral sensing

Hyperspectral sensing is based on reflectance and emittance spectroscopy, the study of light intensity as a function of wavelength that has been emitted, reflected or scattered from a solid, liquid, or gas (Clark, 1999). Light has been studied since early times with the first records written by Greek philosophers and mathematicians [Empedocles (*c.* 490-430BC), Euclid (*c.* 300 BC)]. Spectral analysis or spectroscopy as we know it today began in 1861 with the interpretation by Roger Wilhelm Bunsen and Gustav Kirchhoff of the discovery of dark lines in the solar spectrum by Josef Fraunhofer as spectral absorption features (Born and Wolf, 1999).

Hyperspectral imaging, better known as imaging spectroscopy, especially in USA and Europe, is defined as the simultaneous acquisition of spatially co-registered images, in many, spectrally contiguous bands (>50), measured in calibrated radiance units, from a remotely operated platform (Schaeppman et al., 2006, Goetz, 2009). When used for quantitative analysis, the radiance data are usually reduced to reflectance, an intrinsic property of a target material necessary for spectral analysis (Clark et al., 2003a).

Hyperspectral sensors that are currently commercially available measure reflected light in the 450-2500 nm (visible to short wave infra-red (VNIR to SWIR)) range. These wavelengths and regions are depicted on Figure 1 together with the spectra of

water, vegetation and soil. The data are recorded usually from a light aircraft. Airborne hyperspectral sensors collect similar measurement to laboratory spectrometers commonly used for the measurement of materials such as paint (Newman, 1979) and grain (Finney, et. al., 1987; Shenk, et. al., 1992) for quality analysis. Swaths of discrete pixels of spectra are collected across a flight path while flying along the landscape to form images and pixel sizes down to 3 metre are obtainable.

Recent advances in the technology have lead to the development of airborne hyperspectral sensors that are of a quality comparable to laboratory spectrometers. These airborne instruments are radiometrically calibrated to NIST (National Institute of Standards and Technology; NIST (2008) certifications and therefore, the collection of data is quantitative, repeatable and traceable.

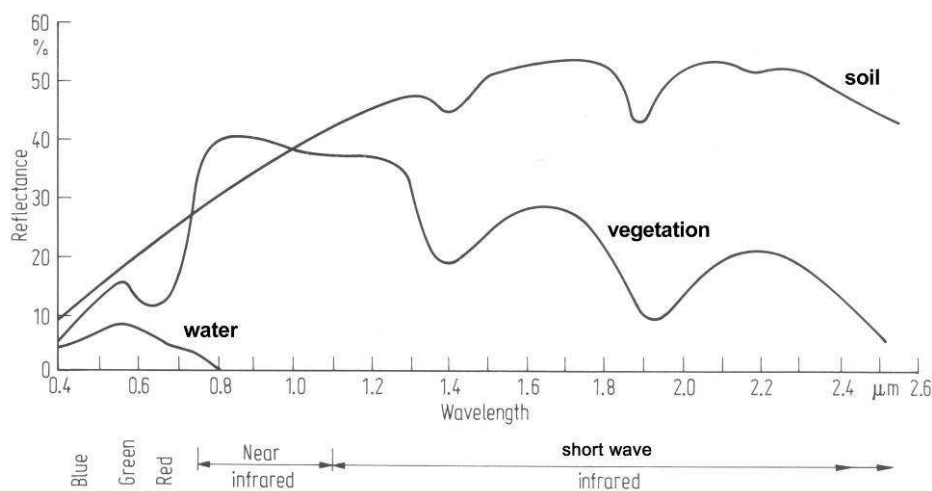


Figure 1: Spectra of water, vegetation and soil in the visible to shortwave infrared range.

Some commercially-available systems include Integrated Spectronic's HyMap (HyVista, 2008), NASA's AVIRIS (Lundeen, 2007), ITRES' CASI and SASI (ITRES, 2008).

1.3 Publications on the use of hyperspectral sensors for environmental assessment and monitoring of mines

The most well known investigations on the use of hyperspectral technology for mining related environmental mapping and assessments are two recent large-scale projects that were conducted in the USA and European Union (EU).

In the USA, the USEPA's Abandoned Mined Lands (AML) project (Slonecker and Williams, 2008, USGS, 2007) was conducted to demonstrate the capabilities of hyperspectral sensors and image processing to address land and environmental managers' requirements. Mapping of secondary minerals related to the acid drainage process were demonstrated with several case histories (Dalton et al., 2004, Rockwell et al., 2000, Rockwell et al., 1999, Swayze et al., 2000) and investigators used the resulting mineral maps in conjunction with other environmental field data to determine the potential contamination risk to the watershed. The cost-effectiveness of this technology was shown to translate to a time saving of two years and a cost saving of approximately US\$2 million for one of the test sites, Leadville (Swayze et al., 2000). There was no multi-temporal work conducted for this project.

The Monitoring and assessing the environmental Impact of mining in Europe using advanced Earth Observation Techniques (MINEO) project (Marsh, 2000) funded by the European Union was undertaken over a three year period costing €8 million. Hyperspectral data were acquired across six mining areas representing a range of environments, commodities being mined and stages in mine development. The project demonstrated the ability to map a variety of environmental impacts of mining including vegetation conditions/health, secondary minerals related to acid mine drainage processes, minerals located in the waste holding facilities such as tailings dams, possible contaminant sources, pathways and receptors, weathering of minerals, mineral-derived dust and water condition (Chevrel, 2003). Standard-off-the-shelf softwares were used for processing the data and generating environmental information maps. Most of the sites had only one dataset and hence multi-temporal monitoring was not demonstrated and verification results to quantify the accuracy of

the mapped products were not reported. The exception is a site in Germany where multi-temporal monitoring of vegetation stress, as a result of subsidence, was demonstrated. Follow on EU funded projects include the EO Miners (<http://www.eo-miners.eu/>) and ImpactMIN (<http://www.impactmin.eu/>) projects which were funded by the EU Framework 7 projects between 2010 and 2013.

Other studies (Ferrier, 1999, Hauff et al., 2003, Krüger et al., 1998, López-Pamo et al., 1999, Mars and Crowley, 2003, Peters et al., 2001, Williams et al., 2002, Rianza et al., 2012) reported in the literature focused mostly on mapping secondary minerals as a result of acid mine drainage processes. The studies mainly report on results obtained from a single dataset and hence do not demonstrate multi-temporal mapping capabilities except for (Rianza and Muller, 2010) and a parallel study by (Zabcic et al., 2009).

It is clear from the published literature that the applications of hyperspectral technology for mining environment applications were mostly one-off studies which were mainly used for assessment purposes. This highlights the gap in the literature documenting the use of the data for multi-temporal monitoring of mining-related environmental conditions.

1.4 Mining related environmental concerns in Australia

The mining industry's major impacts result from clearing, excavating and waste disposal. These practices can cause erosion and soil damage, air pollution, contamination, have adverse affects on the groundwater such as salinisation and acidification, cause loss of flora, fauna and habitat and introduce disease and pests (Wallis and Higham, 1998). Of these impacts, acid mine drainage (AMD) and dust production have been listed as two of the most significant issues facing the mining industry.

1.4.1 Acid drainage, acid mine drainage, acid rock drainage and impacts on the Australian mining industry

Acid rock drainage (ARD) is commonly defined as seepage, with a pH less than 5, originating from a tailings pile, a waste rock pile, or exposed sulfide-rich rock (Shaw et al., 1998). Other terms used for this condition are acid drainage (AD) and AMD. The oxidation process may be induced by a variety of geochemical agents but is usually associated with Fe-oxidising thiobacilli, the most common of which is *Thiobacillus Ferrooxidans*, at pH values below 4.5 (Bigham et al., 1996a).

Acidic waters formed by sulfide oxidation can precipitate a large suite of relatively soluble and insoluble Fe-bearing secondary minerals whose speciation is controlled by pH, degree of oxidation, moisture content, and solution composition (Swayze et al., 2000). With prolonged drying period, a suite of efflorescent salts are produced and when dissolved, will rapidly decrease the pH of acid waters and can result in short-term, catastrophic effects on metal loadings and on aquatic ecosystems (Hammarstrom et al., 2005).

The oxidation of sulfidic mine wastes and the consequent release of AD, is one of the main strategic environmental issues facing the mining industry in Australia (Harries, 1997). Results of a survey conducted from 317 operational and historic mine sites for that study, suggest that approximately 54 sites in Australia are managing significant amounts of potentially acid generating wastes. This means that more than 10% of the wastes are potentially acid generating or there is more than 10 million tonnes (Mt) of potentially acid generating waste. Furthermore, approximately 62 additional sites are managing some potentially acid generating waste equivalent to less than 10% of the total waste and less than 10 Mt.

The additional cost of managing potentially acid generating waste at operating mine sites for the Australian mining industry is estimated to be about \$60 million per year. This includes the costs of cover installation, selective placement of wastes, additional waste characterisation and water treatment as appropriate. The total cost

of managing potentially acid generating mine waste from current mines over a 15 years period was estimated in 1997 to be \$900 million.

Internationally, the costs are significantly more. For example, the Canadian Mine Environment Neutral Drainage (MEND) program estimates the total liability costs for potentially acid generating waste at mine sites in Canada to be C\$2 to C\$5 billion. The Canadian liability represents the cost of remediating the currently estimated inventory of acid generating wastes in Canada. The amount of potentially acid generating mine wastes in Canada is similar to the amount in Australia, but the estimated costs of remediation for Canadian sites is three to five times greater than for Australian sites.

Brukung mine site in South Australia (35° 0'10.56"S, 138°56'31.96"E) is classified together with Rum Jungle in North Territory, Mt Lyell in Tasmania, Captains Flat in New South Wales and Mt Morgan in Queensland as major sources of AD in Australia. This classification can be attributed to several factors including the size and acid generating potential of the exposed waste rock dumps (8 million tonnes consisting of 2% sulfur), exposed quarry benches and tailings storage facility (3.5 million tonnes containing 1.7% sulfur) (Taylor and Cox, 2003). A study conducted by (Agnew, 1994) found that there is potential for 300 000 tons of sulfuric acid to form in Brukung. Further, the Australian Nuclear Science and Technology Organisation (ANSTO) concluded from field trials conducted in 1993-94 at Brukung that the natural oxidation of pyritic minerals may continue to produce acid conditions for a period of 240 to 750 years. The downstream impacts of the Brukung mine site on the community is significant because of the mine's proximity to the town and the Dawesley Creek which runs parallel to the mine is used for agricultural and recreational purposes. A water monitoring program has been in operation collecting data downstream of Dawesley Creek since 1996 (Randall and Cox, 2003). The most recent remediation strategy implemented was the Dawesley Creek diversion project undertaken in 2003, designed to increase the quality of water downstream of the Brukung Mine. The diversion consists of 1.7 km long pipes and the aim was to prevent uncontaminated creek water from mixing with run-off water

from the mine site. The combination of its classification and environmental significance, availability of environmental data and continual remediation effort, made this abandoned mine a unique site to investigate and demonstrate the application of hyperspectral sensing technology for monitoring the AD conditions.

There has been an abundance of studies reported where minerals maps were produced for a single date (Dalton et al., 2004, Ferrier, 1999, Hauff et al., 2003, López-Pamo et al., 1999, Mars and Crowley, 2003, Peters et al., 2001, Rockwell et al., 2000, Shang et al., 2002, Swayze et al., 2000, Williams et al., 2002) using airborne hyperspectral data and, some studies based on laboratory spectral measurements (Kemper and Sommer, 2002, Viscarra Rossel et al., 2006, Chang et al., 2001), but, there are limited published results on the use of remotely-sensed hyperspectral data for multi-temporal monitoring. Recently, (Riaza and Muller, 2010) showed the feasibility of the use of hyperspectral data as climate change indicators.

For hyperspectral data to be useful for environmental practitioners, they must be translated to environmental measurements. In AD, the pH level is of importance but there is a lack of published data which extends the mineralogical mapping to pH mapping except for a parallel study by (Zabcic et al., 2009) which extends the work to another geological environment.

1.4.2 Dust and its impact on the Australian mining industry

Dust derived from the mining and handling of mineral ore has been identified as a major concern for the mining industry in Australia and may be critical to the future viability of a variety of resource industries (CSIRO, 1999). This statement was validated by the incident that arose at the Esperance Port in early December 2006, where approximately 4000 birds were found dead (DEC, 2010). Subsequent investigations tracked the source of the deaths to fugitive lead dust arising from the handling of lead carbonate from the Magellan mine at the Esperance port facilities. Further, mass deaths in March 2007 compelled the Port Authority to halt the handling of lead carbonate ore, threatening to close down the mine. This incident

highlighted among other things, the pressing need for timely, accurate and spatially comprehensive measurements of dust derived from handling of minerals at ports. Investigations by the Department of Environment and Conservation (DEC) to determine the causes of the bird casualties revealed that the likely cause of the deaths was lead poisoning. In April 2007, the transport to and handling of lead carbonate ore from the Magellan Mine to the Port of Esperance was confirmed as the source of lead. The Port Authority was required to provide three-monthly air quality reports to DEC. It appears that a report due on 1st November 2006 was late resulting in the DEC not receiving crucial monitoring data on lead carbonate levels, which were well above historic levels, until 31st January 2007; well after the bird deaths occurred. Also, one of the methods of dust monitoring used at Esperance is dust depositional gauges. This method of monitoring dust deposition has been found to be inaccurate (Hall et al., 1994).

Considering that the resources industry is the backbone of WA's economy and that the ports of WA handle half of Australia's exports by volume (three of which handle the three largest tonnages) there is a pressing demand to find a solution for more effective and efficient monitoring of the ports in order for the mining industry to operate in a sustainable manner.

BHP Billiton Iron Ore (BHPBIO) has been processing iron ore through its facilities at Port Hedland (20°18'41.86"S, 118°34'30.93"E) since 1965 and shipping tonnages have steadily increased over the years to the current levels which are in excess of 100 million tonnes per annum.

Dust emanating from the BHPBIO's processing and shipping operations has been a long standing environmental and community issue at Port Hedland (Ecoscape, 2004). It remains a topical issue with proposals to expand the BHPBIO facility, a new iron ore facility for Fortescue Mining Limited and other commodities such as manganese and salt (ABCNews, 2005). A recent study (Physick, 2001) found that for three

months in 1998, the monthly maximum particulate concentration (PM10¹) recorded at the Boodarie air quality monitoring station, located close to the BHPBIO Boodarie Briquette Plant (20°22'4.06"S, 118°33'30.71"E) exceeded the National Environment Protection Measures (NEPM) standard. However, it was deducted that this condition may be mainly derived from dust raised from the surface; that is, recirculated dust.

One of the main concerns at Port Hedland is whether the dust from the industrial activities has contributed to 'dieback' of mangroves in Stingray Creek and on the south side of Finucane Island (Ecoscape, 2004). A study by (Paling et al., 1996) found that there were no direct link between the dust and mangrove dieback nor have heavy metals around Port Hedland been found to be elevated above regional levels. In 1995 BHPBIO in consultation with the Department of Environment and the community undertook a comprehensive dust management review (BHP, 1996) that identified the additional need to assess the impact of deposited dust on mangroves around Port Hedland harbour.

In 1996, BHPBIO implemented a dust deposition monitoring program using non-directional gauges to measure the dust fallout on the mangroves. The gauge is a well-accepted method that was initially developed in the 1920s (Standard, 2003). Ten sites, each with four gauges, were established but the many risks and physical difficulties of working in the mangroves, such as deep mud and tides, the threat of disease-infested insects (Ross-River virus), the labour-intensive nature of regularly checking the gauges, plus the questionable accuracy of the gauges, prompted BHPBIO to search for a better method of monitoring and assessing the dust. Environmental professionals at BHPBIO were concerned about the lack of quantitative information on the composition and concentration as well as spatial coverage provided by this field-based technique.

Hyperspectral remote sensing technology was seen as one of the potential technology that could address some of the shortcomings of the dust monitoring

¹ Particulate matter measured in the range of 0 to 10 microns. Measurements are in µg/m³.

because vegetation and the material being handled, that is, ferric iron oxide, both have diagnostic spectral signatures and the remotely sensed data can potentially provide spatially-comprehensive measurements of the distribution of the dust. A survey of the literature showed that there is comprehensive understanding of spectral behaviour of ferric iron oxides (Cudahy and Ramanaidou, 1997, Curtis, 1985, Ramanaidou et al., 2008) and there has been research undertaken on the use of hyperspectral data for dust monitoring for applications outside of monitoring dust on leaves (Chudnousky and Ben-Dor, 2008, Chudnovsky et al., 2009, Chudnovsky et al., 2011) but there are no published results on the spectral behaviour of ferric iron oxide on mangrove leaves or the quantification of the dust levels on the leaves.

Chapter 2

LOCATION OF TEST SITES, ENVIRONMENT AND LANDSCAPE SETTINGS AND DATA COLLECTION

2.1 Port Hedland, Western Australia

Port Hedland (location map shown on Figure 2) is approximately 1640 km north of Perth, the capital of Western Australia. The township of Port Hedland is situated adjacent to the Port facilities. These facilities handle a range of commodities including iron ore, manganese, salt, copper, feldspar and petroleum (Ecoscape, 2004). However, the major throughput is iron ore. BHP Billiton Iron Ore (BHPBIO) has been processing iron ore through its facilities since 1965 and shipping tonnages have steadily increased over the years to the current levels in excess of 100 million tonnes per annum. The iron ore from BHPBIO's seven operating mines (Mount Whaleback is one of the world's biggest mining operations) reaches Nelson Point after a 426 km journey on the longest privately operated railroad in Australia. The ore is then screened and crushed to contract size in two ore handling plants named Burgess Point and Funicane Island. Crushed ore is stockpiled before being reclaimed and conveyed to the ore pier where four ship loaders feed the material into ore carriers of up to 160 000 tonnes dead weight. The ore is destined for the steel mills of Australia and world markets including Japan, China, South Korea, Taiwan and Europe. Recently, the third major iron ore player in the industry, Fortescue Mining Ltd, commenced exportation of its ore through Port Hedland.



Figure 2: Location map of Port Hedland in Western Australia and Brukunga in South Australia.

2.1.1 Climate

Port Hedland is located in the arid Tropics of Western Australia. It experiences dry winters and wet summers as indicated on Figure 3. Over a period of 56 years, the records indicates that in summer (December to February), the average maximum temperature is 36°C with an average minimum temperature of 25°C. In winter (June to August), the average maximum temperature is 28°C with an average minimum temperature of 13°C. Although temperatures are warm all year round, rainfall is plentiful during summer (average of 59 mm) and scarce in winter (5 mm).

Port Hedland is located on the Pilbara coast which experiences more tropical cyclones than any other part in Australia. It has been severely impacted by cyclones with 49 cyclones with gale-force wind recorded for Port Hedland since 1910. This is equivalent to one cyclone every two years, and of these, seven caused winds in excess of 170 km/h (BOM, 2008).

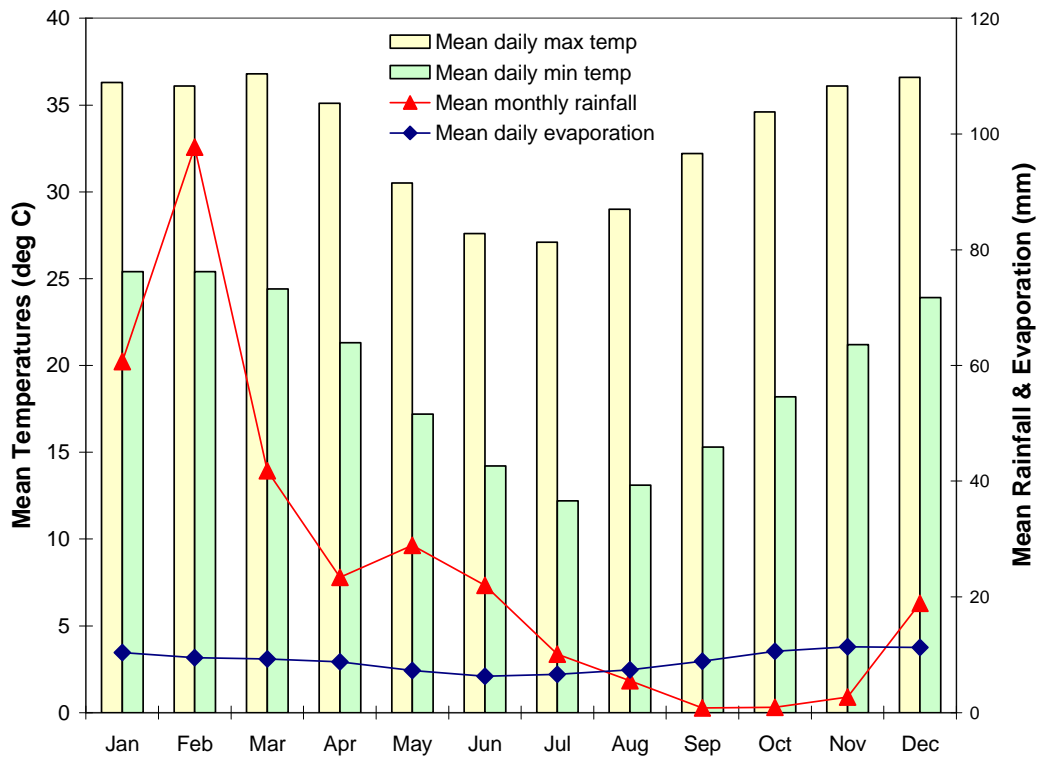


Figure 3: Mean (over a 56 year period) maximum and minimum daily temperatures, monthly rainfall and mean daily evaporation for Port Hedland. Data source: http://www.bom.gov.au/climate/averages/tables/cw_004032.shtml

2.1.2 Source of dust

The iron ore being handled at Port Hedland originates from the iron ore mines located in the Hamersley Province and include the bedded and channel iron deposits (Ramanaidou and Wells, 2012).

2.1.3 Landforms

Port Hedland is situated at the northern margin of the Archean Pilbara Craton within the granite-greenstone terrain. Exposures of granitic bedrock occur inland, separated by a variety of alluvial floodplain deposits associated with the Turner River. The alluvial deposits are siliceous and are derived from the granitic source rocks. Underlying the floodplain deposits are older deltaic sediments associated with ancient drainage systems (PHPA, 2003).

The Port Hedland harbour is located within a low lying tidal flat environment which supports mangrove mud flats. These flats are often separated by beach ridges containing calcareous deposits in the form of eolian dunes and limestone rock platforms/ridges.

The extensive alluvial plains along the coast were mapped by (Beard, 1975) as mostly sand.

(Craig, 1983) identified three coastal landforms in the Pilbara and describes them as:

- Dune ridges formed by vegetation trapping wind-blown sand (an example in the vicinity of Port Hedland is the small hill behind the boat ramp on Finucane Island);
- Storm ridges on the landward side of tidal flats formed by cyclone-generated storm waves (examples can be found at the edges of the mangroves around Port Hedland); and,
- Cheniers which are discrete ridges formed on the tidal flats during storms or low riverine flows (examples of which are amongst the mangroves around Port Hedland).

2.1.4 Vegetation

The coastal vegetation complex is a terrestrial environment gradually merging into a marine environment in a maze of tidal lagoons, samphire flats and mangroves. The three main vegetation communities along the Port Hedland Coast are mangroves, mudflats and spinifex steppes. The vegetation patterns tend to occur as a mosaic consisting of tidal and dune systems, rather than a catenary (regular repeating) sequence because of the lack of topography in the area (Beard, 1975).

2.1.4.1 Mangroves and their relevance

Port Hedland harbour is a complex estuarine system with significant environmental value. Various species of marine organisms including diatoms, plankton, infauna,

epifauna, reptiles and fish are common within the harbour and adjacent waters. A number of listed migratory and threatened species exist in the Port Hedland harbour area including the flatback turtle (*Natador depressus*), the black-ringed sea snake (*Hydrelaps darwiniensis*) and the white-bellied sea eagle (*Haliaeetus leucogaster*) (Wilson, 2008).

The harbour and approach channel for the handling facility was constructed between 1965 and 1976 where some 22.8 million cubic metres of material were removed. Further dredging continued in 1983 when 12.8 million cubic metres of sand and rock was removed to further deepen and widen the channel as well as to extend it some 21 km out to sea (Wallace, 2002). The wide variety of mangrove species in the harbour act as a major source of food and shelter for the marine and terrestrial fauna. Further, they provide a major source of nutrients for the coastal marine environment and stabilise the coastal sediments (Wilson, 2008).

There are approximately 4800 hectares of mangroves across the BHPBIO harbour facility. The dominant mangrove species found around the Port Hedland area are:

- White Mangrove (*Avicennia marina*);
- Club Mangrove (*Aegialitis annulata*);
- River Mangrove (*Aegiceras corniculatum*);
- Spotted-leaved Red Mangrove (*Rhizophora stylosa*),
- Yellow-leaved Spurred Mangrove (*Ceriops tagal*);
- Myrtle Mangrove (*Osbornia octodonta*); and,
- Ribbed-fruited Orange Mangrove (*Bruguiera exaristata*).

(Semenuik et al., 1978).

The distribution of individual mangrove species within a mangrove community is influenced by: the frequency of flooding, soil type, soil salinity, drainage, plant interactions; and animal interactions. This leads to mangrove communities generally containing 2–6 zones, depending on soil and rainfall (Semenuik et al., 1978).

Typical mangrove zonation identified at Port Hedland range from the ocean to the landward salt marshes consisting of:

- Seaward *Avicennia marina*;
- *Rhizophora stylosa*;
- *Ceriops tagal*; and,
- Landward *Avicennia marina*.

(Semenuik et al., 1978)

2.2 Brukunga, South Australia

The abandoned Brukunga Pyrite Mine is located 4 km north of Nairne in the Mount Lofty Ranges and is 40 km east-south-east of Adelaide, the capital of South Australia (see Figure 2). Following a world shortage of sulfur, the Nairne Pyrites Ltd, formed from three fertiliser companies, developed the mine in 1951 to mine pyrite for the manufacturing of superphosphate fertiliser. The richest pyrite zones were mined and a concentrate was produced for processing into sulfuric acid at Port Adelaide. The acid was used to convert insoluble rock phosphate into a soluble fertiliser (PIRSA, 2005).

The township of Brukunga was built to house employees, and the quarry, crushing and treatment plant began operations in 1955. About 300 000 tonnes of ore were mined annually, and pyrite concentrate was railed to the Sulfuric Acid Pty Ltd plant at Birkenhead, a northwestern suburb of Adelaide. The Commonwealth Government underpinned the operation by agreeing to pay a subsidy if the market price of sulfur fell below a certain level, but this was abolished in 1966. By the early 1970s, cheap sulfur was being purchased from natural gas refineries in Canada, and pyrite production at Brukunga ceased in 1972. During the life of the mine 5.5 Mt of ore averaging 11% sulfur were treated for the recovery of 1.3 Mt of concentrates and over 8 Mt of overburden and waste were removed (PIRSA, 2005).

For two decades the Government has operated an acid-water treatment plant at Brukunga to reduce the level of heavy-metal pollution occurring in Dawesley Creek.

Pollution results from the leaching of sulfide minerals contained in the overburden waste-rock dumps and tailings dump that were discarded during mining and milling. The government of South Australia recently committed substantial funding towards the rehabilitation of the historic mine site. Over a three year period (2000-2003), \$5.1 million was spent on the diversion of Dawesley Creek water past the mine site, and the commissioning of a supplementary acid-water treatment plant. The aim of the project was to reduce the heavy-metal pollution in Dawesley Creek to achieve water quality suitable for livestock watering and irrigation use (BMSRB, 2001).

Subsequent to 2003, \$21.1 million or \$3.0 million per annum will be committed over a seven years period to relocating the rock dumps back onto the old quarry bench where they will be blended with limestone to neutralise the dumps. The dumps will be landscaped and planted with native vegetation to form a stable land surface (BMSRB, 2001).

2.2.1 Climate

The climate at Brukunga is essentially Mediterranean with cool wet winters (average temperatures between 14 and 5°C, average rainfall of 103 mm) and warm-hot dry summers (average temperatures between 26 and 11°C, average rainfall of 27 mm). The average rainfall is 766 mm/annum and pan evaporation is 1100 to 1400 mm/annum. Figure 4 shows the climate of Brukunga.

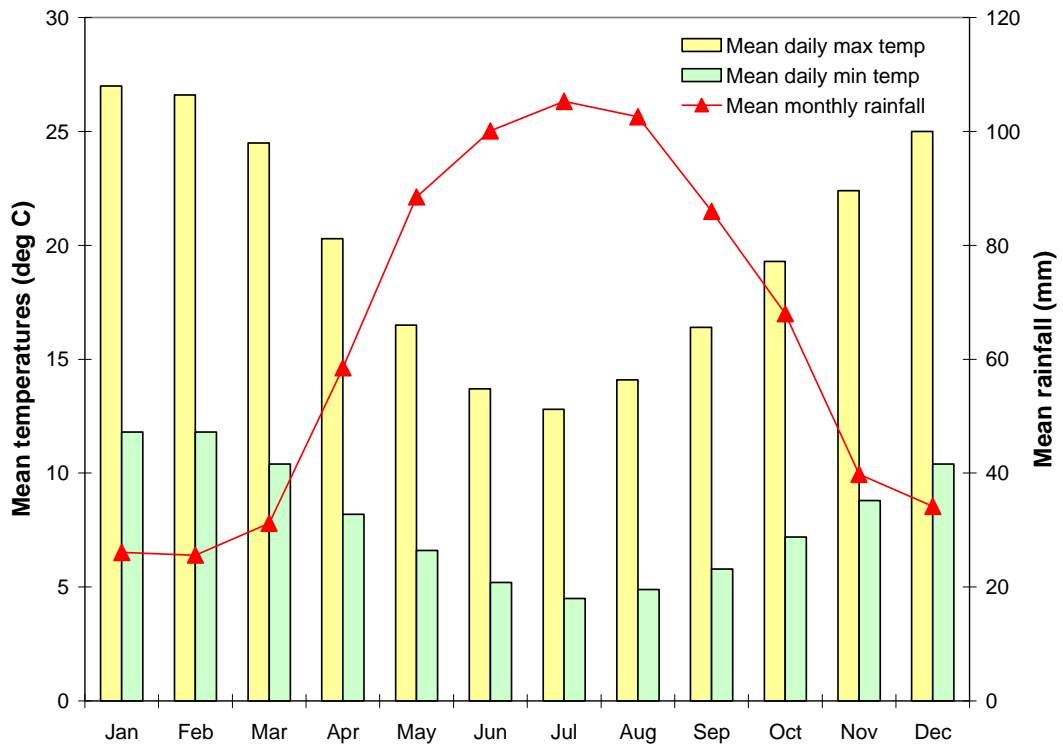


Figure 4: Climatic chart for Mt. Barker (closest weather station to Brukunga). Data source: http://www.bom.gov.au/climate/averages/tables/cw_023733.shtml.

2.2.2 Geology

The host rock of the pyrite ore is the Talisker Calc-siltstone of the Cambrian Lower Kanmantoo Group. This consists of a metamorphosed phyllite with calc-phyllite interbeds (Gravestock and Gatehouse, 1995). The Nairne Pyrite Member from which the pyrite was mined is located in the lower part of the formation. It also hosts several small-scale base-metal deposits.

The iron-sulfide mineralisation occurred as three steeply-E-dipping conformable lenses separated by waste beds. Each of the 15 -30 m thick ore zones consisted of iron sulfide-bearing muscovite schists and gneisses with minor lenses of calcsilicate and quartz plagioclase metasediments. The waste zones consisted of quartz plagioclase granofels and minor calcsilicate granofels, muscovite schists and gneisses. The lenses outcropped as ferruginous gossans with weathering to a depth of 18 m (LaGanza, 1959). The mineralisation was pyrite and pyrrhotite with minor

sphalerite, chalcopyrite, galena and arsenopyrite which are sources of arsenic, cadmium, copper, zinc, antimony, lead, nickel, tin, barium, cobalt, manganese and sulfate (Burt and Gum, 2000b, Burt and Gum, 2000a).

2.2.3 Mining practices

The mining was undertaken by quarrying into the eastern flank of a hillside which forms the western side of a valley traversed by Dawesley Creek, a tributary of the Bremer River. The current layout of the mine site is shown on Figure 5. The quarry runs N-S and is approximately 1800 m long and 150 m wide. On the far west of Figure 5, it consists of an exposed foot-wall and main bench with two deep slots excavated to access deeper ore. Waste rock was placed in two large dumps on the western side of Dawesley Creek and a smaller dump on the eastern side. Material containing more than five per cent sulfide was regarded as ore and processed on site. Tailings were deposited in a valley-fill storage facility on the eastern side of Dawesley Creek (Taylor and Cox, 2003).

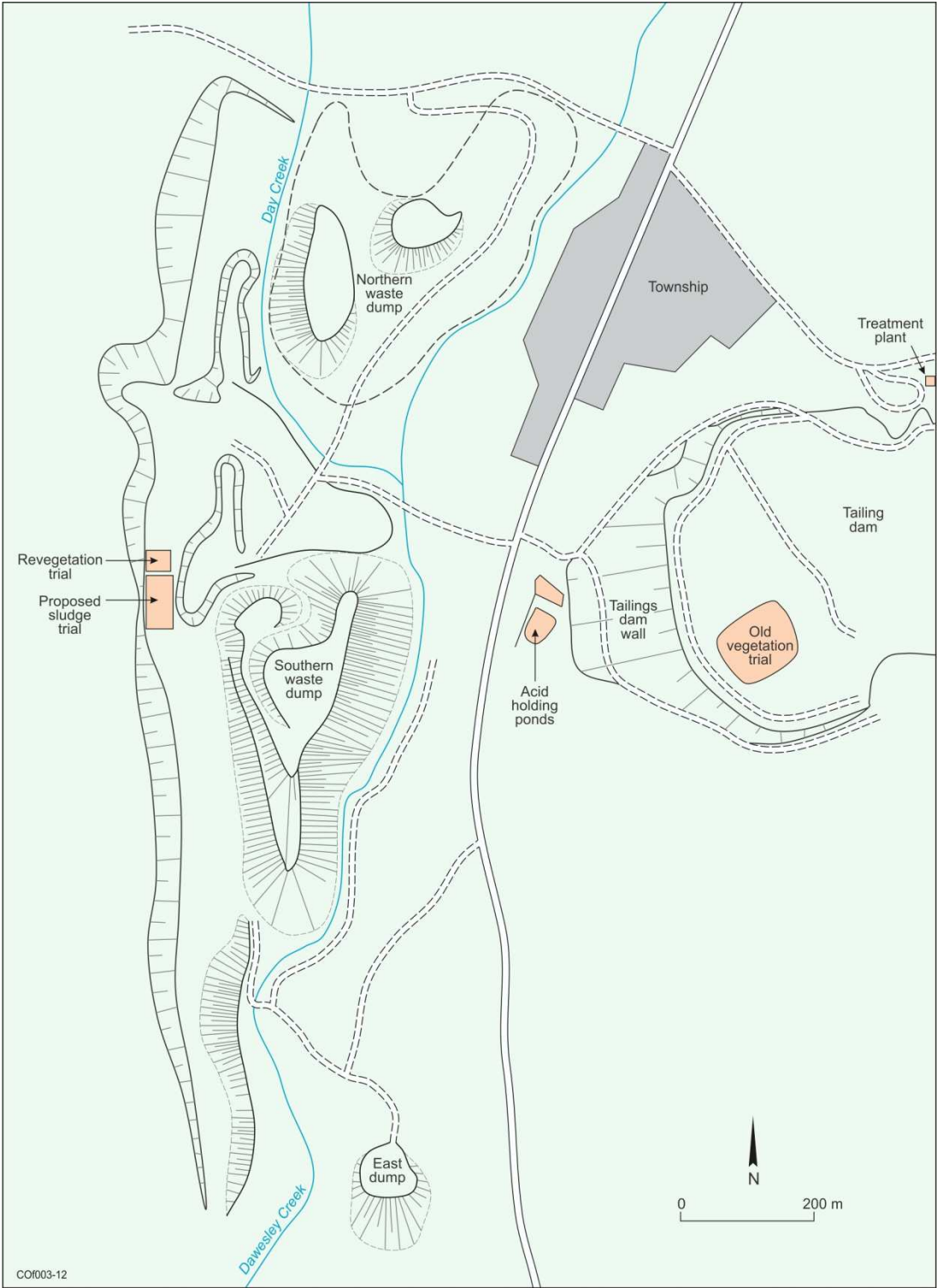


Figure 5: Brukunga Mine Site layout (map reproduced from (Taylor and Cox, 2003).

Chapter 3

INSTRUMENTATION AND SPECTRAL ANALYSIS AND PROCESSING TECHNIQUES

3.1 HyMap

The HyMap instrument (Cocks et al., 1998, HyVista, 2008) manufactured by Integrated Spectronics measures 128 bands across the reflective solar wavelength region of 450 – 2500 nm with contiguous spectral coverage (except in the atmospheric water vapour bands) with bandwidths between 15 – 20 nm. The HyMap sensor is an optomechanically scanned system incorporating spectrographic/detector array modules, an on-board reference lamp and a shutter synchronised to scan line readouts for dark current monitoring.

There are three detectors covering the 450 – 2500 nm spectral range with one in the visible to near infra red range (a 64 array silicon (Si) detector), and; the other two are indium antimony (InSb) 32 array detectors in the short wave infra red ranges. This combination produces two overlapping spectral regions located approximately around 1000 nm and around 2000 nm. The data are usually delivered with the overlapping bands removed and consist of 126 bands rather than the full 128.

The sensor operates on a three-axis gyro stabilised platform to minimise image distortion due to aircraft motion. It is also fitted with a DGPS and an integrated IMU (inertial monitoring unit) to produce geo-located images.

The technical specification of the Hymap is an IFOV of 2.5 mr along track, 2.0 mr across track , FOV of 61.3 degrees (512 pixels) and a GIFOV between 3 – 10 m (typical operational range) and a signal-to-noise ratio of greater than 500:1. The

sensor is fully calibrated at the laboratory. This calibration process usually occurs before each campaign ensuring spectral and radiometric accuracy.



Figure 6: HyMap sensor

3.2 GER-IRIS Mk IV

The "Infrared Intelligent Spectrometer" (IRIS) manufactured by Geophysical Environmental Research Limited (GER) is shown on Figure 7. It measures the bi-directional reflectance spectra of surfaces and materials. The bi-directional reflectance is the brightness of a surface relative to the brightness of a Lambertian surface under identical conditions of illumination. The IRIS is a dual-beam instrument, which simultaneously measures both the target and a known reference Lambertian surface. A Spectralon® (Labsphere, 2006) plate was used as the reference Lambertian surface. The Spectralon® plate used was one that was certified to be a 100 % reflectance target. The advantages of using a dual beam instrument such as the IRIS is that by simultaneously measuring the target and reference, the effects of instrument drift and variations in lighting and humidity usually experienced with single beam instruments are removed. The IRIS measures 875 separate channels between 350 and 3000 nm. The sampling intervals are approximately 2 nm over the 350 - 1000 nm region, 4 nm over the 1000 - 1800 nm

region and 5 nm over the 1800 - 3000 nm region. The spectral resolution is approximately 10-12 nm in the 2000 to 2500 nm region. Three diffraction gratings, mounted on a motor-driven axis, disperse the light into its different wavelengths. Si detectors measure the first (shorter wavelength) 460 channels and lead sulphide (PbS) detectors measure the remaining channels.

The IRIS was used mainly for calibration and validation purposes for the dust case study. It was also used for all laboratory studies in the dust case study for measuring optical properties of mangrove leaves. In the setup for the laboratory studies, the target and reference plates were located approximately 350 mm from the GER IRIS' optical head such that the area sensed was approximately 18 by 35 mm (Please see section 4.2.3 for further details). With each measurement, care was taken to view the samples in the viewport of the GER IRIS to ensure that the entire area sensed is covered by the leaf and reference by the spectralon respectively. There may be a possibility of adjacency effects, however, this is considered to be negligible considering the small area sensed with respect to the background which will predominantly be the leaf or reference as opposed to the surrounding area which is the white area shown on Figure 7.

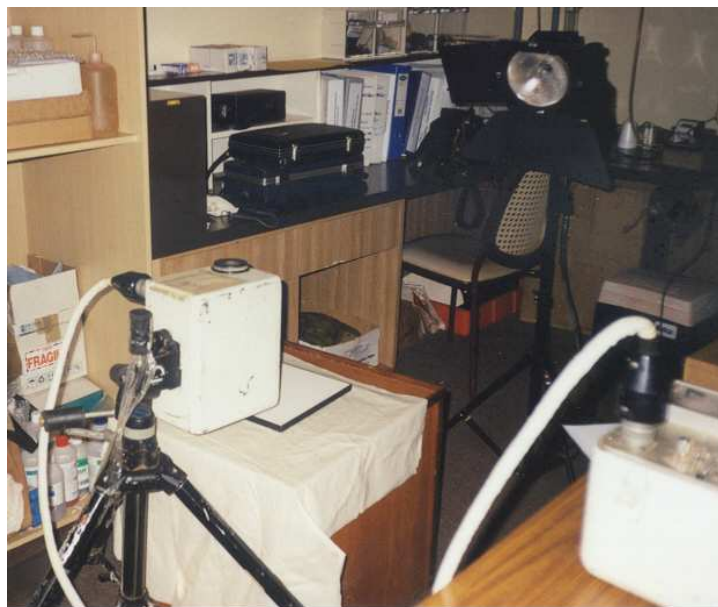


Figure 7: Photo of the experimental set up showing the IRIS, location of lamp, Spectralon and samples.

3.3 ASD FieldSpec® Pro FR

Figure 8 shows a FieldSpec® Pro FR (ASDI, 2008) manufactured by Analytical Spectral Devices (ASD). This spectrometer was used in laboratory to measure samples collected in the field for the AD case study at Brukunga. It was also used for the collection of field calibration and validation data during some of the HyMap acquisitions over both test sites.

The ASD FieldSpec® Pro FR measures in the spectral range of 350 - 2500 nm, has a spectral resolution of 3 nm at 700 nm and 10 nm at 1400/2100 nm, sampling intervals of 1.4 nm between 350 - 1050 nm and 2 nm between 1000 - 2500 nm with a scanning time of 100 milliseconds. This spectrometer has one 512 element Si photodiode array detector operating between 350 - 1000 nm and two separate, thermoelectric (TE) cooled, graded index indium gallium antimony (InGaAs) photodiodes for the 1000 - 2500 nm spectral range.

The Noise Equivalent Radiance (NeDL) is quoted as UV/VNIR 1.4×10^{-9} W/cm²/nm/sr at 700 nm, NIR 2.4×10^{-9} W/cm²/nm/sr at 1400 nm and NIR 8.8×10^{-9} W/cm²/nm/sr at 2100 nm.

Measurements were made with the bare fibre optic cable giving a full angle cone of acceptance field-of-view of 25°.



Figure 8: ASD FieldSpec® Pro FR

3.4 PIMA

The samples collected for the AD case history in Brukunga were measured using the Integrated Spectronics field portable Portable Infrared Mineral Analyser (PIMA)-II spectrometer (ISPL, 1997). The PIMA-II operates in the 1300-2500 nm range and directional-hemispherical reflectance measurements were collected for the Brukunga samples during the 1999 field campaign. The spectral resolution of the PIMA-II is approximately 7 nm and the spectral sampling interval is 2 or 4 nm (selectable). The measurement time is adjustable at 20 - 60 seconds (mode dependent). The PIMA-II has its own internal light source and internal gold reference and plastic wavelength calibration standards. Samples are measured "in contact" with a transparent sapphire window, the area of which is approximately 10 mm diameter. Data acquisition, control and storage are performed via a palmtop PC (HP-200LX) and spectra are stored on 2 MB SRAM PCMCIA card with a capacity of more than 1000 spectra. The PIMA-II spectrometer performs automatic wavelength calibration. The spectra are recorded on a uniform wavelength grid and radiometric calibrations are performed during each spectral scan.



Figure 9: PIMA-II spectrometer

3.5 Analysis and processing tools

The spectral analysis and processing tools used for this study are outlined below.

3.5.1 *Partial least square analysis*

The analysis of the spectral data was performed using Partial Least Squares (PLS) (Geladi and Kowalski, 1986, Wold et al., 2001, Haaland and Thomas, 1988) a multivariate data analysis technique designed to relate multiple response variables X to multiple explanatory variables Y . The PLS software that we used was a CSIRO in-house software call XSpectra (Mason and Berman, 1997) and it is implemented with one-at-a-time cross validation (Wold et al., 2001).

PLS was chosen as the analysis tool as it has the advantage of being able to efficiently handle highly correlated datasets with very many variables, as in the case of our spectral bands. PLS is also useful where the data contain substantial random noise and appropriate when the matrix of predictors (X) has more variables than observations (Y) (as in the case of the spectral bands and the dust levels or pH levels), and when there is multicollinearity among X values (as in the case of spectral bands). The caveat for using this technique is the underlying assumption is that a linear relationship exists between X and Y and hence, by adopting this method of analysis, the assumption is made that the spectral data is linearly correlated to the dust levels and pH levels.

The PLS technique aims to identify the linear combination of the X variables, which best model the Y dependent variables. Specifically,

$$Y = b_0 + b_1X_1 + \dots + b_kX_k + e \quad \text{Equation 1}$$

where the observed response values (Y) (in this case pH and dust levels) are approximated by a linear combination of the values of the spectral intensities (X), coefficients (b) called B-coefficients, and an error term (e). k is the number of spectral bands. The estimated B-coefficients (also called final regression coefficient (FRC)) are determined from the observed Y values and PLS scores for the optimum

number of PLS factors and indicate the correlation between the Y values and each of the X spectral intensities. The FRC can help identify the important X-variables in relationship with a given Y-variable. The FRC contain the spectral information (or key wavelengths) that are most important in driving the PLS model and indicate which variables are important in explaining both the X and the Y-data. The coefficients indicate which X-variables are contributing to the modelling of the structure in the Y-variables (Janik et al., 2007).

That information is used to understand the underlying physico-chemical drivers for the relationships. Inferred from these key wavelengths regions were the physico-chemical parameters the FRCs were predicting. An important factor to consider when using PLS analysis is that the prediction will be constrained by the calibration/training dataset. Therefore, it is crucial that the calibration dataset is comprehensive enough to fully explain the condition to be measured.

PLS has been adopted more recently in spectral laboratory studies to investigate the relationships between physico-chemical parameters and spectral data (Dury et al., 2001, Kemper and Sommer, 2002, McGovern et al., 1999, Polder et al., 2004).

The PLS used was implemented with a one at a time cross validation (Wold et al., 2001). The diagnostic statistics employed to evaluate the accuracy of the predictions were the root mean square error (RMSE) and the ratio of performance to deviation (RPD) (Williams, 1987). The equations used were

$$RMSE = \sqrt{\frac{\sum_{i=1}^N (\hat{y}_i - y_i)^2}{N}}$$

Equation 2

$$RPD = \frac{S_y}{RMSE}$$

Equation 3

where \hat{y} is the predicted value, y is the observed values, N the number of data and S_y is the standard deviation of the observed data.

The RMSE is commonly used to describe the prediction ability of a model and the RPD has been adopted by many researchers in the soil community for evaluating the performance of the model. The interpretation of the RPD values varies (Nduwamungu et al., 2009). We used the commonly adopted guidelines proposed by (Chang et al., 2001). Specifically, $RPD > 2$ predicts well, $1.4 < RPD < 2$ denotes fair prediction and $RPD < 1.4$ indicates poor prediction.

3.5.2 Parameterisation of spectral features

There is an extensive body of knowledge accumulated on the spectral behaviour of surface materials, especially minerals, over the last 20+ years (Clark, 1981b, Clark, 1981a, Clark, 1983, Crowley and Vergo, 1988, Curtis, 1985, Elvidge, 1990, Gaffey, 1986, Gaffey, 1987, Horler et al., 1983, Hunt, 1977, Hunt, 1979, Hunt, 1982, Hunt and Salisbury, 1970, Hunt and Salisbury, 1971, Hunt et al., 1972, Hunt et al., 1973, Salisbury et al., 1991). A variety of parameterisation methods have been developed to exploit this knowledge by capturing diagnostic spectral features of materials of interest. These methods include simple ratios (Gamon et al., 1997, Peñuelas et al., 1995, Tucker, 1979), matching of features using least square fitting to spectra of known materials (Clark et al., 1990), fitting of Gaussian shapes (Clark and Roush, 1984) and simple polynomial fits (Cudahy and Ramanaidou, 1997).

Parameterisation of spectral features was investigated mainly for the ferric iron oxide dust case history. The main reason for pursuing this line of investigation is to determine if the depth of the 900 nm ferric iron oxide crystal field absorption (CFA) feature can be used as an indicator of the abundance of ferric iron oxide as found by Cudahy and Ramanaidou (1997). This had significant consequences in view of issues associated with bidirectional reflectance difference factor (BRDF) found with the airborne data. Polynomial fits was employed for the purpose of analysis in the dust case history.

Tetracorder is a software program containing multiple algorithms which can be commanded as an expert system (Clark et al., 2003b). It is considered here as a form of parameterisation of spectral features as it identifies materials by comparing a

remotely-sensed observed spectrum (the unknown) to a large library of spectra of well-characterized materials, based on known diagnostic features in the library spectra. It has been used extensively for mapping minerals using airborne hyperspectral data associated with contaminated mine sites. However, this method has not been evaluated with multi-temporal hyperspectral datasets.

This study investigated the use of Tetracorder for spectral identification of minerals from chronologically different sets of airborne HyMap hyperspectral data collected from the abandoned Brukunga pyrite mine in South Australia to establish whether mapping minerals over a time series can be used for quantitative measurement and monitoring necessary for environmental management purposes. The time series of data is important for understanding the development of the AD condition over time.

3.5.3 Pixel Mean Normalisation

Pixel-mean normalisation (PMN) is a method developed as part of Log Residuals (Green and Craig, 1985) and has been used to normalise brightness variations that may be related to wavelength independent and multiplicative brightness reflectance difference factor (BRDF) effects, topographic effects and shading. PMN is a processing procedure where for every spectrum in the image, the intensities of each band of a given pixel/spectrum are normalised by the mean intensity of all bands for that pixel/spectrum. Specifically,

$$I_{PMN_i} = \frac{I_i}{I_{mean}}$$

$$I_{mean} = \sum_n^i \frac{I_i}{n}$$

Equation 4

Where I_{PMN_i} is the PMN intensity at band i of the spectrum; I is the intensity value for band i of the spectrum; I_{mean} is the mean intensity value across the spectrum; and, n is the total number of bands in the spectrum.

3.5.4 Continuum removal

Continuum removal (Clark and Roush, 1984) is a method commonly used to normalize a set of measurements to compare individual absorption features from a common baseline and to represent absorptions other than the one of interest.

The continuum is a convex hull fitted over the top of a spectrum using straight-line segments that connect local spectra maxima. The first and last spectral data values are on the hull; therefore, the first and last bands in the output continuum-removed data file are equal to 1.0.

The continuum is removed by dividing it into the actual spectrum for each pixel in the image. Specifically,

$$S_{cr} = (S/C)$$

Equation 5

Where S_{cr} = Continuum-removed spectra, S = Original spectrum, C = Continuum curve

The resulting image spectra are equal to 1.0 where the continuum and the spectra match, and less than 1.0 where absorption features occur.

3.5.5 Atmospheric correction

Three atmospheric correction packages were tested and the most optimal option from the testing was used in this study. They were

1. A CSIRO-developed software AtComp ((Rodger, 2011a), which performs both atmospheric corrections and spectral recalibrations. The atmospheric correction is based on MODTRAN (Berk et al., 1989). The spectral recalibration component of the software, second order difference algorithm (SODA; (Rodger, 2011b)) is based on spectral matching of known gaseous and water vapour spectral features similar to Guanter et al. (2006) with a

difference in that the SODA minimises the residuals of the second derivatives rather than of the reflectances as in the method described in Guanter et al. (2006);

2. FLAASH (Adler-Golden et al., 1998) which performs a MODTRAN-base atmospheric correction and has options for spectral recalibration; and,
3. ATREM (Gao et al., 1993) incorporated a CSIRO developed package called HyCorr (Mason, 2000). This package does not perform spectral recalibration.

Chapter 4

LABORATORY STUDIES

4.1 Introduction

A series of laboratory experiments was conducted as part of the study to develop an understanding of the spectral characteristics of the materials required to be measured, changes in their spectral behaviour with variations in the environmental conditions and other factors that may influence the spectral behaviour. The experiments were required to generate the environmental measurements commonly used by environmental practitioners from spectral data. Currently, there is a lack of spectral-derived environmental measurements in Australia because the use of hyperspectral remote sensing for the assessment and monitoring of mining-related environmental concerns is a relatively new technique. For dust assessment and monitoring, the technology has not been previously applied. For AD, the use of hyperspectral sensors has been limited to a single mineral map without further temporal acquisition (Bierwirth, 2004, Pfitzner and Clifton, 2006).

The data collected from the laboratory experiments was also used to build the spectral algorithms for transforming hyperspectral data into the environmental measurements. The ultimate goal is to apply these algorithms to the remotely-sensed hyperspectral data to produce spatially-comprehensive maps of the environmentally relevant measurements.

4.2 The Port Hedland dust case study

The prime objective of the experimental work was to build a database of the spectral characteristics of ferric iron oxides-dusted mangrove leaves collected at Port Hedland. In addition, an algorithm was developed to correlate dust levels and spectra and used a validation component to assess the robustness of the algorithm.

Experiments were also conducted to address a few concerns related to the sampling procedures and the dust measurement method which may impact the accuracy of the measurements.

4.2.1 Experimental procedures and issues addressed

The experiments conducted, methods and the issues that they were addressing are described below.

1. Impacts of time delay between sample collection and measurement

The logistics of field sampling and location of the sites, require procedures where the mangrove samples are removed from the living plants several hours before they are measured. It was necessary to confirm that this sampling procedure did not introduce conditions dissimilar to the living plants. One of the concerns was that the prolonged period between leaf removal and measurement may cause the leaf to deteriorate. An experiment was devised to investigate the temporal spectral changes of mangroves leaves after removal from plant.

This experiment was conducted on 5 August 2000. For the first experiment, a condition of heat stress was simulated by directing a 1000 watt lamp on the surface of a leaf collected from Six Mile Creek (a site that was assumed to be a clean site) and spectral measurements were recorded at set time intervals over a period of two days. Spectral measurements of the centre of the leaf were made using the IRIS spectrometer every two minutes for four hours and once after 21 hours from the start of the experiment.

2. Effectiveness of dust removal procedure

Another main concern with the procedure used to collect the dust is if it effectively removes all the dust from the leaves. Experiments were performed during three field trips to test this where spectral measurements of the cleaned leaves were compared with leaves from a clean site.

On the 5 August 2000 samples were collected at a site near the gate of the Finucane Island facility and Six Mile Creek. The Finucane Island site was determined from visual observations to have the highest levels of dust around the facility and the Six Mile Creek site is a “naturally” clean site. A total of 11 leaves were measured for Funicane Island and three for Six Mile Creek were measured on this field trip.

On 12 November 2000, *Avecennia marina* leaves were collected from Burgess Point where branches were removed from four mature trees representative of different levels of dust loadings and six leaves were selected from each of the four mangrove branches. Samples from Six Mile Creek were also collected on this occasion. A total of 25 leaves were sampled for Burgess Point and ten were from Six Mile Creek.

Between 12-16 December 2001, data were collected from across the whole facility. A total of 45 samples were from Burgess Point, 40 samples were from Funicane Island and 10 samples were from Six Mile Creek.

For each sample, a single leaf was cut and spectral measurements were made on the adaxial surface of the leaf. The adaxial leaf surface was then cleaned with a wet soft cloth and dried after visible traces of dust were removed. Spectral measurements were subsequently recorded for the cleaned surface. Care was taken to minimise the time between the measurements to prevent collapse of the leaf cells. The spectral measurements are usually completed in one minute and it is estimated that it took one to two minutes to remove the dust from each leaf.

3. Relationship between spectra and dust measurement via PLS analysis

A field campaign was conducted on 12 November, 2000 to explore the relationship between dust level and the spectral response across the whole VNIR-SWIR spectral region. *Avecennia marina* leaves were collected at the Burgess Point where it was known from anecdotal observation to have the highest levels of dust. Samples selected that span from low to high levels of dust. Branches

were removed from four mature trees representative of different levels of dust loadings. Six leaves were selected from each of the four mangrove branches.

Spectra and concurrent measurements of dust levels were recorded from 44 leaves covering a range of dust levels from highly dusted to dry clean mangrove leaves.

4. Relationship between spectra, via spectral parameterisation of the ferric iron oxide crystal field absorption feature, and dust measurement

This analysis was conducted to account for the fact that if the technique were to be transferred to remotely-sensed hyperspectral data, some spectra may be significantly compromised by BRDF. The results of analysis of the airborne data documented on Chapter 5 did in fact find that some regions of the spectrum were significantly compromised by BRDF. This necessitated investigation of a robust method of accurately extracting the abundances of ferric iron oxide from regions of the spectrum that were least affected by BRDF.

This analysis followed the PLS analysis which found the region between 760 nm and 1000 nm to be highly correlated to the ferric iron oxide levels and, a diagnostic feature, namely, the depth of the ferric iron oxide CFA feature near 900 nm which is uniquely related to ferric oxide abundance (Cudahy and Ramanaidou, 1992, Ramanaidou et al., 2008).

Visual observation, as shown on Figure 10 indicated the presence of the ferric iron oxide CFA feature, as observed with the pronounced broad absorption centred at 860 nm, on the dusted leaf samples, both on the adaxial and abaxial surface. Other spectral changes are also observed in the visible (500 - 650 nm) and short-wave (1700-2500 nm). The analysis investigated if it was possible to use the 900 nm ferric iron oxide CFA feature as a predictor of the dust levels.

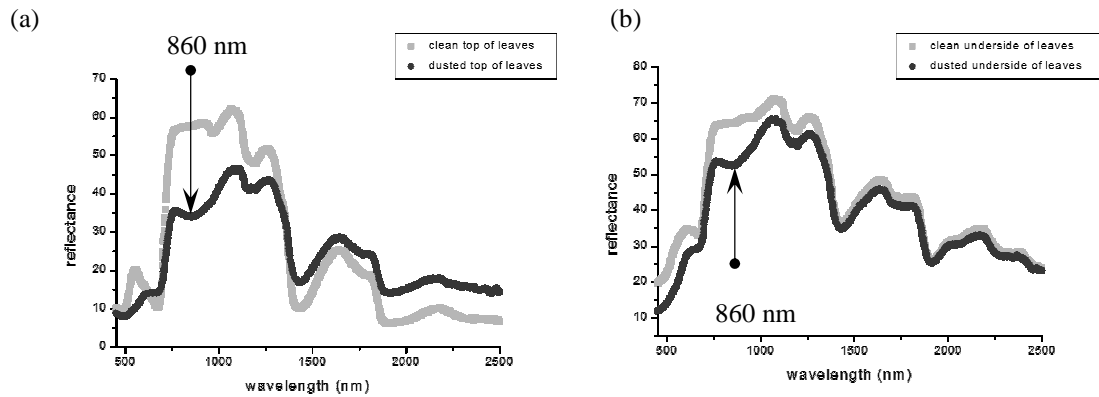


Figure 10: Spectra of naturally clean (grey) and dusted (black) (a) topside and (b) underside of mangrove leaves measured with an GER-IRIS MkIV field spectrometer. The arrows show the location of the ferric iron oxide crystal field absorption feature at 860 nm. The 860 nm absorption indicates that the ferric iron oxide dust is hematite-rich and/or less than 20 μm in particle size (Cudahy and Ramanaidou, 1997).

The depth of the 900 nm ferric iron oxide CFA feature was required for this analysis and this was parameterised using a third order polynomial. We used the depth of the 900 nm ferric iron oxide CFA feature because previous research found that this parameter was uniquely related to the ferric iron oxide content (Cudahy and Ramanaidou, 1992). The following describes the procedure used to calculate the depth of the 900 nm ferric iron oxide CFA feature for all the spectra in the dataset.

Firstly, continuum removal (see 3.5.4) was applied to the region between 770-1070 nm. Continuum removal was also applied to remove albedo variation related to differential lighting and/or the background vegetation. After the continuum removal, a third order polynomial was fitted to the continuum removed spectra to locate the minima on the curve. This is illustrated on Figure 11 where a typical ferric iron oxide spectrum was plotted with crosses. A third order polynomial curve was selected to accommodate the asymmetric ferric iron oxide CFA feature. The third order polynomial curve is also plotted on Figure 11 with a solid line. The depth of the 900 nm CFA feature was calculated as the

vertical distance between the minima of the polynomial curve and the horizontal line joining 770 to 1070 nm as shown on Figure 11. Specifically,

$$D_{CFA} = \frac{I_{p_{wm}}}{I_{l_{wm}}}$$

Equation 6

Where D_{CFA} is the depth of the 900 nm ferric iron oxide CFA feature, $I_{p_{wm}}$ is the continuum removed value at the minima (at wavelength wm) of the 3rd order polynomial curve and, $I_{l_{wm}}$ is the continuum removed value at wavelength location wm on the straight line fitted between 770 and 1070 nm.

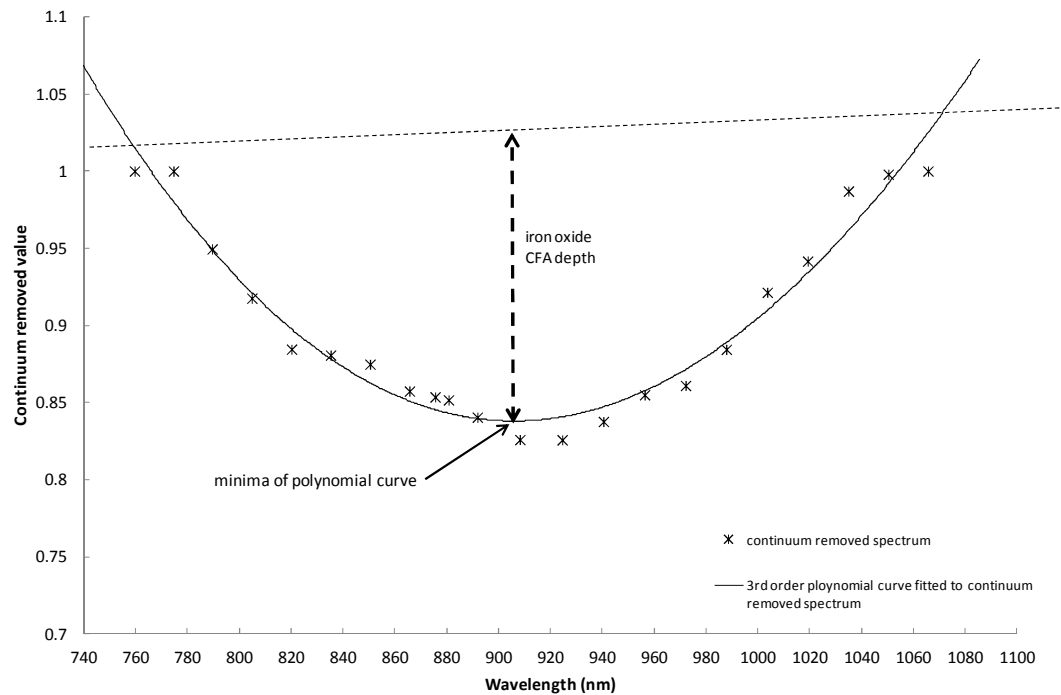


Figure 11: A typical ferric iron oxide spectrum is plotted with crosses together with the third order polynomial curve fit of the spectrum plotted with a solid line. Note that the spectrum is a continuum removed spectrum. The minima of the curve is also marked. The depth of the 900 nm ferric iron oxide CFA feature illustrated on the graph.

Also, as an absorption feature related to leaf water is located at 970 nm, the bands (between 920-1050 nm) affected by this water feature were omitted from the analysis to reduce fitting errors caused by this absorption feature.

There were two parts to this investigation. In the first part, data collected in November 2000 were analysed to determine if the depth of the 900 nm ferric iron oxide CFA feature is related to the dust levels on mangrove leaves.

The second part of this investigation involved the production of a robust dust algorithm developed using a comprehensive dataset covering a complete range of dust levels. The data used for this part of study were collected between 12-16 December 2001 and 21-22 October 2002.

On the first date, the samples were collected from three locations close to Burgess Point, four locations on Finucane Island and one location at Six Mile Creek. Preliminary dust maps using the 900 nm ferric iron oxide CFA depth generated from the airborne data collected in November 1998 helped the selection of the sampling locations. The 1998 data was used as a reference as it was close to the same season as the field sampling. The exact site locations were not recorded but this was not crucial as the main purpose of these samples were for building a set of comprehensive measurements for dust load and concurrent spectral data. For each site, five mangrove trees were selected and a branch from each tree was removed. Five leaves were then selected from each branch for laboratory measurement.

The second field acquisition was concurrent with the airborne acquisition; therefore, data were also collected for the validation of the airborne data at the same time. Four of the sites were located in Burgess Point, five were at Finucane Island and one at Six Mile Creek. The locations of these sites were again selected based on the 1998 dust map and exact locations were recorded using a handheld differential GPS with an accuracy of ± 3 to 5 m (see Table 7). The same sampling procedure was conducted as for December 2001.

site	easting	northing
ba1	666010	7751770
ba2	666448	7751336
ba3	666368	7751381
ba4	666610	7751622
fa1	660511	7753830
fa2	661831	7754264
fa3	662488	7753911
fa4	662818	7752939
fa5	663419	7752762
6m1	674024	7751442

Table 1: GPS locations of field sampling sites acquired in October 2002. The map projection is AGD66, zone 50.

A total of 212 samples were included in the analysis to generate an algorithm for extracting measurements of dust loads from spectral data.

5. Relationship between dust levels on the adaxial and abaxial surfaces

The morphology of the leaf surfaces is such that the adaxial surface is smooth and the abaxial surface is hairy. Dust removal was easily achieved on the adaxial surface but removal from the abaxial surface was difficult to achieve without removal of the hair or destroying the surface. Also, if the dust technique were to be transferred to remotely-sensed hyperspectral data, both the adaxial and abaxial surfaces of the mangrove leaf can be seen from a remote platform. Therefore, this experiment was conducted to determine if measurements of the dust levels

on both surfaces are needed or it would be sufficient to measure only the adaxial surface as the surrogate for the dust levels. In this experiment, spectral data were collected for four dates (April, July, August and November) in 1999 covering the different seasons and hence capturing varying dust levels.

In 1999 a total of 12 sites were sampled where mangrove leaves were collected. These sites were spread across the harbour facility with some coinciding with locations of dust depositional gauges. The GPS locations of these sites are tabulated below.

Sites	Eastings	Northings
PH1	665823.8	7751679.4
PH11	666295.3	7751192.0
PH12	666338.5	7751199.3
PH13	666930.3	7751743.5
PH14	666581.1	7751553.9
PH1A	660380.9	7753656.9
PH2	661723.2	7754125.9
PH21	663582.6	7752401.0
PH22	661907.9	7750539.0
PH23	672052.2	7752067.0
PH3	662455.4	7753228.2

PH4	663319.7	7752620.3
PH5	662658.4	7752772.6

Table 2: GPS locations of field sampling sites acquired in 1999. The map projection is AGD66, zone 50.

4.2.2 Site and sample selection and preparation

All sites were selected in stands of the ubiquitous *Avicenna marina* species as studies undertaken by (Paling et al., 1996) determined that they were the most affected by dust. However, most sites did have proximal stands of *Rhizophora stylosa* and occasional occurrences of *Ceriops tagal* and *Aegiceras corniculatum* and in one instance *Osbornia octodonta*. No extensive vegetation survey was undertaken beyond the immediate study sites. These species were keyed using the methods of (Semenuik et al., 1978) and concur with the published data for the area.

Leave samples were collected from mature stands and near the top of the canopy where they would be visible from an airborne sensor and not affected by varying water heights. Branches representative of the dust level of the area where the collection was done were selected, cut from the trees and placed as quickly as possible into water in order to preserve the leaves.

Other factors considered while selecting samples included access and proximity to a vehicle as it was essential that the leaves be kept in pristine condition so that the measurements were representative of the leaves while they were still on the trees.

The criteria for selection of the mangrove leaves for spectral measurement were flatness, size and shape. Each leaf was cut from the branch and immediately placed under the IRIS for spectral measurement. Although this means that the spectral measurement is only for a section of the leaf, it was assumed that the dust was spread evenly across the leaf and the section being measured was representative of the whole leaf. The adaxial (topside) surface was measured first and then the leaf was

turned over and repositioned for the abaxial (underside) surface to be measured. Measurements of both the adaxial and abaxial surfaces were collected because field observations indicate that viewed from a remote horizontal platform, for example a hyperspectral sensor mounted on the belly of an aircraft, approximately 35-40% of leaves imaged will have their undersides visible as shown on Figure 12 and Figure 13. Finally, the leaves were then placed into plastic covered petrie dishes or plastic vials.



Figure 12: Photo showing a typical mangrove habitat at Port Hedland. Note the orientation of the leaves which show both the abaxial and adaxial surfaces. The photo also shows two depositional gauges which were used to measure the dust impact on the mangroves.



Figure 13: Photos showing a close-up view of mangroves used in this study. The left photo shows a tree affected by dust and the right shows a tree that was in an area

that was not dusty. Note that the orientation of the leaves which show both the abaxial and adaxial surfaces.

4.2.3 Configuration of spectral measurements

A quartz-halogen photoflood lamp placed 112 cm from the IRIS optical head was used to illuminate the samples and the Spectralon reference plate. The lamp was angled approximately 60° to the vertical and located 120 cm above the laboratory floor. The sample and Spectralon plate were placed on a table top at 53 cm above the floor and the distance between the top of the IRIS optical head to the floor was 88 cm while the distance between the bottom of the IRIS optical head and the floor was 62 cm. Leaf samples were cut from the branch and placed directly below the IRIS optical head beside the Spectralon plate. The leaves were orientated to ensure that a flat section of the middle of the leaf was measured. This configuration assumes that the dust distribution in the middle of the leaf was representative of the whole leaf surface.

4.2.4 Measurement of dust levels

The use of the dust depositional gauges (Standard, 2003) for monitoring dust has been a procedure that has been widely used in Australia for over 40 years and, during this time, extensive data have been collected. This method measures dust deposition rate and involves the passive deposition and capture of dust within a funnel and bottle arrangement. Data are usually collected over monthly periods and results are expressed in $\text{g/m}^2/\text{month}$ (ie. the mass of dust deposited per m^2 per month).

This dust monitoring procedure was adopted and written into the regulatory requirements (EPA, 1996) for the operation of the Port Hedland bulk handling facilities. Unfortunately, after many years of monitoring, the environmental practitioners found that the data collected were not quantitative enough to inform management practices as the data collected were often compromised by either climatic events such as cyclones or contaminated by bird droppings or insects. Therefore, because of this and because of the lack of published methods especially

for the measurement of dust on mangrove leaves, it was necessary to develop a method to measure the amount of dust on the leaves. After experimenting with different methods, the final solution was to removed the dust from the adaxial surfaces of the leaves using tissues of know ash content, incinerating the tissues and weighing the dust and ash.

For this method up to two wet tissues² were used to remove all visible traces of dust on the adaxial surface of the leaf after the spectral measurements. These tissues were kept in a covered plastic vial for transport before further analysis.

The use of the tissues are a modification of the surface wipes method (ASTM, 2008, ASTM, 2010, ASTM, 2011) which is commonly used to determine the presence of particular compounds in the air through collecting particles that have settled (deposited) onto indoor or outdoor surfaces. This technique involves wiping a known surface area using a wet filter paper or pad to collect dust which is then sent to a laboratory for analysis. There are currently no Australian standards or United States Environmental Protection Authority (US EPA) methods for using surface wipes for this purpose.

4.2.5 Dust sample preparation and calculation of dust levels

Preparation of the dusted tissue samples consists of drying the tissue samples at 40°C, weighing the samples and combustion of the samples at 800°C. The weights after combustion were recorded after cooling and the tissue ash content subtracted. Consideration was given to weight lost resulting from combustion of ferric iron oxide at such a high temperature. This was calculated at less than 15% if the samples were goethite-rich. Such a high temperature was used to ensure that all the cellulose (leaf) material were incinerated leaving behind only the dust.

² Kimberly-Clark 21x12 cm Delicate Task Wipers. Serial No: 4103

As most sampling had to be processed at the site or at a basic laboratory at the handling facility, the number of samples and the availability of accurate instrumentation made it difficult to weigh each tissue before they were used to remove the dust from the leaves. Therefore, the ash content was estimated at the laboratory in CSIRO where 20 blank tissues were selected as representative samples for the lot. The ash content of the tissues was recorded after combustion at 800°C. The average weight of these 20 samples was used as the ash content of the tissue.

The traditional method of drawing the leaf outline on paper and weighing the paper was used for the purpose of leaf surface area measurement. More sophisticated and automatic methods of determining leaf surface area are now available. For this study, the outline of each leaf was traced onto standard printing paper and then cut out for weighing. Samples of known areas were also made and weighed to be used as the standards. The surface areas of the leaves were obtained by normalising to these standards.

The dust measurements were then standardised to the mass of dust per unit area and hence, in this case, was the ratio between dust weight and leaf area (g/m^2).

4.2.6 Results

4.2.6.1 Impacts of the time difference between sample collection and measurement

Figure 14 show the spectra recorded for the first experiment. The red crosses mark the mean spectrum over the first two hours of exposure. The faint red line marking the standard deviations around the means shows that changes in that period is minimal across the VIS region. Differences seen in the NIR-SWIR region related to water content, is also very small. The blue crossed marks the average spectrum for the second two hours. Increases in the green peak can be seen in the VIS region over this period. There are also increases in the albedo of the NIR plateau. These changes may be attributed to the leaf drying out and the leaf appearing brighter. Furthermore, the slope between the NIR and SWIR is less steep indicating a loss of

water. There is no apparent change in slope between the red edge and the NIR plateau indicating that cell collapse has not occurred in that period.

The magenta crosses mark the mean spectrum 21 hours after the start of the experiment. The mean was calculated from spectra acquired over a 15 minute period. The region between red edge and NIR plateau had developed a steeper slope indicative of cell collapse. The flattening of the slope between the NIR and SWIR was now significant when compared to the spectra collected at the start of the experiment (blue spectrum) and two hours from the start of the experiment (red spectrum). This and the shallower water absorption features around 970 nm, 1400 nm and 1900 nm indicated significant loss of water. Furthermore, the absorption around 1930 nm (most probably related to Xylan, a member of the hemicellulose group) is much more prominent and deeper in the magenta spectrum indicative of the leaf drying.

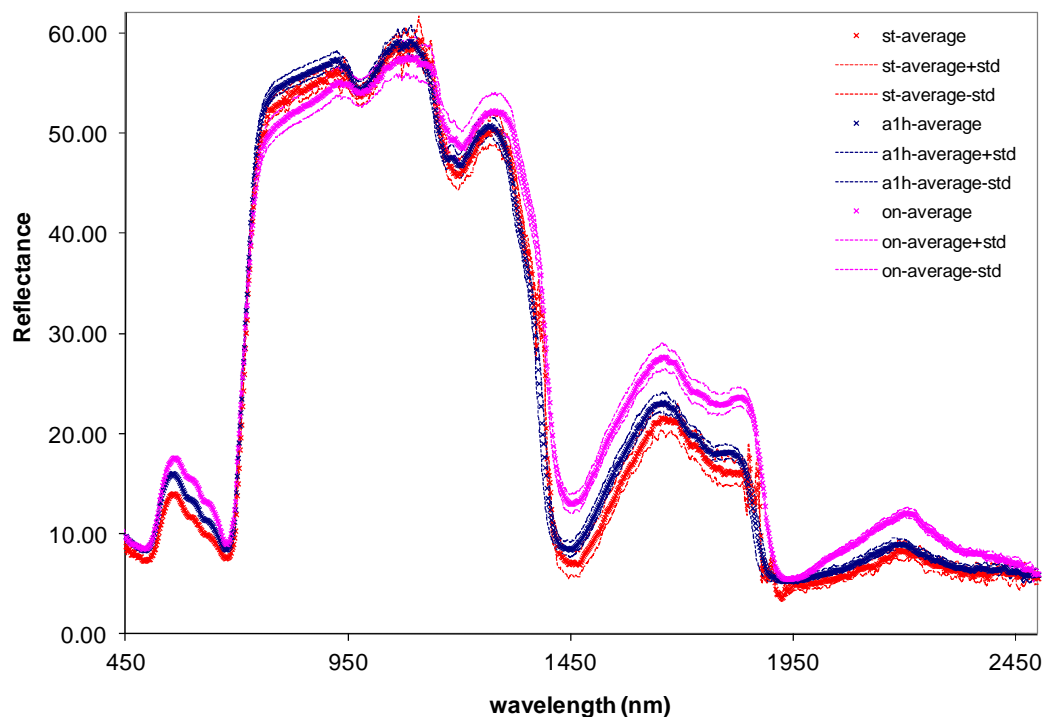


Figure 14: Spectra of a clean *Avecennia marina* leaf collected at Six Mile Creek that was subjected to heat stress over a period of two days. The red crosses show the average spectrum of leaf at the start of the experiment. The red dashed lines show range of the data. The blue crosses show the average spectrum of the leaf after one

hour of exposure to heat stress. The blue dashed lines show the range of the data at that stage of the experiment. The magenta crosses show the average spectrum of the leaf at the end of the experiment after the leaf has been exposed to heat stress and left to dry for two days. The magenta dashed lines show the range of the data at the end of experiment.

4.2.6.2 Effectiveness of dust removal procedure

The average spectra of the “dusty” and “cleaned” leaf samples from each site and each date are plotted on *Figure 15* with the average spectrum from the naturally clean site collected from areas that were not affected by dust from each date. These data show very little variation between the naturally clean sites and the leaves that were cleaned prior to making the spectral measurements. This confirmed that the procedure for the collection of dust was effective.

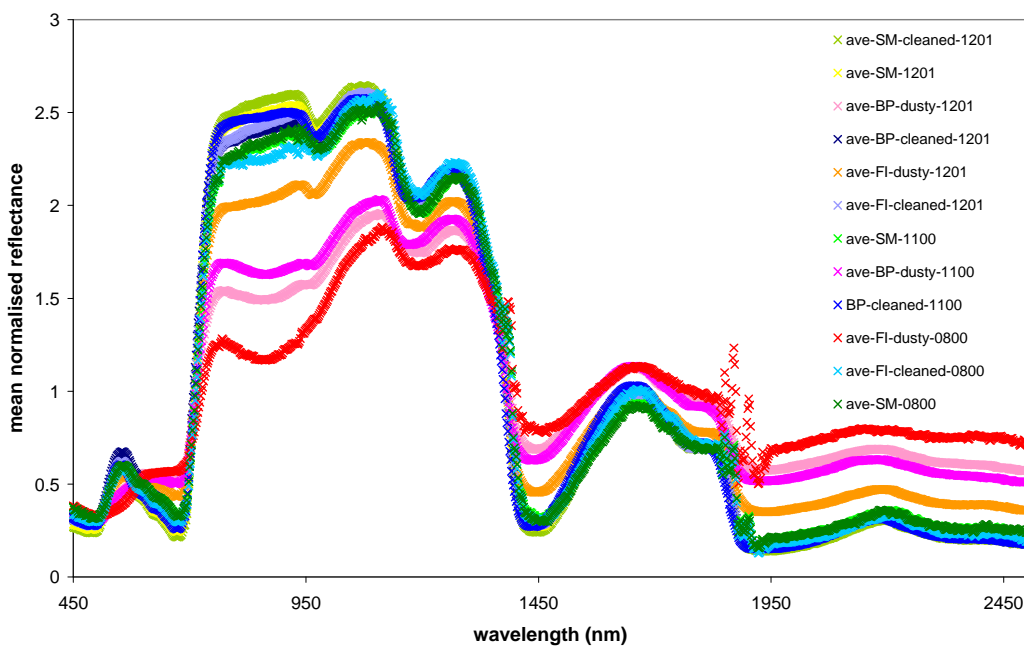


Figure 15: Spectra of highly dusted leaves collected at Funicane Island and Burgess Point. The plot show the spectra of the same leaves after they have been cleaned prior to making the measurements compared with naturally clean collected in areas that were not affected by dust and cleaned leaves from at Six Mile Creek. These data were collected over three field trips on 5 August 2000, 12 November 2000 and 12-16 December 2001. The mean spectrum from each site on each date is plotted.

4.2.6.3 Relationship between spectra and dust measurements using PLS analysis

The data acquired from the field trip in 2001 was used in the PLS analysis to determine the relationship between the spectral data and dust measurements. The spectral data were assigned as the X predictor and the dust measurement as the Y observations in Equation 1. Figure 16 shows the result of the PLS analysis indicating a linear trend at $R^2 = 0.82$ between the dust measurement predicted from the spectral data and the actual dust measurement. Based on the calibration dataset, this result indicates that PLS can be reliably used to predict dust levels. The RMSE was calculated as in Equation 2 using the spectral-predicted dust levels as the \hat{y}_i and the actual dust measurements as the y_i . The resulting RMSE at 0.41 g/m^2 is relatively low. This value may also be used as indicative of the expected error of the dust measurements if spectral data were used to predict them.

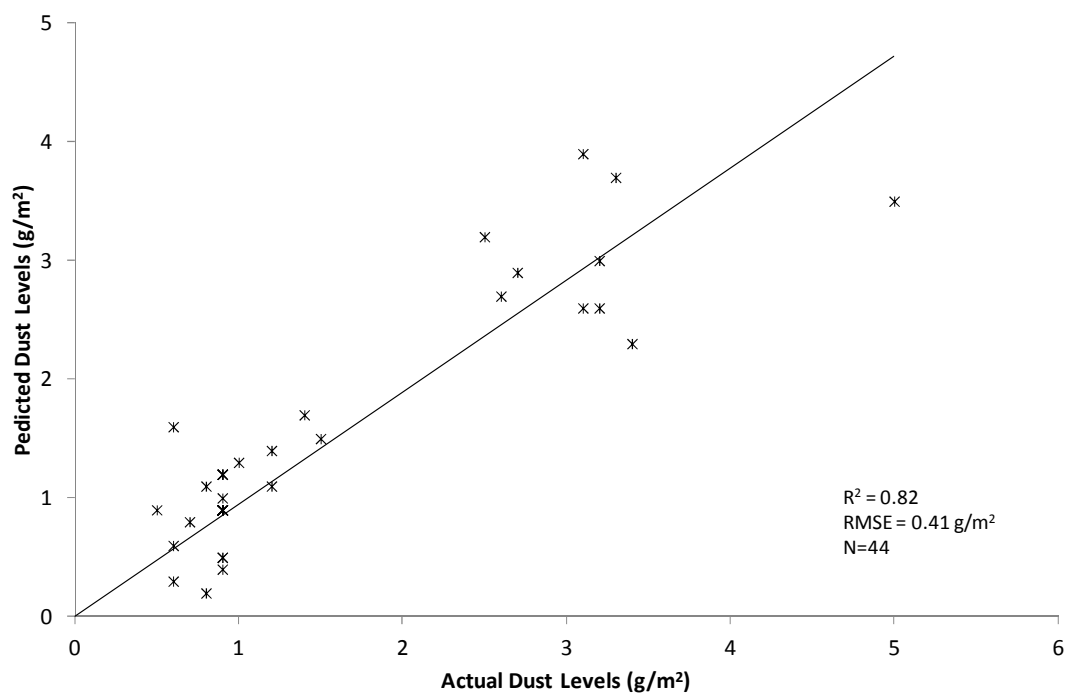


Figure 16: Dust levels measured in laboratory plotted against dust levels predicted from spectral measurements for the calibration dataset.

Figure 17 shows the final regression coefficient (FRC) resulting from PLS analysis (black dots). An interpretation of the FRCs are that they are the weights which when applied to the spectral data predict the dust measurement. The location of the significant FRCs indicated by high positive or negative values can then be interpreted as the spectral regions which were the dominant predictors of the dust levels. In the case of the dust measurement, the spectral bands shown to contribute significantly to the prediction of the dust levels were located at 518, 746, 927, 1261 and 1402 nm (arrows show their location). A typical dusted leaf reflectance spectrum was plotted on Figure 17 (grey dots) to highlight these significant coefficients in relation to the spectral attributes of an iron ore dusted leaf. These results show that the drivers for the prediction of the dust levels from the spectral data were predominantly related to ferric iron oxide. Specifically, significant FRC at 518 nm coincides with the ferric iron oxide charge transfer absorption (Curtis, 1985) and the high FRC at 927 nm is related to ferric iron oxide CFA (Curtis, 1985) and those at at 746 and 1261 nm are at the shoulders of the CFA. It is important to note the significant coefficients near 746 nm. This region is also related to photosynthetic activity in plants (Jensen, 2000) and is highly variable because of the dynamic nature of vegetation. If this region is to be used it necessary to remove or account for the vegetation spectral background that could introduce prediction errors.

The high FRC located at 1402 nm is related to leaf water (Curran, 1989). This region may be affected by significant amounts of ferric iron oxide. Note changes in the top of the shoulder at 1400 nm. However, as this study was performed to support the airborne component and it is necessary for results to be transferable to the airborne platform, less importance was placed in this region as these wavelengths are in the atmospheric water vapour window and hence not available from remotely-sensed data.

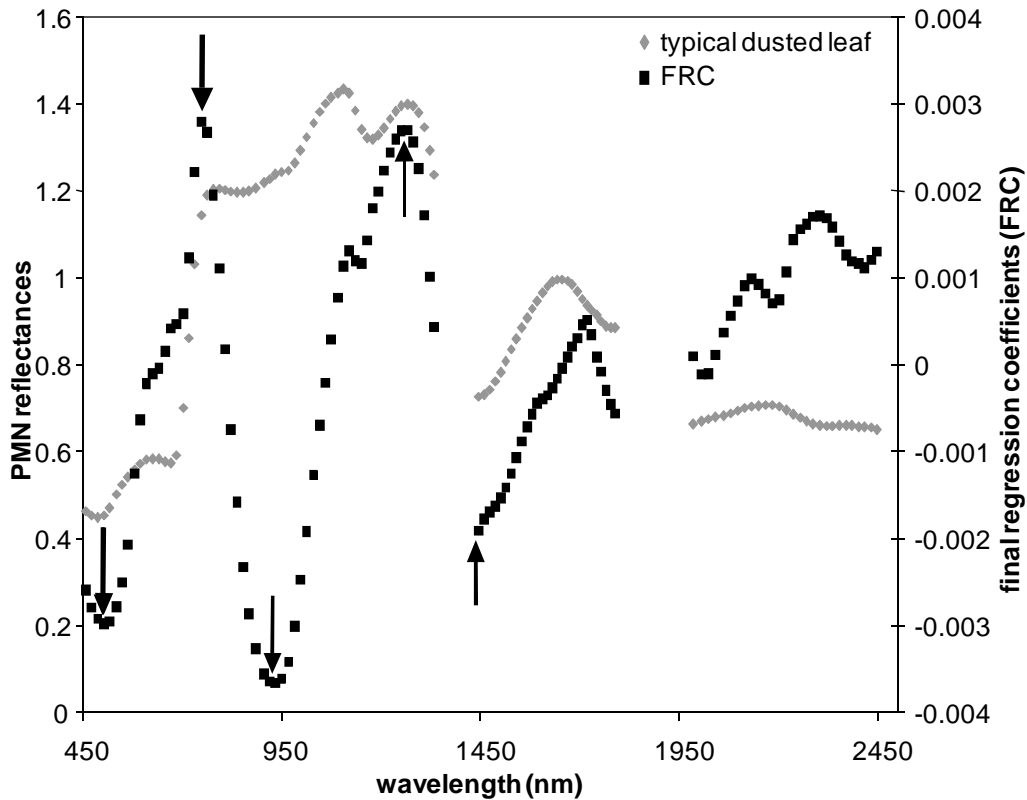


Figure 17: Final regression coefficient results from partial least squares analysis of dust quantity (black dots) and spectra plotted together with a typical dusted leaf spectrum (grey dots). The arrows illustrate significant final regression coefficient.

4.2.6.4 Relationship between spectra, via spectral parameterisation of the 900 nm ferric iron oxide crystal field absorption feature, and dust measurement

Figure 18 shows the result from the first part of the investigation conducted to determine if the depth of the 900 nm ferric iron oxide CFA feature is related to the dust levels on mangrove leaves. The figure shows that the continuum removed depths of the 900 nm ferric iron oxide CFA feature, and on-leaf dust levels are correlated. With a correlation coefficient of 0.95, the result shows that the relationship is significant with a confidence level of 99 %. This confirms that the depth of the 900 nm ferric iron oxide CFA feature can be used as measure of ferric iron oxide dust level. Therefore, the empirical line relating the dust level to the 900

nm ferric iron oxide CFA feature was used as the initial dust algorithm and applied to the early (1998 and 1999) dataset to generate preliminary dust maps to guide further field work.

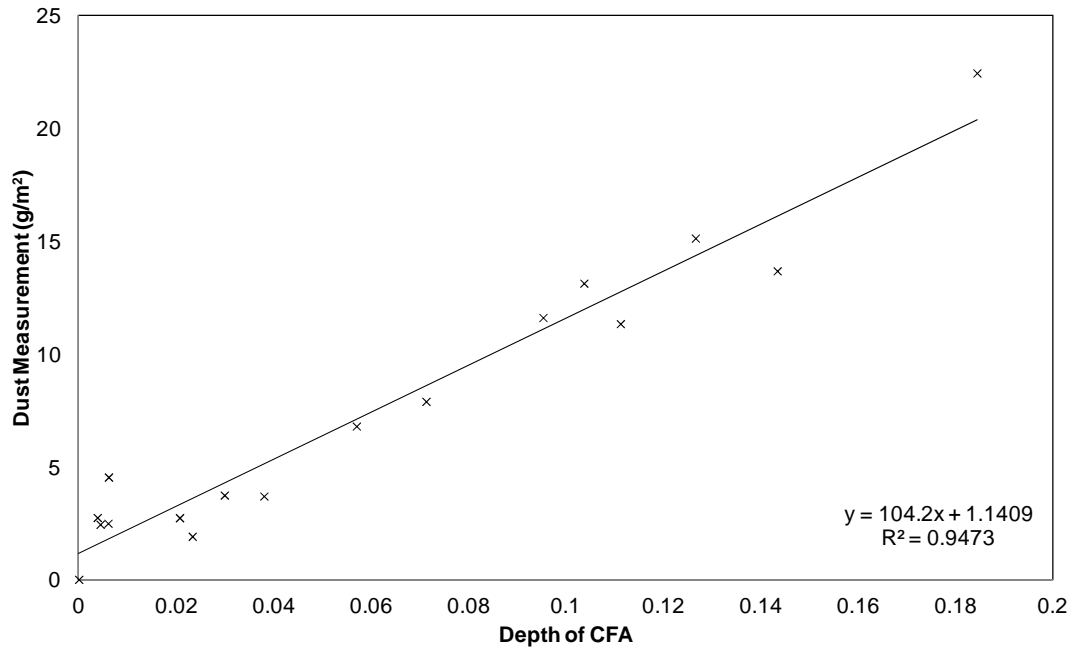


Figure 18: Relationship between mass per unit area and the depth of the CFA feature near 900 nm.

Figure 19 is a scatter plot of the ferric iron oxide dust levels against the depth of the 900 nm ferric iron oxide CFA feature, resulting from data collected for the second part of the experiment conducted for the production of a robust dust algorithm. A straight line was fitted to the data showing a significant correlation (at 99% confidence) at R^2 of 0.70. The empirical relationship was used as the final dust algorithm to generate predicted dust levels from the airborne hyperspectral data. Specifically the equation for the generation of dust level is

$$DL = 74.464D_{CFA} + 1.1622$$

Equation 7

Where DL is the dust levels in g/cm^2 and D_{CFA} is the depth of the 900 nm ferric iron oxide CFA feature.

An interesting observation from the graph is that a 900 nm ferric iron oxide CFA depth of zero does not represent a dust level of zero but $2 \text{ g}/\text{cm}^2$. A plausible explanation for this is that Six Mile Creek, the site used as the clean site with no dust may indeed have some amounts of dust on the mangrove leaves. Interestingly, the average dust load measured for samples collected at Six Mile Creek was $2.1 \text{ g}/\text{cm}^2$. Analyses of the spectra from this site indicate a lack of ferric iron oxide from these samples. This indicates that the levels of dust measured at Six Mile Creek may be generated from natural sources and hence this level of dust may be used as the baseline for the ambient level from natural dust sources.

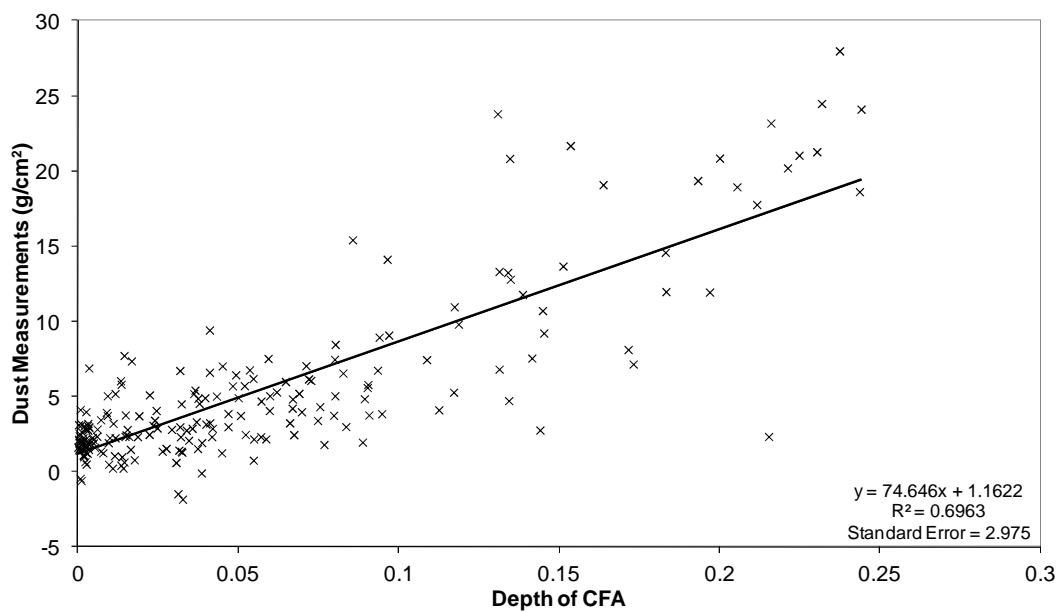


Figure 19: Scatterplot of depth of the CFA feature near 900 nm for ferric iron oxide and the mass per unit area of dust on the leaves.

4.2.6.5 Relationship between dust levels on the adaxial and abaxial surfaces

Using the depth of the 900 nm ferric iron oxide CFA feature as a measure of dust levels as determined from the results in 4.2.6.4, it was found that the levels dust on the adaxial surface is correlated to the levels of dust on the abaxial surface as shown on Figure 20. The correlation coefficient of 0.7 is significant with a confidence level of 99 % confirming that the measurements of dust adaxial surface may be used as a surrogate of dust on the abaxial surface.

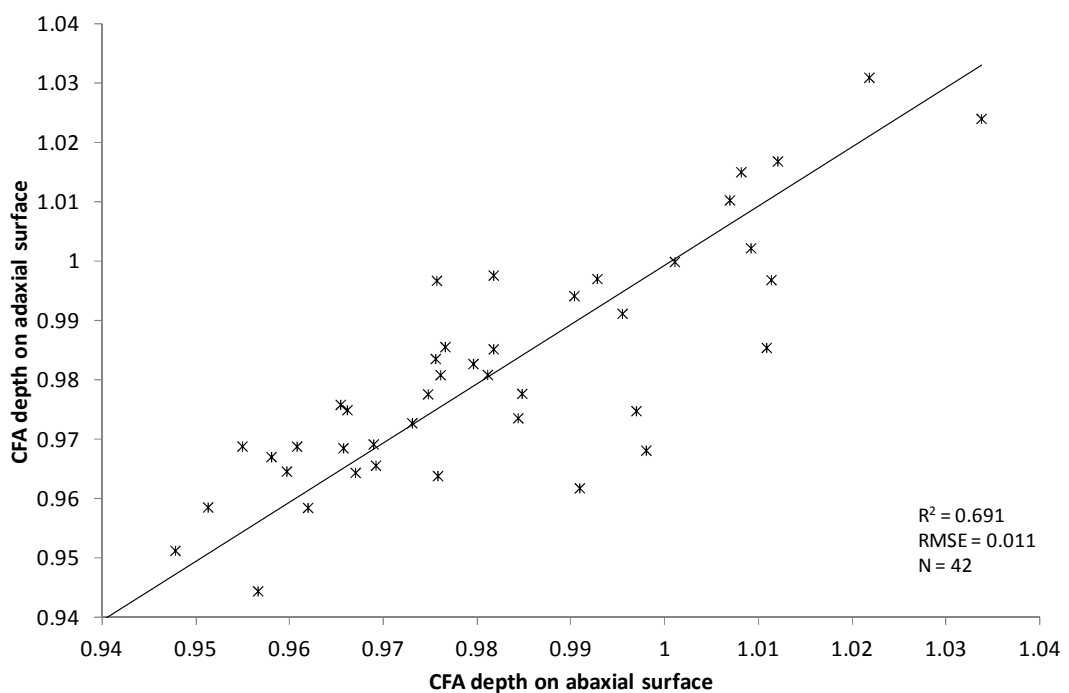


Figure 20: Scatterplot of the levels of dust (based on the depth of the 900 nm ferric iron oxide CFA feature) on the abaxial and adaxial surface of *Avecinnia marina* leaves. Data collected in April, July, August and November 1999.

4.2.6.6 Validation of dust algorithm

The final dust algorithm was validated with data collected on a different date from the same specie of mangrove, that is, *Avecinnia marina*, as well as data from a different species of mangrove, that is, *Rhizophora stylosa*.

Firstly, the dataset collected in November 2000 that used for the preliminary dust algorithm were used as validation data to determine the accuracy of the final dust algorithm. The final dust algorithm was applied the spectra to generated spectral-predicted dust measurements and this was compared to the actual dust levels. *Figure 21* shows this comparison. The data were found to be correlated (confidence level of 99 %) with a correlation coefficient of 0.94. This result indicates that the dust algorithm can confidently generate accurate measurements of dust from spectral data.

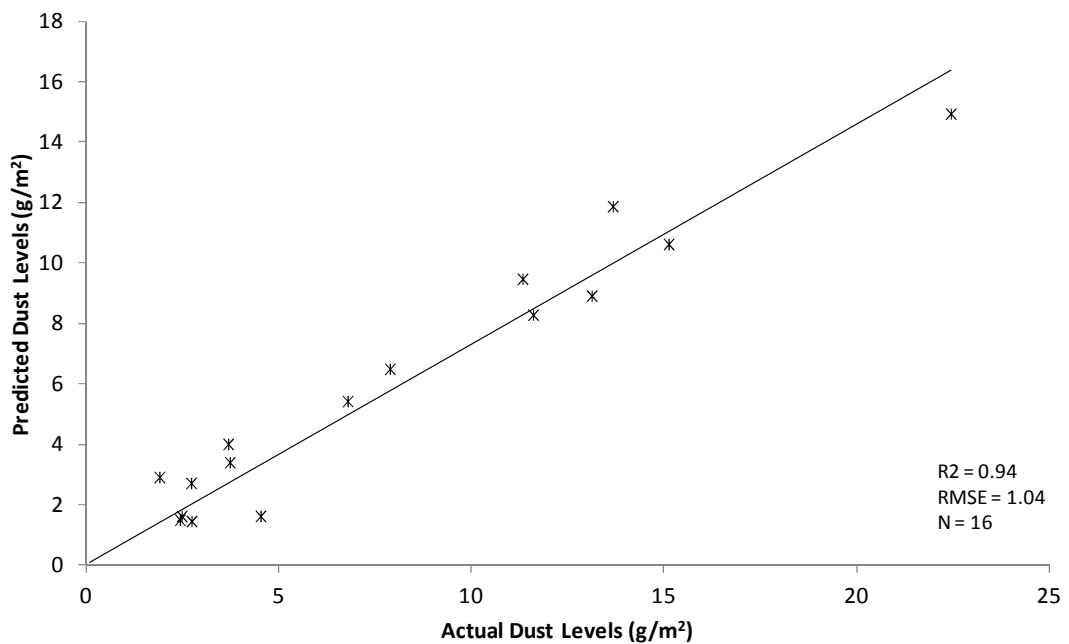


Figure 21: Scatterplot of Actual vs predicted dust amounts for Avecennia marina leaves.

The bulk of experiments conducted for this case history have been performed on *Avecennia marina* leaves as they were determined earlier on in the studies to be the most susceptible to dust loads. However, it was decided to collect some *Rhizophora stylosa* iron ore dusted leaves during the December 2001 field campaign to examine how the dust algorithm performed on a different species of mangroves. The final dust algorithm was applied to *Rhizophora stylosa* spectral data. *Figure 22* show the spectral-predicted dust measurements plotted against the actual dust measurements

recorded for these *Rhizophora stylosa* samples. The results show that these data are highly correlated with a significant correlation coefficient of 0.79. This result indicates that the dust algorithm is generic for at least the two mangrove species examined.

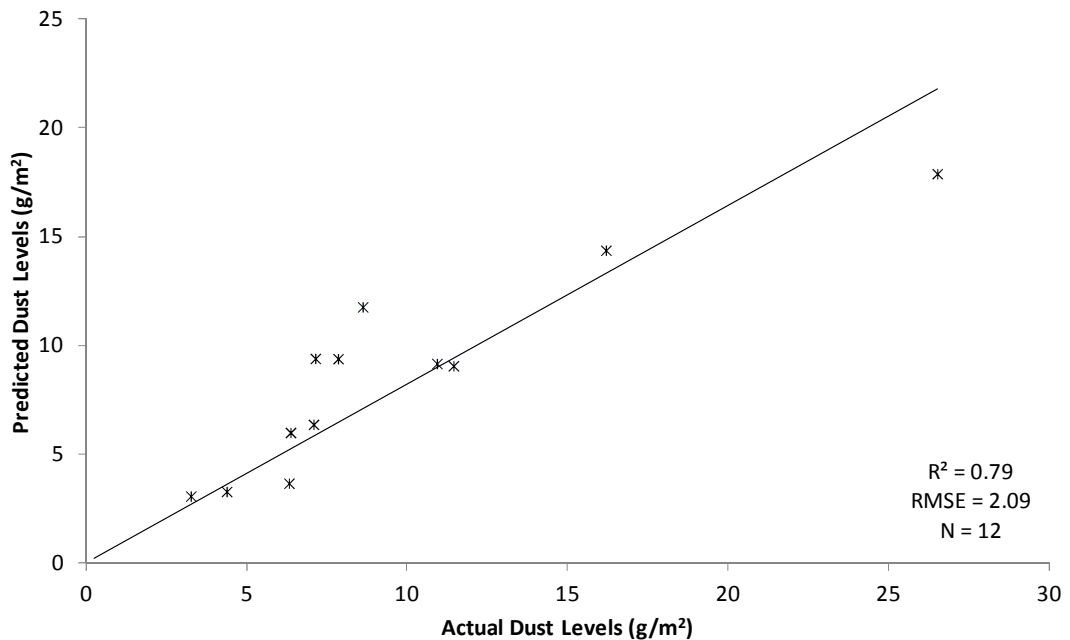


Figure 22: Scatterplot of actual versus predicted dust amounts for *Rhizophora stylosa* leaves.

4.2.7 Conclusion and discussion

A conclusion to be made from the experiment conducted to determine the impact of post-collection time on the leaves is that leaves from *Avecinnia marina* appear to be highly resilient to heat stress and hence the sampling procedure will have minimal impact on the condition of the leaves. Spectrally detectable physiological impact such as cell collapse and reduction of leaf water did not appear until several hours after heat stress was applied and the spectral indications of leaves drying were not present until the next day. These observations may be explained by the physiological make-up of the *Avecinnia marina* which is known to be one of the hardiest species of mangroves that are able to tolerate the least favourable environment (Lear and Turner, 1977). There a number of structural features on

mangrove leaves such as a thick-walled waxy epidermis, salt glands, sunken stomata and well-developed water storage tissue that enable them to withstand the natural environmental stresses on mangroves which include intense light, high temperatures and physiologically dry wind. Furthermore, the rates of transpiration (loss of water vapour), although quite variable in common mangroves, are often about one third of those of most land plants (Lear and Turner, 1977).

With the data collected to determine the effectiveness of dust removal procedure, it may be concluded that there is little variation between the clean sites and the leaves that have been cleaned and hence the procedure for the collection of dust was scientifically acceptable. An interesting outcome of these experiments is that the “cleaned” leaves were very similar to the environmentally clean leaves leading to a possible conclusion that there may be little physiological differences between the dusty and clean leaves. In fact, an examination of the angle between the NIR plateau and the red edge for the data collected for November 2000, shows that the data collected from cleaned leaves displays a right angle whereas the clean leaf data is sloped indicating that the “cleaned” leaves may be photosynthesising better than the clean leaves. However, more experiments are required to make definitive conclusions on this subject and are beyond the scope of this study.

It is recognised that removal of the dust with a wet tissue may affect the result through absorption of tissue-sourced water through the leaf surface. However, it has been assumed that very little water will be absorbed through the leaf surface because; the thick cuticle covering the epidermal layer contains waxes and is therefore hydrophobic. Some water may enter the stomata, though this is unlikely given that most/many stomata will be closed/closing due to; abscission (i.e. limited water supply to leaf) and the reduction of Leaf to Air Vapour Pressure Difference or LAVPD (i.e. a reduction in the driving force of transpiration) since the surface of the leaf is wet (i.e. saturated). This reduced transpiration will limit significant impact of water absorption (Landman, 2002; personal communications).

A conclusion from the experiment conducted to understand the relationship between dust levels on the adaxial and abaxial surfaces is that the measurements of dust on the adaxial surface may be used as a surrogate of dust on the abaxial surface.

The PLS analysis undertaken to understand the relationship between leaf spectra and leaf dust levels shows significant relationship between dust level and spectra at $R^2 = 0.82$. The FRC indicates that the correlations are predominantly related to ferric iron oxide. The results of the PLS analysis provides a model which theoretically may be transferable to the airborne data and used to generate maps of predictions of ferric iron oxide dust amount. However, the transferability may be limited by the quality of the airborne data and processing performed on them as some of the significant spectral features enabling the predictions are reliant on the VNIR. These regions are generally most susceptible to variability in atmospheric conditions and any variable brightness across the imagery and hence will require careful consideration when processing the airborne data. Further, as some of the regions of high FRCs coincide with vegetation spectral attributes and vegetation is highly dynamic, issues related to background vegetation have to be solved before these prediction results can be applied.

The analysis of the relationship between the 900 nm ferric iron oxide CFA feature and dust measurement found that a significant linear relationship exist between them. A spectral algorithm relating the depth of the 900 nm ferric iron oxide CFA feature and ferric iron oxide dust level was developed. The standard error for this algorithm is 2.975 g/m^2 . The dust algorithm was validated with data collected from two species of mangroves: one which was used to develop the algorithm and the other different from the training set. The results indicated that the dust algorithm was valid for at least the two mangrove species tested. The conclusion that can be drawn from this is that the algorithm is robust and also that the algorithm may be transferable to other mangroves and possibly other vegetation. This has implications for the routine use of the method for dust monitoring as the potential for employing a generic algorithm for measuring iron-derived dust is attractive and much easier to

apply operationally than species-specific models. Further work in this area is necessary to confirm this suggestion.

4.3 The acid case study in Brukunga

4.3.1 Methodology

Collection of samples for the Brukunga site was conducted on two field campaigns. The first field campaign in 1999 concurrent with the airborne acquisition, was conducted to validate minerals mapped using the airborne data collected during the first airborne acquisition in 1998.

Additionally, the data collected from the samples from the first campaign were used to conduct a preliminary study of the relationship between pH and spectra features. Recent studies (Bigham et al., 1996a, Bigham et al., 1996b) have found that the secondary minerals produced as a result of acid mine drainage vary with pH. Those precipitates formed at pH 6.5 or higher are predominately ferrihydrite or a combination of ferrihydrite and goethite. Schwertmannite was a major component of the precipitates at pH 2.6 to 4.5 with minor amounts of associated jarosite and goethite. Furthermore, jarosite increases in abundance with decreasing pH below a pH level of 3 and goethite appears at a pH of 3.3 and 3.6. These secondary minerals are Fe-rich and many of them are hydroxyl- and/or water-bearing, making it possible to spectrally identify them on the basis of their diagnostic spectral reflectance signatures (Swayze et al., 1996). Bearing in mind the possibility of identifying these minerals spectrally and that the minerals are related to pH, the feasibility of producing predictions of pH from spectra were tested.

The second field campaign undertaken in 2001 was conducted to collect a more comprehensive range of samples that represented the whole mine environment so that a better understanding of the relationship between spectra and pH can be gained and hence, assist in the development of a better model for the prediction of surface pH of the soil and rocks from spectral data. Validation of the 2001 airborne acquisition was also undertaken.

4.3.1.1 Field sampling method

The first field campaign was conducted concurrent with the 1999 airborne acquisition. Samples were collected from 43 locations across the mine site. The sampling locations are marked on Figure 23. On this occasion, samples were selected based on mineralogical maps produced from airborne hyperspectral data collected in 1998. Samples usually weighing less than half a kilogram were collected from within the top 5 cm of the surface.

The second acquisition consisting of 16 samples was concurrent with the airborne acquisition in 2001. Mineral maps and surface pH maps generated from the 1998, 1999 and 2000 airborne data guided the sample collection. The aims of this field acquisition were to collect samples which span a more comprehensive pH range (>2 to 7) than the previous samples collected in 1999, which were restricted to the 2-4 pH range, and, to cover a more comprehensive range of minerals representative of the Brukunga site. The sizes of the samples were similar to the size of the samples collected in 1999. The total number of samples collected from the two field campaigns was 59.

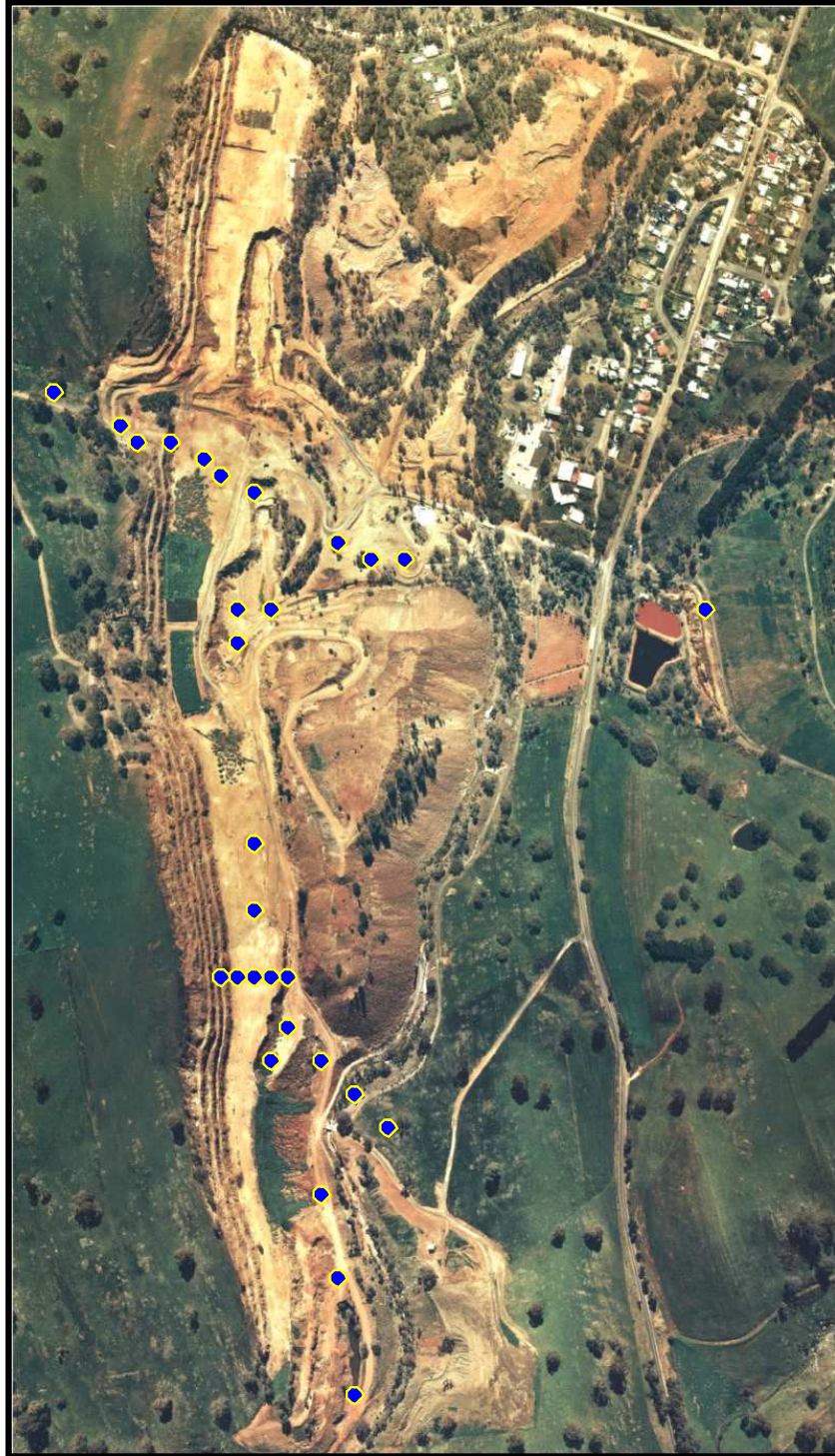


Figure 23: Location of samples collected during the 1999 field campaign at Brukungu.

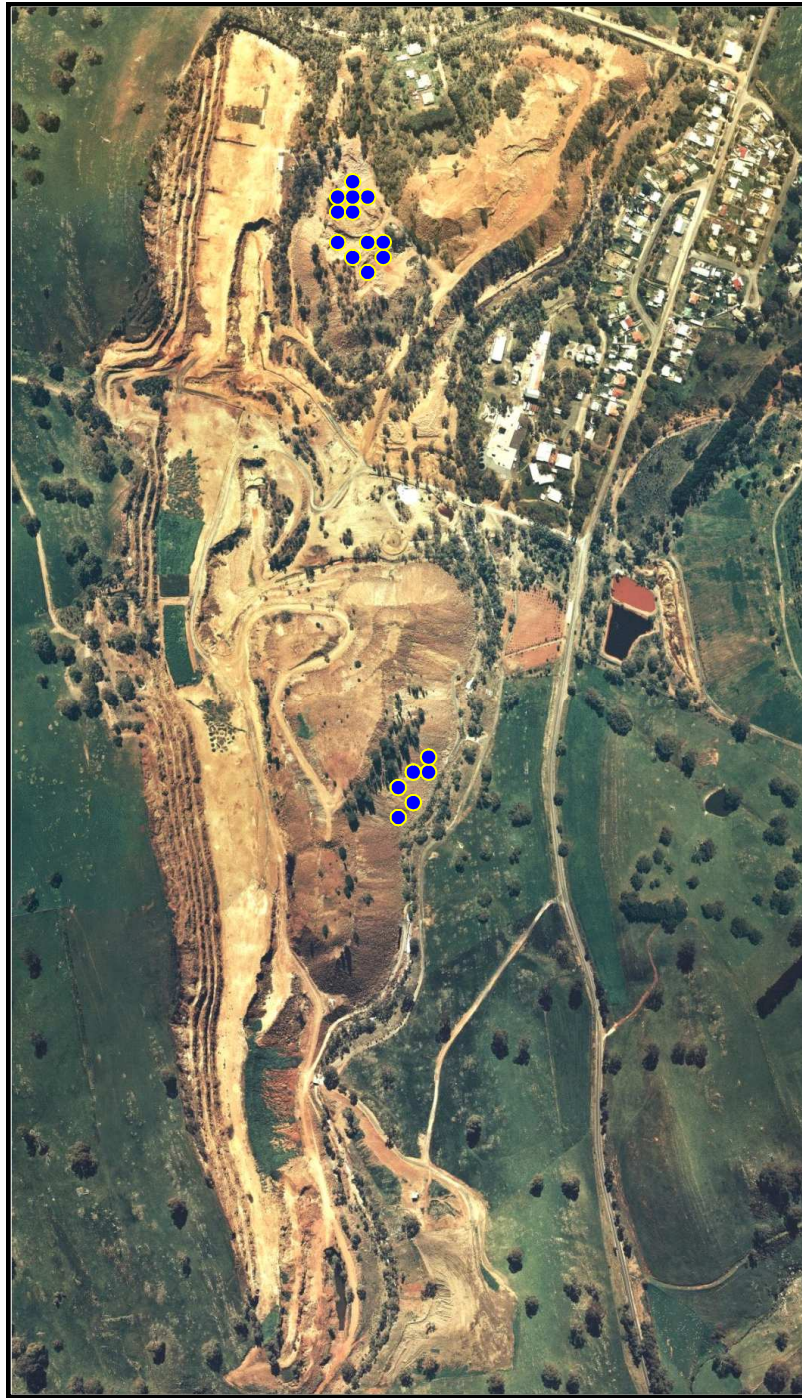


Figure 24: Location of samples collected during the 2001 field campaign at Brukungu.

4.3.1.2 Spectral laboratory measurements

The samples were characterised in the laboratory using an ASD FieldSpec® Pro FR spectrometer, which collected spectral data in the 350-2500 nm range, and a PIMA-II spectrometer, which collected higher resolution spectral data in the 1300-2500 nm SWIR range.

Figure 25 shows the configuration of the ASD FieldSpec® Pro FR. For input, the bare fibre optic was used, giving a FOV of 25 °. This was secured to a laboratory tripod so that the end of the fibre optic was 10 cm vertically from the sample. The sampling area for this configuration is a circle of diameter 4.43 cm. A 1000 watt quartz-halogen photoflood lamp was used to illuminate the samples. The lamp was placed at an angle of approximately 60 ° from vertical.



Figure 25: The ASD FieldSpec® Pro FR configured for laboratory measurements of samples collected at Brukungu.

Spectral measurements were collected from both the rock/soil samples and the pulp sample (sample produced after grinding, drying and chemical analysis). The samples were placed in 11x16.5 cm size plastic containers (as depicted on Figure 26) for measurement. Care was taken to ensure that the pulp samples had even flat surfaces before spectral measurements were collected. Also, care was taken to ensure that the field of view was in the middle of the samples and spectra checked to ensure that the plastic containers were not influencing the measurements.

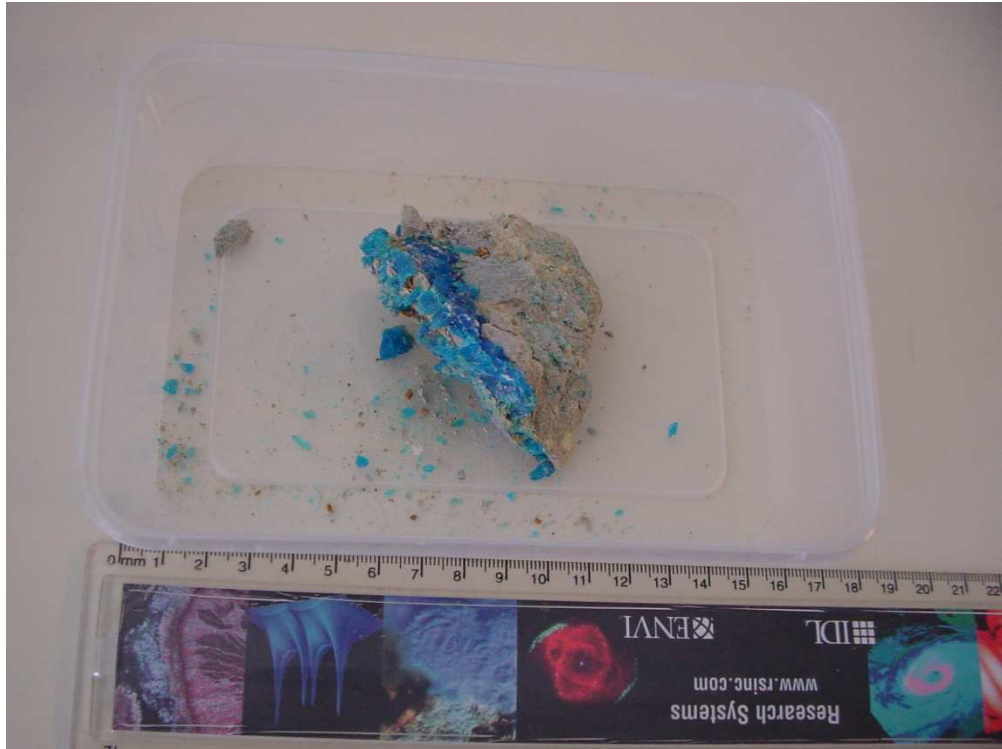


Figure 26: Plastic containers used for holding samples for spectral measurement.

Measurements using the PIMA-II are contact measurements and hence for these measurements, only the rock/soil samples were used.

4.3.2 Chemical analysis

Chemical analysis was performed in a commercial laboratory (Amdel) to measure minerals, elements, rare earth, pH, electrical conductivity (EC) and sulfur. Preparation of the samples included drying at a core temperature of approximately 100°C and then milling in a model LM1 pulveriser to a nominal 90% passing 106 µm. The analyses performed and the methods are tabulated below. Of specific interest to this study is the pH measurement. Specifically, the pH was measured on pulverised samples using a 1:5 ratio of sample to deionised water and analysed using a pH meter with an accuracy of 0.01. The uncertainties in the other measurements can be found in A.2.

The other chemical analyses are usually the standard suites accompanying AD monitoring. They were performed to investigate the relationship between the spectral data and pH to these elements.

4.3.3 Results

4.3.3.1 Relationship between sample spectra and chemistry

The Partial Least Squares analysis, undertaken to investigate the relationship between the laboratory spectral data and pH measurements used 55 samples out of a total of 59 samples collected. Four of the samples were found to be outliers as they were not representative samples for the calibration suite of AD minerals. Specifically, the outliers contained a road surface, two precipitates and one gypsum sample from a waste pile at a nearby farm.

Figure 27 shows the results from the PLS cross-validation analysis. It plots the measured values of pH against corresponding respective predicted values as determined from the PLS analysis. The results show a linear trend with an R^2 of 0.58, indicating general agreement between measured and predicted values. The RPD of the model was 1.536 indicating a fair or satisfactory prediction may be obtained. Further, the RMSE is also relatively low at 0.908.

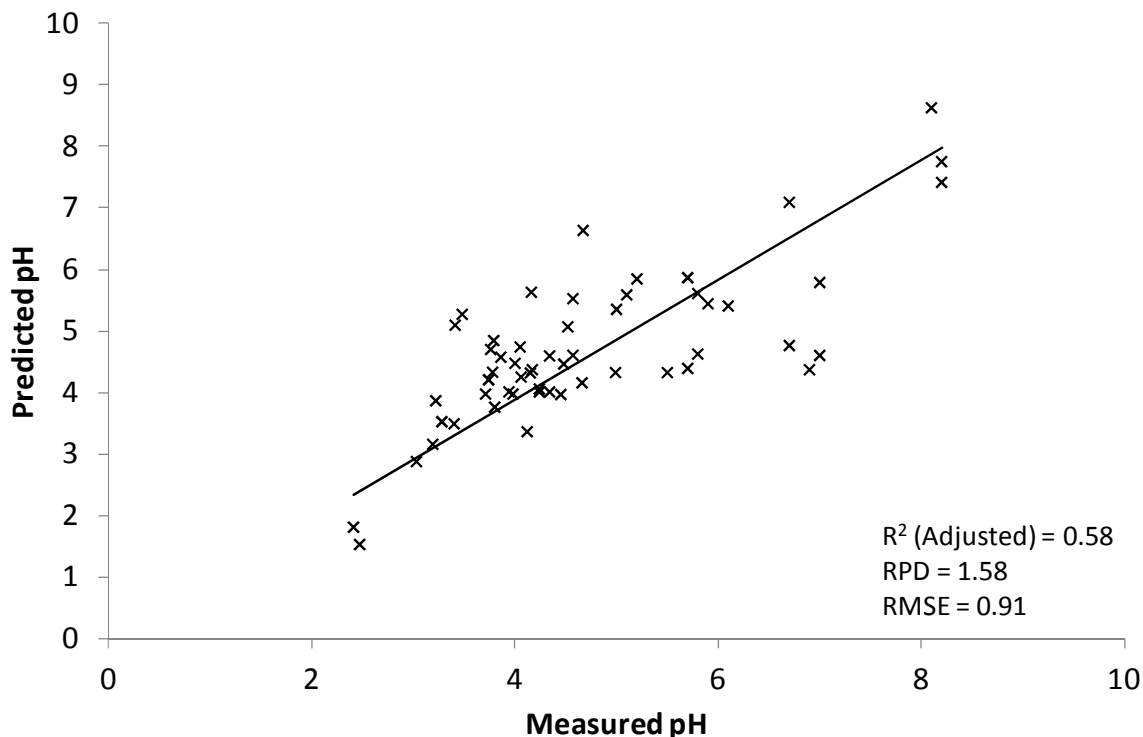


Figure 27: Scatter plot of chemically determined pH measurements against spectral-predicted pH measurements for the calibration dataset. The predicted values were obtained by applying the PLS results to the spectral calibration dataset (laboratory ASD measurements).

Figure 28 shows the final regression coefficients (FRC, plotted in red) from the PLS analysis. For simplicity in interpreting these results, this is plotted together with some typical secondary minerals identified in acid drainage (plotted in black, blue, green, and cyan). The FRC are the factors that are applied to each band of the spectral data to enable the prediction of the pH measurements. Therefore, bands showing high FRCs are bands that can be interpreted as strong contributors to the regression relationship. In this analysis, the bands shown to have a significant contribution are at 437, 582, 910, 1917 and 2260 nm (black broken lines show their location). Relating these significant FRCs to spectral attributes of the AD-related secondary minerals, it is shown that the most significant contribution is attributed to the ferrous iron absorption bands at 582 nm, which is related to ferrous iron charge transfer absorption (Curtis, 1985). This result also illustrates the importance of the of

the 437 nm jarosite feature (Crowley et al., 2003), the second most significant coefficient. It is interesting to note the comparison of the contribution of this feature relative to the 2260 nm feature related to O-H and Fe-O-H (Clark, 1999) which although is significant it has a lesser significance. Equally as important as the 437 nm feature is the 910 nm ferrous iron crystal field absorption (Curtis, 1985). Taken together, this result implies that pH predictions are related primarily to iron mineralogy. An important consideration is the significant coefficients in the VIS region especially around the 550-600 nm especially when trying to apply these results to the airborne imagery. This region is complicated by aerosols which are usually not properly accounted for.

The 1917 nm absorption is in the water absorption region and this feature would not be detectable in airborne data.

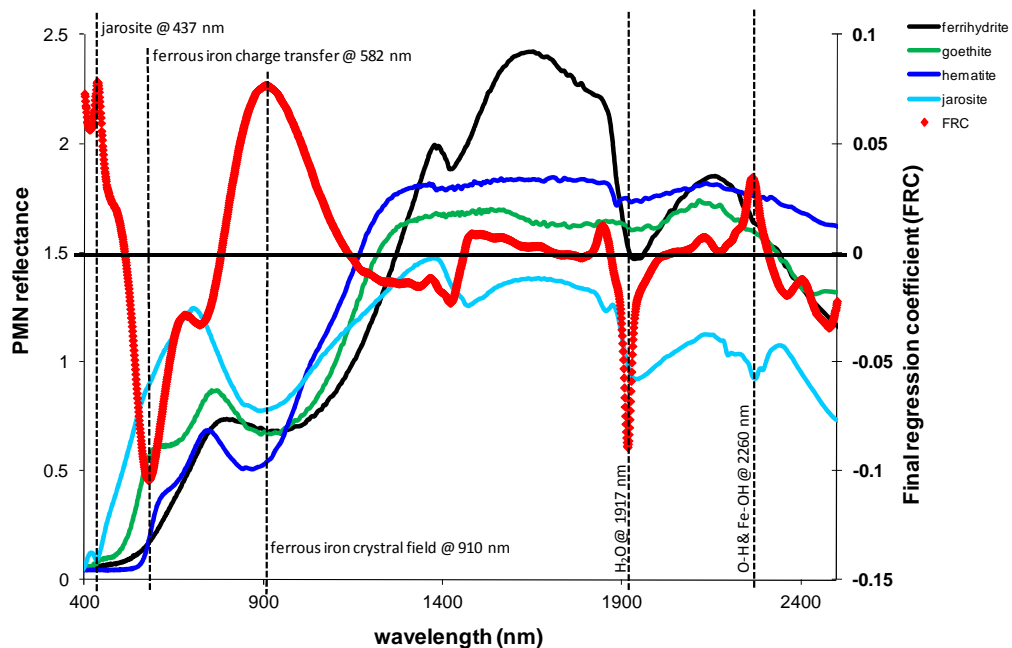


Figure 28: Final regression coefficient (FRC) results from partial least squares (PLS) analysis of pH (yellow) and spectra plotted together with spectra collected in the field in Brukunga (red and orange) and some typical AD related secondary minerals from the USGS library (Clark et al., 2007) (dark blue, dark green, blue and cyan). The vertical lines illustrate significant coefficients from the PLS analysis.

4.3.4 Conclusion and discussion

The results of the PLS cross validation analysis showed a good general linear trend (at $R^2=0.58$ and a relatively low RMSE of 0.91) between pH measured using laboratory analysis and pH predicted using spectral data. The RPD of 1.53 indicate that the model generated from the PLS analysis may be able to provide satisfactory accuracies for the prediction of pH values from spectral data. The analysis of the FRCs produced from the PLS analysis also confirmed that diagnostic spectral features specific to secondary iron minerals were mainly responsible for the relationship, indicating that the PLS equation is appropriate. The conclusion that can be drawn is that it is possible to reliably generate pH predictions from the spectral data with acceptable level of uncertainties.

However, one of the concerns is the high reliance on the VNIR region for inputs to the predictive model. This will have significant implications when applying these predictive models to airborne data as this spectral region can be severely compromised by (i) atmospheric effects, (ii) other acquisition conditions such as time of day and compass directions of the flight paths which influences the severity of BRDF effects and, (iii) the signal at high elevation terrains. The reliance on the VNIR region emphasises the need for proper pre-processing of the data for such issues as solar flux, atmospheric scattering (and atmospheric transmission) and good flight planning. Secondly, for determining pH, the confounding effects of vegetation on the spectra in the VIS-NIR must be addressed. A simple solution for vegetation contamination of imagery is to mask all vegetation affected pixels and produce pH prediction only for the non-vegetated areas. For most situations, this is a logical solution as most acid affected areas at mine sites are free of green vegetation.

4.4 Summary

This Chapter described the results from a series of laboratory experiments conducted as part of the study to develop an understanding of the spectral characteristics of the material required to be measured. Of course, changes in their spectral behaviour with variations in the environmental conditions and other factors may influence the

materials' spectral behaviour. In the case of the dust case history, experiments were also performed to determine some unknown variable which may compromise the measurements made. These could include time lapse between leaf collection and spectral measurement, effectiveness of dust removal and the relationship between properties of the adaxial and abaxial surfaces.

The results from the experiment performed to understand the impacts of the time difference between sample collection and measurement indicate that leaves from *Avecinnia Marina* appear to be highly resilient to heat stress and hence the sampling procedure will have minimal impact on the condition of the leaves. Spectrally detectable physiological impact such as cell collapse and reduction of leaf water did not appear until several hours after heat stress was applied and spectral indications of leaf drying were not present until the next day. Experimental data to understand the relationship between dust levels on the adaxial and abaxial surfaces confirmed that the measurements of dust adaxial surface may be used as a surrogate for dust on the abaxial surface. The data collected to determine the effectiveness of dust removal procedure showed very little variation between the properties of leaves from clean sites and the leaves that have been cleaned thereby confirming the validity of the procedure for the collection of dust.

The PLS analysis undertaken to understand the relationship between spectral response to dust deposition on leaves showed significant relationship between the dust levels and the spectra. The FRC indicated that the correlations were predominantly related to ferric iron oxide. The results of the PLS analysis is a model which, in theory, may be transferable to airborne data to generate maps of predictions of ferric iron oxide dust amount. However, the transferability may be limited by the quality of the airborne data and processing performed as some of the significant spectral features enabling the predictions are reliant on the VNIR spectral regions. These regions are generally most susceptible to the atmospheric conditions and any variable brightness across the imagery and hence will required careful consideration when processing airborne data.

The analysis of the relationship between the 900 nm ferric iron oxide CFA feature and dust levels found that a significant linear relationship existed between them. A spectral algorithm relating the depth of the 900 nm ferric iron oxide CFA feature and ferric iron oxide dust level was developed. The standard error for this algorithm was 2.975 g/m². The dust algorithm was validated with data collected from two species of mangroves: one which was used to develop the algorithm and the other different from the training set. The result of the analysis confirms that the dust algorithm is valid for both mangrove species. This has implications for other vegetation types as the algorithm may also be applicable for other mangrove species and possibly other vegetation. It is important to note that the advantage of the method developed from the dust study will be transferable to other hyperspectral sensors and locations and, relatively free of complicating issues such as BRDF (please see Chapter 5 for more detailed analysis) given well calibrated data.

The results of the PLS cross validation analysis of pH and spectra showed a good general linear trend (at R²=0.58 and a relatively low RMSE of 0.91) between pH measured using laboratory analysis and pH predicted using spectral data. The RPD of 1.53 indicate that the model generated from the PLS analysis may be able to provide satisfactory accuracies for the prediction of pH values from spectral data. The results indicate that diagnostic spectral features specific to secondary iron minerals are responsible for the relationship. These diagnostic features are located mainly in the VNIR region of the spectrum. This high reliance on the VNIR region for the predictive model has significant implications when applying these predictive models to airborne data as this spectral region can be severely compromised by atmospheric and other acquisition conditions such as time of day and compass directions of the flight paths which influences the severity of BRDF effects and the signal at high elevation terrain. More detailed explanation of BRDF and results of analysis of effects can be found in Chapter 5. The reliance on the VNIR region emphasises the need for proper pre-processing of the data for such issues as solar flux, atmospheric scattering (and atmospheric transmission) and good flight planning. Secondly, the confounding effects of vegetation on the spectra in the VIS-NIR must be addressed. A simple solution for vegetation contamination is to mask

all vegetation affected pixels and produce pH prediction only for the non-vegetated areas. For most situations, this is a logical solution as most acid affected areas are free of green vegetation.

Chapter 5

QUANTIFYING THE DIFFERENCE BETWEEN ATMOSPHERIC CORRECTION PACKAGES, IMPACTS OF FLIGHT PLANNING AND SENSOR BIASES

5.1 Introduction

One of the main hypotheses of this research is that algorithms developed from the laboratory study in chapter 4 can be applied to remotely-sensed hyperspectral data to provide quantitative environmental measurements. The question concerns how accurate these measurements will be, given the multitude of complications that may affect the signal being measured by the remote sensor which may have flow on effects to the final estimate of measurement of properties of the target. These complications include the layer of atmosphere that the remote sensor must “see” through to the sensor performance.

Remote sensing, by its very nature, implies that the signal that is acquired must pass through the atmosphere before reaching the sensor (Asrar, 1989). Constituents in the atmosphere (gases and aerosols) and clouds scatter and absorb radiation and as a consequence modulate the reflected radiation. The modulation may manifest as (i) brightness that is variable for each spectral bands where the atmospheric effects are wavelength-dependent, (ii) changes in the spatial distribution of reflected radiation from the target, (iii) changes in the overall apparent brightness of the target, and, (iv)

spatial variations in the apparent surface reflectance where sub-pixel clouds are present (Kaufman, 1989).

The procedure which removes the atmospheric effects from the signal acquired by the remote sensor is known as atmospheric correction or atmospheric compensation. There is a plethora of techniques and software packages developed for the reduction of remotely-sensed hyperspectral data to surface or “apparent” surface reflectances. The techniques are usually divided into two categories: the empirical-based corrections and physics-based radiative transfer modelling techniques.

Internal Average Reflectance (IAR) (Kruse, 1987), flat field (FF) correction (Carrere and Abrams, 1988, Roberts et al., 1986), the Empirical Line (EL), (Carrere and Abrams, 1988, Conel et al., 1987, Roberts et al., 1986) are some of the empirical-based corrections. The empirical-based approaches can generally be categorised into those that use scene-based information to derive the correction factors and those that rely on auxiliary spectral measurements from a field instrument to arrive at the correction factors. The main underlying assumption of these approaches is that the atmospheric constituents across the scene are uniform but this is not often the case especially for water vapour. This method therefore suffers from artefacts and scene-dependencies introduced from this inappropriate assumption. Furthermore, the scene-based methods assume that it is possible to derive within the scene, via the average or a “spectrally neutral area”, a representative spectrum from which the atmospheric correction can be estimated. This is rarely the case. Studies show that these methods usually results in the introduction of artefacts to the corrected spectra (Clark and King, 1987, Kruse, 1987).

The two main physics-based radiative transfer modelling techniques used in the VNIR and SWIR are ATmosphere REMoval Program (ATREM) (Gao et al., 1993) and (MODerate resolution atmospheric TRANsmission) MODTRAN (Adler-Golden et al., 1999, Berk et al., 1989, Matthew et al., 2000). ATREM is no longer supported and hence the majority of commercial atmospheric correction packages, of which there are numerous, are now based on MODTRAN. The main advantage of the physics-based techniques is the use of the data itself to estimate the water vapour

component and this is done on a pixel-by-pixel basis. This component is significant as water vapour is usually heterogeneous throughout a scene (Kaufman, 1989). Other atmospheric components such as ozone, carbon dioxide and oxygen are derived from models and are usually assumed to be uniform within the scene (Kaufman, 1989). However, the shortcoming of the physics-based technique is that current atmospheric radiative transfer models and the solar spectrum have not been characterised with sufficient accuracy to correct the data to the precision of some of the currently available sensors (Clark et al., 2003a).

A large number of commercial off-the-shelf atmospheric correction packages are available for performing physics-based atmospheric correction. The question for the non-specialist is: which one is the right choice? A limited number of publications are available on this subject but they do not quantify the differences. For example, (Ben-Dor et al., 2004) in his evaluation of the different packages concluded qualitatively that most of the physics-based techniques are quite similar in their absolute basis and execution, and produces similar results.

A further complication to atmospheric correction is the common assumption adopted by most available softwares, that the target materials are uniform and lambertian. These include Atmospheric CORrection Now (ACORN) (AIGLLC, 2000), HyCorr, Atmospheric Correction (ATCOR) (AIGLLC, 2000, Richter, 1996, Richter and Schläpfer, 2002) and Fast Line-of-sight Atmospheric Analysis of Spectral Hypercubes (FLAASH) (Adler-Golden et al., 1998). In reality, this is not the case as a given pixel's scattering behaviour can range from lambertian (scatters equally in all directions) to specular (mirror-like) to other strongly anisotropic behaviour. Pure Lambertian scattering is rare in nature as most naturally occurring land surface materials develop a pronounced brightening or "hotspot" effect at the 180° backscattered angle. This hotspot appears when the sun is immediately behind the view direction such that all surfaces, from the micro-scale to the macro-scale, are in full illumination. Shading develops away from this 180° backscattering angle causing the surface to appear increasingly dark or shaded. The backscattered effect is normally the most obvious in bi-directional imagery though pronounced forward

scattering and other reflectance peaks are sometimes observed depending on the anisotropy of the surface. Therefore, a complete hemisphere of surface scattering geometries is possible for every pixel for every wavelength. This phenomenon is characterised by the bidirectional reflectance distribution function (BRDF).

The BRDF is a physical parameter that quantifies the magnitude and distribution of radiance scattered by a surface and is defined by (Nicodemus, 1970) as

$$f_r(\theta_i, \varphi_i; \theta_r, \varphi_r; \lambda) = \frac{L(\theta_r, \varphi_r; \lambda)}{E(\theta_i, \varphi_i; \lambda)}$$

Equation 8

where BRDF is denoted by f_r and measured in units of sr^{-1} . This equation shows BRDF to be the ratio of upwelling radiance L_r reflected in a direction with zenith θ_r and azimuth φ_r , to the solar downwelling irradiance E_i incident from zenith θ_i and azimuth φ_i , at a specific wavelength λ .

The interrelationship between atmospheric correction and BRDF is illustrated by the following equation for the signal (radiance) received at the sensor (Vermote et al., 1994) where,

$$\begin{aligned} \rho_{toa}(\mu_s, \mu_v, \phi) &= \rho_0 + e^{-\tau/\mu_v} e^{-\tau/\mu_s} \rho_s(\mu_s, \mu_v, \phi) \\ &+ e^{-\tau/\mu_v} t_d(\mu_s) \bar{\rho} + e^{-\tau/\mu_s} t_d(\mu_v) \bar{\rho}' \\ &+ t_d(\mu_s) t_d(\mu_v) \bar{\rho} \\ &+ \frac{(e^{-\tau/\mu_s} + t_d(\mu_s))(e^{-\tau/\mu_v} + t_d(\mu_v)) S(\bar{\rho})^2}{1 - S\bar{\rho}} \end{aligned}$$

Equation 9

where ρ_{toa} is the reflectance at the top of atmosphere; ρ_0 is the intrinsic atmospheric reflectance (path reflectance); ρ_s is the surface reflectance; S is the reflectance of the atmosphere for isotropic light entering it from the surface; μ_s is

the cosine of the solar zenith angle; μ_v is the cosine of the view zenith angle; ϕ is the relative azimuth between the sun and view directions; $e^{-\tau/\mu_s}$ and $t_d(\mu_s)$ are the downward direct and diffuse transmittances of the atmosphere along the path of the incoming solar beam; $e^{-\tau/\mu_v}$ and $t_d(\mu_v)$ are the upward direct and diffuse transmittances of the atmosphere in the viewing direction; τ is the optical depth of the atmosphere. $\bar{\rho}$, $\bar{\rho}'$ and $\bar{\bar{\rho}}$ are the surface hemispherical-directional, directional-hemispherical, and hemispherical-hemispherical reflectances (albedos), respectively given by,

$$\bar{\rho}(\mu_s, \mu_v, \phi) = \frac{\int_0^{2\pi} \int_0^1 \mu L \downarrow(\mu_s, \mu, \phi') \rho_s(\mu_s, \mu_v, \phi' - \phi) d\mu d\phi'}{\int_0^{2\pi} \int_0^1 \mu L \downarrow(\mu_s, \mu, \phi') d\mu d\phi'} ,$$

$$\bar{\rho}'(\mu_s, \mu_v, \phi) = \bar{\rho}(\mu_s, \mu_v, \phi) , \text{ and}$$

$$\bar{\bar{\rho}} = \overline{\bar{\rho}'(\mu_s, \mu_v, \phi)} ,$$

$$\approx \frac{\int_0^1 \int_0^{2\pi} \int_0^1 \rho_s(\mu, \mu', \phi) \mu \mu' d\mu d\mu' d\phi}{\int_0^1 \int_0^{2\pi} \int_0^1 \mu \mu' d\mu d\mu' d\phi} ,$$

where $L \downarrow(\mu_s, \mu, \phi')$ is the downwelling diffuse irradiance with the sun at μ_s .

Solving for the BRDF effect is complex especially as every pixel measured remotely has its own BRDF character representing the aggregate of both surface and volume scattering interactions (both single and multiple). Therefore, additive and multiplicative relationships with linear and non-linear associations with potential wavelength-dependencies may be present.

BRDF impact on imagery can usually be minimised with appropriate flight planning where the aircraft flight is either towards or away from the sun. However, such approaches can only be possible for dedicated campaigns. For examples in Port Hedland, airborne hyperspectral data were acquired by HyMap (Cocks et al., 1998)

over on 9 occasions over a period of 10 years. The first acquisition occurred on 13th November 1998. These data were acquired as part of an Australian-wide CSIRO research campaign to evaluate this hyperspectral technology for various applications. This allowed flexibility in terms of timing, flight directions and other considerations in order to collect optimum data. That is, planned acquisitions were at specified times and with flight directions that enabled acquisition of data that was a balance between maximising the sun angle and minimising BRDF effects. These HyMap1 data (450 - 2500 nm) were acquired at 5 m pixel resolution. Another airborne hyperspectral dataset acquired five months later on 24th April 1999 were acquired by a commercial operator conducting another campaign. This meant that the acquisition had to fit into the schedule of the campaign irrespective of optimal acquisition parameters. Therefore, the data were collected at less than optimum condition and hence, contained BRDF effects related to the sun angle and flying direction. Further to that, the HyMap 1 instrument was used to acquire data on 20th October 2002, 4th December 2004 and 9th September 2008 and the HyMap2 sensor was used for acquisitions on 19th April 2004, 21st November 2005, 24th August 2006 and 17th October 2007. Only for 2002 was a dedicated campaign planned with consideration made for the flight time and flight direction selection that maximised the sun angle and minimised BRDF effects. All data collected after 2002 were acquired as part of commercial campaigns and hence, were subjected to the schedules of the operator so it was not possible to adhere to strict flight plans to minimise BRDF effects on the imagery. As a result, the 2004, 2006, 2007 and 2008 data were affected by BRDF while the 2005 data contained minimum BRDF effects.

The other major obstacle to obtaining accurate surface reflectance is sensor biases/noise, which can have a significant influence on the measured signal. Laboratory calibrations of hyperspectral instruments are usually undertaken before they are deployed. However, shifts in radiometric and spectral calibrations can occur. Shifts in band centre wavelengths and changes in spectral resolution may occur when an instrument is airborne or spaceborne due to mechanical vibrations, and changes in instrument temperature and pressure, outgassing and aging of optical or electronic components. (Gao et al., 2004, Guanter et al., 2006). Therefore, in

some cases, spectral recalibrations of the data are necessary to ensure that the data are spectrally accurate.

Spectral accuracy is an important requirement when using hyperspectral data to derive quantitative information (Gao et al., 2004, Green, 1998) because the depth, shape, and location of spectral features are key variables in the characterisation of the corresponding surface materials in either solid, liquid, or gaseous states (Guanter et al., 2006).

Published methods for the spectral recalibration of hyperspectral data mainly rely on the use of narrow spectral features related to atmospheric gaseous and water vapour constituents to guide the spectral shifts required to recalibrate the data. For example, a method developed by Gao et al., (2004) involves matching the atmospheric water vapour, oxygen, and carbon dioxide absorption features, and solar Fraunhofer lines on the image data with the known spectral positions of these spectral features. Based on the premise that incorrect spectral calibration causes spikes in the gaseous absorption regions, Guanter et al., (2006) presents an iterative procedure where radiative transfer implemented atmospheric correction is coupled with successive spectral shifts to arrive at the smoothest surface reflectance.

One of the most important requirements of monitoring data are that the measurements being used are reliable and repeatable through time and the uncertainties associated with the measurements are quantified. The compounding effects of the complications described above have the potential to compromise the quality of the data and prevent the retrieval of accurate surface reflectances which in turn will have a flow on effect to the measurements and interpretation generated from these data. It is therefore essential to remove or minimise the interfering effects of atmospheric absorption and scattering, and instrumental biases and to reduce the spectral data to surface reflectances if accurate identification and mapping of materials are to be obtained from spectral data (Clark et al., 2003a). This chapter describes the analysis undertaken to understand and quantify the uncertainty that may potentially compromise the acquisition of accurate surface reflectances from remotely-sensed hyperspectral data. Specifically, the study examines 1) differences

between atmospheric correction packages; 2) instrument biases, specifically, instrumental spectral miscalibration and, spectral sampling including variations in band-centres and band-widths and, 3) the impact of BRDF caused by non-optimum flight planning.

5.2 Method

For the purposes of determining the differences between atmospheric correction packages and quantifying the effects of sensor spectral miscalibration, I employed three different atmospheric correction packages. The software used were AtComp (Rodger, 2011a) a CSIRO-developed software, FLAASH (Adler-Golden et al., 1998) and HyCorr (Mason, 2000). Detailed descriptions of the software can be found on section 3.5.5.

In order to compare the fundamental differences between the atmospheric correction packages, the atmospheric correction was first performed without the spectral recalibration components. A single dataset, that is, the dataset acquired across Port Hedland in 2006 was used in the evaluation. As much as possible, the same input parameters for prescribing the atmospheric aerosol models and water vapour were used for all the packages. Specifically, the atmospheric model assumed was tropical, the water vapour retrieval was based on the 940 nm water vapour absorption feature, no aerosol model was applied and the visibility was set at 40 km.

The scene location, acquisition parameters and times were retrieved from the GPS and flight log information for the pre-2000 datasets and the report file for the post-2000 datasets as provided by the operator.

Secondly, spectral recalibration using FLAASH and CSIRO-MODTRAN-SODA were applied to the same 2006 dataset and results compared. The spectral recalibrations implemented by both software are based on identification of a series of known atmospheric features. For FLAASH, the features must be specified for each detector of the spectrometer and hence for the HyMap spectral range, the 760 nm O₂ spectral absorption feature, 820, 940 and 1130 nm water vapour spectral features and

2020 nm CO₂ spectral absorption features were selected. The CSIRO-MODTRAN-SODA will automatically determine the spectral features to be used depending on the spectral range.

The CSIRO-MODTRAN-SODA software was applied on 8 of 9 the airborne datasets acquired at Port Hedland to assess the performance of the atmospheric correction and to monitor the performance of the sensors over the time intervals. This dataset containing acquisitions acquired between 1998 and 2007 represents the most comprehensive set of multi-temporal hyperspectral data acquired over an extended period of time in Australia.

In the analysis of the results, the reflectance spectra generated from the airborne hyperspectral data located at a uniform sand bank calibration target (-20° 18' 15.31", 118° 35' 24.13") were compared to the ground truth spectral data acquired. The residuals remaining after the corrections: the ratio between the corrected airborne data and the ground truth data, were generated and used as a representation of the noise/error resulting from the complicating effect. Specifically,

$$S_n = R_a/R_g$$

Equation 10

Where S_n = error or inaccuracy factor, R_a =airborne spectral data and, R_g = ground truth data.

To help illustrate and quantify the impacts of the uncorrected issues on the environmental measurement generated using remotely-sensed hyperspectral data that was not properly corrected, these “noise” were added to the training spectral dataset acquired in the laboratory in 4.2.6.4. Specifically,

$$R_{na} = R_l \times S_n$$

Equation 11

Where R_{na} =noise added spectrum, R_l =laboratory spectrum, S_n = “noise” spectrum

These “noise-added” spectra were then used to generate predictions of dust levels. The error introduced by the uncorrected issue was calculated as the difference between the dust levels generated from the original laboratory spectra and the dust levels generated from the noise-added spectra. Specifically,

$$E = (74.646D_{R_{na}} + 1.1622) - (74.646D_{R_l} + 1.1622),$$

$$E = 74.646(D_{R_{na}} - D_{R_l})$$

Equation 12

Where E is the error/uncertainty of dust levels, $D_{R_{na}}$ is the 900 nm ferric iron oxide CFA depth of noise added spectrum, D_{R_l} is the 900 nm ferric iron oxide CFA depth of laboratory spectrum.

Further to the analysis conducted using the results of the application of the atmospheric correction packages, the following describes analysis performed to determine the uncertainty that may be caused by the changes in sensor spectral calibration. The laboratory training data were resampled to all the bandpasses and bandwidths of the all the acquisitions across Port Hedland. The predictive algorithm for dust levels was incorporated to these resampled data to produced predicted dust levels. The 2006 calibration was used as the base from which all the other year’s calibration were compare. The errors were quantified as the difference between the 2006 predicted dust levels and the predicted dust levels and written in the equation below,

$$E_{wc} = DL_p - DL_{2006} ,$$

$$E_{wc} = (74.646D_{R_n} + 1.1622) - (74.646D_{R_{2006}} + 1.1622)$$

$$E_{wc} = 74.646(D_{R_n} - D_{R_{2006}})$$

Equation 13

Where E_{wc} is the error introduced from a certain set of wavelength calibration, DL_p is the predicted dust level, DL_{2006} is the predicted dust level for 2006, D_{R_n} is the 900 nm ferric iron oxide CFA depth for bandpasses and bandwidths of year n, and $D_{R_{2006}}$ is the 900 nm ferric iron oxide CFA depth for the bandpasses and passes of 2006.

The evaluation of the impact of BRDF caused by non-optimal flight planning consists of the comparison of datasets from the overlap regions between adjacent flight lines acquired on the same date. Two datasets were used in this analysis. The first was acquired in 1998 and had minimal BRDF effects and the second set was acquired in 1999 and included pronounced BRDF effects. PMN was applied (see section 3.5.3) to the airborne reflectance data to provide an understanding of the BRDF impact on the imagery. The PMN effectively removes any wavelength-independent, multiplicative BRDF effects as well as topographic shading, surface albedo (average reflectance) and uncorrected solar irradiance. It was also used to remove variable lighting conditions in the laboratory.

After applying PMN to the airborne data, comparisons were made for targets across the overlap regions between adjacent two flight lines. The targets were examined for consistency between the flight lines. Non-matches between the adjacent flight line signify that the BRDF effects are wavelength-dependent and non-multiplicative. Further to that, the analysis performed included evaluation of the ratios between concurrent polygons on the overlap areas of the adjacent flight lines to locate portions of the regions where the BRDF effects were wavelength independent.

5.3 Datasets used for analysis

The datasets used were the airborne hyperspectral acquired at Port Hedland between and 2008 and associated ground spectral data acquired concurrent with the airborne acquisition.

5.3.1 Airborne data

HyMap airborne hyperspectral data (HyMap (Cocks et al., 1998)) were acquired over the Port Hedland harbour on 9 occasions over a period of 10 years.

The first acquisition occurred on 13th November 1998. These data were acquired as part of an Australian-wide CSIRO research campaign to evaluate this technology for various applications. This allowed flexibility in terms of timing, flight directions and other considerations in order to collect optimum data. That is, we planned the acquisition at the times and with flight directions that enabled us to acquire data that was a balance between maximising the sun angle and minimising BRDF effects. These HyMap1 data (450 - 2500 nm) were acquired at 5 m pixel resolution.

Another airborne hyperspectral dataset was acquired five months later on 24th April 1999, 17 days after a cyclonic event (Tropical Cyclone Gwenda passed through Port Hedland on 7th April 1999). This dataset was acquired using the 96 channel AMS instrument acquiring in the 530 - 2500 nm range. This sensor is the first airborne hyperspectral sensor built by Integrated Spectronics. It has very similar characteristics as the more recent HyMaps except that it has fewer spectral bands and, the regions between 450-550 and 1100 to 1400 nm are not available. These data were acquired by a commercial operator conducting another campaign. This meant that the acquisition had to fit into the schedule of the campaign irrespective of optimal acquisition parameters. Therefore, the data were collected at less than optimum condition and hence, contained BRDF effects related to the sun angle and flying direction.

The HyMap 1 instrument was used to acquire data on 20th October 2002, 4th December 2004 and 9th September 2008. The HyMap2 sensor was used for acquisitions on 19th April 2004, 21st November 2005, 24th August 2006 and 17th October 2007. These data were acquired at 3.5 m pixel spatial resolution.

In 2002, we mounted a dedicated campaign and hence, for the flight planning, consideration was made for the time and flight direction to acquire data that

maximised the sun angle and minimised BRDF effects. All data collected after 2002 were acquired as part of commercial campaigns and hence, were subjected to the schedules of the operator. Therefore, it was not possible to adhere to strict flight plans to minimise BRDF effects. The 2004, 2006, 2007 and 2008 data were affected by BRDF while the 2005 data contained minimum BRDF effects.

5.4 Field spectral data acquired concurrent with airborne acquisition

The field data acquired concurrent to the airborne data were treated as the ground truths and used to estimate the possible errors from the complicating factors. The main dataset used for performing this task was the spectral data acquired across the beach sand. The other data acquired at the other targets were mainly used to validate the results after correction of the airborne data.

5.4.1 Port Hedland

Ground spectral data from two calibration/validation sites were collected using the GER-IRIS MkIV field spectrometer close to the 1998 acquisition. The first validation site is the tennis court located on McGregor St (C.T.0 on Figure 32), next to the racecourse at Port Hedland town. The tennis court is concerted and from visual observations appears to be uniform. The court had a total area of approximately the equivalent of 14x8 pixels.

The calibration site is the sand bank (C.T.2 on Figure 32) at the spit on the coastline next to the Yacht Club on Sutherland St at the Port Hedland town. Spectra of the site collected on two occasions concurrent to airborne data acquisition, are shown on Figure 29. The width of the uniform sand area is approximately 5 pixels and is as long as the coastline. The variations between the different dates have been noted. This is most likely the result of dust as the sand bank is close to the handling facility. Figure 34 shows the average spectrum of sand bank calibration target overlaid on a photo of the site.

The difference is illustrated on Figure 30. It plots the differences between the average spectrum acquired in 2002 and the averages spectrum from 2006. The largest variation can be seen around the regions of the iron oxide absorption features, that is, around the VIS to NIR regions. The maximum difference was approximately 3.9% reflectance and occurs in the NIR region coincident with the iron oxide absorption features.

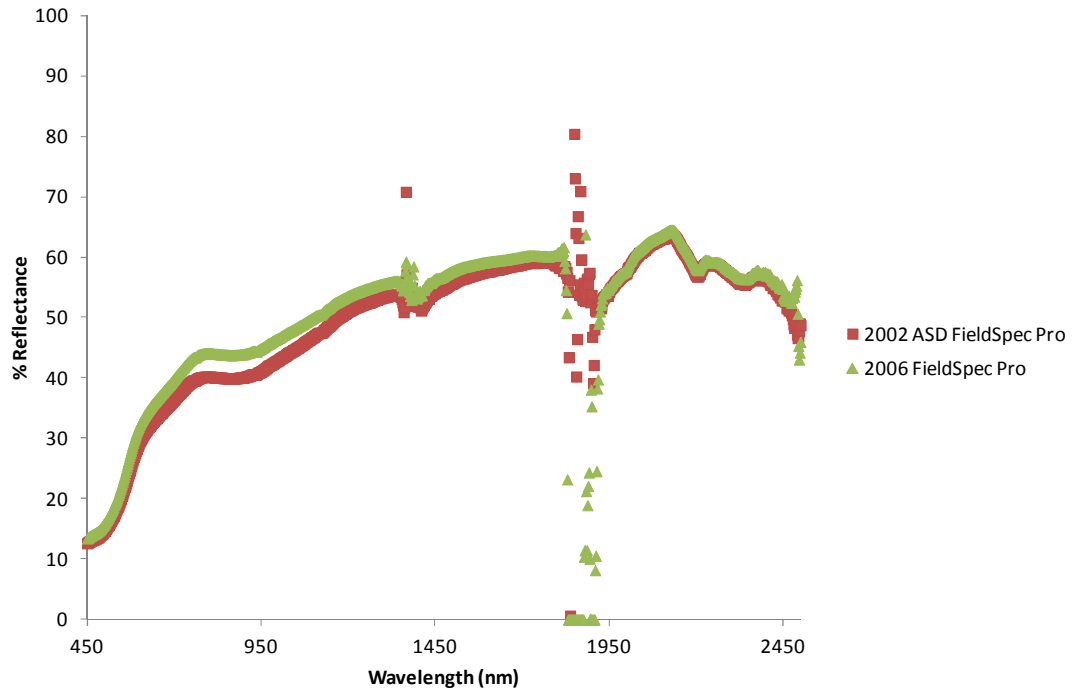


Figure 29: Spectra of sand bank calibration target located at C.T.2 on Figure 32. The average of spectra acquired in 2002 is plotted in red and the green spectrum is the average of spectra acquired in 2006.

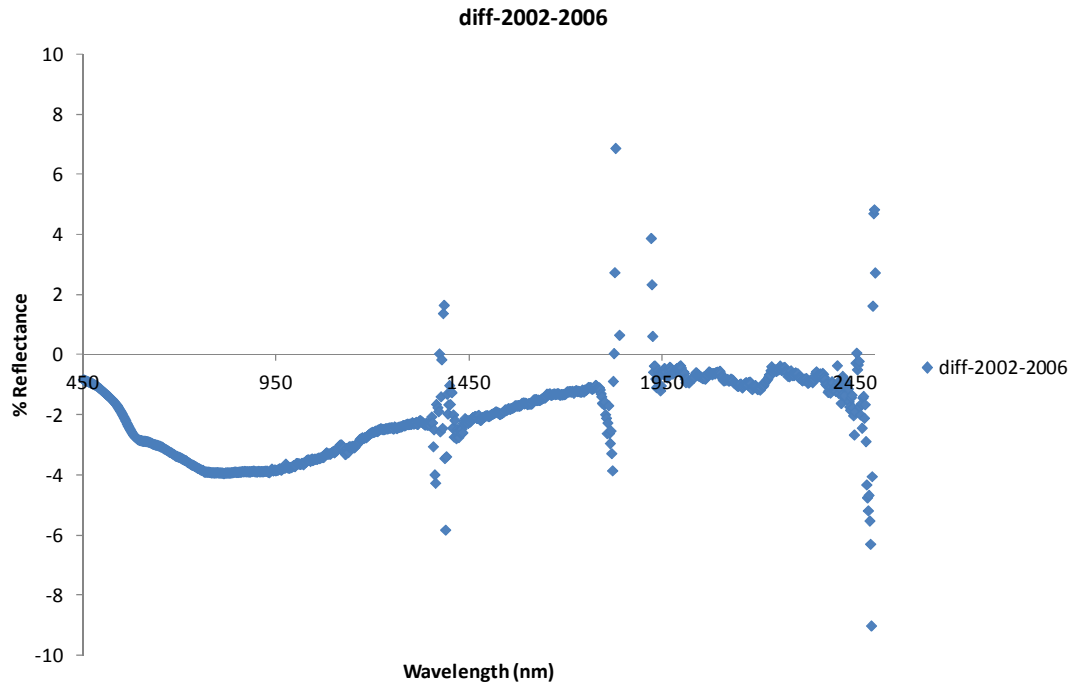


Figure 30: Differences between 2006 and 2002 for the sand bank calibration target (C.T.2).

Despite the variations between dates, the area itself is uniform in nature. The uniformity of the calibration target is illustrated on Figure 31. The blue spectrum shows the average spectrum for all the spectra acquired in 2002. The maximum and minimum of all the spectra for each band are also plotted in red and green respectively. Here, it is shown that the variation is at maximum 4.1% in the VIS, 6.7% in the NIR and 8.7% in the SWIR regions. Note that this variation is within the variation between dates.

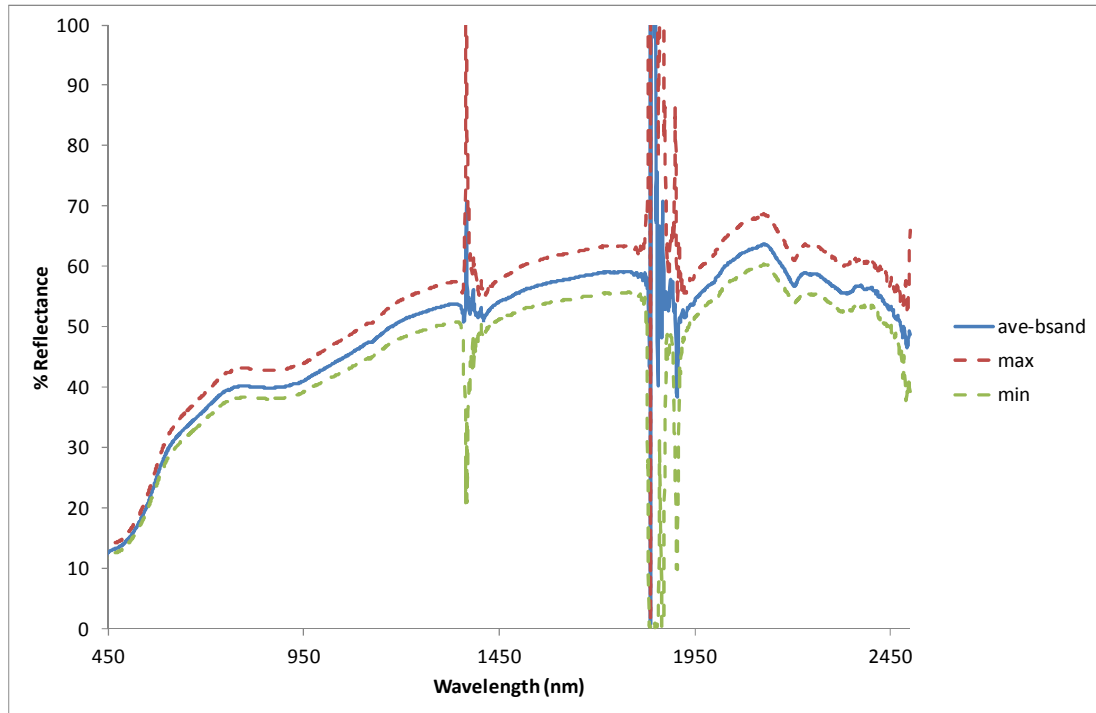


Figure 31: Average spectrum of the sand bank calibration target, C.T.2. The minimum and maximum of all the spectra measured are shown. The measurements were made in 2002 concurrent with airborne hyperspectral data acquisitions.

Ground spectral data from four other validation sites were collected using the ASD Field Probe field spectrometer concurrent with the 2002 and 2006 airborne acquisitions. Figure 32 shows the location of all the validation targets on a map of the Port Hedland town. The validation site shown on Figure 33 is the carpark on Richardson St for the boat ramp near Laurentian Point. The associated average spectrum for the site is overlaid on the photo. The carpark is a large bituminised area and from visual observations appears to be relatively uniform. The size of the entire carpark would cover approximately the equivalent of 20x30 pixels. The third target is shown on Figure 35 together with the average spectrum of the area. It is a cleared area of bare soil of approximately 14x34 pixels located besides Wedge St. A second carpark located on Wedge St was the fourth target measured and the size of this carpark is 13x18 pixels. Figure 36 shows the average spectrum of the surface material of the carpark. The last target was a road, at least five pixels wide next to the stockpiles on the BHPBIO site. Figure 37 is a photo showing the road surface material. The average spectrum of all spectra collected for the road is plotted on the

photo. The locations of all the targets were recorded using a hand-held field GPS and are tabulated on Table 3.

Calibration and Validation Target	Easting	Northing
C.T.1: Carpark 1	664684	7753408
C.T.2: Coastal beach sand strip	665880	7753897
C.T.3: Cleared bare ground	664592	7752874
C.T.4: Carpark 2	664536	7752849
C.T.5: BHPBIO road surface	666437	7751926

Table 3: GPS locations of calibration and validation targets. The map projection is AGD66, zone 50.

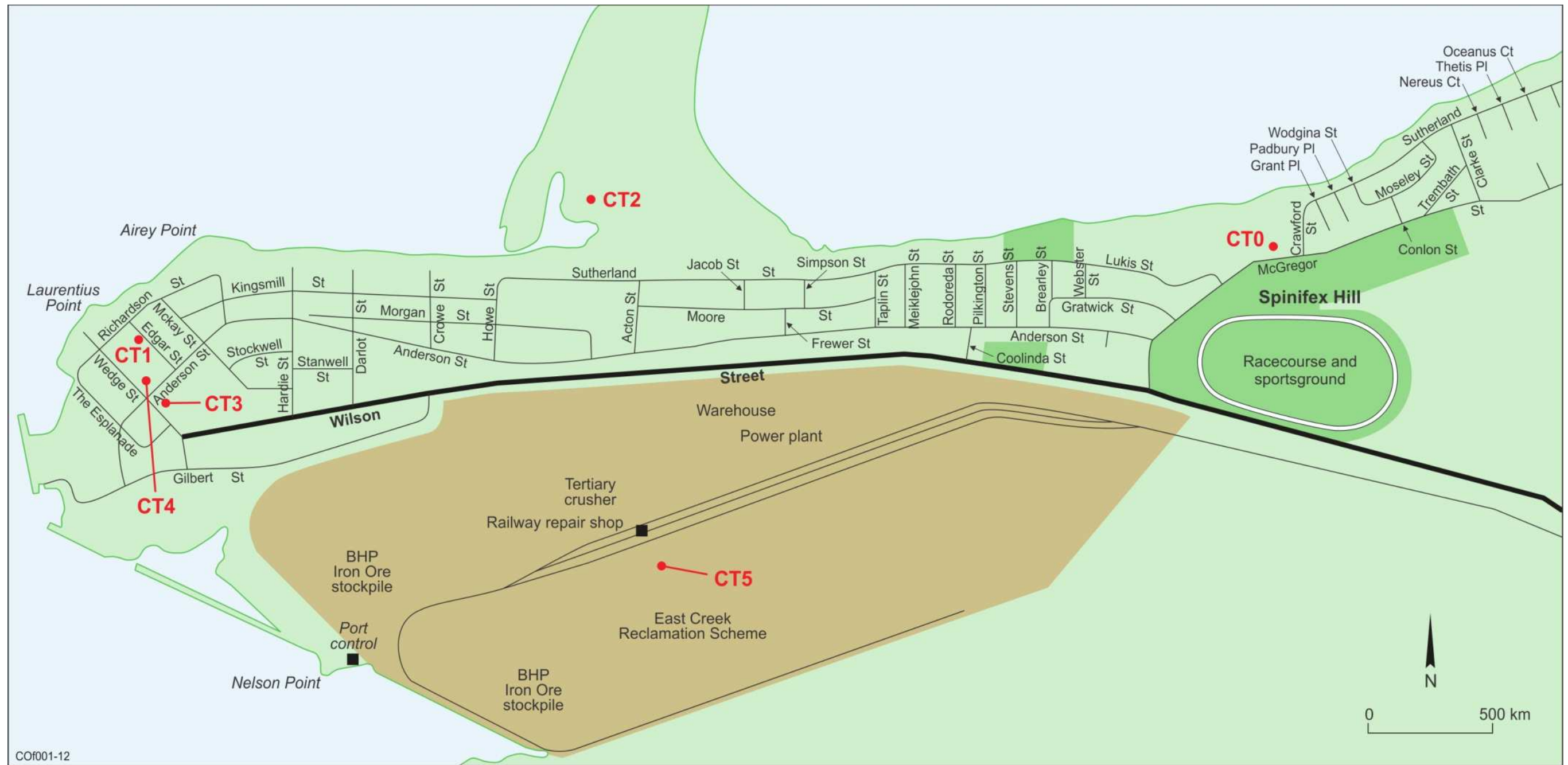


Figure 32: Map of Port Hedland. The locations of the calibration and validation target sites are identified on the map and labelled. C.T. denotes calibration and validation target. The brown areas show the confines of the port handling facility, the areas in green are areas of the township and blue indicate water or the sea.

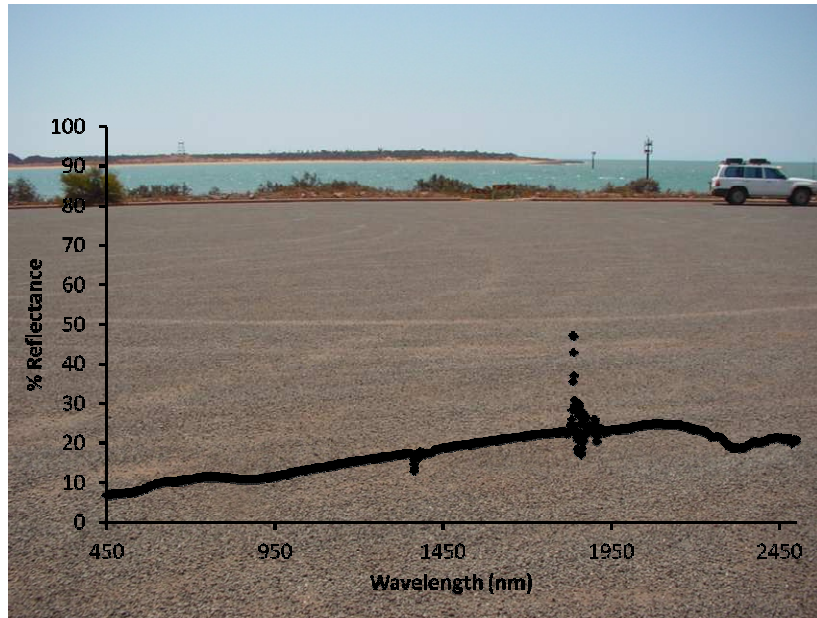


Figure 33: Calibration/validation target C.T.1: Carpark at the boat ramp on Richardson St. in Port Hedland.

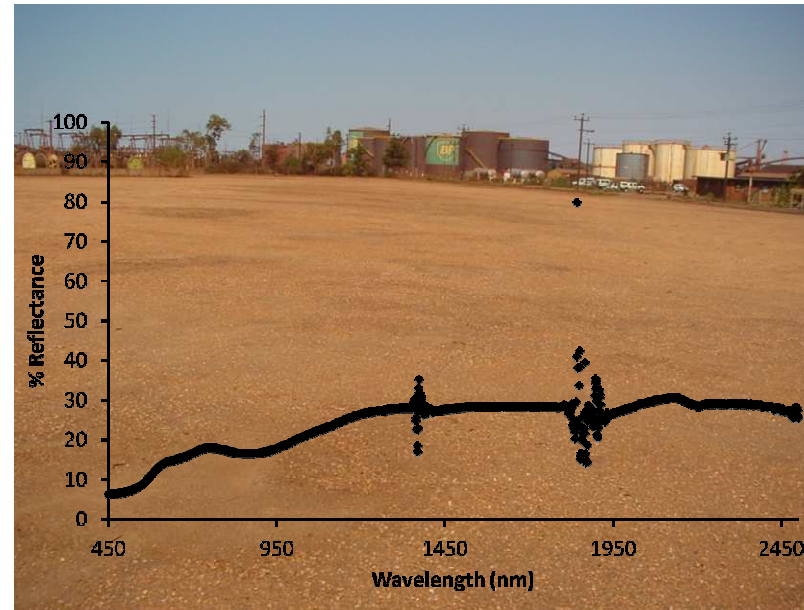


Figure 35: Calibration/validation C.T.3: Large cleared surface on Wedge St., Port Hedland.

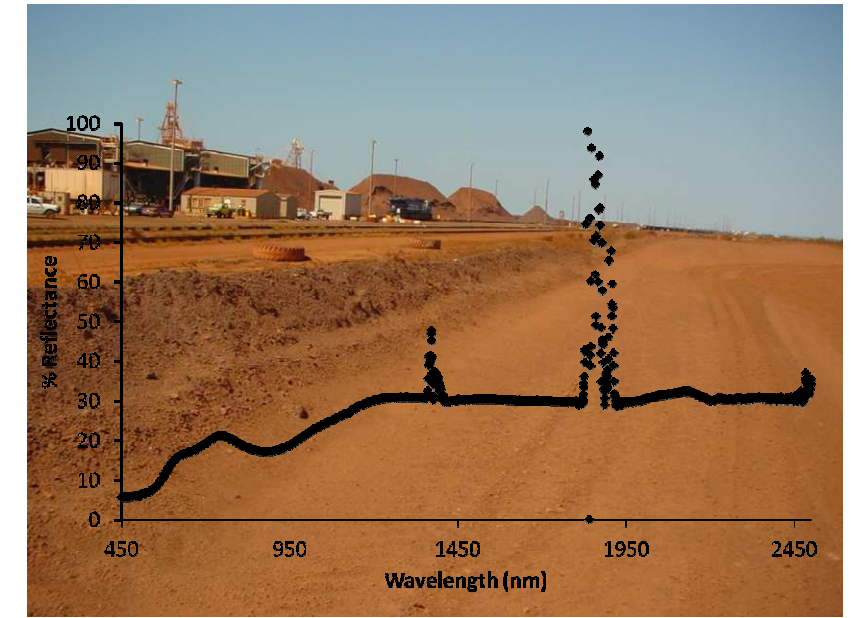


Figure 37: calibration/validation C.T.5: Internal road on the side of the conveyor and stockpile at Burgess Point in the BHPB port operations.

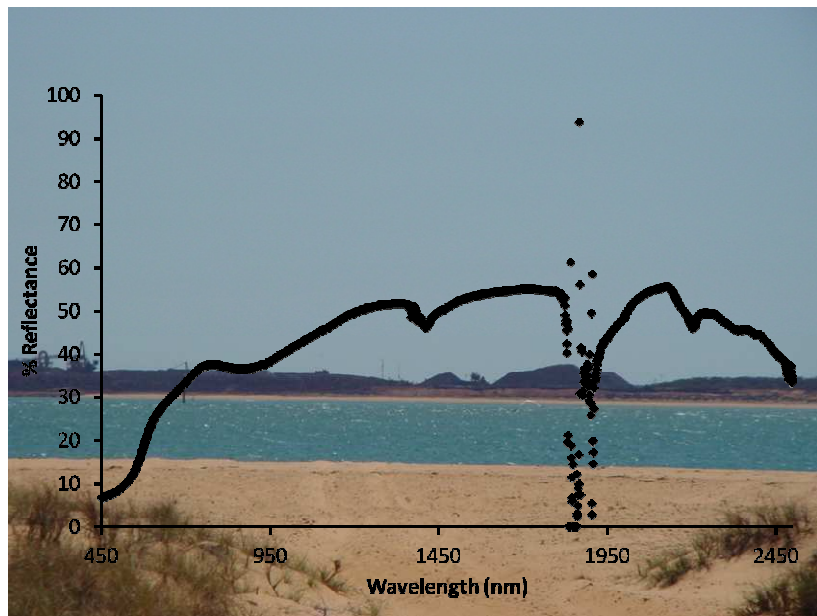


Figure 34: Calibration/validation C.T.2: Coastal sand strip next to the Yacht Club on Sutherland St. in Port Hedland.

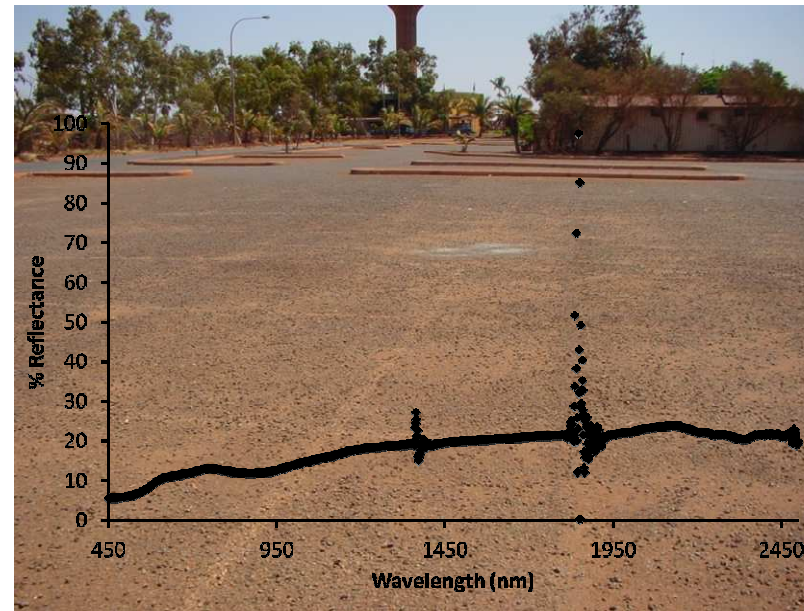


Figure 36: Calibration/validation C.T.4: Carpark on Wedge St., Port Hedland.

5.5 Results

Figure 38 shows the ratio between the ground truth and airborne reflectances extracted from the 2006 airborne hyperspectral data for the sand bank site. In an ideal case, the graph will show horizontal lines at unity where the airborne data equals the ground truth data. The small peaks and troughs usually termed atmospheric offsets, which appear in reality, are related to incomplete modelling of some of the atmospheric components. The atmospheric transmittances are plotted (in black) to better illustrate the relationship of these offsets to the atmospheric components. For example, offsets that are located around 820, 940, 1140, 1400 and 1900 nm can be matched with absorptions related to atmospheric water vapour. Other major offsets are located: around 760 nm which is related to O₂ and around 2020 nm and is related to CO₂.

When comparing the results from the different atmospheric correction packages, the graph indicates that the CSIRO-MODTRAN-SODA atmospheric correction performed very similarly to the FLAASH correction except around the 1400 and 1900 nm water vapour regions. The similarity can mostly be attributed the commonality between them which is the use of MODTRAN. The HyCORR results however, are quite dissimilar with a distinct offset from the other two packages. This may be related to the outdated database in ATREM. Other inconsistencies can be observed in regions between 450 to 550 nm where the HyCORR data shows a large variation between the ground truth and the airborne data. This issue has been identified by others (Clark et al., 2003a) and is related to ATREM's incomplete compensation for aerosols.

When the offsets calculated following Equation 10 and, depicted on Figure 38 were incorporated to the laboratory spectral data used for the development of the dust algorithm described in 4.2.6.4 according to Equation 11 and Equation 12, the predictions for the dust measurements differed by an average of 3.239 g/m² for CSIRO-MODTRAN-SODA, and an average of 3.258 g/m² for FLAASH and an average of 3.325 g/m² for HyCORR when compared to the ideal case of the laboratory data where no atmospheric signal were incorporated. Therefore, the

results indicate that for a dataset similar to the one acquired in Port Hedland in 2006 and for the application of ferric iron oxide dust measurements, the CSIRO-MODTRAN-SODA software provides marginally the best results. Further, the result of the analysis can be interpreted as: if atmospheric correction with an off the shelf package such as FLAASH (without wavelength calibration) was applied to an airborne dataset similar to those acquired in Port Hedland in 2006 and no further calibration was performed using ground calibration targets, the uncertainty when using those data for the measurement of ferric iron oxide dust level is expected to be $\pm 3.258 \text{ g/m}^2$.

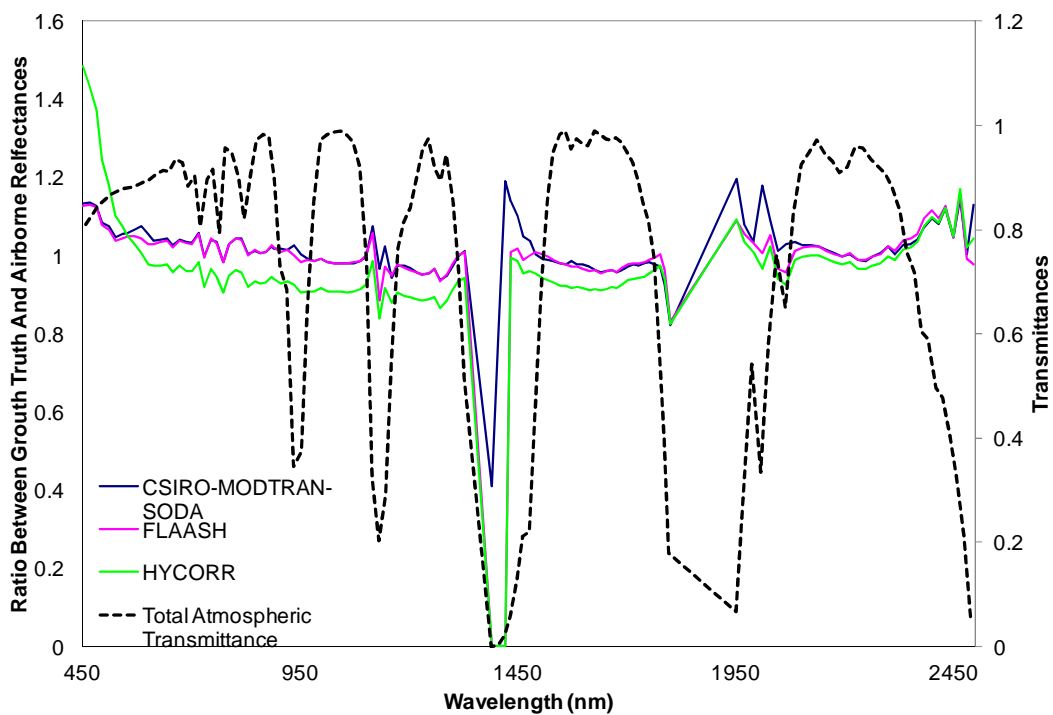


Figure 38: Comparison between CSIRO-MODTRAN-SODA, FLAASH and HyCORR when applied to airborne hyperspectral data acquired in 2006. The blue, pink and green lines (axis on left hand side) show the ratio between the atmospherically corrected data and the ground truth data. The atmospheric transmittances are plotted (in black and axis on right hand side) to illustrate the relationship between the offsets remaining after atmospheric correction and the atmospheric constituents.

Figure 39 plots the ratio between the ground truth and airborne hyperspectral data acquired in 2006. The ratio was calculated according to Equation 10 and the average spectrum for the area of the sand bank site for the ground truth and the airborne

hyperspectral data were used for the graph. The graph depicts the differences between data that had been processed with and without wavelength recalibration. The wavelength recalibrations appear to have minimised/reduced the offsets in most regions for the CSIRO-MODTRAN-SODA and FLAASH softwares. In the case of the CSIRO-MODTRAN-SODA, the most improvements appear at the end of the spectrum in the SWIR region. When the wavelength recalibrated offsets were incorporated to the laboratory training datasets using Equation 11 and Equation 12, the uncertainties or measurement errors were both reduced: to an average of 2.143 g/m^2 when CSIRO-MODTRAN-SODA was used, compared to an average of 2.312 g/m^2 when FLAASH was used. Table 4 summarises these results together with the results from the analysis without the wavelength calibration. It illustrates the impact of instrument calibration on achieving accurate reflectances with atmospheric corrections. The CSIRO-MODTRAN-SODA software reported a wavelength miscalibration of only 2.1, 0.7, 0.4 and 2.1 nm respectively for each of the instrument's detectors and the FLAASH adjustments were 2.9-4.9, 1.1-1.6, 0, 1.5-2.9 nm. Note that the FLAASH recalibration software assumes variable wavelength shifts while the CSIRO-MODTRAN-SODA software assumes a constant shift for each detector. This may be because of the development of the FLAASH software which was based on the correction of the Hyperion satellite smile/frown effect (Felde et al., 2003) while the CSIRO-MODTRAN-SODA software was developed specifically for HyMap processing. This translated to a downstream impact of increasing the uncertainties or measurement error of the dust levels by 29% when using FLAASH and 34% when using CSIRO-MODTRAN-SODA.

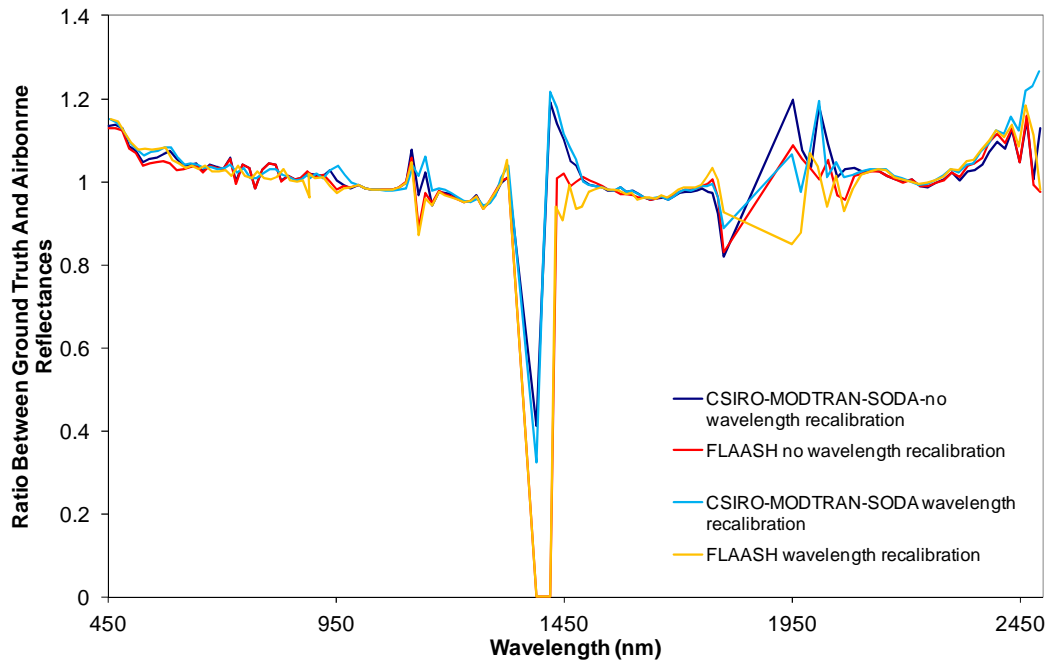


Figure 39: Comparisons for 1) with and without application of wavelength recalibration and 2) between CSIRO-MODTRAN-SODA and FLAASH. The airborne data shown were acquired in 2006.

Software used	CSIRO-MODTRAN-SODA without λ calibration	CSIRO-MODTRAN-SODA with λ calibration	FLAASH without λ calibration	FLAASH with λ calibration	HyCORR
Uncertainty or measurement error of dust levels contributed by the atmosphere	3.239 g/m ²	2.143 g/m ²	3.258 g/m ²	2.312 g/m ²	3.325 g/m ²

Table 4: Additional uncertainties or measurement error expected to be caused by the atmosphere when using airborne hyperspectral data for measuring ferric iron oxide dust levels. Note that these uncertainties were only calculated for the atmospheric conditions during the 2006 acquisition in Port Hedland. These figures will obviously vary with different atmospheric conditions.

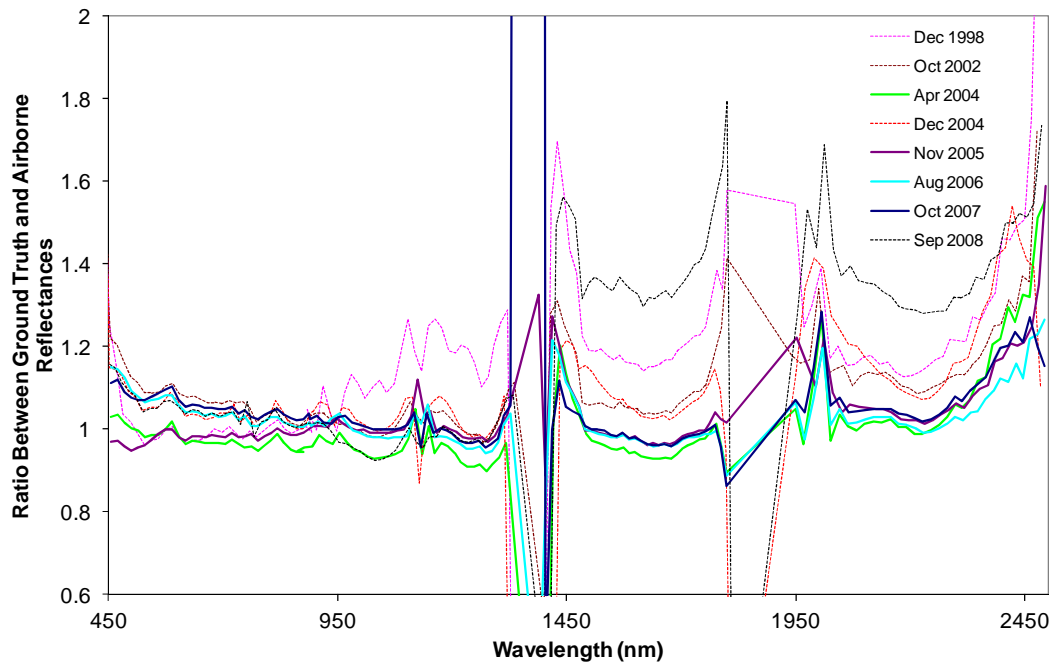


Figure 40 plots the ratios (calculated according to Equation 10) of the ground truth and all the airborne data acquired from 1998 to 2008 except for the 1999 dataset. The average spectrum of the sand bank area for the ground truth and airborne data were used. Firstly, the gross differences were examined. The data were acquired using two different sensors. The broken lines indicate that the data were acquired with the HyMap1 and the solid lines indicate acquisition with the HyMap2 sensor.

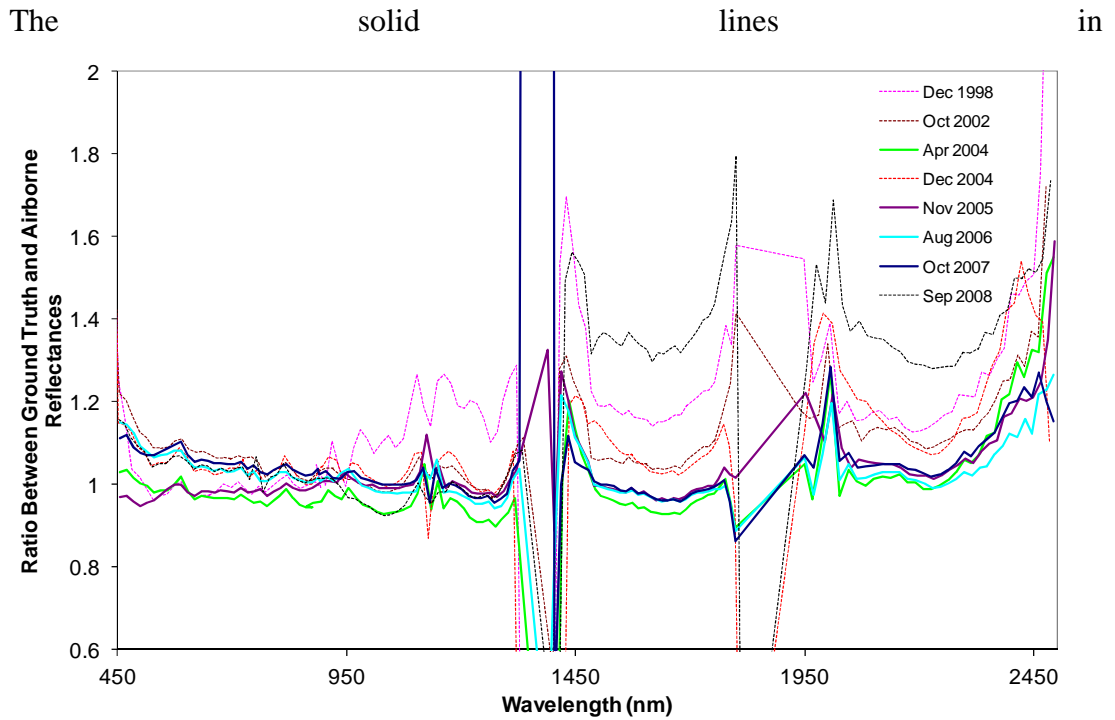


Figure 40 group tightly indicating that the HyMap2 sensor was stable across the years of acquisition. Also, the offsets appear very consistent over time. That is, where there are peaks, the peaks appear consistently over the year and the offsets increase in the same manner at the wings of the major water vapour windows every year. The consistency indicates that the offsets are likely to be related to incomplete modelling of the atmospheric conditions inherent in MODTRAN.

The inconsistencies in the broken lines in

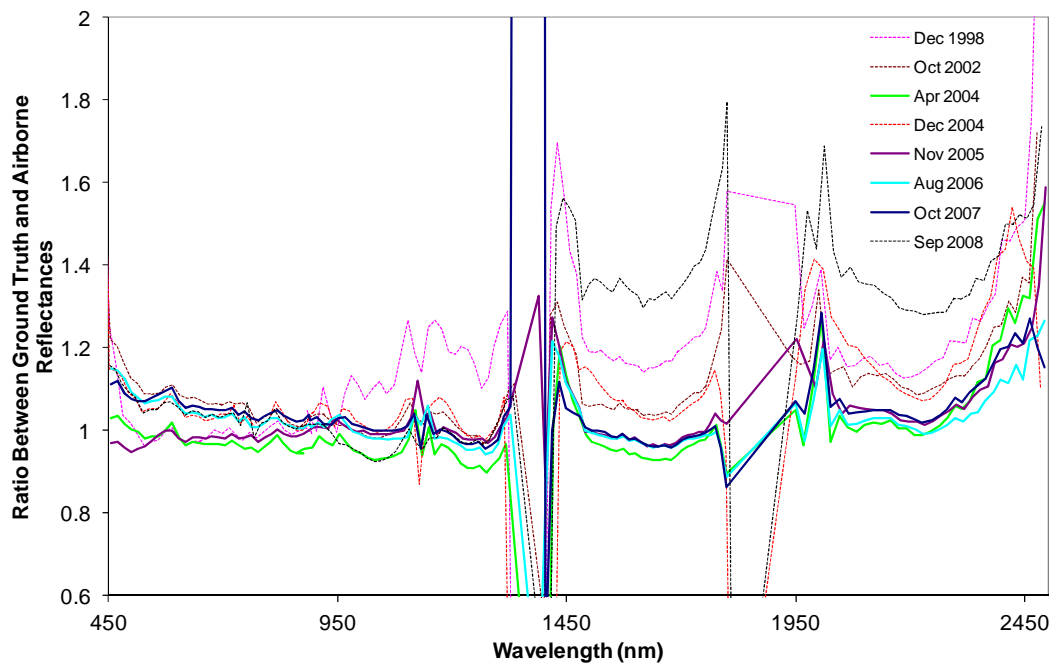


Figure 40 are cause for more concern. The 1998 results were generated at the start of the operation of the sensor and hence calibration of the instrument may be at its infancy. However, the 2002, 2004 and 2008 ratios clearly show miscalibrations in the SWIR detectors for the HyMap1 sensor. This is indicated by the magnitude of the offsets from the VIS and NIR. Note that these miscalibrations will not be a major impact for the measurements of ferric iron oxide dust levels as the algorithm relies mainly on the VIS and NIR regions where the offsets are largely consistent between the years. However, these miscalibrations will have major impacts for algorithms such as the algorithm for the prediction of pH which has a significant reliance on the SWIR region.

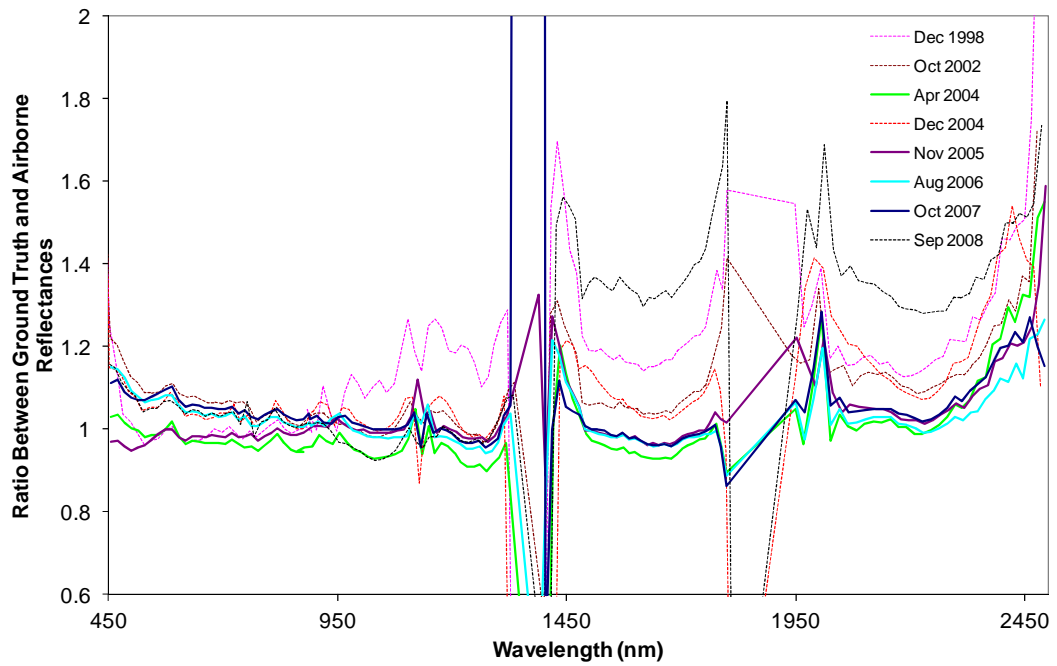


Figure 40: Multi-temporal comparison of the ratio between ground truth and airborne reflectances for the sand bank site. The broken line indicates that the airborne data were acquired using the HyMap1 sensor while the solid line indicates data acquired using the HyMap2 sensor.

The dust algorithm was developed based on the bandpasses and bandwidths of the 2006 data. Therefore, I calculated the uncertainties that may be introduced when the bandpasses and bandwidths vary from the 2006 values using Equation 13 to understand the impact of the changes with the instrument calibration. The results tabulated on Table 5 indicate that the largest impact was with the December 2004 calibration which would introduce an uncertainty of $\pm 1.692 \text{ g/m}^2$ to the dust measurement. The other years calibrations appear to have much smaller impacts.

Acquisition	2008	2007	2005	122004	042004	2002	1998
Uncertainties (g/m ²)	0.165	0.209	0.174	1.692	0.140	0.127	0.064

Table 5: Uncertainties in ferric iron oxide dust levels that may be introduced when the bandpasses and bandwidths vary from the ones used to develop the dust algorithm.

The evaluation and analysis for BRDF effects were performed on the datasets acquired in 1998 and 1999. Figure 41 illustrates two adjacent flight lines of data acquired in Port Hedland on 13th November 1998.

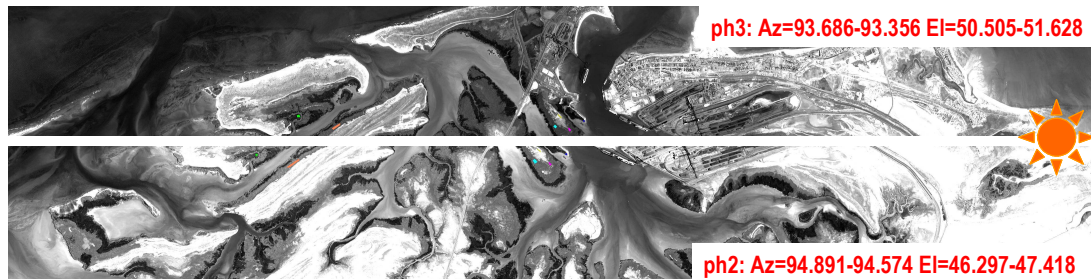


Figure 41: Airborne hyperspectral data acquired on 13th November 1998. Adjoining flight line 2 (lower) and 3(upper) are shown here together with an illustration of the approximate position with respect to the imagery and a description of the sun azimuth (Az) and elevation (El) at the time of acquisition. The flight direction was approximately E-W.

For this analysis, different material types were examined and they were divided into vegetated cover and non-vegetated cover. Within each of these categories, a number of polygons representing different classes within each category were selected across the overlap area between flight line 2 and flight line 3. The arithmetic mean for each polygon was calculated before comparison.

Firstly, the reflectance data were examined for brightness variations that may be related to BRDF. Note that brightness variations may also relate to atmospheric scan angle effects which have not been accounted for in the atmospheric correction

packages. Figure 42 shows the mean reflectance spectra for each polygon extracted from the 1998 airborne data for the vegetated cover types. Note that the spectra shown are reflectance \times 100. The same colour was used to depict corresponding polygons while the different flight lines were identified using different symbols. ph2 on the legend indicate that the polygon was extracted from flight line 2 (lower image on Figure 41) and ph3 indicate that the polygon was extracted from flight line 3 (upper image on Figure 41). Following that, the legend indicates the cover type. For example, ph2:veg1 indicate veg1 cover type on flight line 2.

The results show that the reflectance variation or BRDF behaviour were not similar for all the materials examined. For example, there were little indications of variations between adjoining flight lines for veg6, whereas for veg4, there were clear divergences.

Figure 43 plots the mean spectra of corresponding polygons for the non-vegetated cover category. Note that the spectra shown are reflectance \times 100. The same colour was used to depict corresponding polygons while the different flight lines were identified using different symbols. ph2 on the legend indicate that the polygon was extracted from flight line 2 (lower image on Figure 41) and ph3 indicate that the polygon was extracted from flight line 3 (upper image on Figure 41). Following that, the legend indicates the cover type. For example, ph2:sand1 indicate cover type sand1 on flight line 2.

The graph on Figure 43 indicates that for the non-vegetated cover the reflectance variation or BRDF behaviour varied between different surface cover types. An example where there were little differences between corresponding polygons was sand3 while sand2 displayed incongruence between flight lines.

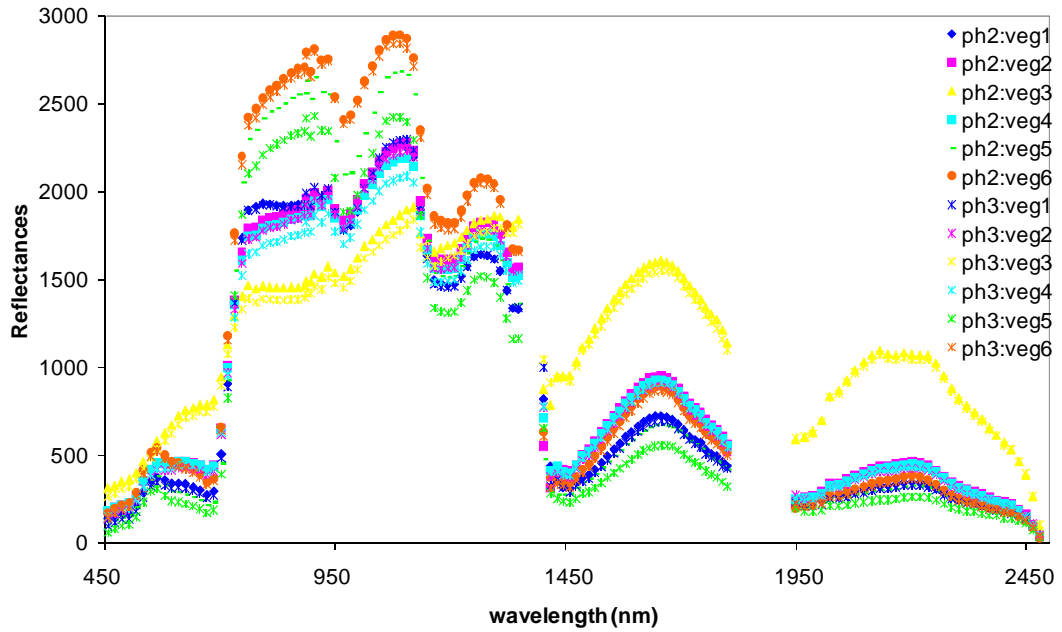


Figure 42: Mean spectra of polygons of vegetated cover extracted from the overlap areas of adjacent flight lines acquired from airborne hyperspectral data on 13th November 1998. Note that the spectra shown are reflectance \times 100. ph2 on the legend indicate that the polygon was extracted from flight line 2 (lower image on Figure 41) and ph3 indicate that the polygon was extracted from flight line 3 (upper image on Figure 41). Following that, the legend indicates the cover type. For example, ph2:veg1 indicate cover type veg1 on flight line 2. 6 different vegetated cover types are shown namely veg1, veg2, veg3, veg4, veg5 and veg6.

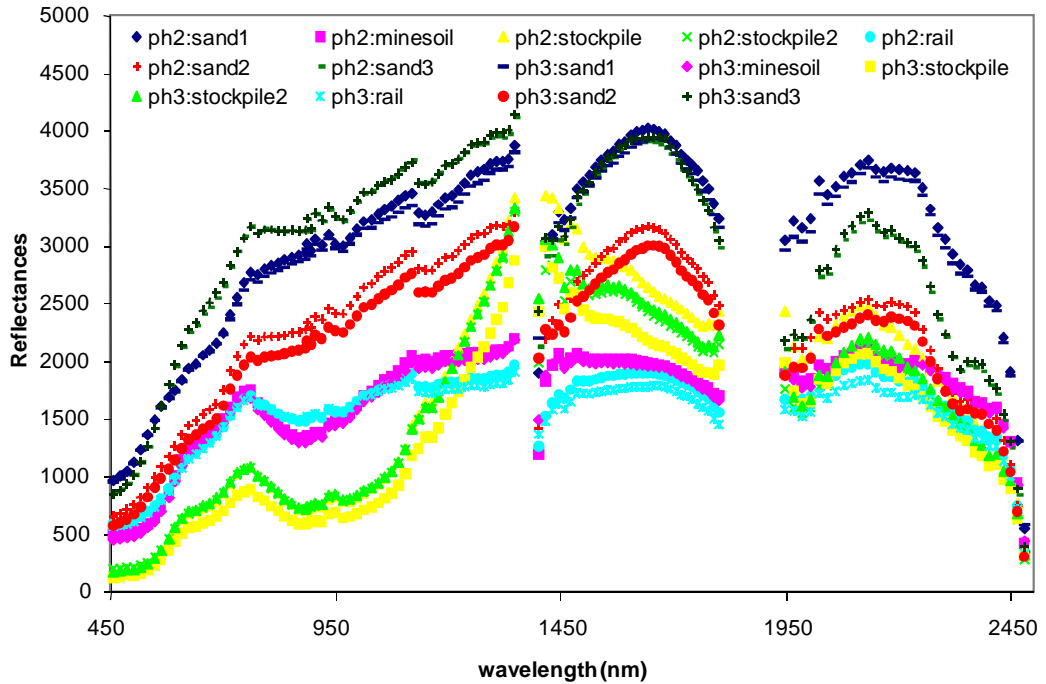


Figure 43: Mean spectra of polygons of non-vegetated cover extracted from the overlap areas of adjacent flight lines acquired by an airborne hyperspectral sensor on 13th November 1998. Note that the spectra shown are reflectance \times 100. ph2 on the legend indicate that the polygon was extracted from flight line 2 (lower image on Figure 41) and ph3 indicate that the polygon was extracted from flight line 3 (upper image on Figure 41). Following that, the legend indicates the cover type. For example, ph2:sand1 indicate cover type sand1 on flight line 2. 6 different non-vegetated cover types are shown namely sand1, sand2, sand3, stockpile, stockpile2, minesoil and rail.

The second objective was to examine the nature of the reflectance variation or BRDF by comparing the PMN reflectance spectra. The PMN reflectance was calculated using Equation 4.

Figure 44 show the PMN spectra for the vegetated cover types. On this graph, the same colour was used to depict corresponding polygons while the different flight lines were identified using different symbols. ph2 on the legend indicate that the polygon was extracted from flight line 2 (lower image on Figure 41) and ph3 indicate that the polygon was extracted from flight line 3 (upper image on Figure

41). Following that, the legend indicates the cover type. For example, ph2:veg1 indicate cover type veg1 on flight line 2.

On Figure 44, the spectra from adjacent flight line are now overlapping indicating that the assumption inherent with the use of PMN that is that the BRDF is wavelength-independent and multiplicative holds largely for most of the materials examined. For the examples used for Figure 42, specifically, the PMN spectra for the concurrent areas for veg6 and veg4 spectra are now coincident. Note the veg5 still displays some divergence indicating that the BRDF of that material may not be wavelength-dependent and multiplicative. This may be the case of heterogeneous vegetation with varying leaf orientation and branch exposures causing multiple scattering.

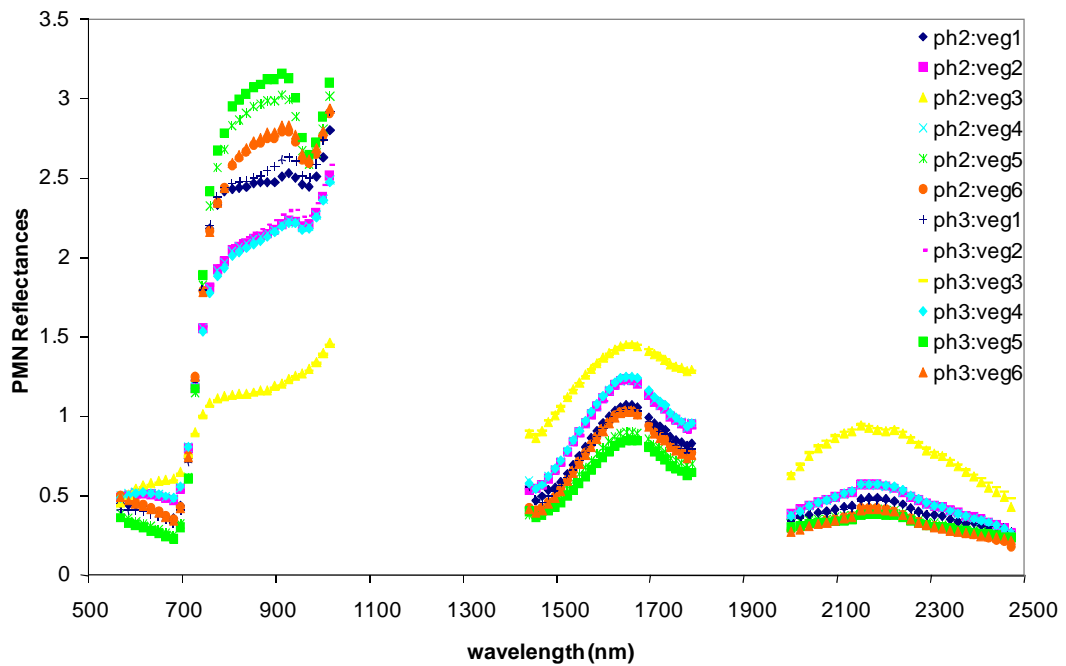


Figure 44: Mean PMN spectra of polygons of vegetated cover extracted from the overlap areas of adjacent flight lines collected on 13th November 1998. ph2 on the legend indicate that the polygon was extracted from flight line 2 (lower image on Figure 41) and ph3 indicate that the polygon was extracted from flight line 3 (upper image on Figure 41). Following that, the legend indicates the cover type. For example, ph2:veg1 indicate cover type veg1 on flight line 2. 6 different vegetated cover types are shown namely veg1, veg2, veg3, veg4, veg5 and veg6.

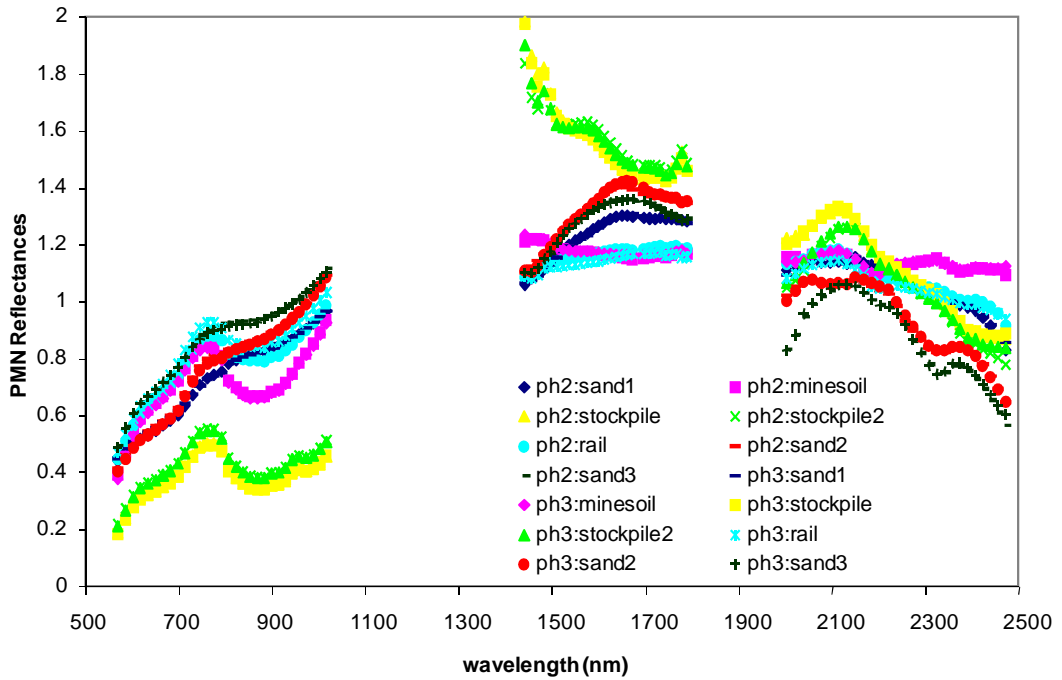


Figure 45: Mean PMN spectra of concurrent polygons of non-vegetated material extracted from the overlap areas of adjacent flight lines collected on 13th November 1998. *ph2* on the legend indicate that the polygon was extracted from flight line 2 (lower image on Figure 41) and *ph3* indicate that the polygon was extracted from flight line 3 (upper image on Figure 41). Following that, the legend indicates the cover type. For example, *ph2:sand1* indicate cover type *sand1* on flight line 2. 6 different non-vegetated cover types are shown namely *sand1*, *sand2*, *sand3*, *stockpile*, *stockpile2*, *minesoil* and *rail*.

Figure 45 show the mean PMN spectra of corresponding polygons for non-vegetated cover extracted from the overlapping area of adjacent flight lines of the airborne hyperspectral dataset. On this graph, the same colour was used to depict corresponding polygons while the different flight lines were identified using different symbols. *ph2* on the legend indicate that the polygon was extracted from flight line 2 (lower image on Figure 41) and *ph3* indicate that the polygon was extracted from flight line 3 (upper image on Figure 41). Following that, the legend indicates the cover type. For example, *ph2:sand1* indicate *sand1* cover type on flight line 2.

The corresponding polygon spectra on Figure 45 display good coherence between adjacent lines which indicate that for the non-vegetated cover examined, the BRDF effects were multiplicative and wavelength-independent.

The next dataset examined was the airborne hyperspectral data collected over Port Hedland harbour on 24th April 1999 shown on Figure 46. These data were from an opportunistic acquisition as an add-on to a larger commercial acquisition campaign where it was difficult to dictate the time of acquisition. The sun's position, which was perpendicular to the flight direction, is illustrated on the image. As a consequence, strong forward scattering was seen as brightening over the water on the side for which the sun is present. The less than optimum condition also caused strong backscatter over the land. This presents as differential illumination across the flight direction and is brightest on the side opposite to the sun.

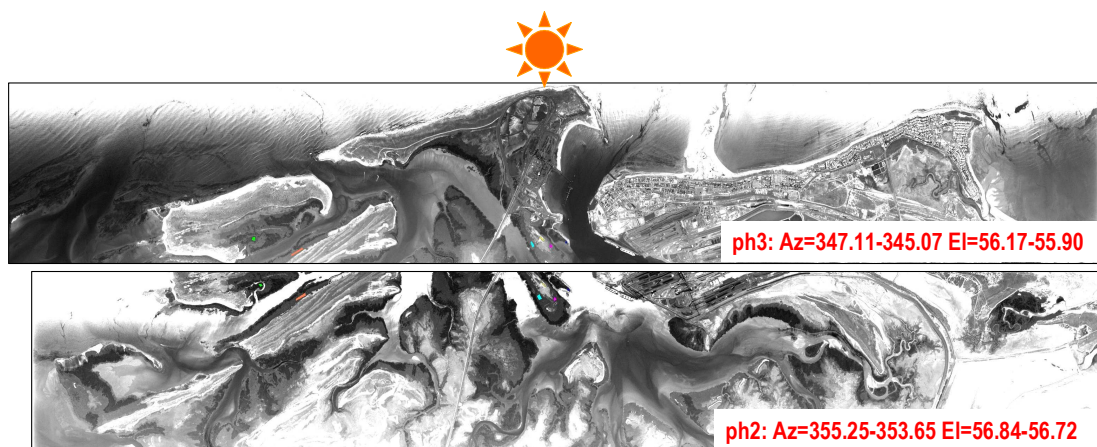


Figure 46: Airborne hyperspectral data acquired on 24th April 1999. Adjoining flight line 2 (lower) and 3(upper) are shown here together with an illustration of the approximate position with respect to the imagery and a description of the sun azimuth (Az) and elevation (El) at the time of acquisition.

I followed a similar workflow as the 1998 data for the evaluation for BRDF effects for this dataset. The polygons used to analyse the 1998 data were replicated onto the 1999 data and used to extract the polygon arithmetic means from the 1999 data and these were examined for mismatches between concurrent polygons on adjacent flight lines.

Figure 47 shows the spectra extracted for different vegetated cover types. Note that the spectra shown are reflectance \times 100. The same colour was used to depict corresponding polygons while the different flight lines were identified using different symbols. ph2 on the legend indicate that the polygon was extracted from flight line 2 (lower image on Figure 46) and ph3 indicate that the polygon was extracted from flight line 3 (upper image on Figure 46). Following that, the legend indicates the cover type. For example, ph2:veg1 indicate veg1 cover type on flight line 2.

The polygon means on Figure 47 are clearly offset from each other for all the vegetated cover types examined and when compared to the 1998 dataset, the disparity between the flight lines appear to be larger. Figure 48 which plots the non-vegetated polygons, too showed that that there were large mismatches between flight lines for all the situations examined. Note that the spectra shown on Figure 47 are reflectance \times 100. The same colour was used to depict corresponding polygons while the different flight lines were identified using different symbols. ph2 on the legend indicate that the polygon was extracted from flight line 2 (lower image on Figure 46) and ph3 indicate that the polygon was extracted from flight line 3 (upper image on Figure 46). Following that, the legend indicates the cover type. For example, ph2:sand1 indicate sand1 cover type on flight line 2.

If the assumption is made that there are no instrument artefacts and that the atmospheric conditions applied were appropriate for the condition at the time of the acquisition then the results shown on Figure 47 and Figure 48 suggest that the main cause for the disparity between flight lines in the 1999 data are BRDF effects.

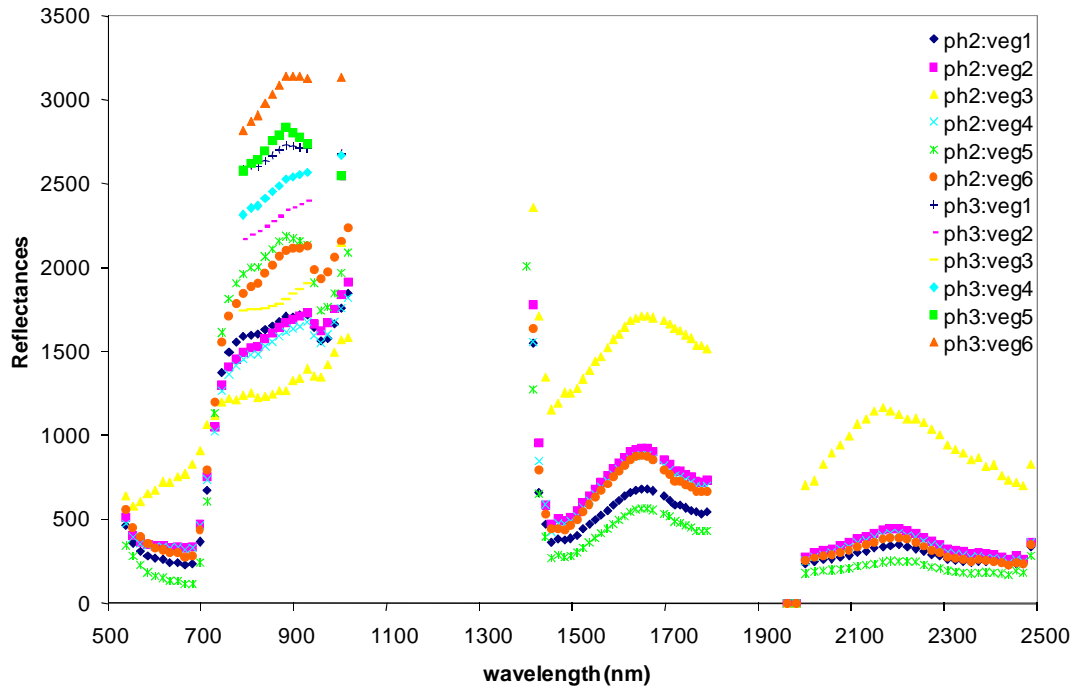


Figure 47: Mean reflectance spectra for polygons of vegetated cover extracted from the overlap areas of adjacent flight lines collected on 24th April 1999. Note that the spectra shown are reflectance $\times 100$. ph2 on the legend indicate that the polygon was extracted from flight line 2 (lower image on Figure 46) and ph3 indicate that the polygon was extracted from flight line 3 (upper image on Figure 46). Following that, the legend indicates the cover type. For example, ph2:veg1 indicate cover type veg1 on flight line 2. 6 different vegetated cover types are shown namely veg1, veg2, veg3, veg4, veg5 and veg6.

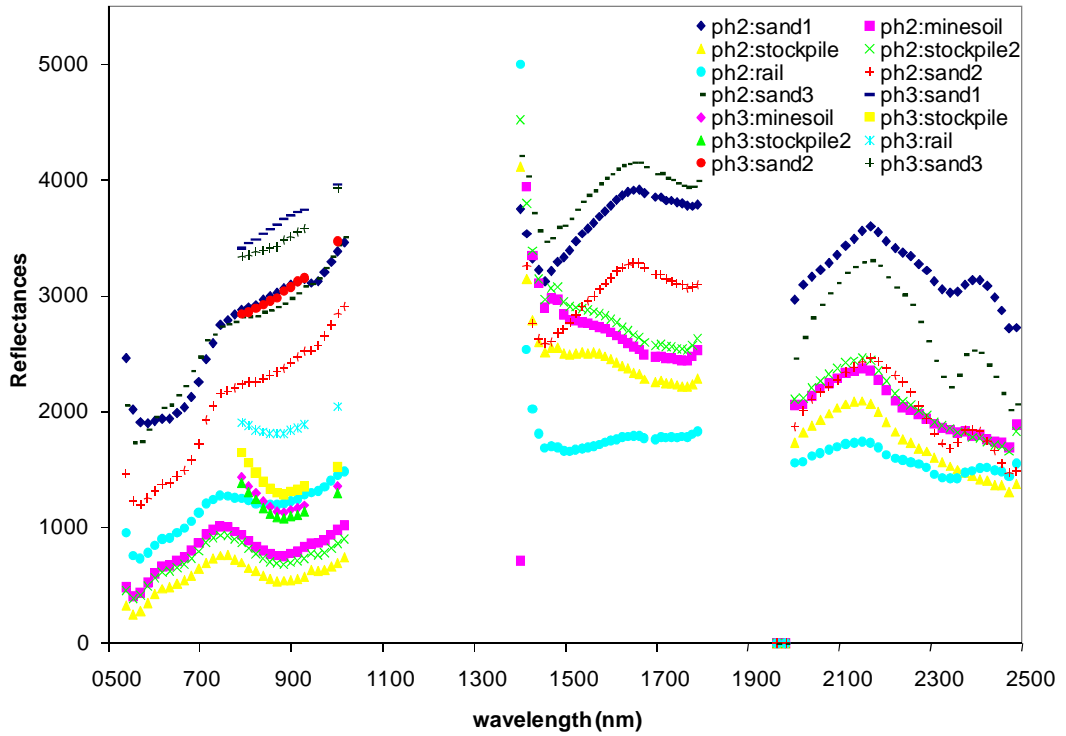


Figure 48: Mean reflectance spectra for polygons of non-vegetated cover types extracted from the overlap areas of adjacent flight lines collected on 24th April 1999. Note that the spectra shown are reflectance \times 100. ph2 on the legend indicate that the polygon was extracted from flight line 2 (lower image on Figure 46) and ph3 indicate that the polygon was extracted from flight line 3 (upper image on Figure 46). Following that, the legend indicates the cover type. For example, ph2:sand1 indicate cover type sand1 on flight line 2. 6 different non-vegetated cover types are shown namely sand1, sand2, sand3, stockpile, stockpile2, minesoil and rail.

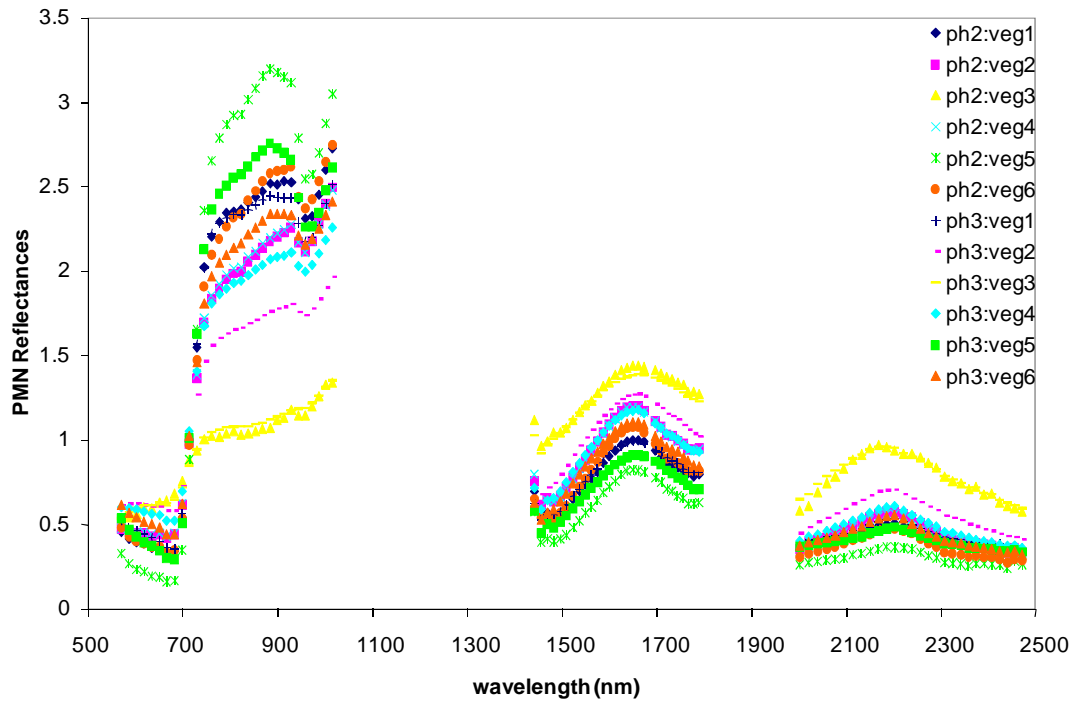


Figure 49: Mean PMN spectra for polygons of vegetated cover types extracted from the overlap areas of adjacent flight lines collected on 24th April 1999. ph2 on the legend indicate that the polygon was extracted from flight line 2 (lower image on Figure 46) and ph3 indicate that the polygon was extracted from flight line 3 (upper image on Figure 46). Following that, the legend indicates the cover type. For example, ph2:veg1 indicate cover type veg1 on flight line 2. 6 different vegetated cover types are shown namely veg1, veg2, veg3, veg4, veg5 and veg6.

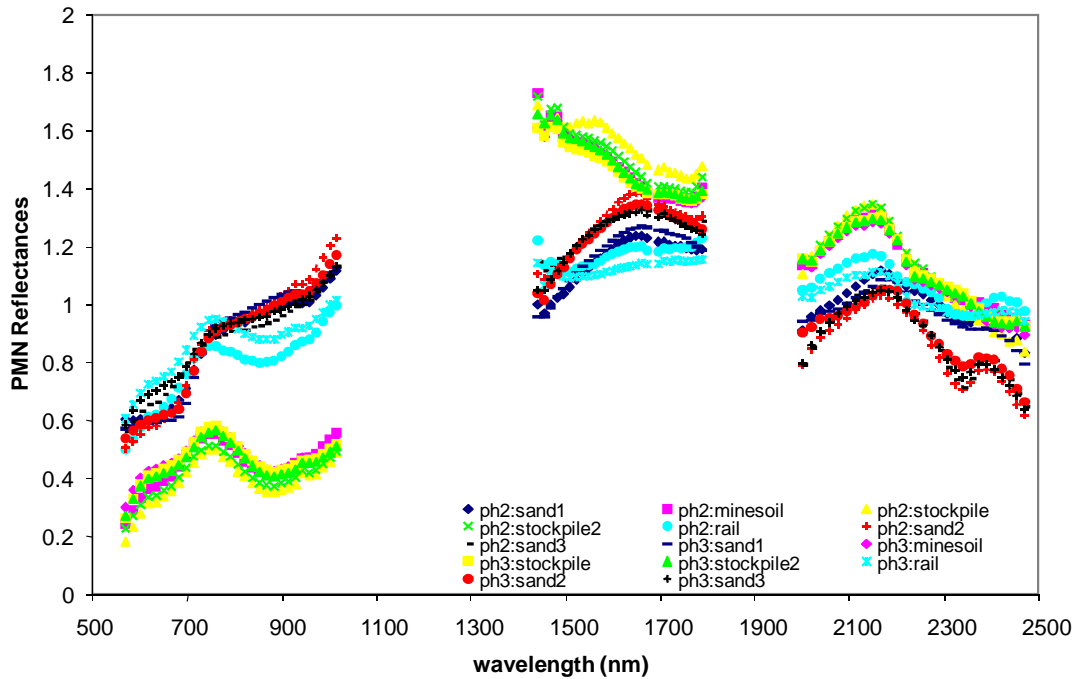


Figure 50: Mean PMN spectra for polygons of non-vegetated cover types extracted from the overlap areas of adjacent flight lines collected on 24th November 1999. ph2 on the legend indicate that the polygon was extracted from flight line 2 (lower image on Figure 46) and ph3 indicate that the polygon was extracted from flight line 3 (upper image on Figure 46). Following that, the legend indicates the cover type. For example, ph2:sand1 indicate cover type sand1 on flight line 2. 6 different non-vegetated cover types are shown namely sand1, sand2, sand3, stockpile, stockpile2, minesoil and rail.

Figure 49 shows the mean PMN spectra of corresponding polygons of the vegetated cover type extracted from the airborne data. Note that the same colour was used to depict corresponding polygons while the different flight lines were identified using different symbols. ph2 on the legend indicate that the polygon was extracted from flight line 2 (lower image on Figure 46) and ph3 indicate that the polygon was extracted from flight line 3 (upper image on Figure 46). Following that, the legend indicates the cover type. For example, ph2:veg1 indicate veg1 cover type on flight line 2.

Figure 49 shows that PMN was successful in matching the corresponding polygon means for some of the vegetated cover types, for example, veg1 and veg3. However, the technique was unsuccessful for others. It is noted that for some of the cover

types that did not match for the whole spectrum, the PMN process appear to be successful for some portions of the spectrum; for example, in the SWIR region.

More success was observable for the non-vegetated cover types shown on Figure 50. On this graph, the same colour was used to depict corresponding polygons while the different flight lines were identified using different symbols. ph2 on the legend indicate that the polygon was extracted from flight line 2 (lower image on Figure 46) and ph3 indicate that the polygon was extracted from flight line 3 (upper image on Figure 46). Following that, the legend indicates the cover type. For example, ph2:sand1 indicate sand1 cover type on flight line 2.

The PMN procedure was able to remove or minimise the disparity between flight lines. Even with the outliers, that is the stockpile and rail polygons, the disparities between flight lines were less than those seen between vegetated cover types. This result and that shown in Figure 45 indicate that, in most circumstances, the BRDF effects for non-vegetated materials appear to be multiplicative and wavelength-independent.

The results for the 1999 data indicated that for some regions of the spectrum the BRDF effects may be wavelength independent. Therefore, further analysis was performed on these data to better understand the wavelength dependencies of the BRDF effects. For this, the ratios between corresponding polygon means were calculated. The results are shown on Figure 51 for the vegetated cover types and on Figure 52 for the non-vegetated cover types. Where the ratios remains constant over a portion of the spectrum, the BRDF effects are determined to be wavelength independent across the portion. Where there are changes, the portion is determined to be wavelength dependent. The graph on Figure 51 shows that the most wavelength dependent region for the vegetated cover types is the visible region before 570 nm and between 630 nm and 740 nm in the VNIR region. However, the ratios remain relatively constant in the region between 570 and 630 nm and 740 to 1000 nm and between 2080 and 2180 nm in the SWIR. For the non-vegetated cover types, Figure 52 shows that the regions before 760 nm are highly wavelength-dependent and wavelength-independencies are exhibited in the region between 760

and 1000 nm and between 1500 to 1760 nm and 2080 and 2180 nm in the SWIR region.

The FRC resulting from PLS analysis described in Chapter 4 were overlaid on the ratios on the Figure 51 and Figure 52 to select regions where the BRDF effects were relatively wavelength independent and also were significant for the prediction of dust levels. The graphs indicate that the regions of high FRCs that coincided with regions where BRDF is wavelength-independent is the region between 760 and 1000 nm. This is a fortuitous result as this region has the highest FRC values which was interpreted to be related to the 900 nm ferric iron oxide CFA. The laboratory study (section 4.2.6.4) found that the depth of this absorption feature is correlated to the dust level. The implication of this is that it is possible to use the relationship between the depth of the 900 nm ferric iron oxide CFA and dust level found from the laboratory study, to generate dust measurements using the 1999 data to obtain accurate and seamless dust maps.

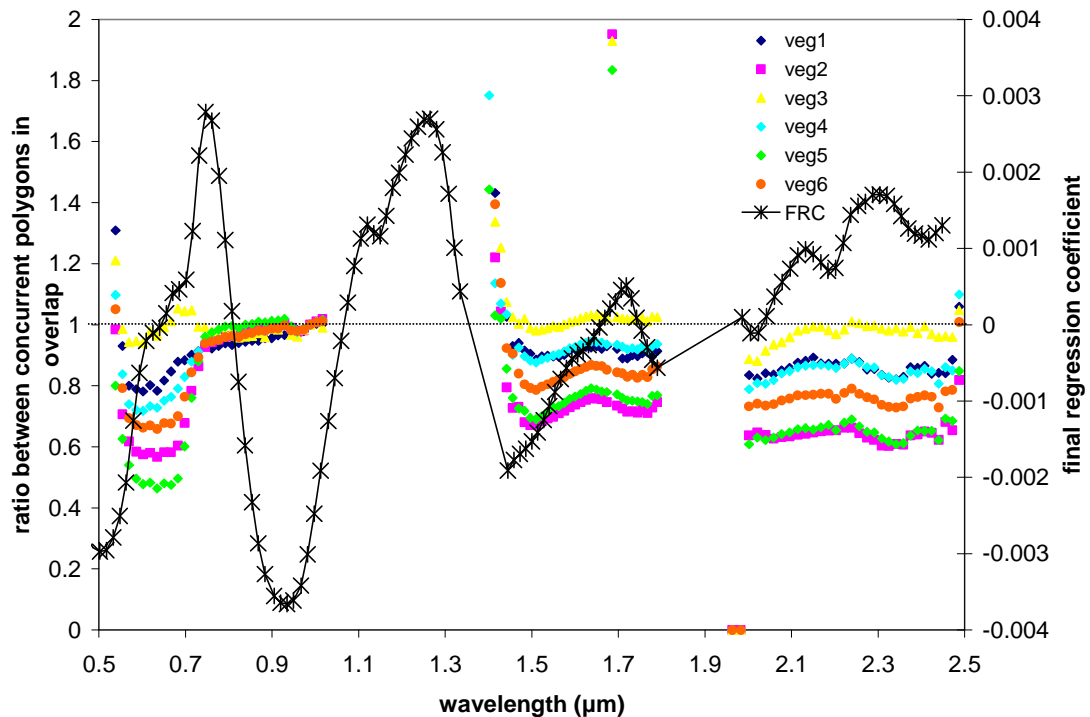


Figure 51: The ratio between the reflectances of corresponding polygon means of vegetated materials extracted from airborne hyperspectral data acquired in 1999

plotted with the final regression coefficient (FRC) results from partial least squares analysis of laboratory reflectance and dust levels. Note that two y-axis are shown. The one on the left of the chart shows the ratio and the one on the right is the FRC.

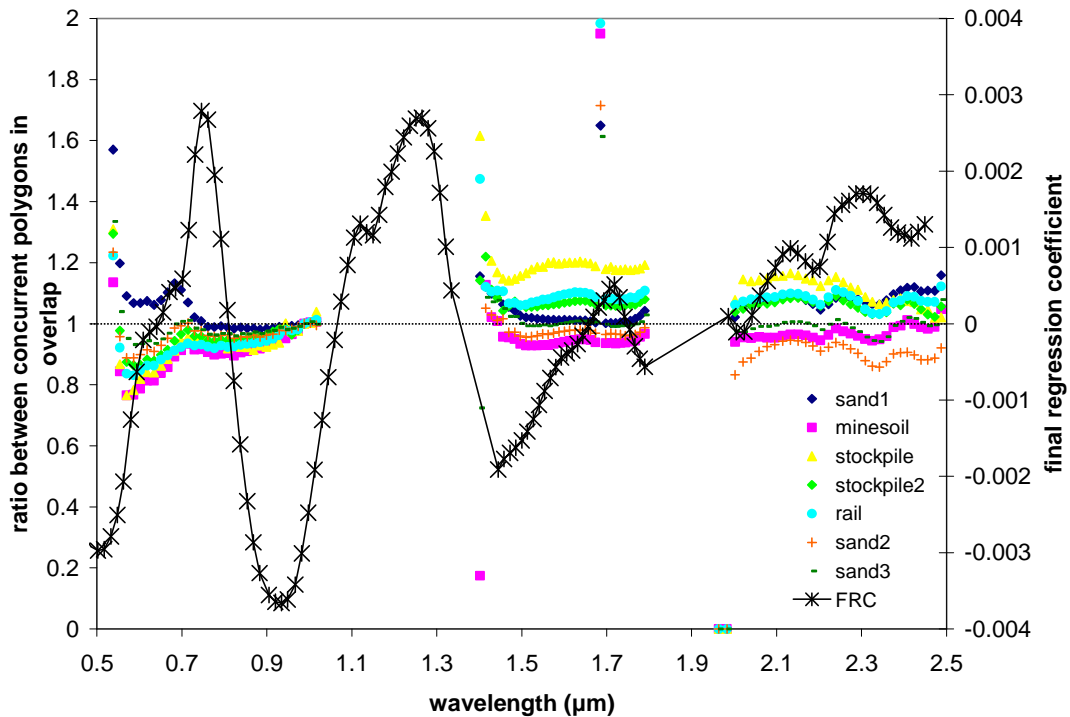


Figure 52: The ratio between corresponding polygons means of non-vegetated cover types extracted from airborne hyperspectral data acquired in 1999 plotted with the final regression coefficient (FRC) results from partial least squares analysis of field data. Note that two y-axis are shown. The one on the left of the chart shows the ratio and the one on the right is the FRC.

The depth of the 900 nm ferric iron oxide CFA feature were calculated (as described Equation 6) to determine the consistency between the flight lines. Figure 53 plots the data extracted from flight line 2 against those for flight line 3 for the airborne data acquired in 1998 which exhibited minimum BRDF effects. The data indicates that there is a one to one correlation between the two flight lines. In contrast, airborne data acquired in 1999 exhibited major BRDF effects. Figure 54 compares data from two adjacent flight lines. This dataset also shows one to one relationship between the flight lines. These results provide confidence that the depth of the 900nm ferric iron oxide CFA feature can be used as a robust measurement of the dust levels.

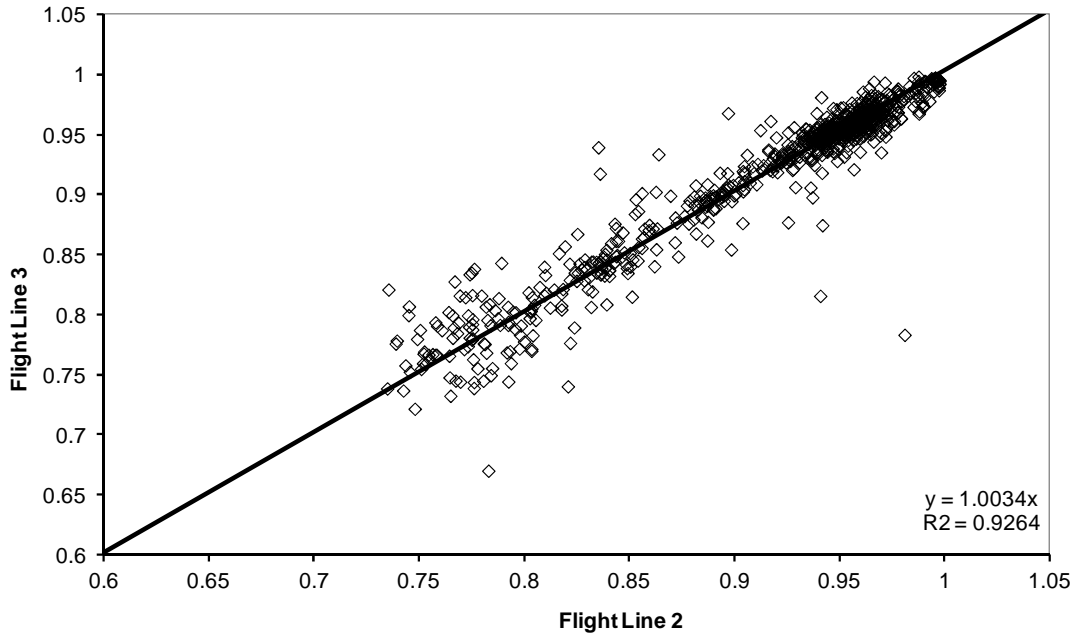


Figure 53: Scatterplot of depth of 900 nm ferric iron oxide CFA feature extracted from adjacent flight lines of airborne hyperspectral data acquired in 1998 which exhibited minimum BRDF effects.

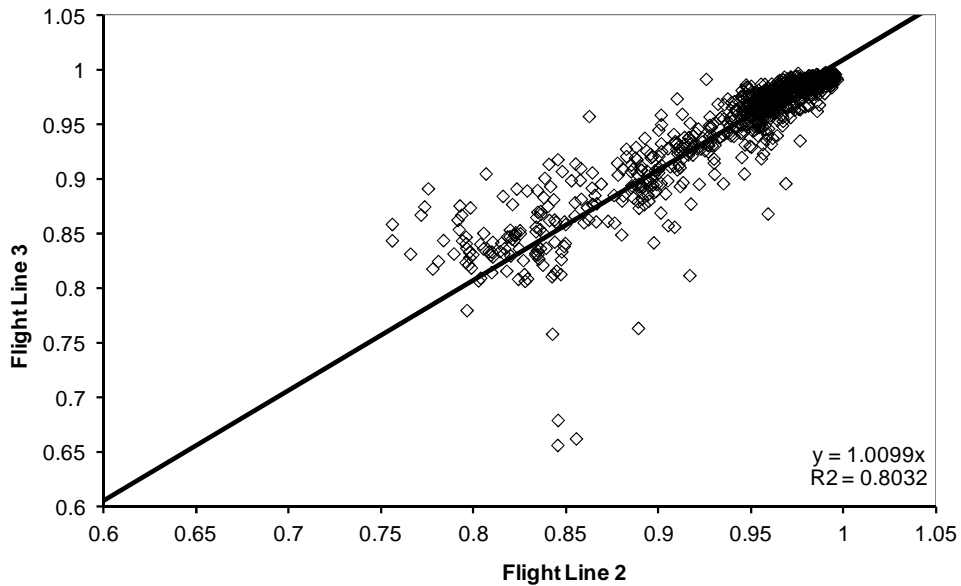


Figure 54: Scatterplot of depth of 900 nm ferric iron oxide CFA feature extracted from adjacent flight lines of airborne hyperspectral data acquired in 1999 which exhibited major BRDF effects.

One of the key requirements in the processing of the airborne data is to validate or confirm that the correction process has been successful in producing satisfactory reflectances. The following presents a subset of the validation results undertaken for this study.

Figure 55 plots the arithmetic means of the PMN reflectances for the calibration target areas extracted from the airborne spectra acquired in 2006 after applying a standard atmospheric correction (solid lines), after removal of atmospheric offsets (dotted lines) and ground truth (dashed lines) for two calibration targets measured close in time to the airborne acquisition. The atmospheric offsets were removed by multiplying by the atmospheric offset residuals generated from the sand bank site as described previously in this section. The targets were located at a beach track (location is close to C.T.2 on Figure 32) and at a car park (see location at C.T.4 on Figure 32 and picture at Figure 36). The atmospheric offsets appear to be effectively minimised after the correction even though the corrections were generated using the different target and compares well with the ground truth data.

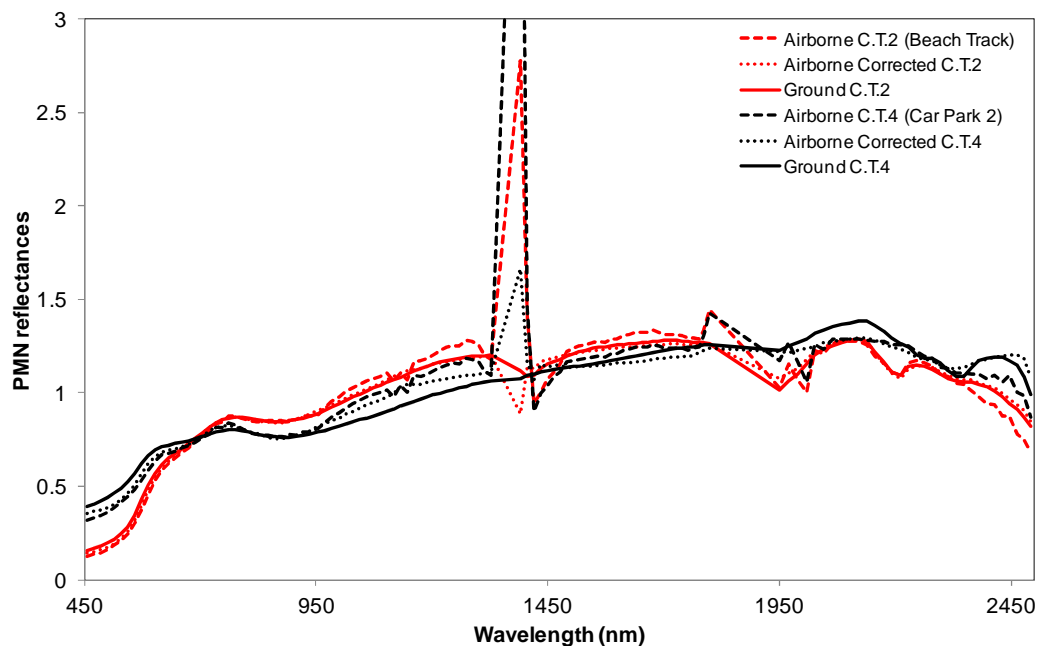


Figure 55: Comparisons of airborne spectra acquired in 2006 after applying *AtComp* atmospheric correction (dashed lines), after removal of atmospheric residual effects (dotted lines) and ground truth (solid lines).

C.T.5, the road in BHPB's handling facility was used as the validation target for the 2002 dataset. These data are shown on Figure 56 where the arithmetic mean of PMN ground reflectance spectra collected from this road is plotted (in green) together with the PMN airborne arithmetic mean spectrum for the airborne data after application of a standard atmospheric correction (blue) and after removal of atmospheric offsets (magenta) using the offsets generated using the sand bank site. It confirms that the processing was effective in minimising artefacts related to incorrectly modelled solar conditions and BRDF and any systematic instrument artefacts.

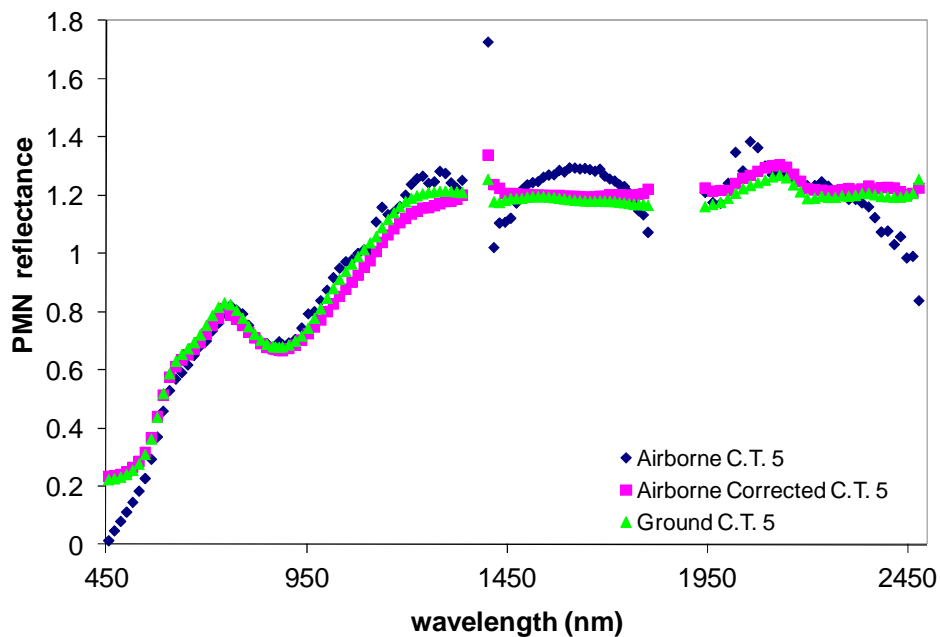


Figure 56: Comparison of PMN spectra acquired in 2002 on the ground (green), after applying a standard atmospheric correction (blue) and after removal of atmospheric offsets (magenta).

A comparison of the PMN reflectance spectra (after atmospheric correction were applied and atmospheric offsets removed) acquired on the two dates that exhibited minimal BRDF and pronounced BRDF is shown in Figure 57. The car park shown on Figure 33 and located at C.T.1 on Figure 32 where vicarious calibration data were acquired was used for this validation exercise. The graph displays good correlation between the two dates and the ground spectra confirm that the correction was

successful in reducing the data to satisfactory reflectances to allow multi-temporal comparisons.

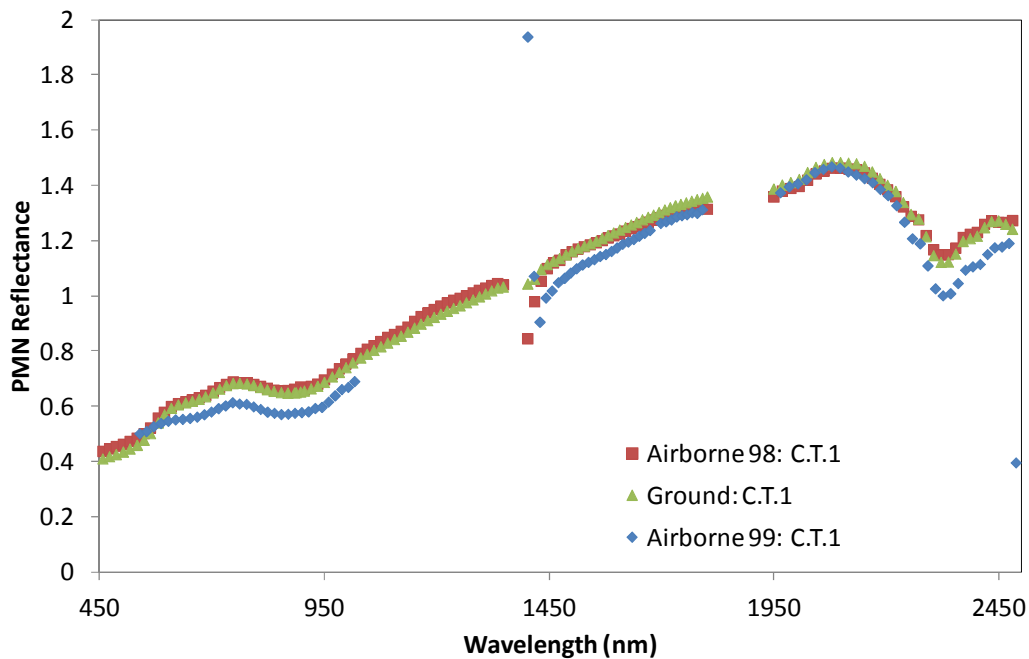


Figure 57: Comparison of PMN spectra extracted from a car park used as a uniform calibration target acquired on the ground (red) and atmospherically corrected and atmospheric offset removed airborne spectra from the 1998 (blue) and 1999 (green) airborne datasets.

5.6 Summary

This chapter documented the results of analyses undertaken to understand and quantify the uncertainty that may potentially compromised the acquisition of accurate surface reflectances from remotely-sensed hyperspectral data which would, in turn, impact on the accuracy of environmental measurements generated from these data. Specifically, the study examined 1) differences between atmospheric correction packages; 2) instrument biases, specifically, instrument spectral mis-calibration and, spectral sampling including variations in band-centres and band-widths and, 3) the impact of BRDF caused by variations in flight planning.

The results of the comparison of the atmospheric correction packages indicate that for a dataset similar to the one acquired in Port Hedland in 2006 and for the

application of ferric iron oxide dust measurements, the CSIRO-MODTRAN-SODA software provides marginally the best results. Further, an interpretation of the result is that if vicarious calibration data from ground calibration targets were not available and only atmospheric correction with an off the shelf package such as FLAASH (without wavelength calibration) was applied to an airborne dataset similar to those acquired in Port Hedland in 2006, the uncertainty when using those data for the measurement of ferric iron oxide dust level is expected to be $\pm 3.258 \text{ g/m}^2$.

The wavelength recalibrations appear to have minimised/reduced the residuals in most regions using both the CSIRO-MODTRAN-SODA and FLAASH softwares and the uncertainties were reduced when using these recalibrated data. The results emphasised the importance accurate instrument calibration for achieving accurate reflectances with atmospheric corrections as wavelength miscalibrations of only 2.1, 0.7, 0.4 and 2.1 nm respectively for each of the instruments can translated to a downstream impact of increasing the uncertainties in ferric iron oxide dust levels by 34%.

Assuming that the atmospheric corrections and recalibration are performed satisfactorily, the comparisons of the datasets acquired from 1998 to 2008 showed that the HyMap2 sensor was stable across the years of dataset acquisition but the data clearly indicates miscalibrations in the SWIR detectors for the HyMap1 sensor. This may not be significant for applications such as the iron oxide dust monitoring as the spectral regions used were not affected but it will affect applications such as the pH monitoring where the PLS analysis shows a reliance on the SWIR region.

The calculations to understand the impact of the changes with the instrument calibration indicate that the uncertainties in the ferric iron oxide dust levels that may be introduced when the bandpasses and bandwidths vary from the 2006 bandwidths and bandpasses range from ± 0.064 to $\pm 1.692 \text{ g/m}^2$.

The analysis of the BRDF behaviours and assessment of the region for minimising BRDF and for prediction of ferric iron oxide dust indicates that the optimum region where BRDF is wavelength-independent and multiplicative is the region between

760 and 1000 nm. This region is also related to the 900 nm ferric iron oxide CFA feature. Dust maps generated from the depth of the 900 nm ferric iron oxide CFA feature from two adjacent flight lines shows a one-to-one relationship between the flight lines on the overlap area.

The flow chart shown on Figure 58 summarises the processing requirements one ought to take into consideration when using remotely hyperspectral data for quantitative multi-temporal monitoring. The processing chain is necessary so that the optimal reflectance data are used and that the data are cross-calibrated to laboratory spectral measurements so that an algorithm generated in the laboratory can be transferred with confidence to field or airborne observations.

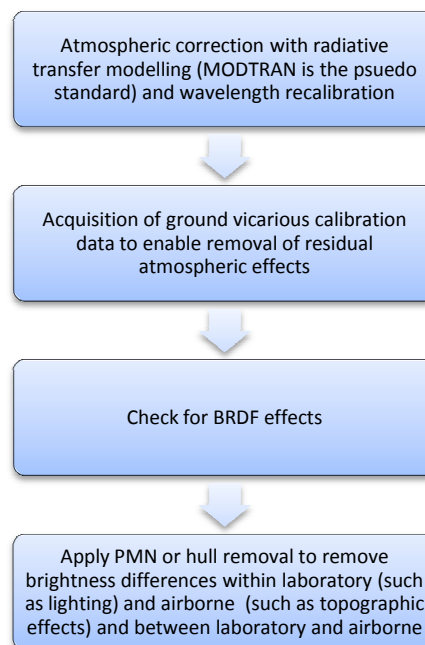


Figure 58: Processing chain to be considered when using remotely-sensed data for quantitative multi-temporal monitoring.

Chapter 6

MAPS OF ENVIRONMENTAL INFORMATION PRODUCTS

6.1 Introduction

One of the major advantages of remote sensing is that it provides the spatial context to better understand the location, distribution and scale of the environmental impacts. This ability is usually lacking in standard monitoring methods. For example, environmental practitioners at Port Hedland found it difficult to ascertain the number of sampling points required and the data were unable to quantify the distribution of the dust using the standard method of placing depositional gauges and high volume dust samplers at discrete points (Piggott, 1998; personal communication). Additionally, for this application, the hyperspectral data are able to provide information on the composition of the dust. Dust depositional gauges do not provide compositional information and the analysis for the composition of the dust for high volume samplers is time consuming and costly.

This chapter presents the maps generated from the application of the spectral algorithms developed in Chapter 4 and applied to airborne hyperspectral data. The data processing would be as determined from the analysis in Chapter 5. These maps demonstrate the ability of remotely-sensed hyperspectral data to provide quantitative and spatially-comprehensive measurement of the environmental variables of concern.

6.2 Method

The previous chapter discussed the processing applied to the airborne data to reduce them to reflectances. The processing included the application of a standard atmospheric correction based on MODTRAN radiative transfer modelling,

wavelength recalibration and removal of atmospheric offsets modelled using a vicarious calibration target. Before the spectral algorithms were applied to the airborne data some additional processing was applied to these reflectance data for both the dust and AD case histories.

In the case of the dataset acquired in Port Hedland for the dust case history the depth of the 900 nm ferric iron oxide CFA feature was calculated as described in Equation 6. This additional processing step ensures that any multiplicative and wavelength-dependent BRDF effects and differences in lighting between the airborne data and laboratory data are removed and ensures consistency between the processing of the laboratory and airborne data. All the above mentioned processing were essential to ensure that the airborne and laboratory data are cross-calibrated so that when the dust prediction algorithm (developed in the laboratory) was applied, the dust maps produced from the airborne data be accurate.

In the case of the dataset acquired in Brukunga for AD, no additional processing was required after reduction of the data to surface reflectance before applying Tetracorder. Tetracorder applies a continuum removal process (as described on Equation 5) to the data which would effectively remove any differential lighting between the laboratory and airborne data and wavelength-dependent and multiplicative BRDF. The examples in Chapter 5 demonstrated that for most non-vegetated cover types tested this was a sound assumption.

In the case of the pH map generation, before application of the spectral predictive algorithms for pH, PMN (as described in Equation 4) was applied to the airborne hyperspectral data to ensure similar processing was used for both the airborne and laboratory datasets. PMN was necessary to remove any brightness effects related to differential lighting in the laboratory and to remove any wavelength-independent, multiplicative effects in the airborne data which may be significant because of the topographic relief of the test site and BRDF effects. The assumption of multiplicative and wavelength-independence is warranted as the surfaces to be mapped for AD are completely denuded of vegetation. It was demonstrated in Section 5.5 that for most non-vegetated material this assumption holds true.

6.3 Airborne datasets analysed

Port Hedland

Airborne hyperspectral data (HyMap (Cocks et al., 1998) were acquired over the Port Hedland harbour on 6 occasions over a period of 10 years.

The first acquisition occurred on 13th November 1998. These HyMap1 data (450 - 2500 nm) were acquired at 5 m pixel resolution. The HyMap 1 instrument was used again to acquire data on 20th October 2002, 4th December 2004 and 9th September 2008.

Another airborne hyperspectral dataset was acquired five months later on 24th April 1999, 17 days after a cyclonic event (Tropical Cyclone Gwenda passed through Port Hedland on 7th April 1999). This dataset was acquired using the 96 channel Airborne Multispectral Sensor (AMS) instrument acquiring spectra in the 530 - 2500 nm range. This sensor was the first airborne hyperspectral sensor built by Integrated Spectronics. It has very similar characteristics as the more recent HyMaps except that it has fewer spectral bands and, the regions between 450-550 and 1100 to 1400 nm are not available.

The HyMap2 sensor was used for acquisitions on 19th April 2004, 21st November 2005, 24th August 2006 and 17th October 2007. These data were acquired at 3.5 m pixel resolution.

Brukunga

HyMap data were acquired over the Brukunga Mine on 3rd April 1998, that is, at the end of the dry summer period. The data were acquired at 5 metre pixel resolution. Three additional datasets over the next three years were captured at the finer pixel resolution of 3.5 metre. Acquired on 9th April 1999, 21st March 2000 and 14th March 2001, all these data were acquired soon after the first major rainfall following the dry summer period.

6.4 Results

6.4.1 Dust maps of Port Hedland, W.A.

The dust maps generated from the application of the dust model generated from the laboratory, to the airborne datasets acquired from 1998 to 2006 are presented in the following.

Figure 59 shows the first of the 6 dust maps generated from the airborne hyperspectral data. The data from which this map was generated were acquired on 13th November 1998.

The Port Hedland handling facility mainly handles iron ore and as a consequence the surround areas generally contain iron ore. Further the background rock and soil cover also contains iron ore. Therefore, the dust maps logically map all ferric iron oxide present in the area. As the interest lay mainly in the dust contaminating the vegetation, a mask was applied to the data to show only ferric iron oxide dust on vegetated cover types. The mask was created by setting a threshold on the Normalised Difference Vegetation Index (Tucker, 1979) (NDVI) created using a red (band closest to 650 nm) and NIR (band closest to 750 nm) band of the airborne hyperspectral data. Specifically,

$$Mask_{in} = NDVI \geq 0.3$$

$$NDVI = \frac{R_{NIR} - R_{red}}{R_{NIR} + R_{red}}$$

Equation 14

Where $Mask_{in}$ is the area being masked in, R_{NIR} is the reflectance value of the NIR band and, R_{red} is the reflectance value of the red band. A threshold of 0.3 was chosen firstly with the common range expected for green vegetation of 0.2 to 0.8 (ITTVIS, 2012) as a first pass and then an iterative process of adjusting the threshold based on known areas of vegetation. Note that the band closest to 650 nm was used

for R_{red} and closest to 750 nm for R_{NIR} . No specific bands are provided here as the bandcentres change each year.

The map is overlaid on a background black and white image of the area to provide spatial context to the map in areas that are not vegetated. The colour coding on the map is such that cool colours (starting with dark blue at 0 g/m²) denote low levels of ferric iron oxide dust and hot colours (ending with red at >8.75 g/m²) indicate high levels. It is important to note that the dust map is seamless even though it is a mosaic of four flight lines indicating that the processing applied to remove the variations between the flight lines has been successful.

The 1998 airborne data were acquired close to the end of the dry season and hence approximates the maximum amount of dust accumulated on the mangrove leaves since the last heavy summer rains. When this map was completed and delivered to the environmental practitioners, it provided for the first time a regional view of the distribution of dust across the handling facility, information that is useful for management but had previously never been attainable (Piggott, 2000; personal communications). An additional advantage of this map is that it provided compositional information. Such information, where one is able to understand the impact of loading iron ore, may be useful for the management of the dust problems and help guide implementation of dust suppression strategies.

The map depicts the highest levels of dust in close proximity to the handling facility at Burgess Point (B.I. on map at Figure 59) and Finucane Island (F.I. on map at Figure 59) with the levels decreasing with increasing distance from these facilities. It is interesting to note that most of the dust appears to have fallen out by the time it is less than 5 kilometres away from the handling facility. The high dust level mapped on the upper right hand corner relates to a sewerage processing site.

Figure 60 shows the ferric iron oxide dust map generated from airborne hyperspectral data acquired in 1999. This acquisition occurred two weeks after a category 2 cyclone and the map clearly depicts the reduction of dust after this event. This image shows that most areas were now mapped as low levels of dust and there

is only a small fringe of high levels surrounding the Port facility and is most likely to be related to the accumulation of dust since the cyclone. This image again confirms anecdotal evidence that environmental practitioners had gathered over the years that severe rain event had the ability to remove dust. Note that the map is again seamless even though the analysis described in Chapter 5 show that these datasets were severely compromised by BRDF effects.

Figure 61, Figure 62, Figure 63 and Figure 64 show ferric iron oxide dust map generated from airborne hyperspectral data acquired in October 2002, December 2004, November 2005 and August 2006. These data were all acquired at the end of the dry season and should represent the maximum accumulation of the dust over that season. They all show very similar dust distribution patterns where the greatest impact is seen closest to the handling facility (located at B.P. and F.I. as showed on Figure 59) and dissipating with distance away from the handling facility. With multi-temporal datasets such as these monitoring can then be undertaken. Some examples of analysis that could be performed include the comparisons of data from year to year to better understand the seasonal impacts and to determine the effectiveness of dust management practices. In an ideal situation, where it would be possible to acquire the data more frequently, the data may also be useful if fed into a real-time dust suppression system where sources of dust close to the highest impact could be more effectively managed.

It is also important to note that, for all the dust maps created from the airborne data in all years, they were again seamless despite the 2004 and 2005 datasets impacted by BRDF. This again confirms that the processing of the airborne data was effective and the dust algorithm appropriate.

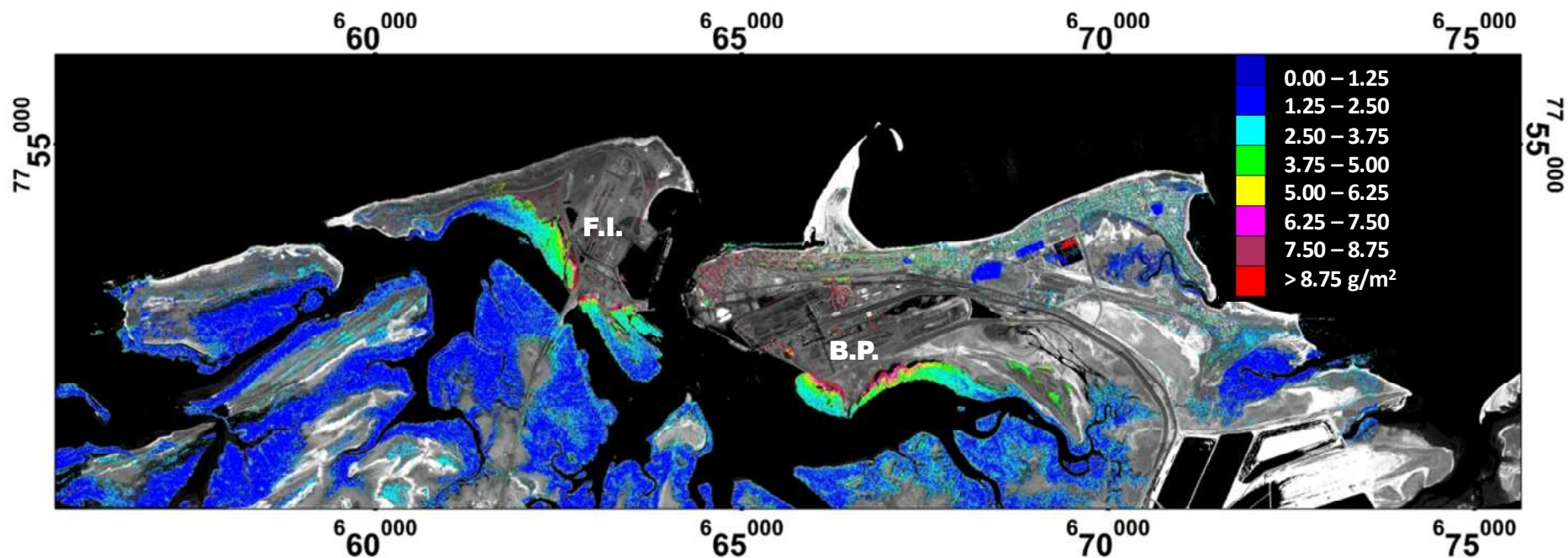


Figure 59: Map of ferric iron oxide dust levels on mangroves and other vegetation surrounding Port Hedland harbour generated from the application of dust algorithms to airborne hyperspectral data acquired on 13th November 1998. The colour coding is such that cool colours (starting with dark blue) denote low dust levels and hot colours (ending with red) are high dust levels. The dust measurements are in units of g/m². The location of Burgess Point is indicated with B.P. and Funicane Island is at F.I.

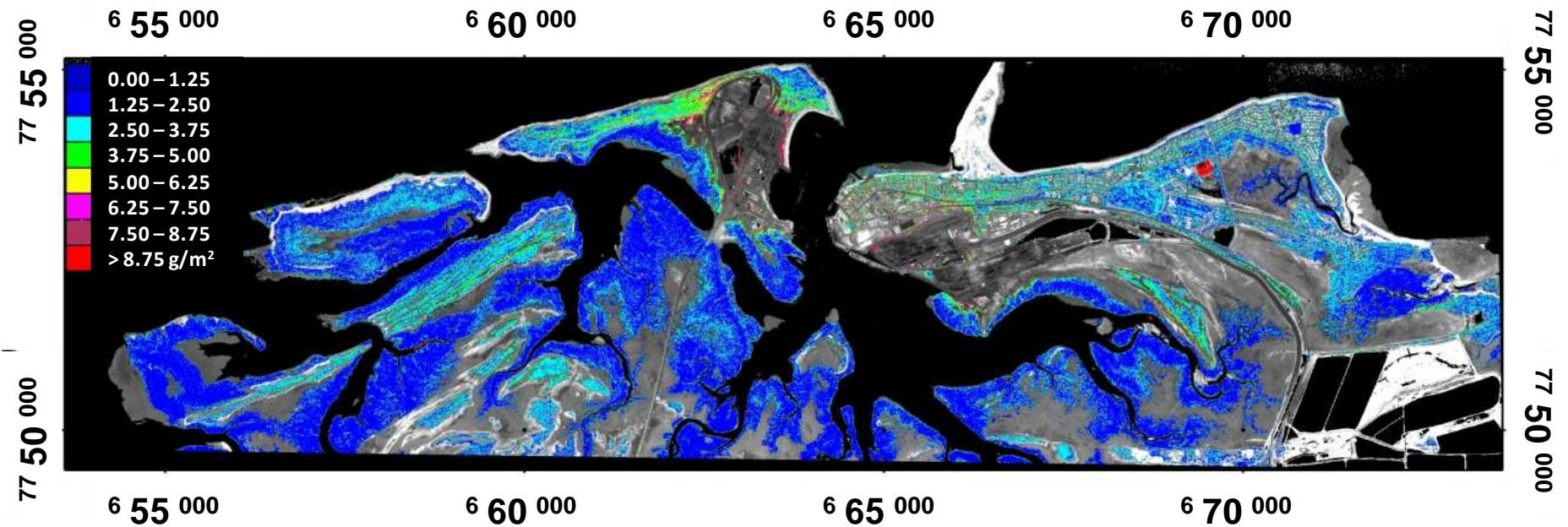


Figure 60: Map of ferric iron oxide dust levels on mangroves and other vegetation surrounding Port Hedland harbour generated from the application of dust algorithms to airborne hyperspectral data acquired on 24th April 1999. The colour coding is such that cool colours (starting with dark blue) denote low dust levels and hot colours (ending with red) are high dust levels. The dust measurements are in units of g/m^2 .

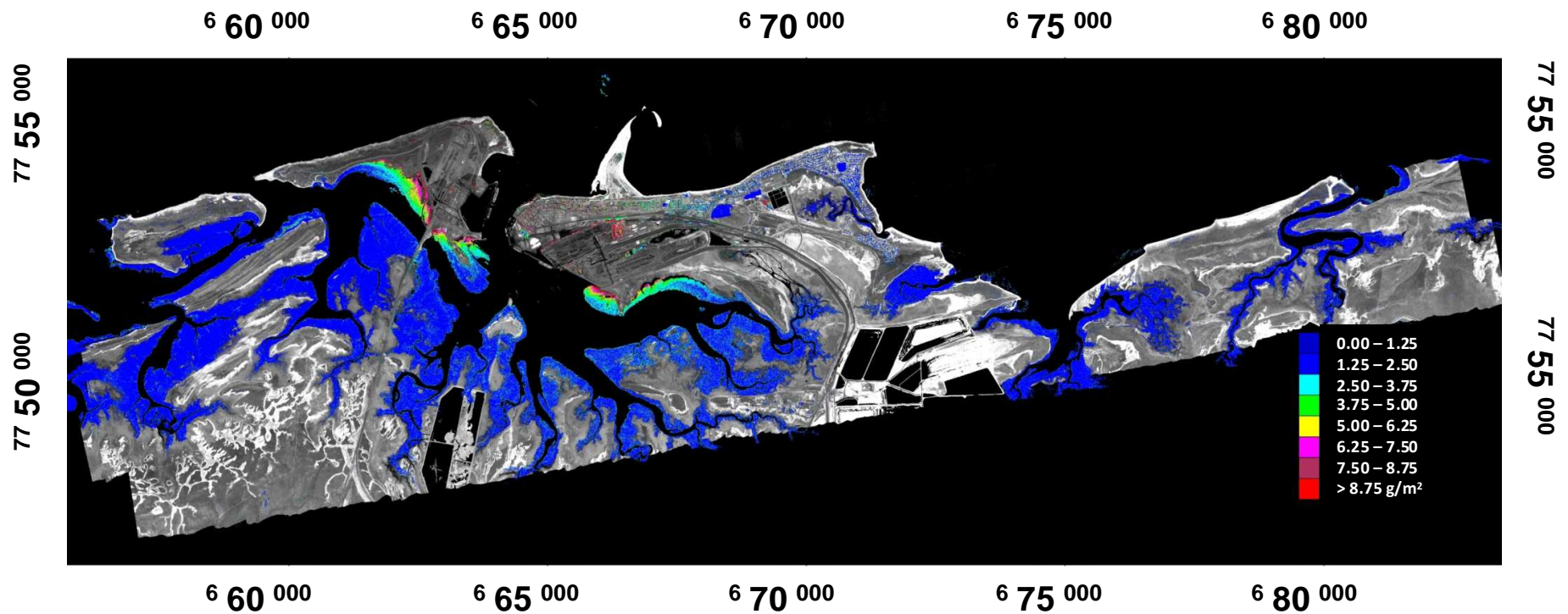


Figure 61: Map of ferric iron oxide dust levels on mangroves and other vegetation surrounding Port Hedland harbour generated from the application of dust algorithms to airborne hyperspectral data acquired on 20th October 2002. The colour coding is such that cool colours (starting with dark blue) denote low dust levels and hot colours (ending with red) are high dust levels. The dust measurements are in units of g/m².

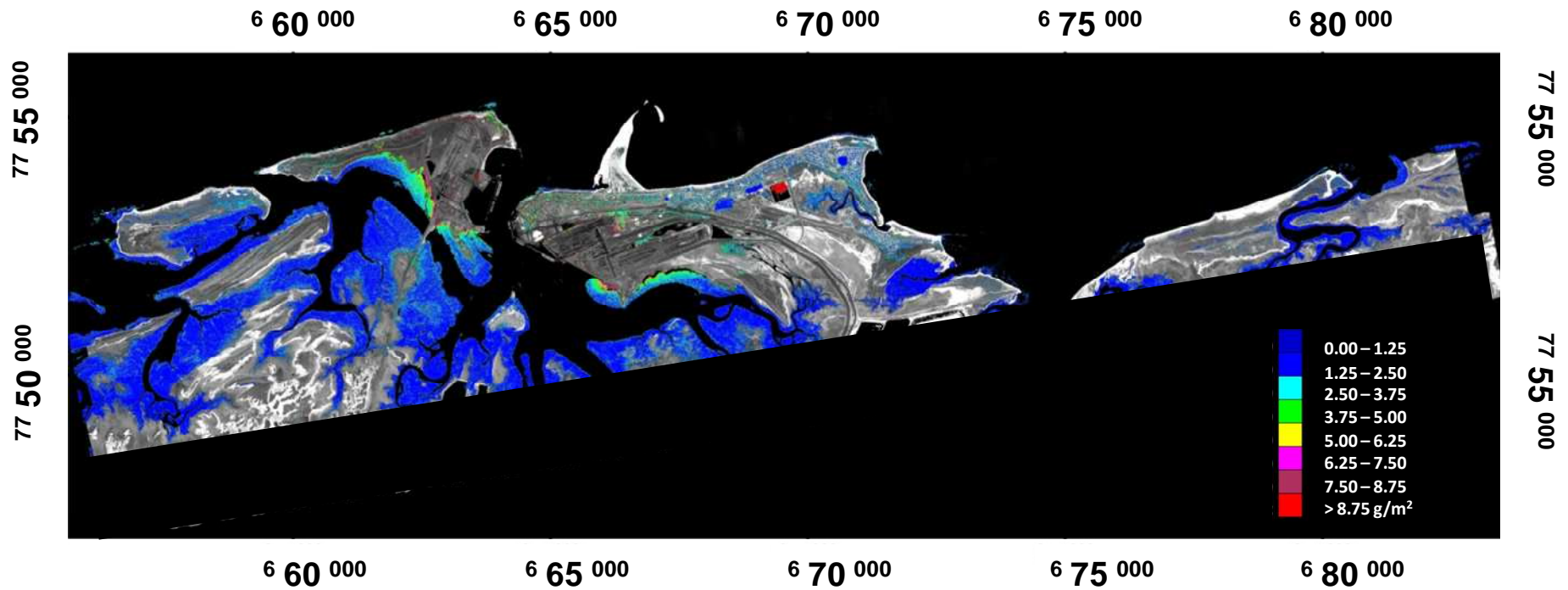


Figure 62: Map of ferric iron oxide dust levels on mangroves and other vegetation surrounding Port Hedland harbour generated from the application of dust algorithms to airborne hyperspectral data acquired on 4th December 2004. The colour coding is such that cool colours (starting with dark blue) denote low dust levels and hot colours (ending with red) are high dust levels. The dust measurements are in units of g/m^2 .

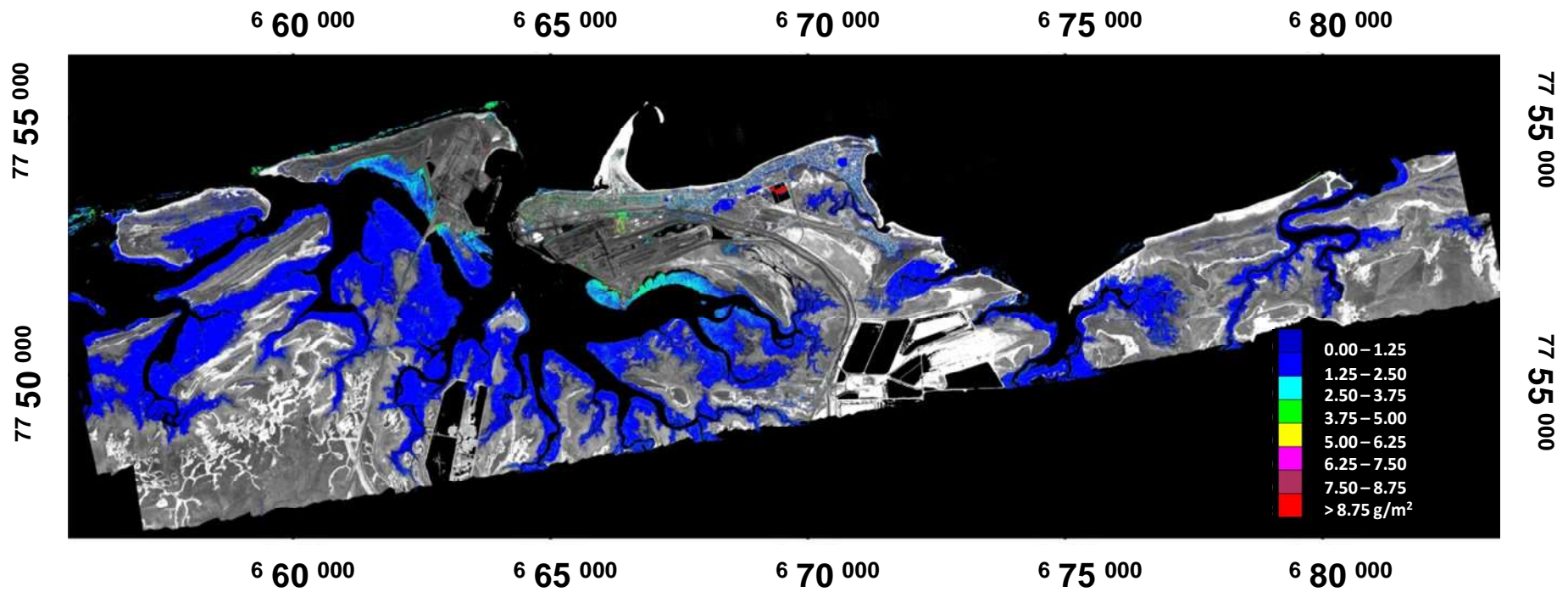


Figure 63: Map of ferric iron oxide dust levels on mangroves and other vegetation surrounding Port Hedland harbour generated from the application of dust algorithms to airborne hyperspectral data acquired on 21st November 2005. The colour coding is such that cool colours (starting with dark blue) denote low dust levels and hot colours (ending with red) are high dust levels. The dust measurements are in units of g/m^2 .

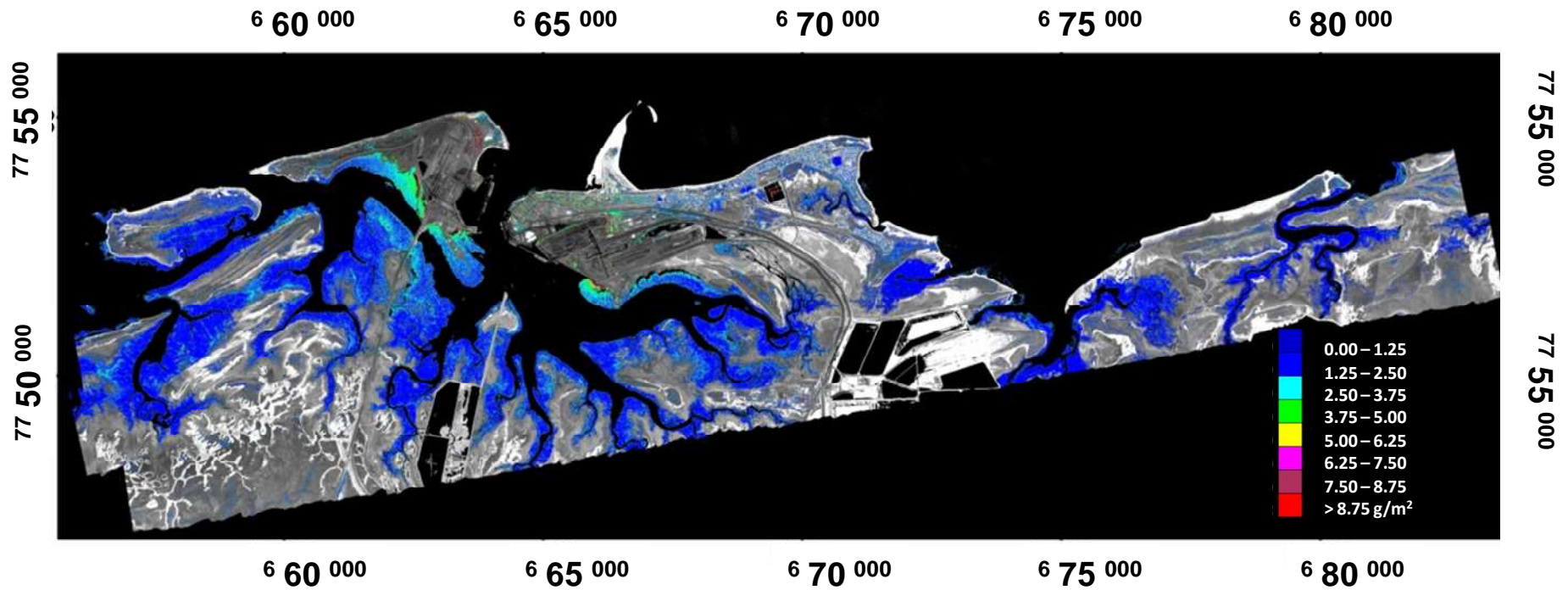


Figure 64: Map of ferric iron oxide dust levels on mangroves and other vegetation surrounding Port Hedland harbour generated from the application of dust algorithms to airborne hyperspectral data acquired on 24th August 2006. The colour coding is such that cool colours (starting with dark blue) denote low dust levels and hot colours (ending with red) are high dust levels. The dust measurements are in units of g/m^2 .

6.4.2 Mineral maps of Brukunga, S.A.

Mineral maps produced using Tetracorder on the SWIR and VNIR spectral data for all four dates are presented on Figure 65 and Figure 66. Although all maps of minerals represented in the Tetracorder command file were generated, only key minerals (and mineral mixtures) potentially related to acid drainage at Brukunga were used for the multi-temporal assessment. It is also possible to incorporate tailored spectral libraries to the command file but it was not done in this case.

Figure 65 shows the minerals mapped using the SWIR data. The mineral maps generated show general agreement for all four dates of imagery. There were two types of jarosite mapped. These are interpreted to be fine grain jarosite with no excess water and water rich jarosite. Note that the library samples in Tetracorder were produced synthetically in the laboratory, that is, they were either produced from (i) mixtures of pure mineral standards, (ii) mixture of different mineral samples collected in the field and mixed in the laboratory or (iii) addition of spectra of different of minerals. Water rich jarosite were mapped around areas which are wet, that is, at the base of the mine benches on the western side of the mine and around areas where water ponding occurs and at the acid treatment pond. This pond is usually filled with liquid and hence it is very likely to be wet. Water rich jarosite appear at very similar locations across the landscape on all four dates. However, there is less water rich jarosite mapped across the mine benches on the west side in 1998 and 1999. This is because these data were acquired late in the day with long shadows at steep faces and hence, low signal-to-noise characterised the data acquired at these steep mine faces and benches. Further, the pixel resolution for the 1998 acquisition was also lower than the later years' data. The other jarosite, fine grain jarosite with no excess water, showed similar, albeit slowly changing distributions over the exposed benches, mine faces, dumps and treatment facility over the four years.

Gypsum, a by-product of acid neutralisation was mapped across the pit floors. Although climatic variation can contribute to the changes seen, the major changes

seen over the years are consistent with the handling of this product according to mine management practices for disposal of this material. The mapped location of gypsum is where the products of the neutralisation process are distributed after being moved from the acid treatment pond.

The minerals mapped in the VNIR region that were relevant to acid drainage condition are shown on Figure 66. The minerals presented are coarse grain jarosite, fine grain jarosite, jarosite+goethite and goethite. The results from the VNIR appear to be generally consistent over 1998, 1999 and 2001 but 2000 appears to be an outlier. Three focus areas will be used to illustrate this observation.

Firstly, the area in Figure 66 marked by the red polygon was examined. This area is mapped predominantly as jarosite+goethite with minor fringes of goethite around the edges and small areas of fine grain jarosite. The patterns of occurrences are consistent across all dates.

Secondly, the area marked by the black rectangle is mapped predominantly as coarse grain jarosite in 1998, 1999 and 2001 in Figure 66. Small amounts of goethite and fine grain jarosite are also mapped (Note that the steep faces are not mapped in 1998 and 1999 because of low signal levels in the hyperspectral data acquired in this areas). In 2000 however, the proportion of coarse grain jarosite compared to goethite is different showing more goethite on this map.

Thirdly, the area in Figure 66 marked by the orange rectangle is assessed. This area is mapped mainly as coarse grain jarosite and has patches of jarosite+goethite and goethite distributed across the area in 1998, 1999 and 2001. There is also a small patch of fine grain jarosite mapped on 2001 and minor amount in 1999 and 1998. A different pattern is observed in 2000 where the area is mapped as mainly goethite and patches of coarse grain jarosite.

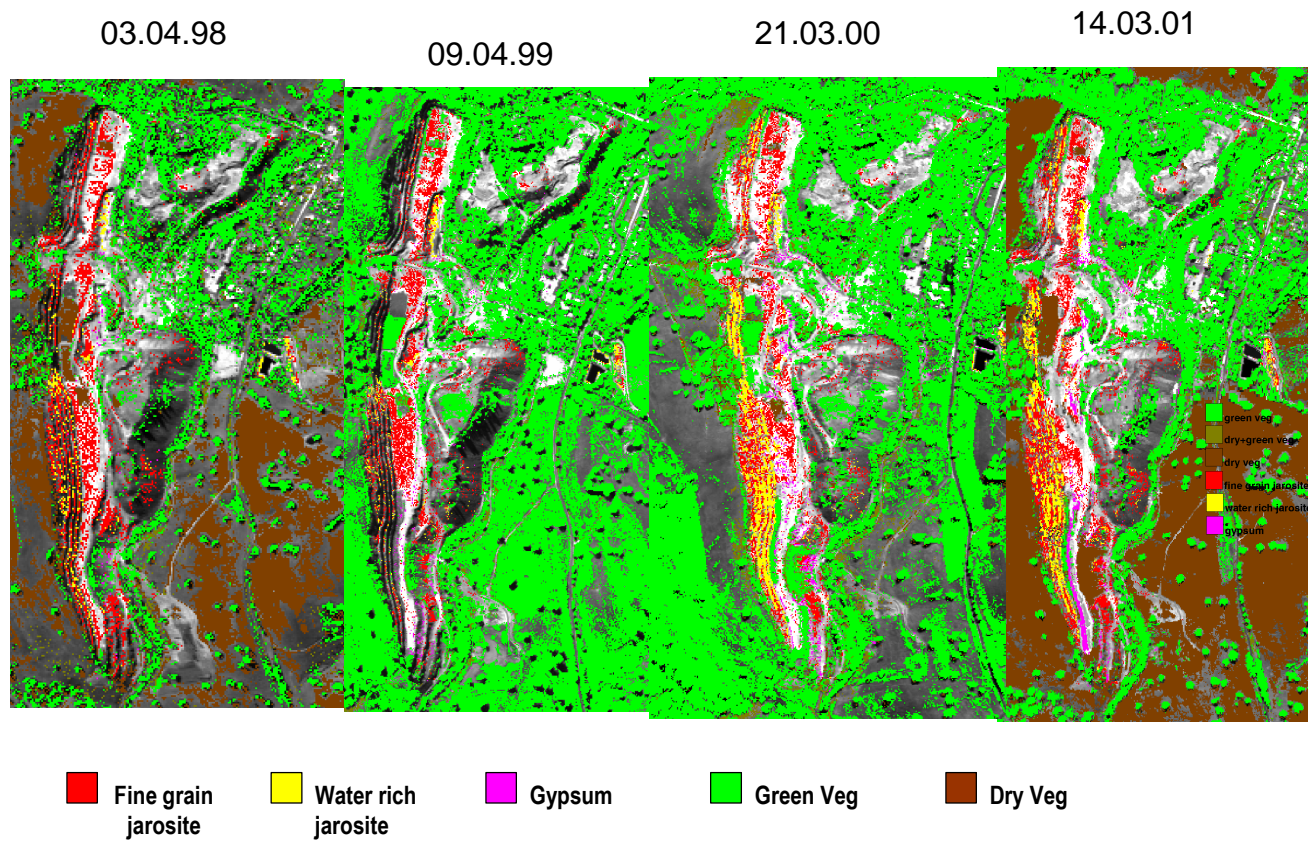


Figure 65: Multi-temporal series map of secondary AD minerals produced using data collected over Brukunga Pyrite Mine over a four year period mapped by Tetracorder using the SWIR region of the spectrum.

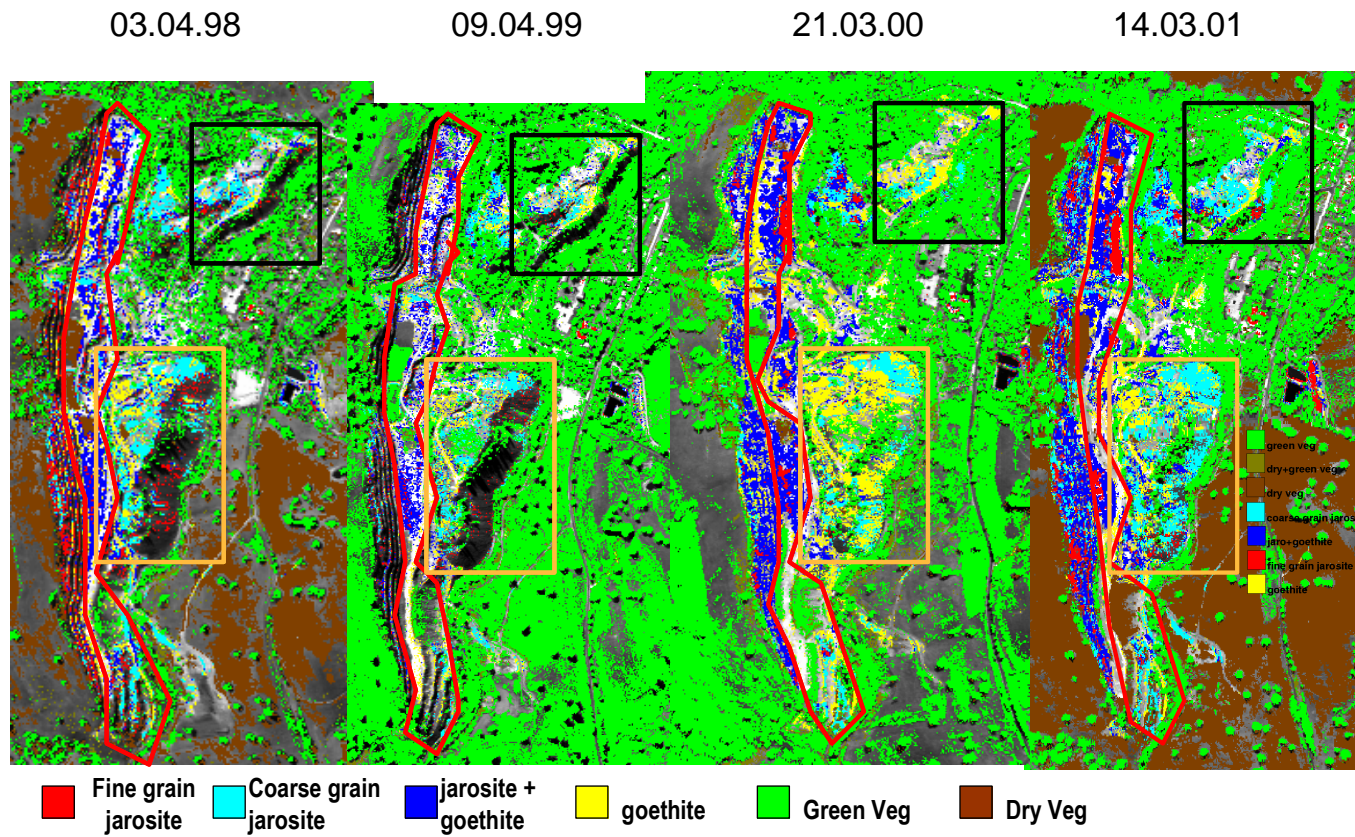


Figure 66: Multi-temporal series map of secondary minerals produced using data collected over Brukungu Pyrite Mine over a four year period mapped by Tetracorder using the VNIR region of the spectrum.

The rainfall data collected at the meteorological station closest to Brukunga is shown on Figure 67 to help explain the differences in observations seen between the years. The star symbols in the figure depict the time of acquisition for the HyMap data for each year. Figure 67 shows that for 1998 and 2001 the airborne data acquisition occurred after a period of several months of low rainfall. The low precipitation preceding the acquisition may explain the abundance of jarosite mapped for these two years as jarosite once formed will persist in a dry climate until the next wet cycle. The abundance of goethite mapped is low possibly because goethite is destroyed by exposure to acid waters released intermittently from the acid salt build ups after a small rain shower. The low rainfall allows the acid build up to occur. There is further evidence of a low rainfall period from the types of vegetation mapped where more dry than green vegetation is mapped in 1998 and 2001 when compare to vegetation patterns in 1999 and 2000. The appearance of more green vegetation in 1999 may be the result of recent rainfall (Figure 67 shows a high rainfall in the month before data acquisition) that can quickly influence the vegetation condition but may not have been as large as in the year 2000 to cause similar patterns in the minerals mapped.

This may be an explanation why goethite is mapped in 2000 in the location where jarosite was mapped in the previous year's data. With a big rain event, the acid salt build ups could have been washed away. In this event, the goethite, which is formed from jarosite remains as the storage of acid salts, that create acid waters to dissolve it is no longer present (Swayze et al., 2000).

The mineral distribution for 1999 is more similar to those of 1998 and 2001 although a high rainfall month was recorded for the month preceding the acquisition. The measurement however, was not as high as 2000 and hence, the acid build up may not have totally washed off. However, conclusive explanation can only be found through field verification. An alternative explanation is that the VNIR maps may not be accurate, possibly a function of less than optimum atmospheric correction, instrument calibration or the grouping thresholds imposed by Tetracorder. This is less likely as mapping appears to be consistent in three of the four dates and the

sensor appears to have improved in performance in the later years enabling better accuracy in the mapping.

It is only possible to use the jarosite minerals to compare the mapping between the SWIR and VNIR region. Jarosites are mapped in similar areas for the two regions but the abundance of jarosite mapped in the VNIR region was greater than in the SWIR. For example, areas that are mapped as coarse grain jarosite using the VNIR region are not present in the SWIR map. This confirms results obtained from the PLS analysis in section 4.3.3 that the SWIR region is not as sensitive for mapping acid drainage related minerals. Specifically, Figure 28 shows the higher FRCs are mainly in the VNIR regions while the FRCs in the SWIR are smaller. Also, the jarosite diagnostic features in the SWIR can be dominated by clay minerals.

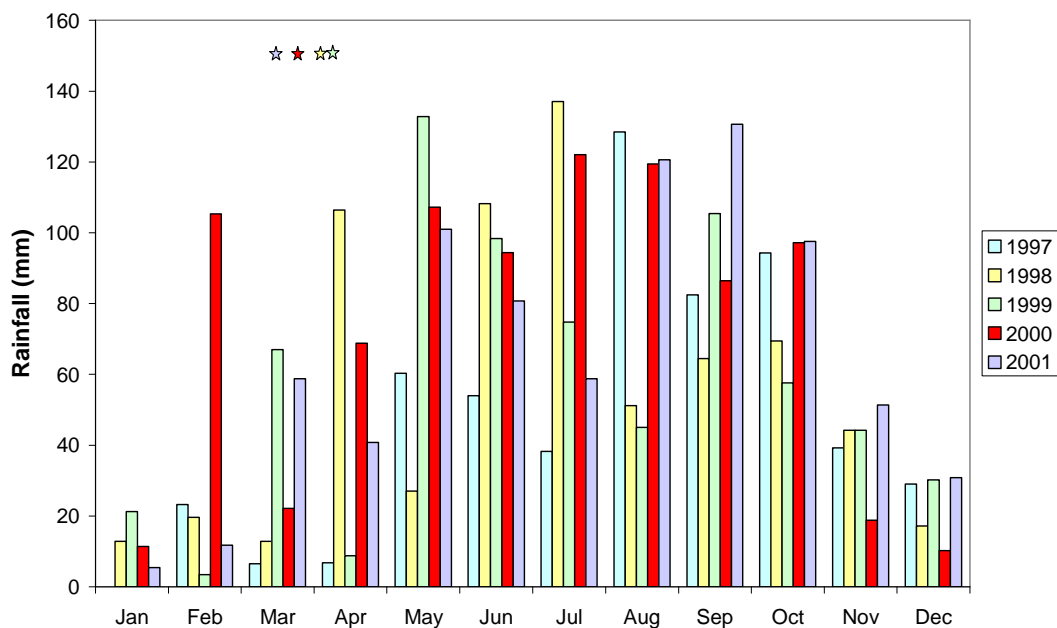


Figure 67: Rainfall chart for the period 1997 to 2001 collected at Mt. Barker meteorological station, closest to the Brukunga Mine. The rainfall data measurements are in millimetres. The star symbols depict the time of year of acquisition of the HyMap datasets.

6.4.3 pH maps of Brukunga, S.A.

Figure 68 shows a multi-temporal series of pH maps generated from the HyMap data using the predictive algorithm produced from the laboratory study. Areas mapped with pH levels between 0-7 are shown in colour. The colour coding here is such that the most acid areas are mapped in the hot colours (red indicates pH of 0-2) down to neutral areas in blue (pH 6-7). The other areas outside of these pH ranges show a black and white background image to provide a perspective of the area.

When the datasets were compared between years, the total areas that contain pH between 0-7 were smaller in the 1998 and 1999 data. Similar to the issues when mapping jarosite, this is related to the low sun angle when the data were acquired resulting in long shadows at steep faces and low signals from these steep mine faces and benches. These data emphasise the importance of flight planning to optimise the quality of the data acquired. Aside from this, there was consistency between the years where the ranges of pH mapped at the mine area were consistently between three and five. This is in close agreement with water pH data collected downstream of the mine for those years (Randall and Cox, 2003).

Besides the steep mine faces where there are uncertainties with the mapping, there were larger areas of pH 2-3 mapped in the 2000 and 2001 data especially around the waste rock dumps and some of the benches of the mine. This may relate to the higher water flow in those two years when compared to 1998 and 1999 reported in (Randall and Cox, 2003). Interestingly, there was a corresponding increase in sulphate, aluminium and iron loads for 2000 and 2001 as well.

These maps have the potential to provide environmental practitioners with a spatially-comprehensive view of the whole mine which may help better understand the progress of rehabilitation efforts or pinpoint areas to concentrate remediation efforts. The following is an example of how these maps can be used is to define areas where rehabilitation/remediation have occurred and their progress as well as areas that need further investigation as determined from these time series maps. The areas marked A, B and C in Figure 68 were identified by environmental practitioners working at

the mine as the “problem” areas and hence have received concentrated remedial efforts. At these locations, the pH maps show that the acid holding pond (marked B) was stable (no change) over the four years and the top right waste rock (marked A) has small changes. In 1998 and 1999, this area was mapped as having small patches of pH 3-4, surrounded by pH 4-5 which were surrounded by a larger area of pH 5-6. In 2000 and 2001 the patches of pH 3-4 was larger with corresponding decrease in the sizes of the pH 4-5 and 5-6 areas. The middle waste rock (marked C) had changes mainly on north-eastern corner where in 1998 and 1999, the pH values were mainly in the 4-6 range. There were small patches of pH 3-4. In 2000 and 2001 the pH 3-4 patches were larger.

The largest changes, however, were observed in areas not previously identified by the environmental practitioners. Two such areas are located across the south-western mine benches (marked D) and across the north-western mine floors (marked E). Although the steep faces of mine benches at D were not mapped in 1998 and 1999 because of the low signal related to shadows, there is a general trend which shows an increase in acidity in 2000 and 2001. This area is predominantly mapped as pH 3-4 with small patches of pH 2-3 and 4-6 in 2000 and 2001 but is mapped predominantly as pH 4-6 with small patches of pH 3-4 in 1998 and 1999. The variation observed at location A, C, D and E could be a result of the higher precipitation in 2000 and 2001 compared to 1998 and 1999. Investigation of rainfall data and the water data collected (Randall and Cox, 2003) for those years confirms this.

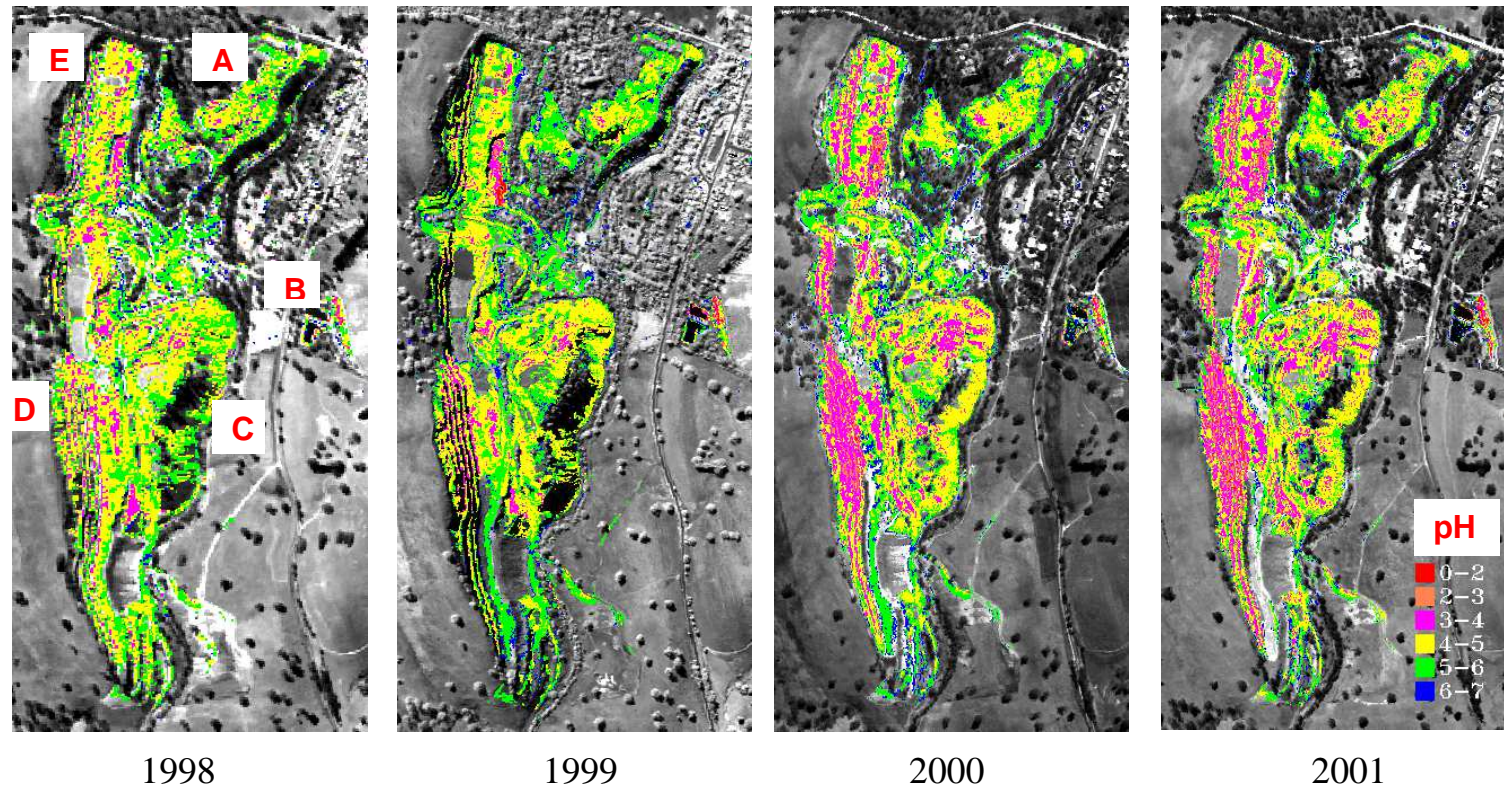


Figure 68: pH maps generated from application of a predictive algorithm (produced from laboratory chemical and spectral measurements) to multi-temporal airborne hyperspectral data collected over the Brukunga Mine using the HyMap sensor. (A) indicates location of top waste rock dump, (B) the location of the acid treatment pond, (C) the middle waste rock dump, (D) the south-western mine benches and (E) the north-western mine floors.

6.5 Summary

This chapter presented the maps generated from the application of the spectral algorithms developed in the laboratory applied to airborne hyperspectral data. The maps demonstrate the ability of remotely-sensed hyperspectral data to provide quantitative and spatially-comprehensive measurement of the environmental variables of concern.

The ferric iron oxide dust maps provided a regional view of the distribution of dust across the handling facility. The five years of data shown consistently indicated that the greatest dust impact was in close proximity to the handling facility at Burgess Point and Finucane Island with the levels decreasing with increasing distance from these facilities. The data indicates that the dust had essentially fallen out less than 5 kilometres from the source.

All the dust maps created from the airborne data in all years were again seamless between adjacent flight lines despite some of the datasets impacted by BRDF effect. This confirms that the processing of the airborne data was effective, that the dust algorithm was appropriate and that monitoring can be quantitatively undertaken with these multi-temporal datasets. Some examples of analysis that could be performed include the comparisons of data from year to year to better understand the seasonal impacts and to determine the effectiveness of dust management practices. In an ideal situation, where it would be possible to acquire the data more frequently, the data may also be usefully fed into a real time dust suppression system where sources of dust close to the highest impact zones could be more effectively managed.

An additional advantage of the dust maps is that they provide compositional information. Such information, where one is able to understand the impact of loading iron ore, may be useful for the management of the dust problems and help guide implementation of dust suppression strategies.

The image acquired that was captured after a cyclonic event indicated that severe rainfall events have the potential to remove the dust from the vegetation confirming

anecdotal evidence that environmental practitioners had gathered over the years that severe rain event had the ability to remove dust.

The maps produced using Tetracorder in the SWIR region are generally consistent across a multi-temporal series of data collected over the four year period. The ability of Tetracorder to consistently map similar minerals in the SWIR region over the four dates confirms that the SWIR region of the airborne sensor is stable across the four years. However, for the application of acid drainage monitoring, mapping in this region may not be sufficient as it was found, from an associated study, that this region is not as significant as the VNIR region for mapping the secondary minerals crucial for determining acid drainage conditions (Swayze et al., 2000).

In the VNIR region, Tetracorder was able to produce consistent maps for three of the four years. The reasons for the one outlier observation may be attributed to environmental changes, pre-processing or instrument calibration. It is not possible to conclude which of these are contributing factors as field verification was not performed close to acquisition. One lesson learnt is that rapid follow-up is necessary to validate the mineral mapping results derived for a given airborne overpass. Unfortunately, in only two of the four years was follow-up fieldwork performed. More precisely controlled experiments such as this study are required to establish if this method can be used operationally for quantitative environmental monitoring.

The pH maps produced from the airborne hyperspectral data acquired from 1998 to 2001 were consistent between the years the ranges of pH mapped at the mine area were consistently between pH three and five which is in close agreement with water pH data collected downstream of the mine for those years (Randall and Cox, 2003). The inconsistencies that do exist can be related to the low signal in the data resulting in the inability to map some areas in the 1998 and 1999 data. This highlights the importance of flight planning to ensure that optimal data are acquired.

When comparing between years, the data indicate larger areas of pH 2-3 mapped in the 2000 and 2001 data compared to 1998 and 1999 especially around the waste rock dumps and some of the benches of the mine. This may relate to the higher water

flow in those two years when compare to 1998 and 1999 reported in (Randall and Cox, 2003).

These maps have to potential to provide environmental practitioners with a spatially-comprehensive view of the whole mine which may help better understand the progress of rehabilitation efforts or pinpoint areas to concentrate efforts.

Chapter 7

VALIDATION OF ENVIRONMENTAL INFORMATION PRODUCTS

7.1 Introduction

One of the most important requirements of environmental monitoring is that the measurements being used are accurate so that comparisons between dates and locations can be made reliably. Validation is defined as the process of assessing, by independent means, the quality of the data products derived from the system outputs (Lecomte, 2008). Validation of parameters is an essential component of nearly all remote sensing-based studies and there are many considerations in performing validation. The most common technique is comparing ground measurements to remote sensing observations or modelled results (Council, 2009).

This chapter describes the validation performed in this project to ensure that the dust, mineral and pH maps can be used with a significant level of confidence.

7.2 Method

The validation of the dust, mineral and pH maps were performed using the classical technique of comparing *in situ* measurements collected concurrent or near concurrent to the airborne acquisitions. Independent measurements obtained from laboratory analysis, relevant for each of these maps were performed. The laboratory analyses are described separately below for each of the maps.

7.2.1 Validation for dust maps

In situ spectral data were used for the validation of the dust maps. Spectral measurements for the validation were undertaken in the laboratory in a similar fashion as the laboratory experiments described in Chapter 4. Laboratory measurements were employed as it was not possible to collect them in the field because of the measurement logistics in taking the available spectrometers, and their power sources, to the sites that, in many cases, were only accessible at low tide. Also, these low tide conditions often did not coincide with best solar illumination times and cloud cover.

Validation data were acquired twice during this study. These were coincident with the airborne acquisition in 1998 and 2002. The sampling locations in 1998 which occurred at the early stages of the project depended strongly on the location of the dust deposition gauge and anecdotal accounts of the distribution of the dust. The location of the site where validation samples were collected in 1998 is shown on Table 6. Leave samples were collected from different trees randomly selected from an area of at least 15by15 metres (and more often larger) to provide a representation of an area larger than 3by3 pixels on the image.

Dust Deposition Gauge Locations (Datum:AGD 66)			
Location	Site No.	Latitude	Longitude
Tunnel area	1.0	20° 19' 37.42"	118° 35' 13.53"
*Tunnel portal 10 m	1.1	20° 19' 00.48"	118° 33' 54.28"
Funicane Island	2.0	20° 18' 19.13"	118° 32' 51.38"
*Funicane Island Causeway Tunnel Side	2.1	20° 19' 04.36"	118° 33' 44.43"
*Causeway Mainland West	2.3	20° 19' 11.23"	118° 33' 33.26"

*Causeway Mainland East	2.4	20° 19' 13.35"	118° 33' 36.50"
*2 km East 50 m	5.1	20° 19' 57.00"	118° 33' 19.72"
*location of BHPBIO TS505 dust sampler 10 m	7.1	20° 19' 32.19"	118° 35' 18.08"
*Slipway 15 m East	7.3	20° 19' 49.11"	118° 35' 34.25"

*Table 6: Description and locations of depositional gauge sites (denote with *) and additional sampling sites collected in 1998.*

The second field acquisition period was in October 2002 and was concurrent with the airborne acquisition. Airborne validation data were also collected at the same time. Four of the sampling sites are located in Burgess Point, five were at Finucane Island and one at Six Mile Creek. The locations of these sites were again selected based on the 1998 dust map. The locations of the sites were recorded using a differential GPS with an accuracy of ± 3 to 5 metres and they are listed in Table 7.

site	easting	northing
ba1	666010	7751770
ba2	666448	7751336
ba3	666368	7751381
ba4	666610	7751622
fa1	660511	7753830
fa2	661831	7754264
fa3	662488	7753911

fa4	662818	7752939
fa5	663419	7752762
6m1	674024	7751442

Table 7: GPS locations of field sampling sites acquired in October 2002. Datum is AGD 66, zone 50.

Validation was performed for the 900 nm ferric iron oxide CFA depth, the main input parameter for the dust algorithm. The processing of the validation data were consistent with the methods used for processing the laboratory and airborne spectral data. That is, the depth of the 900 nm ferric iron oxide was calculated as in Equation 6. These ground data were then compared with the 900 nm ferric iron oxide CFA depth generated from the airborne data at the same location.

7.2.2 Validation of Tetracorder mineral maps

7.2.2.1 X-ray diffraction (XRD)

XRD was used to provide independent validation of the results obtained from the minerals mapped using tetracorder. XRD measurements to determine mineralogy of the samples collected at Brukunga from the 1999 campaign, described in Chapter 4 and located on Figure 23 were performed using the Philips XL-40/CP unit.

Qualitative identification of the relevant AD minerals and their abundances was performed via identification of the presence/absence of the 3 major peaks (tabulated on Table 8) in the XRD pattern - or 'diffractogram'. The traces were matched to library traces of secondary AD minerals expected in the sample. XPlot (CSIRO, 2005) was used to perform this analysis. Furthermore, to facilitate more accurate comparisons, the traces were calibrated before the comparisons. 40 of the 41 samples analysed contained quartz and hence the 40 XRD patterns were calibrated to the quartz standard.

There were some challenges with the identification of some of the minerals. For example, it was difficult to separate between jarosite and natrojarosite especially with the presence of bassanite as the peaks of the three minerals overlap. Also, some of the AD secondary minerals such as schwertmannite and ferrihydrite are in the class of “poorly crystalline” or “X-ray amorphous” minerals with the XRD patterns expected to show broad peaks. Identification of these minerals was difficult.

Note that the samples were dried at 100 °C and hence little traces of gypsum were found in the samples even though some samples were collected at the gypsum pile. This was because the drying process dehydrated the gypsum to bassanite or anhydrite.

Mineral	Peak location (d-spacing (nm))		
	Peak 1	Peak 2	Peak 3
Jarosite	3.080	3.110	5.080
Goethite	4.183	2.450	2.693
Schwertmannite	2.550	3.390	4.860
Ferrihydrite	2.500	2.210	1.960
Pyrite	2.700	1.633	2.4209
Hematite	2.690	1.690	2.510
Gypsum	2.871	4.280	2.684
Bassanite	3.006	2.807	6.000
Natrojarosite	3.006	3.122	5.060
Muscovite	9.980	2.554	2.556
Melanterite	4.900	3.776	4.560
Rozenite	4.470	5.460	3.400
Epsomite	4.216	4.200	5.980
Copiapite	18.400	9.230	5.570
Halotrichite	4.810	4.300	3.500

Table 8: Minerals related to AD and their three major peaks locations. Note that there are overlaps in peaks for some minerals. For example, goethite, hematite, pyrite, gypsum and bassanite have overlapping peaks at around 2.70-2.80 and goethite, epsomite and halotrichite have overlapping peaks at around 4.20-4.30.

7.2.2.2 Spectral interpretation

Interpretations of the reflectance spectral of the same samples used for the XRD analysis were performed to facilitate comparisons between the ground and airborne spectra and spectral results and XRD. Minerals were identified from the laboratory

reflectance based on their known diagnostic features. For the ferric iron oxides and hydroxide minerals, the features were:

- the 430 nm Fe^{3+} crystal field absorption (CFA) diagnostic of the presence of jarosite and charge transfer (CT) Fe^{3+} -O feature possibly superimposed over Fe^{2+} CT for melanterite/rozonite (Crowley et al., 2003);
- the presence of the 650 nm Fe^{3+} CFA feature diagnostic of goethite and hematite (Morris et al., 1985) and jarosite (Crowley et al., 2003);
- the location of the left shoulder of the 900 nm Fe^{3+} CFA feature, that is, if located at shorted wavelengths close to 720 nm, indicates the presence of jarosites (Crowley et al., 2003). If located at wavelengths around 740-750 nm, it is indicative of goethite and/or hematite (Morris et al., 1985) and, the location of the left shoulder of the 900 nm Fe^{2+} CFA feature located at around 600 nm indicates melanterite and/or rozenite (Crowley et al., 2003);
- the location of the 900 nm Fe^{3+} CFA: wavelengths shorter than 870 nm indicate the presence of hematite; wavelengths between 870-920 nm indicates the presence of goethite (Morris et al., 1985) and wavelength longer than 900 nm indicate the presence of jarosites (Clark, 1999). The Fe^{2+} CFA feature for melanterite is located at around 892 nm and rozenite at 978 and 1170 nm (Crowley et al., 2003);
- the location of the right shoulder of the 900 nm Fe^{3+} CFA: this usually located at around 1000-1200 nm for goethite and hematite (Morris et al., 1985) and located at 1200 nm and longer for jarosites. The right shoulder of the Fe^{2+} CFA for melanterites and rozenites is located around 1400 nm (Crowley et al., 2003); and,
- the presence of the 2265-2270 nm jarosite feature related to a combination of O-H and stretch and Fe-O-H bend (Clark, 1999).

For gypsum and/or bassanite, the main feature that was used in identification was the feature around 1750 nm related to H₂O (Clark, 1999). This is not ideal as this not a main feature but the additional features, for example around 2265 nm overlaps with the jarosite feature. Consequently, it was difficult because of the mix of minerals to clearly identify this mineral for many of the samples.

In the case of muscovite, the two main features used were the 2200 nm and 2350 nm features, related to Al-O-H bond (Clark, 1999).

7.2.3 Validation of pH maps

The samples that were used for the validation were collected in 2001 concurrent with the airborne acquisition. The chemical analysis performed on the samples to obtain pH measurements are described in Chapter 4.

7.2.4 Site location

The validation sites were located on the airborne data using the GPS location acquired using a hand-held GPS and visual location on the maps while in the field. Taking into account the expected accuracy of the GPS during the period of selective availability (GPS.GOV, 2011) which may be up to ± 100 metres (USGS, 1999) and the limitation of the accuracy of the georeferencing of the 1999 (see Chapter 8) where INS GPS data were not available, an area of at least 5 by 5 pixels was used. For the dust map, the arithmetic mean of a 5 by 5 pixel area was extracted from each location. In the case of the mineral mapping, the main mineral(s) mapped for the area were recorded as the mineral(s) present. For the pH maps, the range of pH values mapped using the airborne data were recorded.

7.3 Results

7.3.1 Dust map

Validation data collected during the November 1998 acquisition were combined with the data from 2002 to obtain a total of 16 validation points. Figure 69 plots these *in*

situ data against the airborne data. It shows that the ground and airborne measurements are well correlated. The correlation at an R^2 of 0.70 is significant with a confidence level of 99% showing that the CFA depth from the airborne data is comparable to results obtained from the ground spectral measurements. This result indicates that the dust algorithm can be transferred to the airborne platform and the airborne data should be able to produce accurate dust measurements. Additionally, if the standard error of 0.0161 was to be converted to dust levels via the dust algorithm via Equation 7, then the standard error to be expected from the airborne dust level is 2.364 g/m^2 .

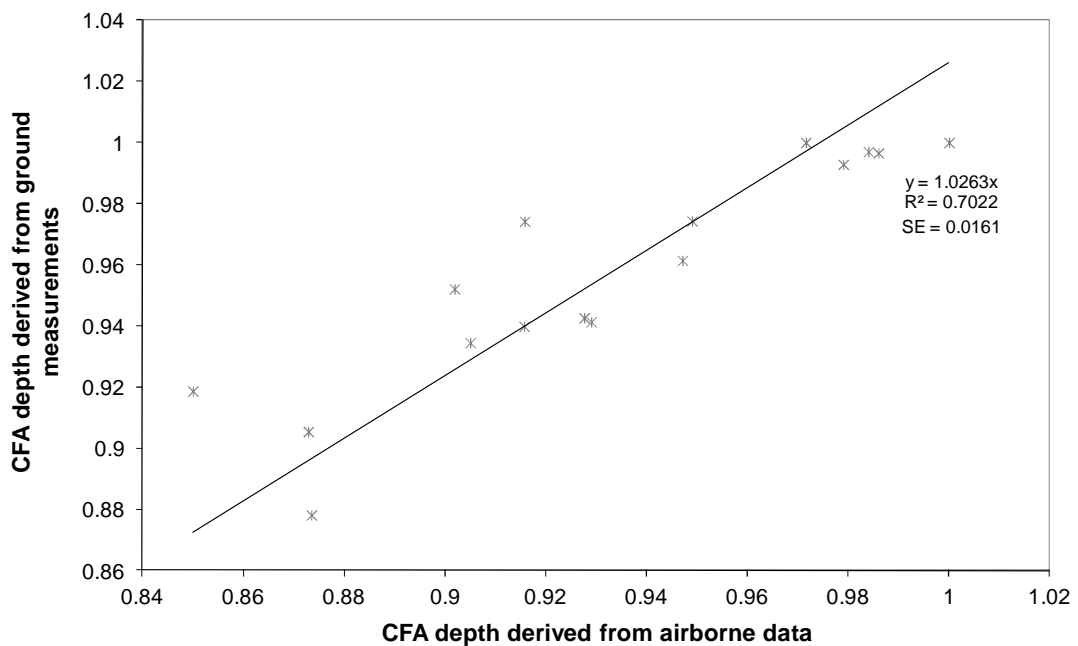


Figure 69: Scatterplot of field measured dust values plotted against airborne extracted dust measurements.

7.3.2 Mineral maps

Table 9 shows the results of spectral interpretation of samples collected in 1999 together with XRD results from these samples. The dominant minerals identified with XRD were jarosite, goethite, hematite, melanterite, rozonite, muscovite, gypsum and bassanite. In the case of goethite and hematite, they were combined as there were overlaps in the XRD peak locations for these minerals as well as other

minerals such as pyrite and epsomite. Melanterite and rozonite were combined as they have similar spectral features. Gypsum and bassanite also have similar spectral features and overlapping XRD peaks.

Table 9 [a] presents the evaluation of the minerals identified from the ground spectra compared with the minerals mapped when Tetracorder was applied to the airborne data. The colour code is such that green signifies agreement between the ground and airborne spectra and that they both identified the mineral, light green indicates that agreement between airborne and ground identification and the mineral was not identified. Red signifies that the mineral was identified on the ground spectra but not in the airborne spectra and orange indicates that the ground spectra did not identify the mineral but the airborne spectra did. Only the main AD minerals mapped using Tetracorder and presented in Chapter 6 were analysed.

The best agreement between the airborne and ground mineral identification was found for goethite/hematite where 33 out of 39 sites were mapped similarly. Jarosite was identified correctly in 32 out of 39 sites and gypsum was correctly assigned in 31 out of 39 sites. In summary, the results show that the airborne and ground data agreed for 82.1% of the samples.

Table 9[b] shows the minerals mapped by Tetracorder compared with the mineral identified using XRD on the ground samples. Only the main AD minerals mapped using Tetracorder are shown here as well. The colour code is such that green signifies agreement between the XRD and airborne spectra and that they both identified the mineral, light green indicates that agreement between airborne and XRD identification and the mineral was not identified. Red signifies that the mineral was identified on the XRD but not on the airborne spectra and orange indicates that the XRD did not identify the mineral but the airborne spectra did.

The best identification of minerals when using Tetracorder applied to the airborne data was for jarosite where 32 out of 39 sites were correctly identified. For goethite/hematite, correct identification occurred for 29 out of 39 sites. The identification for gypsum was somewhat lower where just over half (21) of the sites

were correctly assigned. This may be related to the small sample of gypsum in the tetracorder library. However, overall the results still indicate that the tetracorder mapping have a high level of reliability as indicated by the Tetracorder mapping was in agreement with the XRD results in 70.1% of the cases.

Table 9[c] compares the identification of minerals from the spectral data compared with those identified by XRD. Note that a more comprehensive set of minerals are presented here.

For jarosite, there was concurrence between the spectral interpretation and XRD for 38 out of 39 samples. In the one case where there was no concurrence. It was not possible to clearly identify the jarosite peaks in the XRD trace. For goethite, the spectral and XRD interpretation agreed 37 out of 39 samples. Here again, the disagreement between the spectral and XRD results was where spectrally, goethite was identified but it was not possible to positively identify goethite with XRD. In the case of muscovite, 38 out of 39 samples agree between spectra and XRD. The outlier sample consisted mainly of calcite. For rozenite/melanterite, all the samples agreed. However, the number of samples with this mineral was very low – there were only four samples containing rozenite/melanterite. Gypsum/bassanite were the most difficult to positively identify spectrally. This was because most of the spectral features of these minerals had overlaps with other minerals present in the samples. Therefore, the number of concurrence between spectra and XRD was the lowest for this group at 35 out of 39 samples.

In summary, the samples collected in 1999 consist mainly of jarosite and muscovite (38 out of 39 samples), followed by goethite (37 out of 39 samples). There were minor amounts of melanterite and/or rozenite and gypsum/bassanite.

shows a good general linear trend at R^2 of 0.72, RPD of 1.96 and a relatively low RMSE of 0.57. The agreement between the pH predicted using the airborne imagery and those obtained from the ground truth samples indicate that pH can be reliably predicted using airborne hyperspectral data.

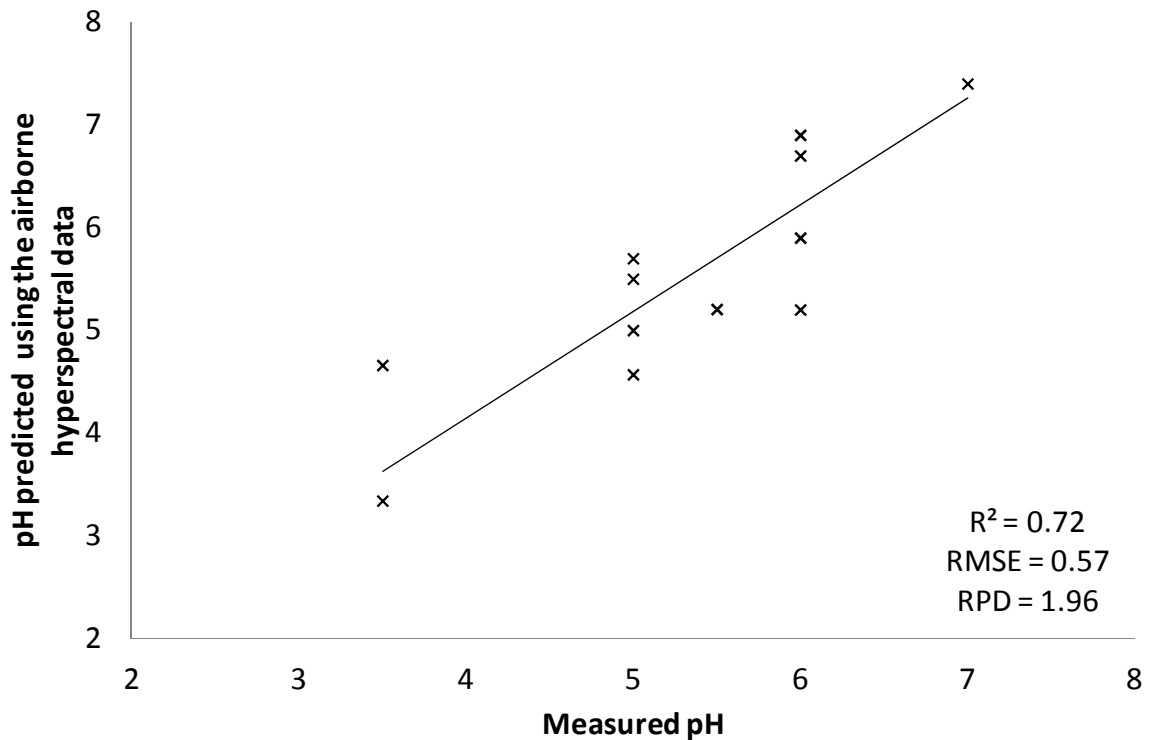


Figure 70: pH measured using chemical analysis plotted against pH values predicted on the airborne hyperspectral data.

7.5 Summary

The accuracy of measurement collected for monitoring must to be quantified so that comparisons can be made with those data with knowledge of the expected errors in the results. The accuracy of the environmental information maps generated from airborne hyperspectral data were validated in this chapter.

The validation approach adopted was the classical technique of comparing an independent set of ground truth data to the airborne maps. This technique is known to be limited because of the mismatch in scale between the airborne and ground

measurement (Council, 2009). Further, there are technological challenges in locating the exact pixels. These challenges include the accuracy of the GPS as well as the limitations of some of the data which were acquired without INS GPS. Although ground control points (GPCS) were used to georectify the imagery that did not have INS GPS, the accuracy were lacking as insufficient GCPS could be found to sufficient account for the complex geometric correction required to correct for all the aircraft movement (roll, pitch and yaw) inherently captured on the imagery.

Despite the limitations, the results of the validation indicated that (1) spectral data can be used to reliably produce ferric iron oxide dust maps and the uncertainty in the ferric iron oxide dust maps were calculated as $\pm 2.364 \text{ g/m}^2$; (2) Tetracorder mapping of AD minerals are 70.1% accurate; and, (3) pH maps generated from airborne hyperspectral data as evidenced by the R^2 of 0.72, RPD of 1.96 and a relatively low RMSE of 0.57.

Chapter 8

DETECTION OF TEMPORAL VARIATION

8.1 Introduction

One of the prerequisites for the accurate mapping of change between multi-temporal data is that the imagery is geographically located between dates. As most data nowadays are analysed together with other datasets, another important requirement is that the data are also accurately geographically located to base map.

Two significant developments occurred during the course of this study: improved software by the data providers ensured better geographical location of the imagery given an accurate digital elevation model (DEM) and; the availability of off-the-shelf software that permitted the automatic registration of images. These were tested to determine their suitability for providing geolocation data with sufficient accuracy for multi-temporal change detection mapping.

8.2 Method

The test dataset used for this review was the Port Hedland data acquired in 2006. The Port Hedland dataset formed the ideal case where the area has no significant topography, a detailed DEM and orthophotograph at 1 spatial metre resolution were available and the imagery covered areas where abundant features, such as buildings, roads, etc. were available for geographical location.

During the course of this study, HyVista the operator of the HyMap instrument and one of the main providers of airborne hyperspectral data in Australia upgraded their techniques to include the incorporation of more detailed DEMs and other

improvements to enhance co-registration between flight lines. The result of this improvement and processing was tested.

The technique includes the incorporation of a high resolution DEM with the information from the Inertial Navigation System (INS) with Global Positioning System (GPS) data. The INS GPS information maps the movement of the aircraft for roll, pitch and yaw and the geographic position at the nadir position is acquired concurrent with the airborne data acquisition. This information is used to assign each pixel to the correct location on the ground. Note that previously, only Shuttle Radar Topography Mission (SRTM) DEMs at a resolution of 90 metres were used for this purpose.

To determine the accuracy of the geographical-location, the 2006 HyMap data were firstly overlaid on a 1 metre resolution orthophotograph supplied by BHPBIO and visually inspected for disparity between the two. Secondly, the overlaps between two flight lines were inspected for determining the accuracy of co-registration of adjacent flight lines.

Further analysis includes comparisons between the 2006 data which was processed with the improved geographical location software and historical datasets acquired in Port Hedland, which were not processed with this software, to determine the improvements achieved. The accuracies of the geographical-location for the historical data were compared with the 2006 to determine their impact on change detection analysis. The analysis was undertaken with the assumption that the 2006 geographically located data had the most accurate geographic coordinates. Several locations along each flight line were inspected.

Evaluation was also performed using the Environment for Visualizing Images (ENVI) automatic co-registration routine to determine if it could improve the alignment between adjacent flight lines. The alternative to using automated software such as this is a laborious process of manually selecting tie points between the reference, that is, for example the base map and the image that is to be corrected. Obviously, this is not an operational solution.

ENVI's automatic image co-registration tool uses area-based matching and feature-based matching algorithms to obtain tie points, which are as follows:

- Area-based image matching compares the grayscale values of patches of two or more images and tries to find conjugate image locations based on similarity in those greyscale value patterns; and,
- Feature-based image matching extracts distinct features from images then identifies those features that correspond to one another. This is done by comparing feature attributes and location (ENVI 4.2, 2006)

The evaluation was performed for

- The geo-location of the HyMap data acquired in 2006 to the 1 m resolution orthophotograph, where a band combination forming a natural image was used for the HyMap data and was compared with the orthophotograph; and,
- The co-registration of HyMap data acquired at Port Hedland in 2005 to 2006, where the bands corresponding to the green wavelength region for the two years were compared.

Lastly, difference maps were produced by arithmetic subtraction between years. These data were generated to demonstrate the multi-temporal monitoring capabilities using such data.

8.3 Results

Figure 71 shows that the HyMap image was displaced from the orthophotograph by up to 3 pixels in the northwest direction. This displacement, depicted on Figure 72, is similar across the whole image. This result indicates that one can expect geographical-location errors of the HyMap to be ± 3 pixels. This translates to ± 9 metres for data acquired at 3 metre pixel resolution.

The imagery shown on Figure 73 shows that there were also mismatches of up to 3 pixels between flight lines as shown on Figure 74. However, this displacement is unequal across the image. For example, inspection of one overlap area shows a 2-3

pixel displacement in the southeast direction at the western end of the image (left image on Figure 74), a 2-3 pixel displacement in the northwest direction in the centre of the image (middle image on Figure 74) and no displacement in the eastern end of the image (right image on Figure 74). Differential movements of the aircraft are the likely cause of the disparate displacement. This indicates that the INS GPS and/or processing have not accounted for these movements.

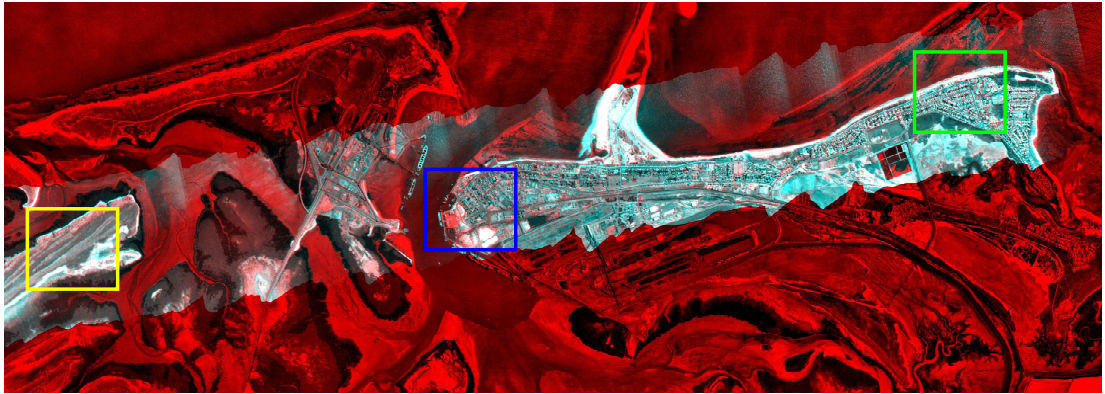


Figure 71: 1 metre resolution ortho photo (red) overlaid with geographically-located HyMap image (cyan). Yellow, blue and green boxes show enlarged regions in the figure below.



Figure 72: Selected areas at the ends and middle of the flight line enlarged for clarity. Areas of white, black and grey are where the HyMap imagery agrees with the orthophotograph. Areas in red show the correct location and areas in light blue/cyan show displacement between the orthophotograph and the geographically-located HyMap imagery.

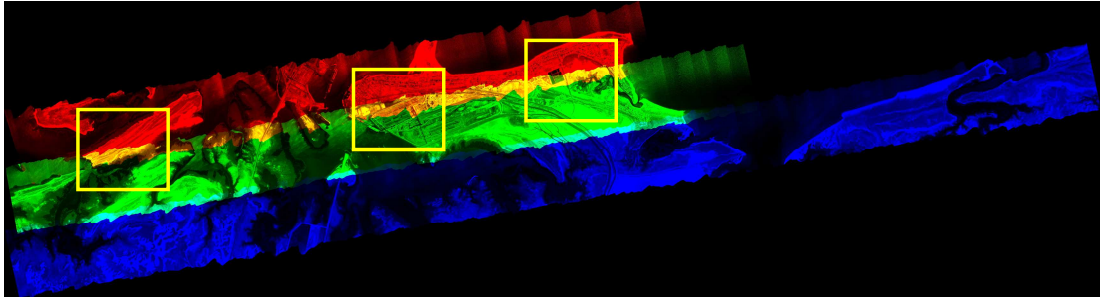


Figure 73: Three adjacent flight lines shown in red, green and blue. The overlap areas appear as yellow and cyan. The yellow boxes show enlarged regions in the figure below.



Figure 74: Selected areas at the ends and middle of the flight line enlarged for clarity. Areas in yellow show agreement between the flight lines whereas areas of red or green show displacements between flight lines.

Table 10 summarises the results of the comparison between the 2006 data and the historical data preceding 2006 to determine the geo-location accuracies of the other datasets. Note that only datasets that were processed with INS GPS information were analysed. The 1998 and 1999 datasets were not tested as they were geographically located using manual selections of control points between the orthophotograph and the imagery. Table 10 shows that the historical airborne hyperspectral data were up to ± 5 pixels displaced from the 2006 data and that the displacement were unequal in size and direction across the image. The results indicate that if data from 2002, April 2004 and December 2004 were to be compared with the 2006 data, the location of sites may be offset by up to ± 15 metres.

Location	2005	Dec 2004	Apr 2004	2002
1	1N	1S	4NE	3N
2	1N	5NE	5E	5NW
3	1S	4E	4E	4NW
4	2W	2W	0	1NW
5	1W	0	0	2NW
6	3SW	2S	1NE	2N
7	1W	2S	1SW	2NE

Table 10: Pixel displacements from 2006 dataset to historical HyMap dataset.

SITES		AREA-BASED MATCHING		FEATURE-BASED MATCHING	
Reference	Uncorrected image	Total selected	Correctly identified	Total selected	Correctly identified
2006 PH	2005 PH	17	9	8	0
1m ortho photo	2006 PH	12	3		

Table 11: Results of the evaluation of ENVI's automatic co-registration software. PH= Port Hedland

Table 11 shows the tie points generated from the use of the area-based matching together with the feature-based matching. After the tie points were automatically generated they were visually checked to determine their accuracy. These results are also summarised on Table 11. The results indicate that the area-based matching is able to generate more tie points and the points found are more accurate. However, only up to half the points found were correct which indicate that the software may not be applicable at this stage.

Notwithstanding that there are geographic location issues with the dataset acquired in Port Hedland, difference maps were generated from them to demonstrate the possibilities for multi-temporal monitoring. Interpretations of the changes were performed where spatially coherent changes are observed over areas larger than 10 pixels. Figure 75 shows the difference in dust levels between 1999 and 1998. The 1998 data were acquired at the end of the dry season where the total accumulation of dust over that season was mapped by the hyperspectral data while the 1999 data was acquired just two weeks after a cyclone. The colour coding ranges from purple to red where purple denotes a decrease of $<5 \text{ g/m}^2$ in 1999 when compared with 1998 and red denotes an increase of $>5 \text{ g/m}^2$ in 1999 when compared with 1998. The map indicates an overall decrease in dust level in 1999 when compared with 1998. This result confirms anecdotal observations made by environmental practitioners that heavy rainfall washes off the dust.

Figure 76 shows the difference in dust levels between 2002 and 2004. Note the change in colour coding for the dust levels for the maps and others following it. The colour coding is such that cool colours (starting with dark blue) denote decreased levels in 2004 when compared with 2002 and hot colours (ending with red) are increased levels. The map indicates that there was a small overall decrease in the dust levels of dust between 2002 and 2004 with the largest decrease observable around the fringes closest to the Port facility at Burgess Point and Finucane Island (location indicated on Figure 59). Outside of this fringe, there is also a slight decrease in the level of dust. However, this decrease is within the average dust levels measured on leaves collected at the control, non-dusty sites. The rainfall data

together with the monthly and yearly throughput as well as the total tonnages from the first major rain event to the date of the data acquisition are plotted on Figure 85 to assist in understanding the cause of the decrease. When comparing the yearly tonnage throughput between 2002 (red broken lines) and 2004 (green broken lines), the increase between the two years was approximately 27%. However, to better understand the dust levels mapped on the imagery, an alternative method for determining the accumulation of dust seen, is to calculate the amount from the first major rain event to the time of the data acquisition. Previous studies indicate that a heavy rain event has the ability to wash much of the dust off the mangroves. If this is taken into consideration then it can be assumed that dust accumulation began after the first major rainfall and continued to the date of the airborne data acquisition. With this assumption the increase in tonnage is 171% between 2002 (red solid line in Figure 85) and 2004 (green solid line in Figure 85). This figure is much higher than the yearly increase because the first heavy rain was much later in 2002 (red columns in Figure 85), occurring in June compared to February in 2004 (green columns Figure 85). Therefore, the overall trend of decrease in the dust levels is recorded despite an increase of tonnage throughput at the Port facilities from 2002 to 2004. Furthermore, the total rainfall in 2004 is larger than those for 2002. An explanation for the decrease in dust levels may be attributed to the continual improvement of the dust suppression system implemented between 2002 and 2004.

Figure 77 shows the difference in dust levels between 2004 and 2005. Again, on the regional scale the data indicate that little differences were recorded between the two years except for an increase found on the top right hand corner (red patch) which may be attributed to dusting on the sewerage treatment area. On the local scale, a small reduction in dust levels was recorded around the fringes closest to the handling facility at Burgess Point (Figure 80) and Finucane Island (Figure 81). Outside of this fringe, the differences in dust levels are within the background levels as previously indicated from measurements at non-dusty control sites. Examining Figure 85 shows that the tonnage throughput of iron ore at Port Hedland over the whole year (blue broken lines) increased by 15% when compared to 2004 (green broken lines). If the dust level is considered to have accumulated between the first significant

rainfall and date of data acquisition, then the throughput in that period decreased to 49% of the previous year's level (ratio between blue solid line and green solid line). This may account for the reduction seen surrounding the Port facility. However, it must be noted that 2005 was a very dry year with the heaviest rainfall being half that of the previous year and hence, the residual dust or the base level of dust on the mangroves in 2005 would be higher than in 2004.

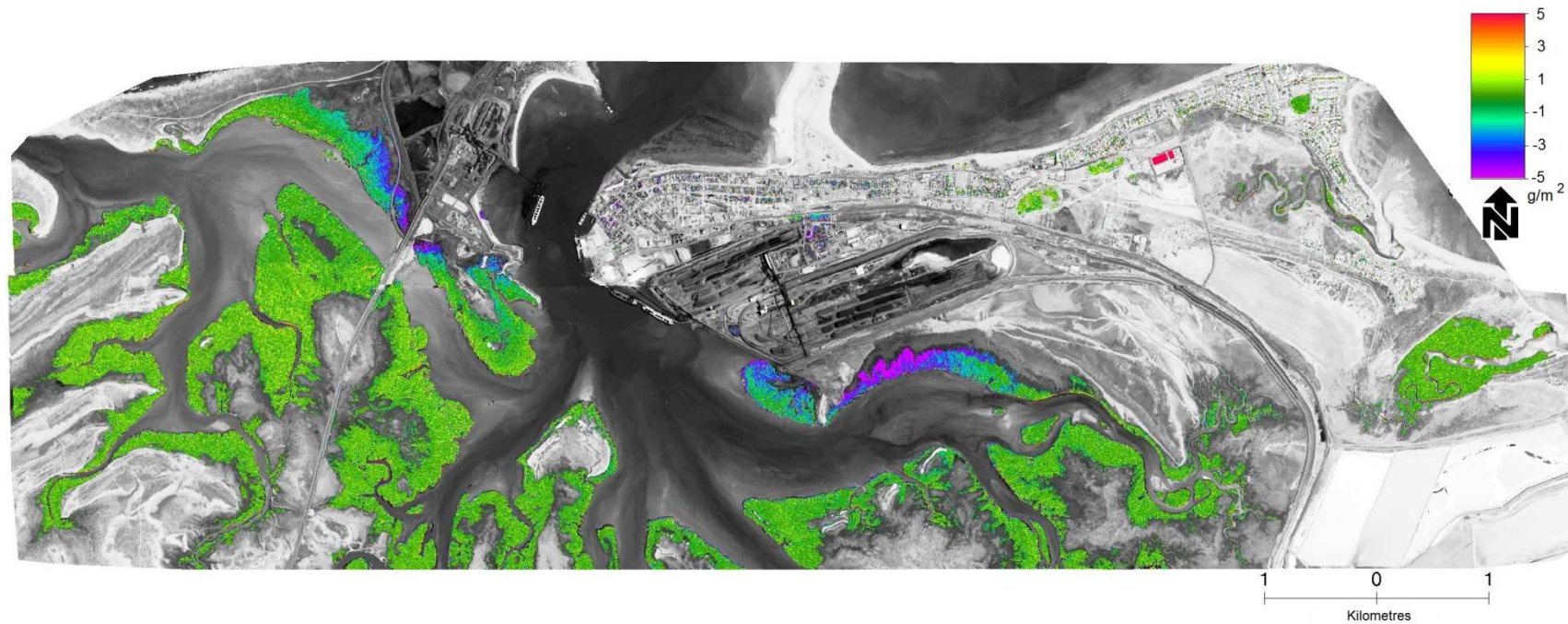


Figure 75: Change map of dust levels on mangroves and other vegetation surrounding Port Hedland harbour derived from airborne hyperspectral data. The difference between dust levels generated from airborne hyperspectral data acquired on 13th April 1999 and 13th November 1998 is shown. The colour coding is such that cool colours (starting with purple) denote decreased levels in 1999 when compared with 1998 and hot colours (ending with red) are increased levels. The dust measurements are in units of g/m^2 .

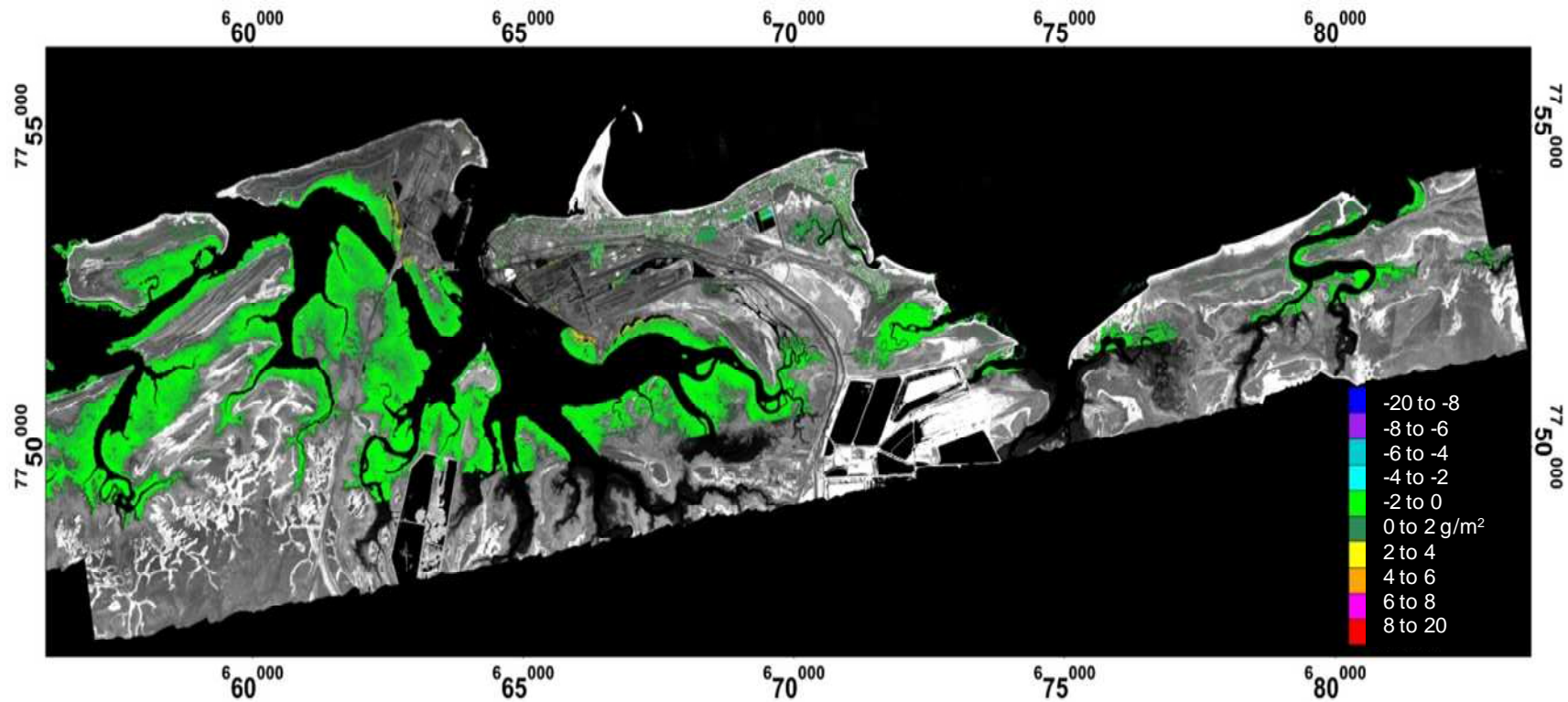


Figure 76: Change map of dust levels on mangroves and other vegetation surrounding Port Hedland harbour derived from airborne hyperspectral data. The difference between dust levels generated from airborne hyperspectral data acquired on 4th December 2004 and 20th October 2002 is shown. The colour coding is such that cool colours (starting with dark blue) denote decreased levels in 2004 when compared with 2002 and hot colours (ending with red) are increased levels. The dust measurements are in units of g/m.²

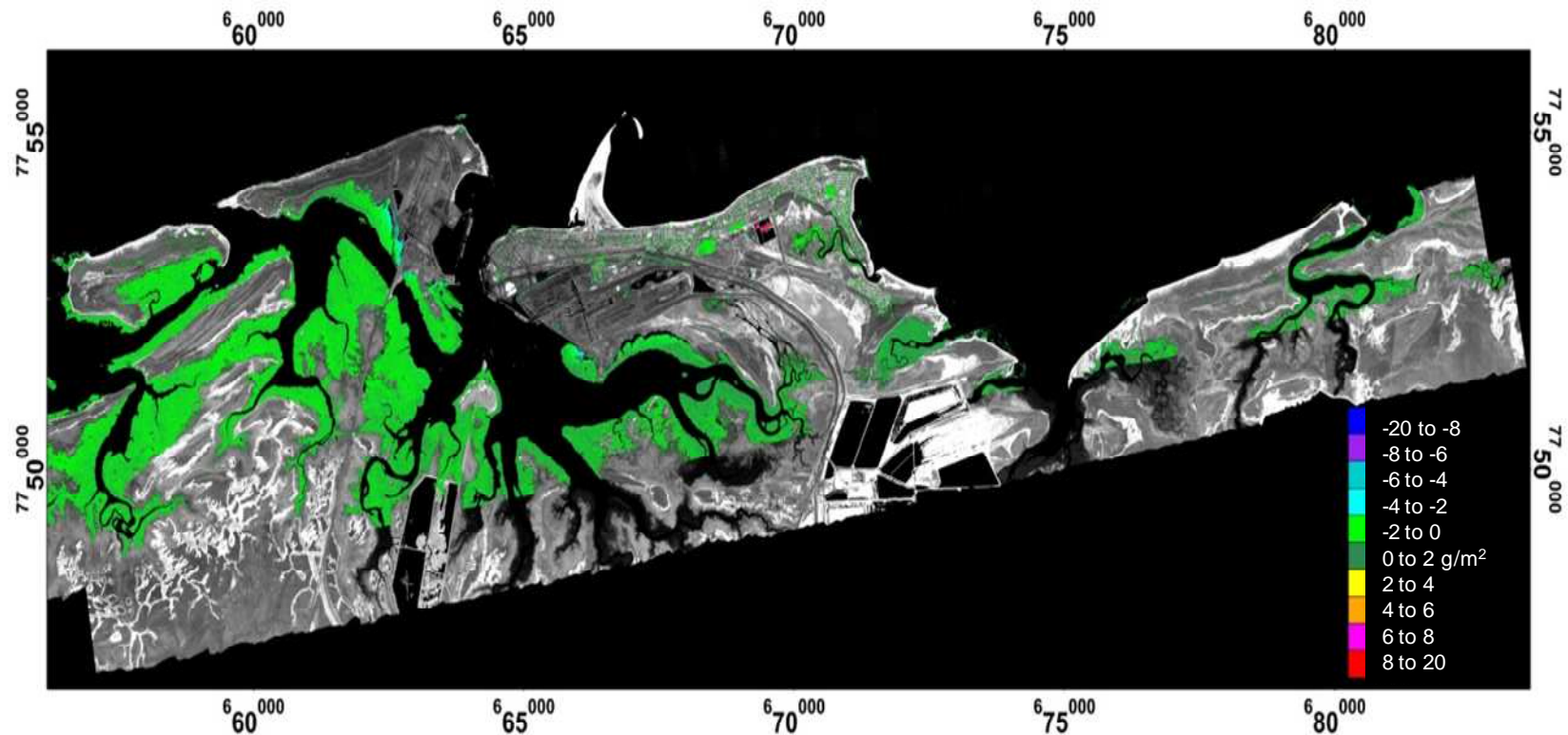


Figure 77: Change map of dust levels on mangroves and other vegetation surrounding Port Hedland harbour derived from airborne hyperspectral data. The difference between dust levels generated from airborne hyperspectral data acquired on 21st November 2005 and 4th December 2004 is shown. The colour coding is such that cool colours (starting with dark blue) denote decreased levels in 2005 when compared with 2004 and hot colours (ending with red) are increased levels. The dust measurements are in units of g/m².

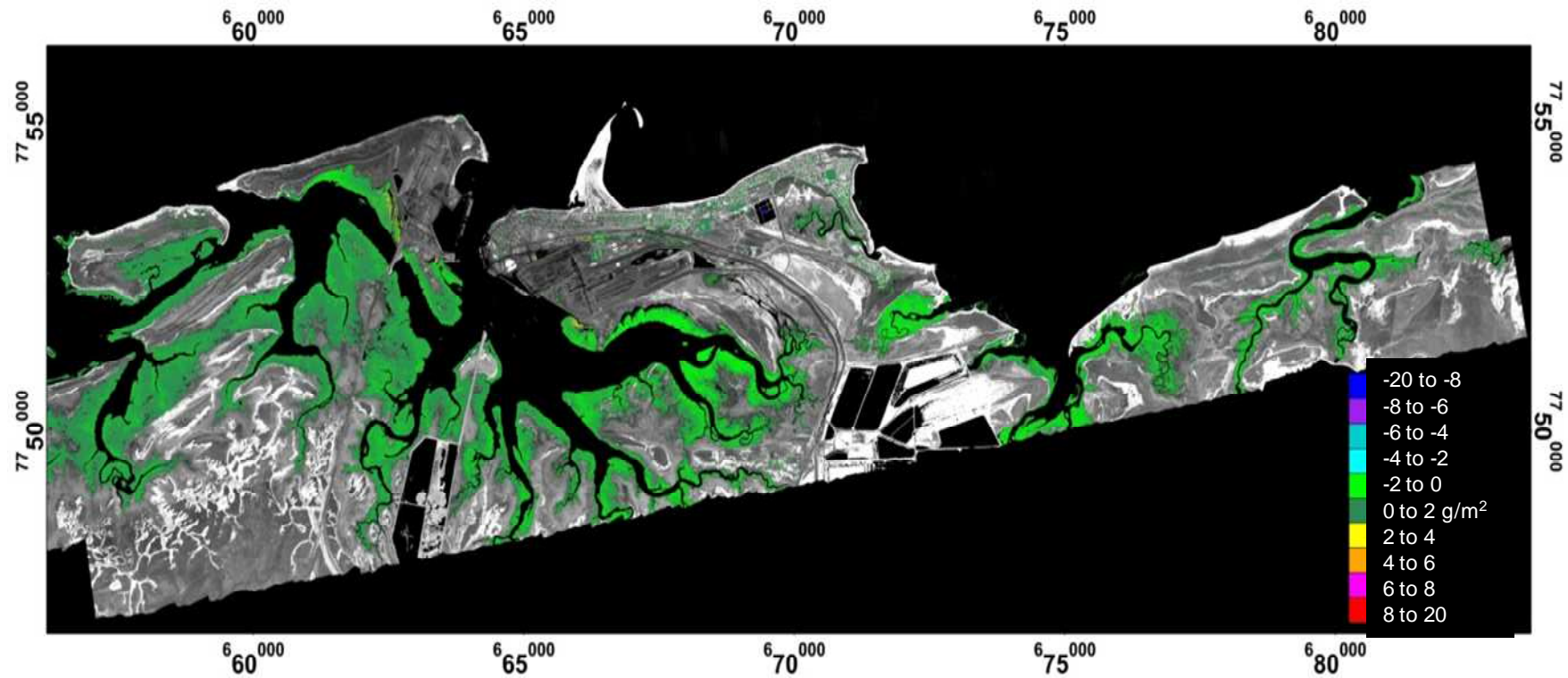


Figure 78: Change map of dust levels on mangroves and other vegetation surrounding Port Hedland harbour derived from airborne hyperspectral data. The difference between dust levels generated from airborne hyperspectral data acquired on 24th August 2006 and 21st November 2005 is shown. The colour coding is such that cool colours (starting with dark blue) denote decreased levels in 2006 when compared with 2005 and hot colours (ending with red) are increased levels. The dust measurements are in units of g/m².

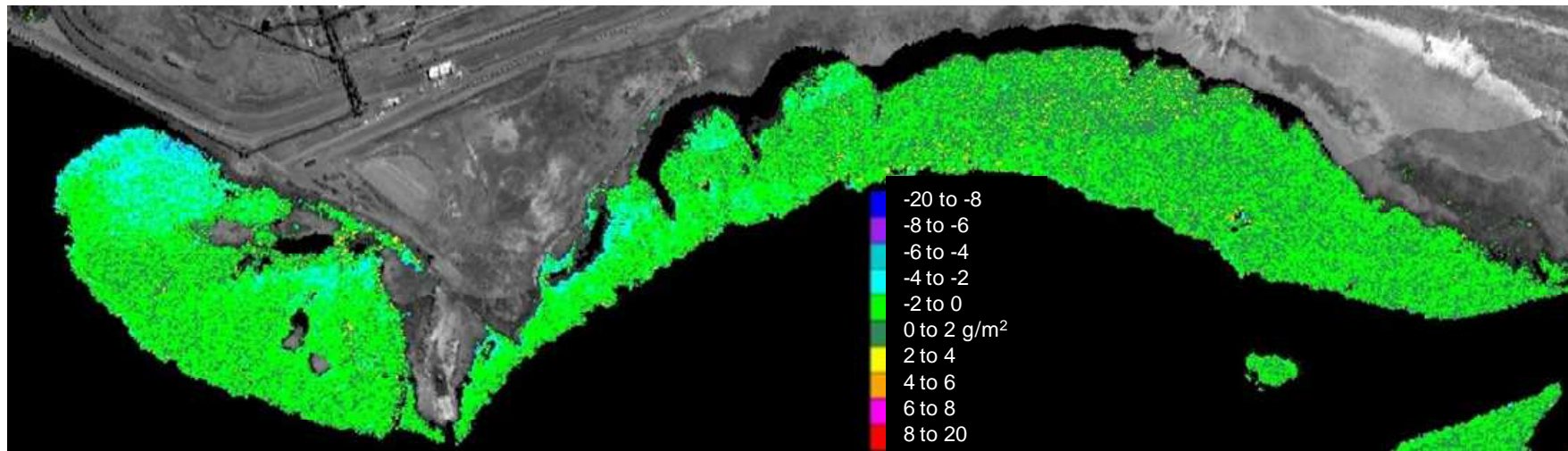


Figure 79: Change map of dust levels on mangroves and other vegetation surrounding Burgess Point derived from airborne hyperspectral data. The difference between dust levels generated from airborne hyperspectral data acquired on 4th December 2004 and 20th October 2002 is shown. The colour coding is such that cool colours (starting with dark blue) denote decreased levels in 2004 when compared with 2002 and hot colours (ending with red) are increased levels. The dust measurements are in units of g/m^2 .

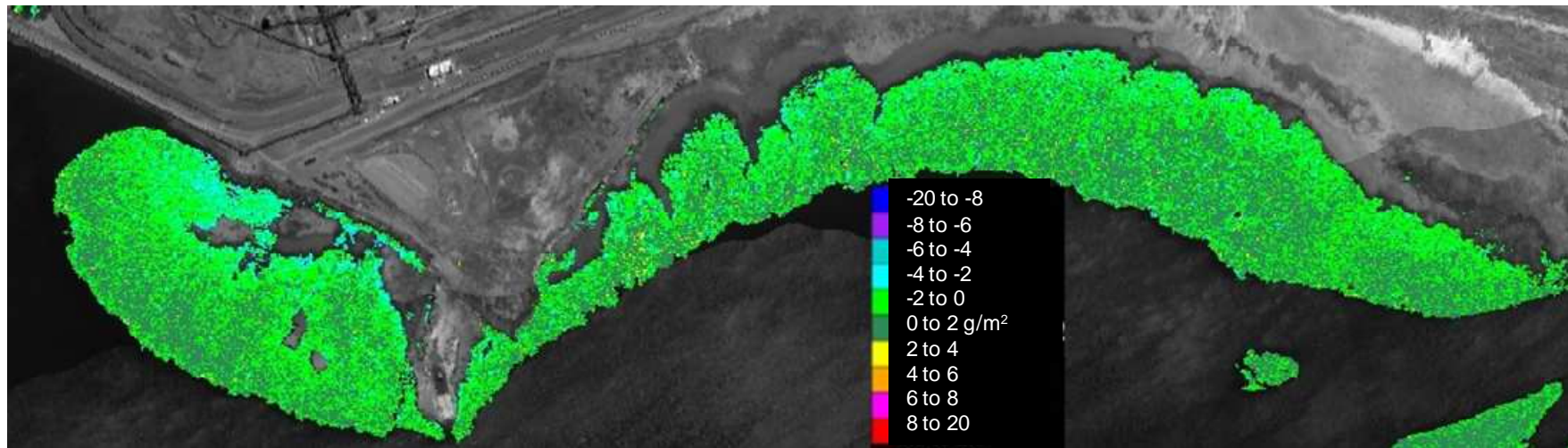


Figure 80: Change map of dust levels on mangroves and other vegetation surrounding Burgess Point derived from airborne hyperspectral data. The difference between dust levels generated from airborne hyperspectral data acquired on 21st November 2005 and 4th December 2004 is shown. The colour coding is such that cool colours (starting with dark blue) denote decreased levels in 2005 when compared with 2004 and hot colours (ending with red) are increased levels. The dust measurements are in units of g/m^2 .

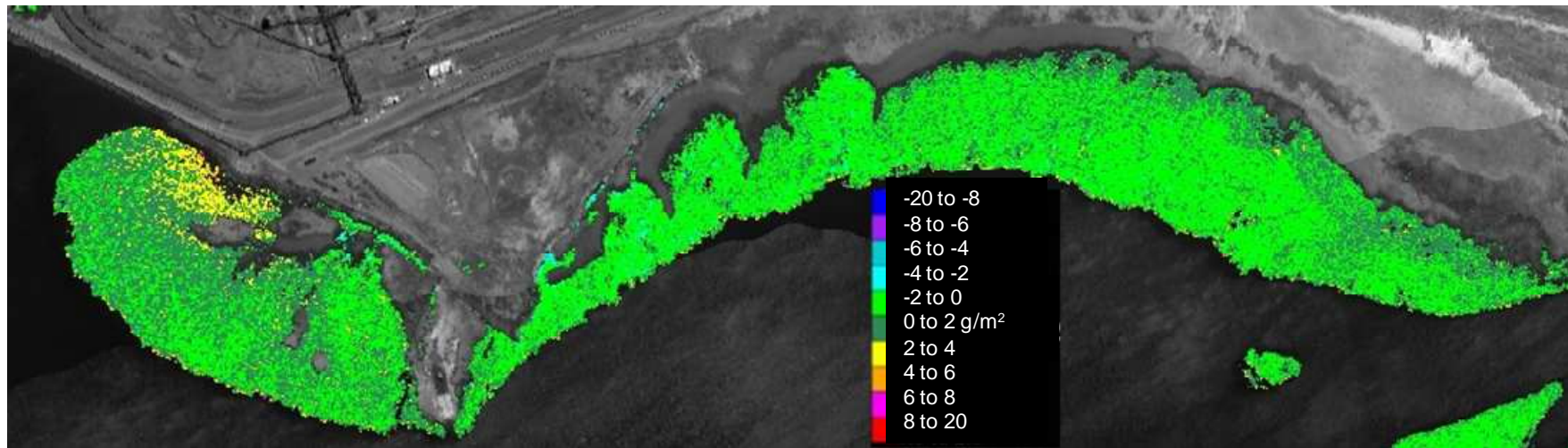


Figure 81: Change map of dust levels on mangroves and other vegetation surrounding Burgess Point derived from airborne hyperspectral data. The difference between dust levels generated from airborne hyperspectral data acquired on 24th August 2006 and 21st November 2005 is shown. The colour coding is such that cool colours (starting with dark blue) denote decreased levels in 2006 when compared with 2005 and hot colours (ending with red) are increased levels. The dust measurements are in units of g/m^2 .

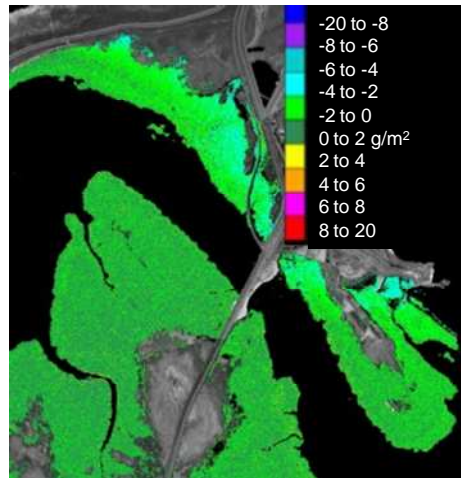


Figure 82: Change map of dust levels on mangroves and other vegetation surrounding Funicane Island derived from airborne hyperspectral data showing the difference in dust levels between 4.12.2004 and 20.10.2002. The colour coding is such that cool colours (starting with dark blue) denote decreased levels in 2004 when compared with 2002 and hot colours (ending with red) are increased levels. The dust measurements are in units of g/m^2 .

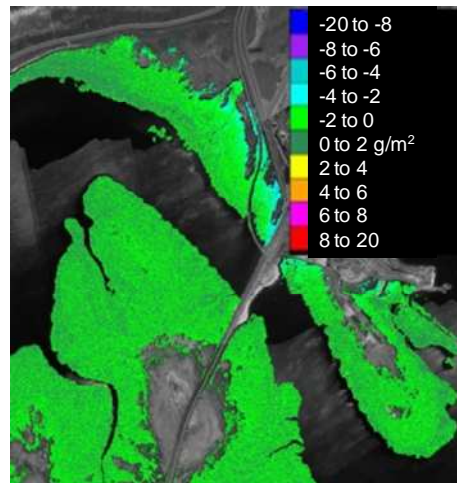


Figure 83: Change map of dust levels on mangroves and other vegetation surrounding Funicane Island derived from airborne hyperspectral data showing the difference in dust levels between 21.11.2005 and 4.12.2004. The colour coding is such that cool colours (starting with dark blue) denote decreased levels in 2005 when compared with 2004 and hot colours (ending with red) are increased levels. The dust measurements are in units of g/m^2 .

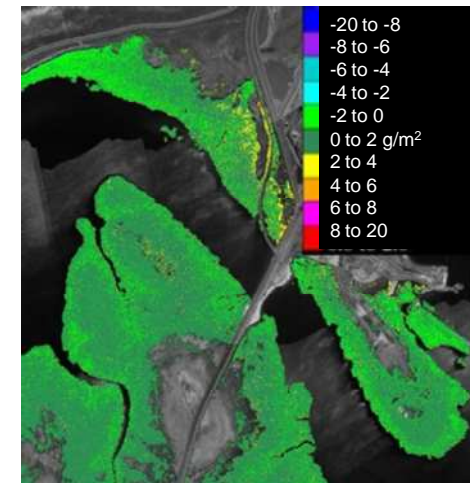


Figure 84: Change map of dust levels on mangroves and other vegetation surrounding Funicane Island derived from airborne hyperspectral data showing the difference in dust levels between 24.8.2006 and 21.11.2005 is shown. The colour coding is such that cool colours (starting with dark blue) denote decreased levels in 2006 when compared with 2005 and hot colours (ending with red) are increased levels. The dust measurements are in units of g/m^2 .

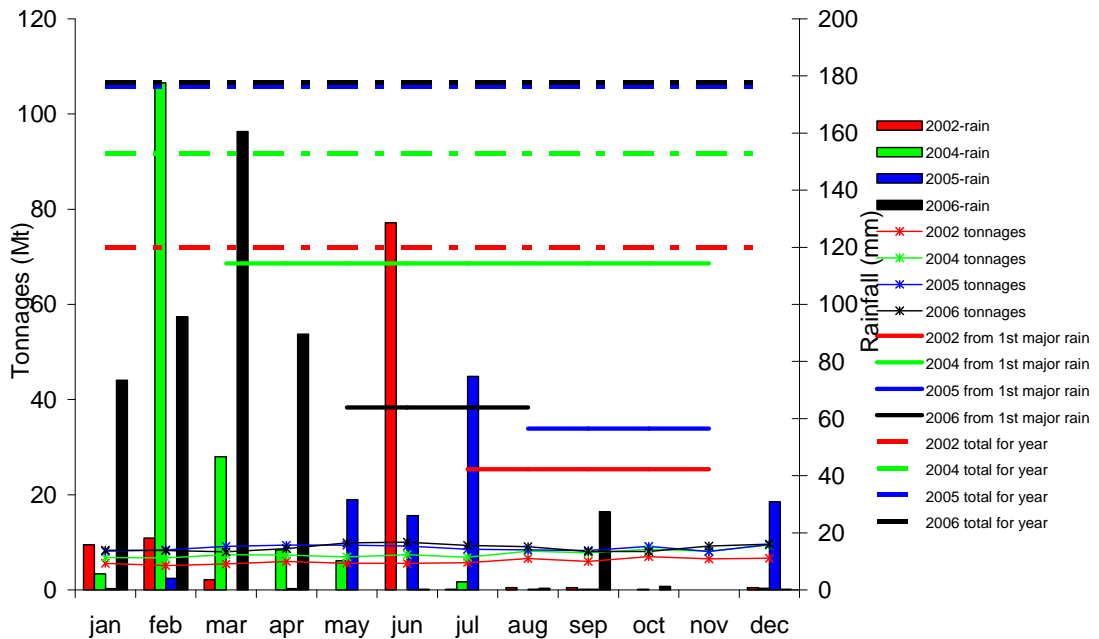


Figure 85: The columns show the rainfall data. The line graph plots the monthly throughput. The broken horizontal lines show the total throughput and the solid horizontal lines depicts the total throughput from the first major rain event to the time of the data acquisition. The graphs are colour coded so that red represents 2002, green 2004, blue 2005 and black 2006. Note that the black broken line denoting the 2006 total for year is slightly overlapped with the blue broken lines denoting 2005 total for year.

Figure 78 maps the difference in dust levels between 2005 and 2006. Overall, the image indicates a trend of slight increase towards the west of the imagery surrounding Funicane Island and the construction site of the Fortescue Metals Group (FMG) facility. Towards the east of the imagery there appears to be a slight decrease. These trends are however, within the range of variability of the background dust levels.

Proximal to the handling facility there is a small increase that is concentrated on the fringes of mangroves surrounding the Port facilities at Burgess Point (Figure 81) and Funicane Island (Figure 84). Figure 85 shows that the total tonnages of material handled in the whole year for 2006 (black broken line) increased by 0.8% when compared to the previous year (blue broken line). If total tonnages resulting in the dust accumulation is considered to be from the first major rainfall to the time of the

data acquisition, then the tonnages increased by 13% between the two years (black solid line compared to blue solid line). This could explain some of the increase seen around the fringe mangroves around Funicane Island and Burgess Point.

At Burgess Point, the increase affected a smaller area at Burgess Point where it was restricted to an area of approximately 1000 square metres. Beyond this area at Burgess Point, proximal to the handling facility, there is minimal difference and even a slight decrease seen at the fringes. Note that the increases/decreases seen between 2005 and 2006 may be larger in amplitude than those between 2002 and 2004. This is because, as previously explained, 2005 was a fairly dry year. In contrast, 2006 was a fairly wet year, with two consecutive months of heavy rainfall, one of which was close to twice that of 2005 and the other of the same level as 2005. This would leave the mangroves with a lower residual/base level of dust in 2006 than those of 2005. Years 2002 and 2004 on the other hand had comparable rainfall and hence most probably also comparable base levels of dust.

8.4 Summary

This chapter documented the results obtained from the assessments of new techniques available from a major data provider and image processing software to improve geographic location of airborne hyperspectral data and demonstrated the potential of using the data for multi-temporal monitoring.

The result of the analysis of HyVista's registration indicates that the geographical-location errors of the HyMap imagery may be up to ± 9 metres for data acquired at 3 metre pixel resolution. Further, there were also mismatches of up to ± 9 metres between flight lines and that the offsets may be different across the image.

Comparison of historical airborne hyperspectral data acquired preceding to 2006 with those acquired in 2006 found that the historical data were up to ± 15 metres displaced from the 2006 data and that the displacement were unequal in size and direction across the images.

The assessment of the software available from ENVI for automated geographic location of the hyperspectral indicated that the area based matching is able to generate more tie points and the points found are more accurate. However, only up to half the points found were correct which indicate that the software may not be applicable at this stage.

Difference maps calculated from the dust maps for Port Hedland demonstrated the potential use of the approach using airborne hyperspectral data for multi-temporal monitoring. The data were able to indicate the effects of seasonal impacts such as cyclonic events. Comparisons of data obtained at similar periods each year demonstrate the possible results of dust suppression in reducing the dust levels as well as the impact of infrastructure development in increasing the dust levels.

Chapter 9

CONCLUSION AND THE IMPLICATIONS OF STUDY FOR MINE ENVIRONMENTAL MONITORING

The mining industry in Australia are constrained by regulatory requirements to demonstrate that the environments surrounding mines and mining infrastructures are not adversely impacted by exploration and mining. The gathering of quantitative environmental measurements/data is a key component required to support environmental management and policies. Quantitative data are required for various purposes including determining baseline environmental conditions before the commencement of mining, routine monitoring and evaluation of status of the environment after closure of the mine and/or infrastructures.

Hyperspectral remote sensing provides calibrated data which can be applied to provide quantitative and spatially-comprehensive environmental data on a routine basis. This study sought to address the main impediments to their use for mining-related environmental assessment and monitoring which were:

- 1) The scarcity of published information on the spectral behaviour of environmental properties;
- 2) The lack of associated models to transform spectral data to environmental measurements; and,
- 3) the paucity of case histories demonstrating the ability to produce accurate and repeatable measurements from remotely-sensed hyperspectral data on a

multi-temporal basis especially for monitoring environmental conditions associated with mining activities.

This study undertook to demonstrate the potential use of hyperspectral remote sensing for monitoring two of Australia's major environmental concerns, namely dust and acid mine drainage. The test sites were located at Port Hedland in Western Australia, the world's largest bulk export port (PHPA, 2011) and Brukunga in South Australia, one of the major sites impacted by acid mine drainage.

Experimental studies provided an understanding of the spectral characteristics of the material required to be measured, changes in their spectral behaviour with variations in the environmental parameters and other factors that may influence the spectral behaviour. In the case of the dust case history, it was found that the spectra are significantly related to dust levels and that the drivers of the correlations are predominantly related to ferric iron oxide. Further, the study found a significant linear relationship between the ferric iron oxide crystal field absorption features and the dust levels. A spectral algorithm relating the depth of the CFA and ferric iron oxide dust level was developed with a standard error of 2.98 g/m². Validation of the dust algorithm found that it was appropriate for at least two species of mangrove. This has implications for other vegetation as the algorithm may also be applicable for other mangroves and possibly other species.

The laboratory study for the pH case study found a good general linear trend (at R²=0.58 and a relatively low RMSE of 0.91) between pH measured using laboratory analysis and pH predicted using spectral data. The RPD of 1.53 indicate that the model generated from the PLS analysis may be able to provide satisfactory accuracies for the prediction of pH values from spectral data. The diagnostic spectral features responsible for the relationship was found to be specific to secondary iron minerals indicating that the predictive algorithm for pH resulting from the PLS analysis may be transferable to other spectral datasets to provide pH measurements.

Remotely-sensed spectral data may be afflicted with issues ranging from atmospheric contamination to instrument aberrations which must be accounted for in order to provide accurate maps when spectral algorithms developed in the laboratory are transferred to these data. The study found that care must be taken in the acquisition and processing of the remotely-sensed hyperspectral data to minimise the uncertainties that may potentially compromise the resulting maps. Here, I found that for a dataset similar to the one acquired in Port Hedland in 2006 for the purpose of dust monitoring, the use of MODTRAN radiative transfer modelling, wavelength recalibration and incorporation of vicarious calibration data from ground calibration targets to minimise the residual atmospheric effects are necessary. Without proper processing the uncertainty when using those data for the measurement of ferric iron oxide dust level may be up to $\pm 3.26 \text{ g/m}^2$.

The results also indicated that instrument calibration is significant for achieving accurate results as wavelength miscalibrations of only 2.1, 0.7, 0.4 and 2.1 nm respectively for each of the instruments can translated to a downstream impact of increasing the uncertainties by up to 34%. Further, the changes in the instrument calibration may introduce uncertainties ranging from ± 0.06 to $\pm 1.69 \text{ g/m}^2$ based on the differences in bandwidths and bandpasses between 2006 and 1998 to 2005. Further, inter-year comparisons of all the airborne datasets indicated that the HyMap2 sensor was stable but HyMap1 sensor contained miscalibrations in the SWIR detectors.

The analysis of the BRDF behaviours and assessment of the region for minimising BRDF impact on the prediction of dust levels indicates that the optimum region where BRDF is wavelength-independent and multiplicative is the region between 760 and 1000 nm. This is also related to the 900 nm ferric iron oxide CFA and indicates that dust maps generated from the depth of the 900 nm ferric iron oxide CFA from two adjacent flight lines will provide seamless mosaics with multiple adjacent flight lines.

The accuracy of the geographic location of the maps is another crucial element for multi-temporal monitoring. Assessments were performed on HyMap imagery data

acquired in 2006 acquired at 3 metre pixel resolution. I found that navigation errors of up to ± 9 metres were to be expected and there can also be mismatches of up to ± 9 metres between flight lines with differential offsets across the image. Furthermore, differential displacements up to ± 15 metres may be expected when using historical data preceding 2006. Therefore, if these historical datasets were compared with the current data, the geographic location uncertainties may be up to ± 17.49 metres.

The application of the spectral algorithms developed in the laboratory using airborne hyperspectral data provided maps which demonstrated the ability of remotely-sensed hyperspectral data to provide quantitative and spatially-comprehensive measurement of the environmental variable of interest.

The ferric iron oxide dust maps provided a global view of the distribution of dust across the handling facility. The five years of data analysed consistently indicated that the greatest dust impact was in close proximity to the handling facility at Burgess Point and Finucane Island with the levels decreasing with increasing distance from these facilities. The images indicated that most of the atmospheric dust had precipitated out less than 5 kilometres from the source. All the dust maps created from the airborne data in all years were seamless (despite some of the datasets impacted by BRDF effects) confirming that monitoring can be quantitatively undertaken with these multi-temporal datasets. Further, validation of the dust maps indicated that spectral data can be used to reliably produce ferric iron oxide distribution dust maps and the uncertainty in the dust maps were calculated as ± 2.36 g/m². Difference maps calculated from the dust maps indicated that seasonal impacts, such as cyclonic events, can reduce the dust levels and demonstrated the possible results of dust suppression in reducing the dust levels as well as the contrasting impact of infrastructure expansion in increasing the dust levels.

The study found that mineral maps produced using Tetracorder in the SWIR region are generally consistent across a multi-temporal series of data collected over the four year period. However, for the application of acid drainage monitoring, SWIR mapping may not be sufficient as it was found, from an associated study, that this spectral region is not as significant as the VNIR region for mapping the secondary

minerals crucial for determining acid drainage conditions (Swayze et al., 2000). In the VNIR region, Tetracorder was able to produce consistent maps for three of the four years. The reasons for the one outlier may be attributed to environmental changes, pre-processing or instrument calibration. It is not possible to conclude which of these are contributing factors as field verification was not performed for all acquisitions. However, validation performed with data acquired in 1999 showed that Tetracorder mapping of AD minerals is 70.1% accurate.

The pH maps produced from the airborne hyperspectral data acquired from 1998 to 2001 are consistent between the years where the ranges of pH levels mapped at the mine area were consistently mapped between three and five which is in close agreement with water pH data collected downstream of the mine for those years (Randall and Cox, 2003). The inconsistencies that do exist can be related to the low signal in the data resulting in the inability to map some areas in the 1998 and 1999 data. This highlights the importance of flight planning to ensure that optimal data are acquired.

The comparison of the datasets between years demonstrated the potential to use these maps to better understand the progress of rehabilitation efforts or to pinpoint areas on which to concentrate efforts. For example, the areas of pH 2-3 around the waste rock dumps and some of the benches of the mine which are larger in the 2000 and 2001 data when compared to 1998 and 1999 which may indicate areas that require further attention. Validation of the 2001 pH map indicates that pH can be reliably predicted using airborne hyperspectral data as evidenced by a good general linear trend between the predicted and measured data at R^2 of 0.72, RPD of 1.96 and a relatively low RMSE of 0.57.

This study has demonstrated the application of remotely-sensed hyperspectral data for multi-temporal monitoring for two significant environmental issues in mining. It showed that the technology is clearly beneficial by providing spatially-comprehensive and quantitative measurements thereby filling the gaps of current methods.

The method developed for monitoring ferric iron oxide dust is expected to make a significant contribution to the monitoring of dust at port facilities, transportation routes, mines and other areas where dust is impacting on the environment. The method has already been recognised by government regulators and the mineral industry with the Golden Gecko (CSIRO, 2004) and WA Government Environment Air Quality (DEC, 2004) Awards. For future applications, the laboratory validation indicates that it is likely that the method will be directly transferable to at least 7 ports around WA where iron ore is exported. This includes Esperance where mass bird deaths were found in 2006 and where there are still ongoing concerns. Although the issues at Esperance relates to lead carbonate dust, the method developed is still relevant as one of the facilities is used for exporting iron ore.

The relevance of the pH and mineral mapping study is demonstrated by the fact that the approach and pH algorithm was adopted for the processing of airborne data acquired for an EU study to assess the use of remotely-sensed data to monitor and understand the risk of mine waste in support of the EU Mine Waste Directive (EC, 2006).

The protocols developed for the processing of the airborne data is generic for any application and it is anticipated that such a guide will be useful to others wishing to employ hyperspectral sensing for quantitative measurements. This will become more relevant in the near future when the technology become more accessible with more commercial operators in the market place following the availability of off-the-shelf systems (Skauli et al., 2010, SpecIM, 2011) and the launch of future satellites projected in the next five years (Ogawa et al., 2011, Stuffer et al., 2009).

When the use of hyperspectral remote sensing is accepted as routine practice, I believe that the quantification of errors performed for this study will make an important contribution as it is likely that a statement of expected accuracy, stability and resolution (time, space) of the product, including, where possible, a comparison with the requirements stated in the Satellite Supplement (or any subsequent revision) will be required as shown by the requirements of climate data (WMO, 2009).

I would expect that in the next 5 to 10 years, the application of hyperspectral remote sensing for environmental management would be in a similar position as multispectral remote sensing is currently where 57% of the nation's earth observation programs are dependent on Landsat TM and 37% on MODIS (GA, 2010). The benefits of this study will be realised when this happens.

APPENDICES

A.1 A recipe for the environmental practitioner

If you are like any of the environmental practitioners that I know, you probably will have little time to read a long thesis. Therefore, I am writing this chapter as a recipe or a quick reference guide to assist you in you're planning to incorporate hyperspectral remote sensing in your work. The recipe is also summarised in a diagrammatic form on Figure 86.

Preparation

Before you order remotely-sensed data, there are a few background considerations. Firstly, clearly define the environmental issue and the environmental parameter that you will use to monitor the condition. For example, the environmental issue at Port Hedland was dust contamination possibly causing detrimental effects on mangroves and, the parameter that was required by BHPBIO to monitor impact was levels of iron ore-derived dust on mangroves. If possible, identify the current techniques used to make the environmental measurements. Some questions that you may want to consider include: is positive identification of the parameter required such as the case of the composition of the dust and that it is on vegetation or is it sufficient to be able to detect a surrogate of the quantity of interest? This is important as some environmental contaminants cannot be detected using hyperspectral sensing – only materials which possess spectrally diagnostic features can be positively identified.

Secondly, check if any method has been developed/published for the application. If not, consider a tiered laboratory experiment where firstly a small set of samples representative of the ranges expected for the environmental parameter will be measured with a spectrometer. If diagnostic spectral signature(s) relevant for the environmental parameter is/are found then consider a more comprehensive experiment where a complete set of samples representative of the range of values expected for the site are to be measured. Concurrent with these spectral

measurements, acquire independent measurements (eg. weight of dust deposited on leaf samples) which will be used for calibration of the spectral algorithm as well as validation.

Thirdly, after you have completed the laboratory experiment, consider using a statistical analysis package such as Partial Least Square (see section 3.5.1 for more information) to study the relationship between the environmental parameter and the spectral measurements. If you are intending on transferring the predictive algorithm directly to another set of spectral data then consider the quality of the data that will be transferred to. For example, will there be complications such as sky/scene brightness variations which will compromise the results? Also, note that the algorithm is most likely only applicable for the site (or sites with similar meteorological conditions, geographic setting, ecosystem, etc.) where the calibration data have been acquired.

Lastly, consider the scale at which you require to monitor the environmental variable of interest. That is, do you need to understand the impact on every leaf on a single tree or will you be required to manage the impact on the whole catchment? This spatial scale will determine which platform to use. If the platform chosen is either satellite or airborne then the following recipe will guide you with the selection and processing of the data.

Ingredients:

For the acquisition

Clear skies (less than 10% cloud and cloud shadow, no anomalous atmospheric dust loading, no haze, no smoke)

No rain during and at least 7 days preceding acquisition

Low wind conditions

Sun elevation angle higher than 30° sun elevation (and not less than 60° if over water)

Sun in front or behind the flight line (if airborne)

Vicarious calibration targets being measured concurrently (at least 1 for checking and 1 for validation if possible)

Deploy or identify calibration targets and measure the spectral properties in the field preferably concurrent to the remote data acquisition.

For the sensor

Signal-to-noise-ratio (SNR) of better than 200:1 (relative to a 60% reflectance standard at mid-latitude summer atmospheric condition)

Wavelength accuracies of $\pm 1\text{nm}$ or better

Radiometric accuracies of $\pm 10\%$ or better

Sidelaps of more than 20%

Availability of most recent calibration record

For the processing

Atmospheric correction using radiative transfer modelling based on MODTRAN or equivalent with wavelength calibration capabilities.

PMN (see explanation and equation on section 3.5.3) or similar to check for BRDF (see explanation on Chapter 5)

Method

1. After delivery of data, check data for clouds, smoke, haze, side laps, data coverage and any possible aberrations in the data signal. Apply a standard analysis tool such as minimum noise fraction (MNF; (Green et al., 1998)) to check for noise in the data.
2. Apply atmospheric correction that incorporates radiative transfer modelling with MODTRAN or equivalent and wavelength recalibration. Note that most

data providers will deliver up to this level of processing but please specify that no form of smoothing is to be applied to the spectral data. Use the data acquired from the vicarious calibration target to model the atmospheric residuals and determine if there are any radiometric calibration issues related to the sensor. Remove residual atmospheric effects using vicarious calibration measurements. Check results with an independent vicarious target.

3. Check for coherence between flight line. If mismatch occurs, apply PMN and assess the nature of the BRDF. If the BRDF is wavelength-dependent and not multiplicative, consider regions of the spectrum where a simple wavelength-independent, multiplicative correction may apply. Check if these regions are relevant for predicting the environmental parameter. Refine the algorithm to use only regions that are not affected by BRDF.
4. Apply the appropriate spectral algorithm to the remotely-sensed data. Check map for coherence between flight lines. Check map against validation data.

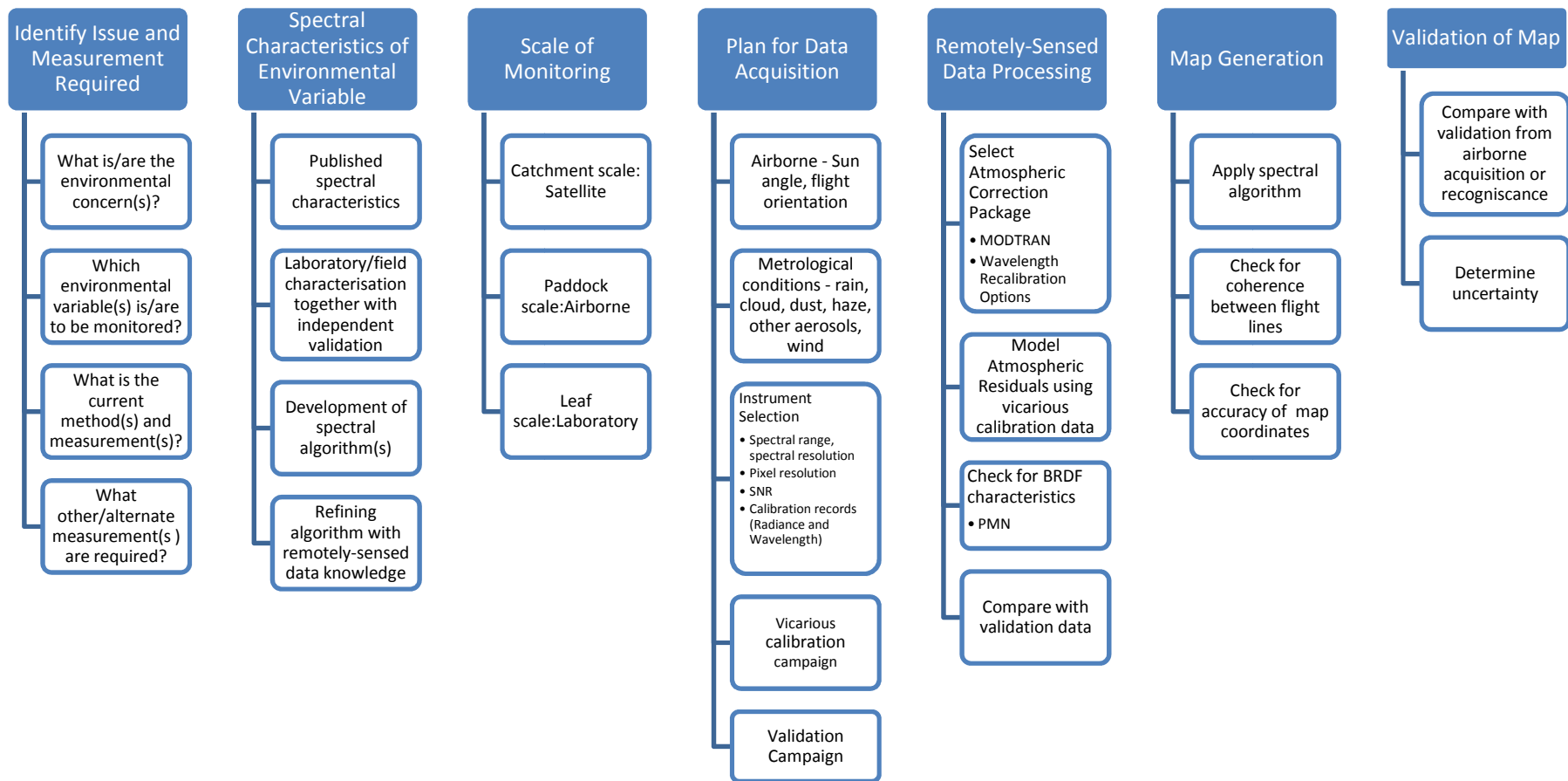


Figure 86: A recipe for the integration of hyperspectral data for environmental monitoring.

A.2 Methods and uncertainties in chemical analysis of Brukunga samples

PREP5	For samples up to 500 g in weight, the samples will be dried at a core temperature of approximately 100°C. The total sample will then be milled in an LM1 pulveriser to a nominal 90% passing 106 µm.
IC4	A 0.1 g subsample of the analytical pulp is fused with lithium metaborate followed by dissolution to give a “total solution”. The solution is presented to an ICPOES for the determination of elements of interest. Al ₂ O ₃ (0.01%) CaO(0.01%) K ₂ O(0.01%) Total Fe as Fe ₂ O ₃ (0.01%) MgO(0.01%) MnO(0.01%) Na ₂ O(0.01%) P ₂ O ₅ (0.01%) SiO ₂ (0.01%) TiO ₂ (0.01%) L.O.I.
IC4M	A 0.1 g subsample of the analytical pulp is fused with lithium metaborate followed by dissolution to give a “total solution”. The solution is presented to an ICPMS for the determination of elements of interest. Ag(1 ppm) As(15 ppm) Ba(10 ppm) Be(0.5 ppm) Bi(3 ppm) Cd(3 ppm) Co(15 ppm) Cs(3 ppm) Ga(1 ppm) Hf(1 ppm) In(0.5 ppm) Mo(2 ppm) Nb(15 ppm) Rb(0.5 ppm) Sb(1 ppm) Sn(10 ppm) Sr(5 ppm) Ta(2 ppm) Te(5 ppm) Tl(3 ppm) Th(0.5 ppm) U(0.5 ppm) V(5 ppm) W(3 ppm) Y(1 ppm) Zr(15 ppm)
IC3M	A subsample of up to 0.5 g of the analytical pulp is digested using an HF/multi acid digest and the solution is presented to an ICPMS for the quantification of the elements of interest. Range is to 0.1%. Some elements may be inappropriate due to mineralisation present. Ag(0.1 ppm) As(0.5 ppm) Bi(0.1 ppm) Cd(0.1 ppm) Cs(0.1 ppm) Ce(0.05 ppm) Co(0.2 ppm) Cu(0.5 ppm) Ga(0.1 ppm) In(0.05 ppm) La(0.05 ppm) Mo(0.1 ppm) Nb(0.5 ppm) Ni(2 ppm) Pb(0.5 ppm) Rb(0.1 ppm) Sb(0.5 ppm) Se(1 ppm) Sr(0.1 ppm) Te(0.2 ppm) Th(0.02 ppm) Tl(0.1 ppm) U(0.02 ppm) W(0.1 ppm) Y(0.05 ppm) Zn(0.5 ppm)
IC3R	Rare earth suite from IC3 digest with measurement by ICPMS. Ce(0.05 ppm) La(0.05 ppm) Dy(0.02 ppm) Er(0.05 ppm) Eu(0.02 ppm) Gd(0.05 ppm) Ho(0.02 ppm) Lu(0.02 ppm) Nd(0.02 ppm) Pr(0.05 ppm) Sm(0.02 ppm) Tb(0.02 ppm) Tm(0.05 ppm) Yb(0.05 ppm) Y(0.05 ppm)
SIE4	Solution is analysed by pH meter.
SIE6	Sample is extracted with a ratio of 1:5 in water, mixed for 1 hour and left to settle. Solution is presented to EC meter for determination of EC
LECO1	The sample is ignited at high temperature in a stream of oxygen. The resulting sulfur dioxide is measured by an infra-red detector using a LECO analyser. S(100 ppm)

Table 12: Methods and uncertainties of chemical analysis performed on the Brukunga samples taken from Amdel Labs.

A.3 Airborne data acquired over Brukunga

HyMap1 data were acquired over the Brukunga Mine on 3rd April 1998, that is, at the end of the dry summer period. The data were acquired at 5 m pixel resolution. Three additional datasets over the next three years were captured at the finer resolution of 3.5 m pixel with the HyMap1 sensor. Acquired on 9th April 1999, 21st March 2000 and 14th March 2001, all these data were acquired soon after the first major rainfall following the dry summer period.

A.3.1 Invariant target measurement at Brukunga

Most of the data for the Brukunga site was acquired opportunistically while the sensor was in the vicinity of the site. Therefore, it was not possible to collect ground spectral measurements concurrent with each overflight for the calibration and validation of these data. As a result, an iterative process was used to select the calibration/validation targets. The process is described below.

Firstly, to guide the selection of calibration/validation targets, the airborne data for all four dates were examined and potential sites were manually selected from inspections for invariance and statistics across the four dates. A total of 27 sites were initially selected and was narrowed to the final three through a process of elimination based on proximity to mine site, proximity to each other, ease of access, surrounding environments, local knowledge of the history of these sites to confirm their suitability for their size and homogeneous nature. Examinations of these targets on the airborne images reveal little changes over the four years. The three targets are located close to the State Training Centre, Pyrites Road, Brukunga SA 5252. They are next to each other and are approximately 20x20 metres each. The first target is a dark bitumised area shown on Figure 88 and Figure 89. The second target is an area covered with light concrete pavers as shown on Figure 90 and Figure 91. The third target consists of light concrete as shown on Figure 92 and Figure 93.

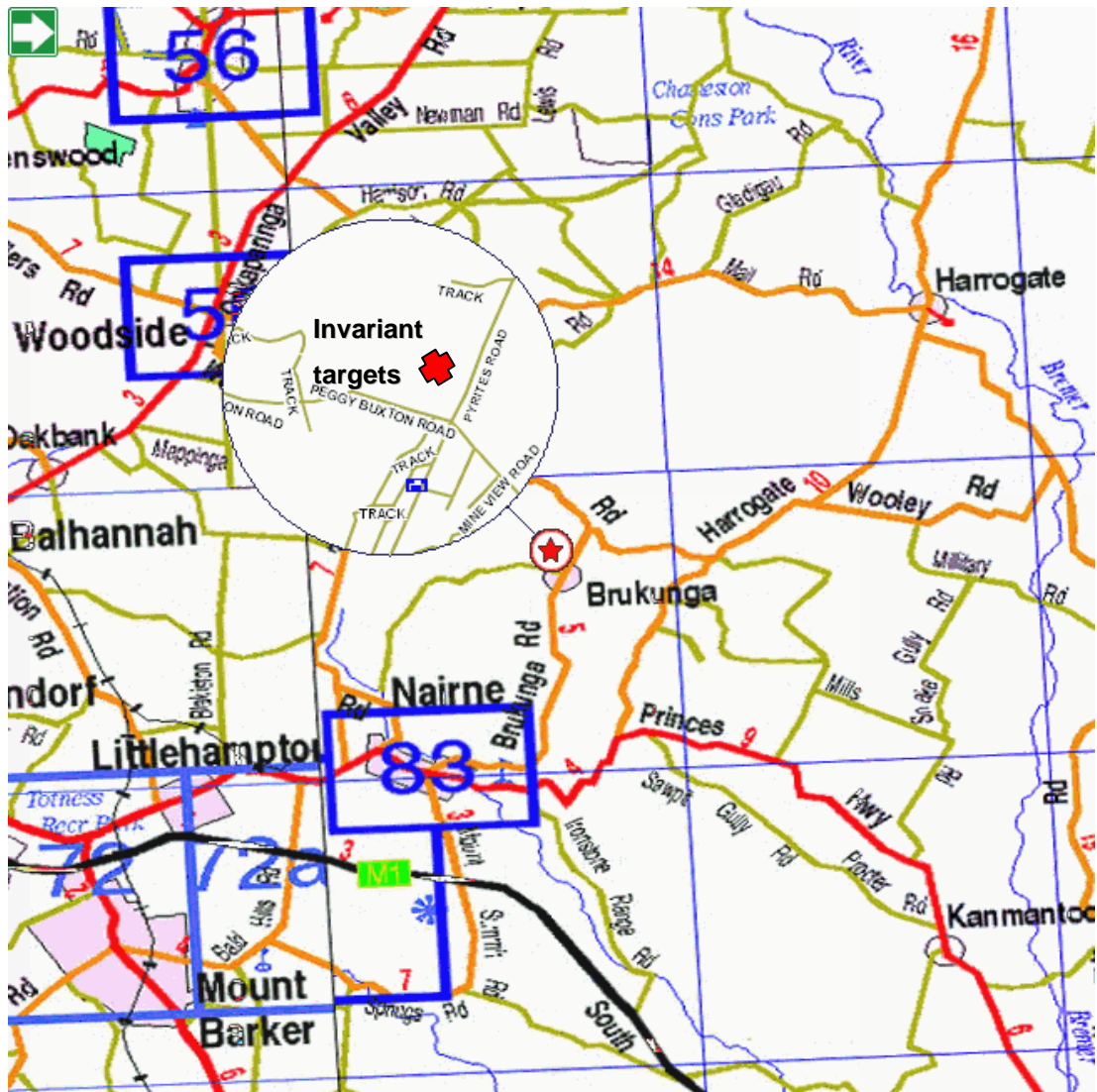


Figure 87: Location of calibration targets (reproduced from http://www.street-directory.com.au/sd_new/mapsearch.cgi)

An ASD FieldSpec® Pro FR spectrometer was used to collect ground spectral measurements from the final three calibration targets. Forty spectra were collected over each of these calibration target



Figure 88: Bitumen



Figure 90: Concrete pavers



Figure 92: Concrete



Figure 89: Bitumen close-up

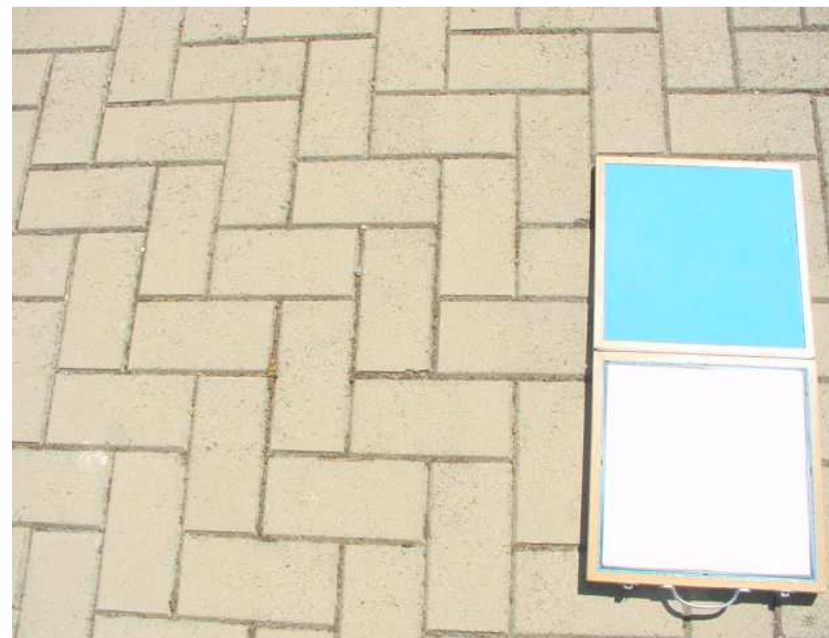


Figure 91: Concrete pavers close-up.

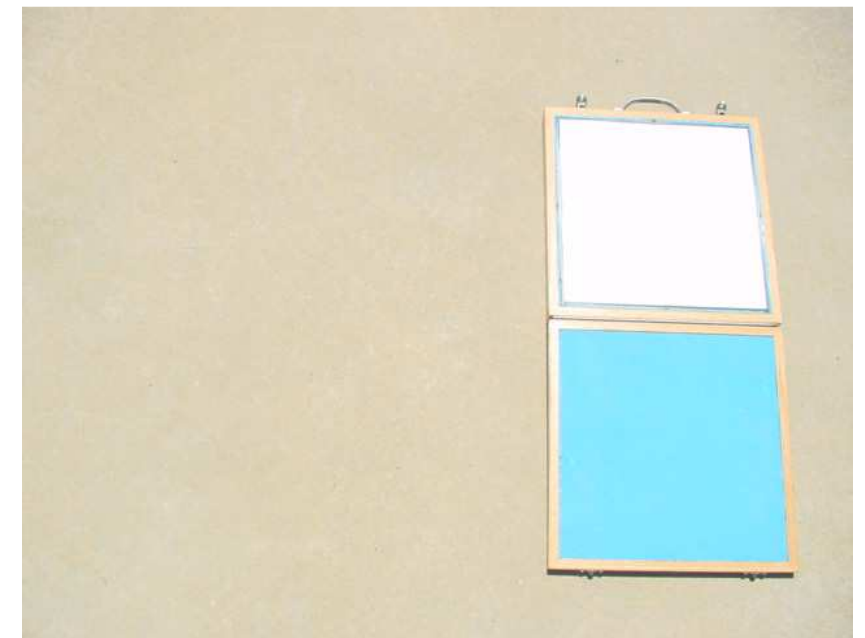


Figure 93: Concrete close-up

Table 13 presents the mineralogical information derived from the spectral data measured on the samples collected at Brukunga in 2001 concurrent with the airborne acquisition. In summary, the samples contain dominantly goethite and muscovite with some samples containing minor amounts of jarosite. There were also a few samples which contain some Fe sulphates, most possibly melanterite and one sample contains halotrichite.

Sample	Goethite	Jarosite	Muscovite	Halotrichite	Melanterite
1	✓	✓small	✓	✗	✗
2	✗	✗	✓	✗	✗
3	✗	✓	✓	✗	✓possibly
4	✓	✗	✓	✗	✗
5	✗	✗	✓	✗	✗
6	✗	✓	✓	✗	✗
7	✓	✓small	✓	✗	✗
8	✓	✓small	✓	✗	✗
9	✓	✓	✓	✗	✓possibly
10	✓	✓small	✓	✗	✗
11	✓	✓small	✓	✗	✗
12	✓	✗	✓	✗	✗
13	✓	✗	✓	✗	✗
14	✓	✓small	✓	✗	✗
15	✓	✓small	✓	✗	✗
16	✓	✓small	✓	✗	✗
17	✓	✓	✓	✗	✓possibly
18	✓	✓small	✓	✗	✗
19	✓	✓small	✓	✗	✗
20	✓	✗	✓	✗	✗
21	✗	✗	✗	✓	✗

Table 13: Minerals contained in samples collected in 2001. Mineralogical information derived from spectral data collected from the samples.

A.4 Published outputs by the author on the current research

Journals and other refereed publications

1. C.C.H. Ong and T.J. Cudahy (2013) Mapping Contaminated Soils: Using Remotely-Sensed Hyperspectral Data to predict pH. European Journal of Soil Sciences (paper accepted for publication)
2. Cindy Ong, Ian Lau, Robert Hewson, David Tongway & Andreas Eisele (2008) MERIWA Project M385: The Development of a Hyperspectral

Environmental Measurement Tool for Monitoring Mining Related Infrastructure and Rehabilitation

3. C.C.H. Ong, T.J. Cudahy, M.S. Caccetta, M.S. Piggott and P.T. Hick (2003) Deriving quantitative dust measurements related to iron ore handling from Airborne Hyperspectral Data. Mining Technology (Trans. Inst. Min. Metall.) Vol. 112 A1-A6

Conference papers

1. Cindy Ong (2012) Quantifying The Uncertainties In The Use Of Remotely-Sensed Hyperspectral Imagery For Monitoring Dust. In Proceedings of IEEE International Geoscience and Remote Sensing Symposium: Remote Sensing for a Dynamic Earth, 22-27 July, Munich, Germany
2. C. Ong (2007) The use of airborne hyperspectral data to quantify the extent and amounts of iron ore dust from port facilities. In Proceedings of Dust Management in Mining (invited presentation)
3. C. Ong (2007) Environmental mapping and monitoring for the resources industry: Operational requirements from future hyperspectral imaging systems. The third international Workshop for Space, Aeronautical and Navigational Electronics (WSANE 2007) (keynote paper)
4. R.N. Clark, Boardman, J., Mustard, J., Kruse, F., Ong, C., Pieters, C. and Swayze, G. (2006) Mineral Mapping and Applications of Imaging Spectroscopy. pp1986-1989 Proceedings of 2006 IEEE International Geoscience and Remote Sensing Symposium and 27th Canadian Symposium on Remote Sensing, Denver, Colorado, Vol III
5. C.Ong (2005) Hyperspectral Technology for Best Practice Mine Environmental Management - Dream or Reality? Airborne Imaging Spectroscopy Workshop, Bruges, Belgium, 7th October 2005 (keynote paper)
6. C.Ong (2005) Hyperspectral sensing: providing a regional prespective for soil contamination assessment and monitoring 9th International Conference on Soil-Water Systems Bordeaux Convention Center, Bordeaux / France, 3 - 7 October 2005

7. Cudahy T., C. Ong, M. Caccetta, A. Cornelius, R. Hewson, M. Wells, M. Skwarnecki, S. Halley and P. Hausknecht (2005) The contribution of hyperspectral technology throughout the entire mineral resources development chain: environmentally sustainable exploration and mining. 4th EARSeL Workshop on Imaging Spectroscopy, Warsaw, Poland, 27-29 April 2005
8. Mark Piggott, Cindy Ong and Bill Biggs (2005) The path towards operational use of hyperspectral technology as an environmental management tool – the dust mapping case history. 4th EARSeL Workshop on Imaging Spectroscopy, Warsaw, Poland, 27-29 April 2005
9. C.C.H. Ong, T.J. Cudahy and M.S. Caccetta (2002) Deriving quantitative environmental measurements from airborne hyperspectral data – lessons learnt in Australia MINEO Science Workshop (invited paper)
10. C. Ong, T.J. Cudahy and G. Swayze (2003) Predicting Acid Drainage Related Physicochemical Measurements Using Hyperspectral Data. pp. 363-373 Proceedings of the 3rd EARSeL Workshop on Imaging Spectroscopy, Herrsching, Germany, 13-16 May 2003
11. C. Ong, G. Swayze, and R. Clark (2003) An Investigation Of The Use Of The Tetracorder Expert System For Multi-Temporal Mapping Of Acid Drainage-Related Minerals Using Airborne Hyperspectral Data. pp. 357-362 Proceedings of the 3rd EARSeL Workshop on Imaging Spectroscopy, Herrsching, Germany, 13-16 May 2003
12. C.C.H. Ong and T.J. Cudahy (2002) Deriving Quantitative Monitoring Data Related to Acid Drainage Using Multi-temporal Hyperspectral Data. Summaries of the 12th JPL Airborne Earth Science Workshop, JPL Publication
13. C.C.H. Ong, T.J. Cudahy, M.S. Caccetta, M.S. Piggott and P.T. Hick (2002) Deriving quantitative dust measurements related to iron ore handling from Airborne Hyperspectral Data. Proceedings for Iron Ore 2002, Perth 9-11th September, AusIMM Publication Series No,7/2002, pp177-180 (best presentation award)

14. C.C.H. Ong, T.J. Cudahy, M.S. Caccetta, M.S. Piggott and P.T. Hick (2002) Deriving Dust Quantity On Mangroves From Airborne Hyperspectral Data. Airborne Remote Sensing Conference, Miami, May 2002 (best of conference award)
15. C. Ong, T. Cudahy, M. Piggott, M. Caccetta and P. Hick (2001) Quantifying dust loading on mangroves using hyperspectral techniques. Proceedings of International Geoscience and Remote Sensing Symposium, Sydney (published on CDROM)
16. Hick, P. Ong, C., Reinhaekel, G., Cudahy, T., Wilson J. and Caccetta, M. (2001) Airborne Hyperspectral sensing case studies for environmental management in the mining industry. Proc of the workshop "Hyperspectral Focus Group" Adelaide
17. Ong, C., Hick, P., Piggott, M., Caccetta, M., Cudahy and Wilson J. (1999) Hyperspectral Remote Mapping and Monitoring of Iron Ore Dust on Mangroves. Proceedings of the AMEEF Conference on Innovation, Fremantle August 1999, pp1-
18. Hick, P and Ong, C (1999) The Role of Remote Sensing for Measuring Mining Impact on the Australian Arid Environment and the Link to Ecological Function. Proceedings of the AMEEF Conference on Innovation, Fremantle August 1999, pp1-

Reports

1. C. Ong and M. Caccetta (2004) Deriving quantitative dust parameters in relation to the environmental management of iron ore handling at Port Hedland. CEM report
2. Cindy Ong, Erick Ramanaidou and Thomas Cudahy (2001) Part 1a: Deriving quantitative dust parameters for the management of iron ore handling at Port Hedland, WA: Characterisation of background and iron ore dust (spectral studies) Division Of Exploration And Mining Report 790R pp 1-27

3. Ong, C., Caccetta, M. and Hick, P., (2000) Spectral techniques to assess the quantity and effects of dust on mangroves at Port Hedland CEM Report for BHPIO Number 691c pp1-22
4. Cindy Ong, Michael Caccetta and Peter Hick (1999) The development of a baseline digital high-resolution dataset for monitoring rehabilitation and status of Mangroves in the Port Hedland Harbour region. Exploration and Mining Report No. 474c. pp1-13

A.5 Copy Right Permission



**Minerals & Energy Research Institute
of
Western Australia**



PERMISSION TO USE COPYRIGHT MATERIAL AS SPECIFIED BELOW

Figure 71, section 9.4.1 and 9.4.2 of section 9.4 "Change Detection" from MERIWA Report M271: Cindy Ong, Ian Lau, Robert Hewson, David Tongway and Andreas Eisele (2008) MERIWA Project M385: "The Development of a Hyper-spectral Environmental Measurement Tool for Monitoring Mining Related Infrastructure and Rehabilitation."

On the understanding that the sections cited above were undertaken solely by Ms Ong, I hereby give permission for Cindy Ong to include the above-mentioned materials in her higher degree thesis for the Curtin University of Technology, and to communicate this material via the Australasian Digital Thesis Program. This permission is granted on a non-exclusive basis and for an indefinite period.

I confirm that MERIWA is the copyright owner of the specific material.

Permission to use this material is subject to MERIWA's contribution to the research work being duly acknowledged.

Signed: 

Name: Ross Marshall

Position: Executive Officer

Date: 9/01/2013

MINERAL HOUSE
100 PLAIN STREET (CNR ADELAIDE TCD)
EAST PERTH WESTERN AUSTRALIA 6004

Telephone: (08) 8222 3307
Facsimile: (08) 8222 3727
EHS: www.dmp.wa.gov.au/meriwa

REFERENCES

- ABCNEWS. 2005. *Port Hedland Wants Dust Problem Solved* [Online]. Available: <http://www.abc.net.au/news/stories/2005/02/25/1310989.htm>.
- ADLER-GOLDEN, S., BERK, A., BERNSTEIN, L. S. & RICHTSMEIER, S. 1998. FLAASH, A MODTRAN4 atmospheric correction package for hyper-spectral data retrievals and simulations. *Summaries of the seventh JPL airborne earth science workshop*. Pasadena, California: NASA JPL.
- ADLER-GOLDEN, S. M., MATTHEW, M. W., BERNSTEIN, L. S., LEVINE, R. Y., BERK, A., RICHTSMEIER, S. C., ACHARYA, P. K., ANDERSON, G. P., FELDE, G., GARDNER, J., HOKE, M., JEONG, L. S., PUKALL, B., RATKOWSKI, A. & BURKE, H. H. 1999. Atmospheric Correction for Short-wave Spectral Imagery Based on MODTRAN4. . *SPIE Proceedings on Imaging Spectrometry*, 3753, 61-69.
- AGNEW, M. 1994. *Weathering products and geochemistry of waste residues at the Brukunga Pyrite Mine, Adelaide Hills, S.A. in relation to environmental impacts*. Honours, University of Adelaide.
- AIGLLC. 2000. *ACORN (Atmospheric CORrection Now)* [Online]. Boulder, CO: Analytical Imaging and Geophysics. Available: http://www.aigllc.com/imspec_transition.htm.
- ASDI. 2008. *FieldSpec3 Spectroradiometer - Portable Remote Sensing Equipment* [Online]. Boulder, CO. Available: <http://www.asdi.com/products-fs3.asp>.
- ASRAR, G. 1989. *Theory and Applications of Optical Remote Sensing*, Washington, DC, John Wiley and Sons.
- ASTM 2008. ASTM D6966 - 08 Standard Practice for Collection of Settled Dust Samples Using Wipe Sampling Methods for Subsequent Determination of Metals. ASTM International (American Society for Testing and Materials).
- ASTM 2010. ASTM E1728 - 10 Standard Practice for Collection of Settled Dust Samples Using Wipe Sampling Methods for Subsequent Lead Determination. ASTM International (American Society for Testing and Materials).
- ASTM 2011. ASTM E1792 - 03(2011) Standard Specification for Wipe Sampling Materials for Lead in Surface Dust. ASTM International (American Society for Testing and Materials).
- BEARD, J. S. 1975. *The Vegetation of the Pilbara Area, Vegetation Survey of Western Australia – Explanatory Notes to Sheet 5, 1:1 000 000 Vegetation Series*. Perth, WA: University of Western Australia Press.

- BERK, A., BERNSTEIN, L. S. & ROBERTSON, D. C. 1989. MODTRAN: a moderate resolution model for LOWTRAN7. Hanscom AFB, MA: Air Force Geophysical Laboratory.
- BHP 1996. Port Hedland Dust Management Programme. Consultative Environmental Review. Perth, WA: BHP Iron Ore Pty Ltd.
- BIERWIRTH, P. 2004. *Methods of spectral geology utilizing airborne-hyperspectral and satellite remote sensing: applications for exploration and acid-mine drainage*, Australian National University.
- BIGGS, B. 2004. Our Needs, Experiences and Aspirations: A Regulator's Perspective (Workshop on Environmental Measurements from Hyperspectral Data). *12th Australasian Remote Sensing and Photogrammetry Conference*. Fremantle, WA.
- BIGHAM, J. M., SCHWERTMANN, U. & PFAB, G. 1996a. Influence of pH on mineral speciation in a bioreactor simulating acid mine drainage. *Applied Geochemistry*, 11, 845-849.
- BIGHAM, J. M., SCHWERTMANN, U., TRAINA, S. J., WINLAND, R. L. & WOLF, M. 1996b. Schwertmannite and the chemical modelling of iron in acid sulfate waters. *Geochimica et Cosmochimica Acta*, 12, 2111-2121.
- BMSRB 2001. State Government Commits \$26.1 million to Brukunga Mine Site Rehabilitation. *Working Together*. Brukunga, SA: Brukunga Mine Site Remediation Board (BMSRB).
- BOM. 2008. *Tropical Cyclones Affecting Port Hedland* [Online]. Port Hedland, WA: Bureau of Meteorology (BOM).
- BORN, M. & WOLF, E. 1999. *Electromagnetic theory of propagation, interference and diffraction of light*. , Cambridge Press.
- BURTT, A. C. & GUM, J. C. 2000a. The Dawesley-Bremer Catchment: Phase 2 sampling program for potential environmental contaminants. Report 2000/00019. Adelaide: PIRSA.
- BURTT, A. C. & GUM, J. C. 2000b. Soil and stream sediment sampling of the Dawesley-Bremer Catchment for potential environmental contaminants. Report 2000/00002. Adelaide: PIRSA.
- CARRERE, V. & ABRAMS, M. J. An assessment of AVIRIS data for hydrothermal alteration mapping in the Goldfield mining district, Nevada. . *In*: VANE, G., ed. Airborne Visible/Infrared Imaging Spectrometer (AVIRIS) Performance Evaluation Workshop 1988 Pasadena, California. JPL, 134-154.
- CHANG, C. W., LAIRD, D. A., MAUSBACH, M. J. & HURBURGH, C. R. 2001. Near-infrared reflectance spectroscopy-principal components regression

- analyses of soil properties. *Soil Science Society of America Journal*, 65, 480-490.
- CHEVREL, S. 2003. Assessing and monitoring the environmental impact of mining activities in Europe using advanced Earth Observation techniques MINEO IST-1999-10337. BRGM.
- CHUDNOUSKY, A. & BEN-DOR, E. 2008. Application of visible, near-infrared, and short-wave infrared (400-2500 nm) reflectance spectroscopy in quantitatively assessing settled dust in the indoor environment. Case study in dwellings and office environments. *Science of the Total Environment*, 393, 198-213.
- CHUDNOVSKY, A., BEN-DOR, E., KOSTINSKI, A. B. & KOREN, I. 2009. Mineral content analysis of atmospheric dust using hyperspectral information from space. *Geophysical research letters*, 36.
- CHUDNOVSKY, A., KOSTINSKI, A., HERRMANN, L., KOREN, I., NUTESKU, G. & BEN-DOR, E. 2011. Hyperspectral spaceborne imaging of dust-laden flows: Anatomy of Saharan dust storm from the Bodele Depression. *Remote Sensing of Environment*, 115, 1013-1024.
- CLARK, R. N. 1981a. The Spectral Reflectance of Water-Mineral Mixtures at Low Temperatures. *Journal of Geophysical Research*, 86, 3074-3086.
- CLARK, R. N. 1981b. Water Frost and Ice: The Near-Infrared Spectral Reflectance 0.65-2.5 μm . *Journal of Geophysical Research*, 86, 3087-3096.
- CLARK, R. N. 1983. Spectral Properties of Mixtures of Montmorillonite and Dark Carbon Grains: Implications for Remote Sensing Minerals Containing Chemically and Physically Adsorbed Water. *Journal of Geophysical Research*, 88, 10635-10644.
- CLARK, R. N. 1999. Spectroscopy of Rocks and Minerals, and Principles of Spectroscopy. In: RENCZ, A. (ed.) *Manual of Remote Sensing*. New York: John Wiley and Sons, Inc
- CLARK, R. N., GHALLAGHER, A. J. & SWAYZE, G. A. Material absorption band depth mapping of imaging spectrometer data using a complete band shape least-squares fit with library spectra. In: GREEN, R. O., ed. *Second Airborne Visible/Infrared Imaging Spectrometer (AVIRIS) Workshop*, 1990 Pasadena, CA.: JPL Publication, 176-186.
- CLARK, R. N. & KING, T. V. V. Causes of spurious features in spectral reflectance data. In: VANE, G., ed. *3rd Airborne Imaging Spectrometer Data Analysis Workshop*, 1987 Pasadena, CA. NSASA JPL, 132-137.
- CLARK, R. N. & ROUSH, T. L. 1984. Spectral Properties of Mixtures of Montmorillonite and Dark Carbon Grains: Implications for Remote Sensing

Minerals Containing Chemically and Physically Adsorbed Water. *Journal of Geophysical Research*, 89, 6329-6340.

- CLARK, R. N., SWAYZE, G. A., LIVO, K. E., KOKALY, R. F., KING, T. V. V., DALTON, J. B., VANCE, J. S., ROCKWELL, B. W., HOEFEN, T. & MCDOUGAL, R. R. Surface Reflectance Calibration of Terrestrial Imaging Spectroscopy Data: a Tutorial Using AVIRIS. *In: GREEN, R. O., ed. 11th Airborne Earth Science Workshop, 2003a Pasadena, CA. JPL Publication, 43-63.*
- CLARK, R. N., SWAYZE, G. A., LIVO, K. E., KOKALY, R. F., SUTLEY, J. B., DALTON, J. B., MCDOUGAL, R. R. & GENT, C. A. 2003b. Imaging spectroscopy: Earth and planetary remote sensing with the USGS Tetracorder and expert systems. *Journal of Geophysical Research*, 108(E12), 5-1 to 5-44.
- CLARK, R. N., SWAYZE, G. A., WISE, R., LIVO, E., HOEFEN, T., KOKALY, R. & SUTLEY, S. J. 2007. USGS digital spectral library splib06a: U.S. Geological Survey Digital Data Series 231. *In: USGS (ed.). USGS.*
- COCKS, T., JENSSEN, R., STEWART, A., WILSON, I. & SHIELDS, T. The Hymap Airborne Hyperspectral Sensor : The System, Calibration And Performance. . 1st EARSEL Workshop on Imaging Spectroscopy, October 1998 1998 Zurich, Switzerland. EARSEL, 37-42.
- CONEL, J. E., GREEN, R. O., VANE, G., BRUEGGE, C. J. & ALLEY, R. E. AIS-2 radiometry and a comparison of methods for the recovery of ground reflectance. . *In: VANE, G., ed. Third Airborne Imaging Spectrometer Data Analysis Workshop 1987 Pasadena, CA. JPL Publication, 18-47.*
- COUNCIL, N. R. 2009. *Uncertainty Management in Remote Sensing of Climate Data: Summary of a Workshop*, The National Academies Press.
- CRAIG, G. 1983. Pilbara Coastal Flora. Perth: Western Australian Department of Agriculture.
- CROWLEY, J. K. & VERGO, N. 1988. Near-infrared reflectance spectra of mixtures of kaolin group minerals: use in clay studies. *Clays and Clay Minerals*, 36, 310-316.
- CROWLEY, J. K., WILLIAMS, D. E., HAMMARSTROM, J. M., PIATAK, N., CHOU, I.-M. & MARS, J. C. 2003. Spectral reflectance properties (0.4–2.5 μm) of secondary Fe-oxide, Fe-hydroxide, and Fe-sulphate-hydrate minerals associated with sulphide-bearing mine wastes. *Geochemistry: Exploration, Environment, Analysis*, 2 2003, 219-228.
- CSIRO 1999. Summaries of Dust Workshop. *Dust Workshop*. Clayton, Vic: CSIRO Minerals.

- CSIRO. 2004. *CSIRO Dust Busters Shares Golden Gecko* [Online]. CSIRO: CSIRO. Available: <http://www.csiro.au/files/mediaRelease/mr2004/goldengecko.htm> [Accessed 30.12.2011 2011].
- CSIRO. 2005. *Xplot for windows XRD manipulation program* [Online]. Glen Osborne, SA: CSIRO Land and Water. Available: <http://www.clw.csiro.au/services/mineral/xplot.html> [Accessed 10.10.2008 2008].
- CUDAHY, T. J. & RAMANAIDOU, E. R. 1992. Relationships between spectral properties and ferric oxides. Perth, WA: CSIRO.
- CUDAHY, T. J. & RAMANAIDOU, E. R. 1997. Measurement of the hematite:goethite ratio using field visible and near-infrared reflectance spectrometry in the channel iron deposits, Western Australia. *Australian Journal of Earth Sciences*, 44, 411-420.
- CURRAN, P. J. 1989. Remote Sensing of Foliar Chemistry. *Remote Sensing of Environment*, 30, 271-278.
- CURTIS, B. 1985. *Evaluation of the physical properties of naturally occurring (III) oxyhydroxides on rock surfaces in arid and semi-arid regions using visible and near infrared spectroscopy*. PhD, PhD Thesis, University of Washington.
- DALTON, J. B., BOVE, D. J. & MLADINICH, C. S. 2004. Remote Sensing Characterization of the Animas River Watershed, Southwestern Colorado, by AVIRIS Imaging Spectroscopy. Scientific Investigations Report 2004-5203. Denver, CO: USGS.
- DEC. 2004. *SGIO Western Australian Environment Award 2004* [Online]. Department of Environment and Conservation: Department of Environment and Conservation. Available: http://portal.environment.wa.gov.au/pls/portal/docs/PAGE/DOE_ADMIN/OTHER_REPOSITORY/TAB1276265/WINNERS_2004.PDF [Accessed 30.12.2011 2011].
- DEC. 2010. *Esperance lead and nickel update* [Online]. WA: Department of Environment and Conservation. Available: <http://www.dec.wa.gov.au/content/view/3484/1729/> [Accessed 05.01.2012 2012].
- DURY, S., TURNER, B., FOLEY, B. & WALLIS, I. 2001. Use of high spectral resolution remote sensing to determine leaf palatability of eucalypt trees for folivorous marsupials. *JAG*, 3, 328-336.
- EC 2006. Directive 2006/21/EC of the European Parliament and of the Council of 15 March 2006 on the management of waste from the extractive industries and

- amending Directive 2004/35/EC. In: COUNCIL, E. P. A. (ed.). European Parliament and Council.
- ECOSCAPE 2004. 2004 – 2009 Port Hedland Coastal Management Plan. Fremantle, WA: Ecoscape.
- ELVIDGE, C. D. 1990. Visible and near infrared reflectance characteristics of dry plant materials. *Remote Sensing of Environment*, 11, 1775-1795.
- EPA 1996. Upgrade of Dust Management at Funicane Island and Nelson Point, Port Hedland. In: AUTHORITY, E. P. (ed.). Perth, WA: Environmental Protection Authority.
- FELDE, G. W., ANDERSON, G. P., COOLEY, T. W., MATTHEW, M. W., ADLER-GOLDEN, S. M., BERK, A. & LEE, J. 2003. *Analysis of Hyperion data with the FLAASH atmospheric correction algorithm*.
- FERRIER 1999. Application of Imaging Spectrometer Data in Identifying Environmental Pollution Caused by Mining at Rodaquilar, Spain *Remote Sensing of Environment*, 68, 125-137.
- GA 2010. A National Space Policy: Views from the Earth Observation Community. In: AUSTRALIA, G. (ed.). Canberra: Geoscience Australia.
- GAFFEY, S. J. 1986. Spectral reflectance of carbonate minerals in the visible and near infrared (0.35-2.55 μm): Calcite, aragonite and dolomite. *Am. Mineral.*, 71, 151-162.
- GAFFEY, S. J. 1987. Spectral reflectance of carbonate minerals in the visible and near infrared (0.35-2.55 μm): Anhydrous carbonate minerals. *Journal of Geophysical Research*, 92, 1429-1440.
- GAMON, J. A., SERRANO, L. & SURFUS, J. S. 1997. The photochemical reflectance index: an optical indicator of photosynthetic radiation-use efficiency across species, functional types, and nutrient levels. *Oecologia*, 112, 492-501.
- GAO, B. C., HEIDEBRECHT, K. B. & GOETZ, A. F. H. 1993. Derivation of scaled surface reflectances from AVIRIS data. *Remote Sensing of Environment*, 44, 165-178.
- GAO, B. C., MONTES, M. J. & DAVIS, C. O. 2004. Refinement of wavelength calibrations of hyperspectral imaging data using a spectrum-matching technique. *Remote Sensing of Environment*, 90, 424-433.
- GELADI, P. & KOWALSKI, B. R. 1986. Partial Least-Squares Regression: A Tutorial. *Analytica Chimica Acta*, 185, 1-17.

- GOETZ, A. F. H. 2009. Three decades of hyperspectral remote sensing of the Earth: A personal view. *Remote Sensing of Environment*, 113, S5-S16.
- GPS.GOV 2011. Selective Availability. In: NATIONAL COORDINATION OFFICE FOR SPACE-BASED POSITIONING, N., AND TIMING & COMMITTEE., C. G. S. I. (eds.). USA: Coast Guard Navigation Center.
- GRAVESTOCK, D. I. & GATEHOUSE, C. G. 1995. Stansbury Basin in the Geology of South Australia – The Phanerozoic. In: J.F., D. & PREISS, W. V. (eds.) *SADME Bulletin*.
- GREEN, A. A., BERMAN, M., SWITZER, P. & CRAIG, M. D. 1998. A transformation for ordering multispectral data in terms of image quality with implications for noise removal. *IEEE Transactions on Geoscience and Remote Sensing*, 26, 65-74.
- GREEN, A. A. & CRAIG, M. D. Analysis of aircraft spectrometer data, with logarithmic residuals In: VANE, G. & GOETZ, A., eds. Airborne Imaging Spectrometer Data Analysis Workshop, April 8-10 1985 Pasadena, California. NASA JPL, 111-119.
- GREEN, R. O. 1998. Spectral calibration requirement for earth-looking imaging spectrometers in the solar-reflected spectrum. *Applied Optics*, 37, 683-690.
- GUANTER, L., RICHTER, R. & MORENO, J. 2006. Spectral calibration of hyperspectral imagery using atmospheric absorption features. *Applied Optics*, 45, 2360-2370.
- HAALAND, D. M. & THOMAS, E. V. 1988. Partial Least Squares. *Analytical Chemistry*, 60, 1193-1200.
- HALL, D. J., UPTON, S. L. & MARSLAND, G. W. 1994. Designs for a deposition gauge and a flux gauge for monitoring ambient dust. *Atmospheric Environment*, 28, 2963-2979.
- HAMMARSTROM, J. M., SEAL II, R. R., MEIER, A. L. & KORNFELD, J. M. 2005. Secondary sulfate minerals associated with acid drainage in the eastern US: recycling of metals and acidity in surficial environments. *Chemical Geology*, 215, 407-431.
- HARRIES, J. 1997. Acid mine drainage in Australia: Its extent and potential future liability. Kingston, ACT: Supervising Scientist.
- HAUFF, P. L., COULTER, D. W., PETERS, D. C., SARES, M. A., PROSH, E. C., HENDERSON III, F. B. & BIRD, D. Using Aviris In The NASA BAA Project To Evaluate The Impact Of Natural Acid Drainage On Colorado Watersheds In: GREEN, R. O., ed. 11th Airborne Earth Science Workshop, 2003 Pasadena, CA. JPL Publication.

- HORLER, D. N., DOCKRAY, M. & BARBER, J. 1983. The red edge of plant leaf reflectance. . *International Journal of Remote Sensing*, 4, 273-288.
- HUNT, G. R. 1977. Spectral signatures of particulate minerals, in the visible and near-infrared. *Geophysics*, 42, 501-513.
- HUNT, G. R. 1979. Near-infrared (1.3-2.4 μm) spectra of alteration minerals-Potential for use in remote sensing. *Geophysics*, 44, 1974-1986.
- HUNT, G. R. 1982. Spectroscopic properties of rocks and minerals. *In: CARMICHAEL, R. S. (ed.) Handbook of Physical properties of rocks*. Boca Raton: CRC Press.
- HUNT, G. R. & SALISBURY, J. W. 1970. Visible and near infrared spectra of minerals and rocks. I. Silicate minerals,. *Mod. Geology*, 1, 283-300.
- HUNT, G. R. & SALISBURY, J. W. 1971. Visible and near infrared spectra of minerals and rocks. II. Carbonates. *Mod. Geology*, 2, 23-30.
- HUNT, G. R., SALISBURY, J. W. & LENHOFF, C. J. 1972. Visible and near infrared spectra of minerals and rocks. V. Halides, arsenates, vanadates, and borates. *Mod. Geology*, 3, 121-132.
- HUNT, G. R., SALISBURY, J. W. & LENHOFF, C. J. 1973. Visible and near infrared spectra of minerals and rocks. VI. Additional silicates. *Mod. Geology*, 4, 85-106.
- HYVISTA. 2008. *HyMap Sensor* [Online]. Sydney, NSW: HyVista. Available: <http://www.hyvista.com/technology/sensors>.
- ISPL. 1997. *PIMA II Description* [Online]. Sydney, NSW: Integrated Spectronics. [Accessed 10.10.2008 2008].
- ITRES. 2008. *ITRES Sensor Products* [Online]. Calgary, Alberta: ITRES. Available: http://www.itres.com/Sensor_Products.
- ITTVIS 2012. ENVI4.8 Help Colorado, USA: ITT - Visual Information Solutions.
- IWASAKI, A., OHGI, N., TANII, J., KAWASHIMA, T. & INADA, H. 2011. Hyperspectral Imager Suite (HISUI) -Japanese hyper-multi spectral radiometer Geoscience and Remote Sensing Symposium (IGARSS), 2011 IEEE International 24-29 July 2011 2011 Vancouver, BC. Geoscience and Remote Sensing Symposium (IGARSS), 2011 IEEE International 1025 - 1028.
- JANIK, L. J., SKJEMSTAD, J. O., SHEPHERD, K. D. & SPOUNCER, L. R. 2007. The prediction of soil carbon fractions using mid-infrared-partial least square analysis. *Australian Journal of Soil Research*, 45, 73.

- JENSEN, J. 2000. *Remote Sensing of the Environment: An Earth Resource Perspective*, N.J., Prentice Hall.
- KAUFMAN, Y. J. 1989. The Atmospheric Effect On Remote Sensing And Its Correction. In: ASRAR, G. (ed.) *Theory And Applications Of Optical Remote Sensing*. Kong, J.A. ed.: John Wiley and Sons.
- KEMPER, T. & SOMMER, S. 2002. Estimate of Heavy Metal Contamination in Soils after a Mining Accident Using Reflectance Spectroscopy *Environmental Science Technology*, 36, 2742-2747.
- KRÜGER, G., ERZINGER, J. & KAUFMAN, H. 1998. Laboratory and airborne reflectance spectroscopic analyses of lignite overburden dumps. *Geochemical Exploration*, 64, 47-65.
- KRUSE, F. A. Mapping hydrothermally altered rocks in the northern Grapevine Mountains, Nevada and California with the Airborne Imaging Spectrometer. In: VANE, G., ed. 3rd Airborne Imaging Spectrometer Data Analysis Workshop 1987 Pasadena, CA. NASA JPL, 148-166.
- LABSPHERE. 2006. *Spectralon® Reflectance Standards* [Online]. North Sutton, New Hampshire: Labsphere. Available: <http://www.labsphere.com/productdetail.aspx?id=800&catid=> [Accessed 09.10.2008].
- LAGANZA, R. 1959. Pyrite investigations at Nairne, SA. *Economic Geology*, 54, 895-902.
- LANDMAN, P. 2002. *RE: Absorption of water on leaf surface*. Type to ONG, C.
- LEAR, R. & TURNER, T. 1977. *Mangroves of Australia*, St Lucia Queensland, University of Queensland Press.
- LECOMTE, P. 2008. GEO/CEOS Workshop on Quality Assurance of Calibration and Validation Processes: Establishing an Operational Framework. *Terms and Definitions* [Online]. Available: <http://calvalportal.ceos.org/cvp/web/guest/calval-related-documents> [Accessed 23.12.2011].
- LLOYD, M. V., BARNETT, G., DOHERTY, M. D., JEFFREE, R. A., JOHN, J., MAJER, J. D., OSBORNE, J. M. & NICHOLS, O. G. 2002. Managing the Impacts of the Australian Minerals Industry on Biodiversity. Queensland: Australian Centre for Mining Environmental Research.
- LÓPEZ-PAMO, E., BARENTTINO, D., ANTON-PACHECO, C., ORTIZ, G., ARRÁNZ, J. C., GUMIEL, J. C., MARTÍNEZ-PLEDEL, B., APARICIO, M. & MONTOUTO, O. 1999. The extent of the Aznalcóllar pyritic sludge spill and its effects on soils. *The science of the total environment*, 242, 57-88.

- LUNDEEN, S. 2007. *AVIRIS Airborne Visible/Infrared Imaging Spectrometer* [Online]. Pasadena, CA: NASA JPL. Available: <http://aviris.jpl.nasa.gov/>.
- MARS, J. C. & CROWLEY, J. K. 2003. Mapping mine wastes and analyzing areas affected by selenium-rich water runoff in southeast Idaho using AVIRIS imagery and digital elevation data. *Remote Sensing of Environment*, 84, 422-436.
- MARSH, S. H. 2000. The MINEO Project: Earth Observation of mine pollution in Europe. . *GRSG Newsletter*.
- MASON, P. 2000. HYCORR Users Manual. Sydney, Australia: CSIRO.
- MASON, P. & BERMAN, M. 1997. XSPECTRA REFERENCE MANUAL Manual revision 1.5 (covering XSpecra version 2.9.0). 2.9.0 ed. Sydney: CSIRO.
- MATTHEW, M. W., ADLER-GOLDEN, S. M., BERK, A., RICHTSMEIER, S. C., LEVINE, R. Y., BERNSTEIN, L. S., ACHARYA, P. K., ANDERSON, G. P., FELDE, G. W., HOKE, M. P., RATKOWSKI, A., BURKE, H.-H., KAISER, R. D. & MILLER, D. P. Status of Atmospheric Correction Using a MODTRAN4-based Algorithm. Algorithms for Multispectral, Hyperspectral, and Ultraspectral Imagery VI. , 2000. SPIE, 199-207.
- MCGOVERN, A. C., ERNILL, R., KARA, B. V., KELL, D. B. & GOODACRE, R. 1999. Rapid analysis of the expression of heterologous proteins in *Escherichia coli* using pyrolysis mass spectrometry and Fourier transform infrared spectroscopy with chemometrics: application to a α -interferon production. . *Journal of Biotechnology*, 72, 157-167.
- MORRIS, R. V., LAUER JR., H. V., LAWSON, C. A., GIBSON JR., E. K., NACE, G. A. & STEWART, C. 1985. Spectral and Other Physicochemical Properties of Submicron Powders of Hematite (Fe₂O₃), Maghemite (Fe₂O₃), Magnetite (Fe₃O₄), Goethite (FeOOH), and Lepidocrocite (FeOOH). *Journal of Geophysical Research*, 90, 3126-3144.
- NDUWAMUNGU, C., ZIADI, N., PARENT, L. É., TREMBLAY, G. F. & THURIÈS, L. 2009. Opportunities for, and limitations of, near infrared reflectance spectroscopy applications in soil analysis: A review. *Canadian Journal of Soil Science*, 89, 531-541.
- NICODEMUS, F. E. 1970. Reflectance nomenclature and directional reflectance and emissivity. *Applied Optics*, 9, 1474-1475.
- NIST. 2008. *About NIST Calibration Services* [Online]. National Institute of Standards and Technology (NIST). Available: <http://ts.nist.gov/MeasurementServices/Calibrations/index.cfm>.
- OGAWA, K., MATSUNAGA, T., YAMAMOTO, S., KASHIMURA, O., TACHIKAWA, T., IWASAKI, A., TSUCHIDA, S., TANII, J. &

- ROKUGAWA, S. 2011. Operation Planning for Japanese Future Hyperspectral and Multispectral Sensor: HISUI and Usage of Cloud Climate Data. In: MEYNART, R. N. S. P. S. H. (ed.) *Sensors, Systems, and Next-Generation Satellites Xv*.
- PALING, E. I., HUMPHRIES, G., MCCARDLE, I. & THOMSON, G. 1996. The Effects of Iron Ore Dust on Mangroves 1: Lack of Evidence for Stomatal Damage. Perth, WA: Murdoch University.
- PEÑUELAS, J., BARET, F. & FILELLA, I. 1995. Semi-empirical indices to assess carotenoids/chlorophyll a ratio from leaf spectral reflectance. . *Photosynthetica* 3, 1:22, 1-230.
- PETERS, D. C., HAUFF, P. L., DILLENBECK, E. D., PEPPIN, W. A. & PROSCH, E. C. Environmental site characterization for the international smelter area and Bauer Mill, Utah, using hyperspectral data. International Geoscience and Remote Sensing Symposium (IGARSS), 2001 Sydney, NSW. IEEE, 299-301.
- PFITZNER, K. & CLIFTON, R. 2006. Integration of airborne CASI and gamma ray data for mine site characterisation. *Journal of Spatial Science*, 51, 163-175.
- PHPA 2003. Port Hedland Port Authority Planning Study Phase 2 Report (302/00394/2) 18-Aug-03. Port Hedland Port Authority.
- PHPA. 2011. *Records Continue to Tumble at PHPA* [Online]. Port Hedland Port Authority Webpage: Port Hedland Port Authority. Available: [http://www.phpa.wa.gov.au/docs/PHPA_Press_Release_-_July_2011\(2\).pdf](http://www.phpa.wa.gov.au/docs/PHPA_Press_Release_-_July_2011(2).pdf) [Accessed 29.12.2011 2011].
- PHYSICK, W. L. 2001. Meteorology and Air Quality of the Pilbara Region. Aspendale, Vic: CSIRO.
- PIGGOTT, M. 1998. *RE: Issues with Depositional Gauges and High Volume Samplers*. Type to ONG, C.
- PIGGOTT, M. 2000. *RE: Dust Distribution Across Port Hedland*. Type to ONG, C.
- PIRSA. 2005. Notes on Brukunga Pyrite Mine. Available: http://www.pir.sa.gov.au/_data/assets/pdf_file/0003/10668/brukunga_pyrite_mine_031105.pdf.
- POLDER, G., VAN DER HEIJDEN, G. W. A. M., VAN DER VOET, H. & YOUNG, I. T. 2004. Measuring surface distribution of carotenes and chlorophyll in ripening tomatoes using imaging spectrometry. . *Postharvest Biology and Technology*, 34, 117-129.
- RAMANAIDOU, E. R., WELLS, M., BELTON, D., VERRALL, M. & RYAN, C. 2008. Mineralogical and microchemical methods for the characterization of

- high-grade banded iron formation-derived iron ore. *Society of Economic Geologists*, 15, 129-156.
- RANDALL, J. E. & COX, R. C. 2003. 2002 Water Quality Monitoring at Brukunga. Adelaide: PIRSA.
- RIAZA, A., BUZZI, J., GARCIA-MELENDZ, E., CARRERE, V., SARMIENTO, A. & MULLER, A. 2012. River acid mine drainage: sediment and water mapping through hyperspectral Hymap data. *International Journal of Remote Sensing*, 33, 6163-6185.
- RIAZA, A. & MULLER, A. 2010. Hyperspectral remote sensing monitoring of pyrite mine wastes: a record of climate variability (Pyrite Belt, Spain). *Environmental Earth Sciences*, 61, 575-594.
- RICHTER, R. 1996. A spatially adaptive fast atmosphere correction algorithm. *International Journal of Remote Sensing*, 11, 159-166.
- RICHTER, R. & SCHLÄPFER, D. 2002. Geo-atmospheric processing of airborne imaging spectrometry data: Part 2. Atmospheric/topo-graphic correction. *International Journal of Remote Sensing*, 23, 2631-2649.
- ROBERTS, D. A., YAMAGUCHI, Y. & LYON, R. J. P. Comparison of various techniques for calibration of AIS data. In: VANE, G. & GOETZ, A. F. H., eds. 2nd Airborne Imaging Spectrometer Data Analysis Workshop, 1986 Pasadena. NASA JPL, 21-30.
- ROCKWELL, B. W., CLARK, R. N., CUNNINGHAM, C. F., SUTLEY, S. J. G., C., MCDOUGAL, R. R., LIVO, K. E. & KOKALY, R. F. Mineral mapping in the Marysvale volcanic field, Utah using AVIRIS data. In: GREEN, R. O., ed. 9th Annual JPL Airborne Earth Science Workshop, 2000 Pasadena. NASA JPL, 407-417.
- ROCKWELL, B. W., CLARK, R. N., LIVO, K. E., MCDOUGAL, R. R., KOKALY, R. F. & VANCE, J. S. Preliminary materials mapping in the Park City region for the Utah USGS-EPA Imaging Spectroscopy Project using both high- and low-altitude AVIRIS data. In: GREEN, R. O., ed. 8th Annual JPL Airborne Earth Science Workshop, 1999 Pasadena. NASA JPL, 365-375.
- RODGER, A. 2011a. AtComp. 4.0 ed. Perth: CSIRO.
- RODGER, A. 2011b. SODA: A new method of in-scene atmospheric water vapor estimation and post-flight spectral recalibration for hyperspectral sensors Application to the HyMap sensor at two locations. *Remote Sensing of Environment*, 115, 536-547.

- SALISBURY, J. W., WALTER, L. S., VERGO, N. & D'ARIA, D. M. 1991. *Infrared (2.1-25 μm) spectra of minerals*, Baltimore, The Johns Hopkins University Press.
- SCHAEPMAN, M. E., GREEN, R. O., UNGAR, S., BOARDMAN, J., PLAZA, A. J., GAO, B. C., USTIN, S., MILLER, J., JACQUEMOUD, S., BEN-DOR, E., CLARK, R., DAVIS, C., DOZIER, J., GOODENOUGH, D., ROBERTS, D. & GOETZ, A. F. H. The future of imaging spectroscopy - Prospective technologies and applications. 2006 IEEE International Geoscience and Remote Sensing Symposium, 2006 Denver. IEEE, 2005-2008.
- SEMENUK, V., KENNEALLY, K. F. & WILSON, P. G. 1978. *Mangroves of Western Australia*, Perth, WA, Western Australian Naturalists' Club.
- SHANG, J., STAENZ, K., LEVESQUE, J., HOWARTH, P., MORRIS, B. & LANTEIGNE, L. Mine tailings characterization using PROBE data (preliminary results). International Geoscience and Remote Sensing Symposium (IGARSS), 2002 Toronto, Canada. IEEE, 2921-2923.
- SHAW, S. C., GROAT, L. A., JAMBOR, J. L., BLOWES, D. W., HANTON-FONG, C. J. & STUPARYK, R. A. 1998. Mineralogical study of base metal tailings with various sulfide contents, oxidized in laboratory columns and field lysimeters. *Environmental Geology*, 33 (2/3), 209-217.
- SKAULI, T., HAAVARDSHOLM, T. V., KASEN, I., ARISHOLM, G., KAVARA, A., OPSAHL, T. O. & SKAUGEN, A. 2010. An airborne real-time hyperspectral target detection system. In: SHEN, S. S. & LEWIS, P. E. (eds.) *Algorithms and Technologies for Multispectral, Hyperspectral, and Ultraspectral Imagery Xvi*. Bellingham: Spie-Int Soc Optical Engineering.
- SLONECKER, E. T. & WILLIAMS, D. J. 2008. *Imaging Spectroscopy for Detecting Fugitive Environmental Contaminants* [Online]. Reston, Virginia: U.S. Environmental Protection Agency.
- SPECIM. 2011. *AISA Series* [Online]. SpecIM. Available: <http://www.specim.fi/products/aisa-airborne-hyperspectral-systems/aisa-series.html> [Accessed 02.01.2012 2012].
- STANDARD, A. N. Z. 2003. Methods for sampling and analysis of ambient air. Method 10.1: Determination of particulate matter—Deposited matter—Gravimetric method. Australia: Australian/New Zealand Standard.
- STUFFLER, T., FOERSTER, K., HOFER, S., LEIPOLD, M., SANG, B., KAUFMANN, H., PENNE, B., MUELLER, A. & CHLEBEK, C. 2009. Hyperspectral imaging-An advanced instrument concept for the EnMAP mission (Environmental Mapping and Analysis Programme). *Acta Astronautica*, 65, 1107-1112.

- SWAYZE, G. A., CLARK, R. N., PEARSON, R. M. & LIVO, K. E. Mapping Acid-Generating Minerals at the California Gulch Superfund Site in Leadville, Colorado using Imaging Spectroscopy. *In: GREEN, R. O., ed. 6th Annual JPL Airborne Earth Science Workshop, 1996 Pasadena. NASA JPL, 231-234.*
- SWAYZE, G. A., SMITH, K. S., CLARK, R. N., SUTLEY, S. J. P., R.M., VANCE, J. S., HAGEMAN, P. L., BRIGGS, P. H., MEIER, A. L., SINGLETON, M. J. & ROTH, S. 2000. Using imaging spectroscopy to map acidic mine waste. *Environmental Science and Technology, 34, 47-54.*
- TAYLOR, G. F. & COX, R. C. The Brukunga Pyrite Mine – A Field Laboratory for Acid Rock Drainage Studies. 6th ICARD, 2003 Cairns, Queensland. ICARD, 93-106.
- TUCKER, C. 1979. Red and photographic infrared linear combinations for monitoring vegetation. *Remote Sensing of Environment, 8, 127-150.*
- USGS 1999. The Global Positioning System (Fact Sheet 062-99). *In: (USGS), U. S. G. S. (ed.). Reston, VA, USA: USGS.*
- USGS. 2007. *USGS Abandoned Mined Lands Initiative* [Online]. USGS. Available: <http://amli.usgs.gov/>.
- VERMOTE, E. F. T., D. , DEUZE, J. L., HERMAN, M. & MORCRETTE, J. J. 1994. *Second simulation of the satellite signal in the solar spectrum (6S), 6S user guide, Version 0*, Greenbelt, MD, NASA Goddard Space Flight Center.
- VISCARRA ROSSEL, R. A., WALVOORT, D. J. J., MCBRATNEY, A. B., JANIK, L. J. & SKJEMSTAD, J. O. 2006. Visible, near infrared, mid infrared or combined diffuse reflectance spectroscopy for simultaneous assessment of various soil properties. *Geoderma, 131, 59-75.*
- WALLACE, J. M. 2002. Ports and Harbours. *In: MCCARTHY, G. (ed.) Technology in Australia 1788-1988.* Melbourne, Vic: Australian Science and Technology Heritage Centre.
- WALLIS, R. & HIGHAM, A. 1998. Progress towards ecologically sustainable development. *In: KNIGHT, J. (ed.) State of the Environment Report Western Australia 1998.* Perth: Department of Environmental Protection.
- WILLIAMS, D. J., BIGHAM, J. M., CRAVOTTA, C. A., TRAINA, S. J., ANDERSON, J. E. & LYON, J. G. 2002. Assessing mine drainage pH from the color and spectral reflectance of chemical precipitates. *Applied Geochemistry, 17, 1273-1286.*
- WILLIAMS, P. C. 1987. Variables affecting near-infrared reflectance spectroscopic analysis. *In: Near-Infrared Technology in the Agricultural and Food Industries* Saint Paul, MN.: American Association of Cereal Chemists Inc.

WILSON, C. 2008. Environmental Management Plan PL-101. *In*: PHPA (ed.). Port Hedland, WA: Port Hedland Port Authority.

WMO 2009. Guideline for the Generation of Satellite-based Datasets and Products meeting GCOS Requirements GCOS-128 (WMO/TD No. 1488). World Meteorological Organization.

WOLD, S., SJÖSTRÖM, M. & ERIKSSON, L. 2001. PLS-regression: a basic tool of chemometrics. *Chemometrics and Intelligent Laboratory Systems*, 58, 109–130.

ZABCIC, N., RIVARD, B., ONG, C. & MULLER, A. USING AIRBORNE HYPERSPECTRAL DATA TO CHARACTERIZE THE SURFACE PH OF PYRITE MINE TAILINGS. 2009 First Workshop on Hyperspectral Image and Signal Processing: Evolution in Remote Sensing, 2009 Grenoble. IEEE, 154-157.

Every reasonable effort has been made to acknowledge the owners of the copyright material. I would be pleased to hear from any copyright owner who has been omitted or incorrectly acknowledged.